Polymer Brushes
—
Wetting Properties and μ-Patterning

Dissertation

zur Erlangung des Grades
„Doktor der Naturwissenschaften"
im Promotionsfach Chemie

am Fachbereich Chemie, Pharmazie und Geowissenschaft
der Johannes Gutenberg-Universität Mainz

vorgelegt von
Sebastian Georg Johannes Emmerling
geboren in Kandel, Pfalz
Mainz, 2010

Dekan: [redacted]

1. Berichterstatter: [redacted]
2. Berichterstatter: [redacted]

Tag der mündlichen Prüfung: 23.09.2010

Die vorliegende Arbeit wurde am Max-Planck-Institut für
Polymerforschung in Mainz unter Anleitung von

[redacted]

in der Zeit von November 2007 bis August 2010 angefertigt.

”Credo ut intelligam.”

Saint Augustine (354-430 AD), Bishop of Hippo

Abstract

In this work polymer brushes on both flat and curved substrates were prepared by *grafting from* and *grafting to* techniques.

The brushes on flat substrates were patterned on the μm-scale with the use of an inkjet printer. Thus it was demonstrated that chemistry with an inkjet printer is feasible. The inkjet printer was used to deposit microdroplets of acid. The saponification of surface-immobilized ATRP initiators containing an ester bond occurred in these microdroplets. The changes in the monolayer of ester molecules due to saponification were amplified by SI-ATRP. It was possible to correlate the polymer brush thickness to effectiveness of saponification. The use of an inkjet printer allowed for simultaneously screening of parameters such as type of acid, concentration of acid, and contact time between acid and surface. A dip-coater was utilized in order to test the saponification independent of droplet evaporation. The advantage of this developed process is its versatility. It can be applied to all surface-immobilized initiators containing ester bonds.

The technique has additionally been used to selectively defunctionalize the initiator molecules covering a microcantilever on one side of a cantilever. An asymmetric coating of the cantilever with polymer brushes was thus generated. An asymmetric coating allows the use of a microcantilever for sensing applications.

The preparation of nanocomposites comprised of polyorganosiloxane microgel particles functionalized with poly(ethyl methacrylate) (PEMA) brushes and linear, but entangled, PEMA chains is described in the second major part of this thesis. Measurement of the inter-particle distance was performed using scanning probe microscopy and grazing incidence small angle X-ray scattering. The matrix molecular weight at which the nanocomposite showed microphase separation was related to abrupt changes in inter-particle distance. Microphase separation occurred once the matrix molecular exceeded the molecular weight of the brushes. The trigger for the microphase separation was a contraction of the polymer brushes, as the measurements of inter-particle distance have revealed. The brushes became impenetrable for the matrix chains upon contraction and thus behaved as hard spheres. The contraction led to a loss of anchoring between particles and matrix, as shown by nanowear tests using an atomic force microscope.

Polyorganosiloxane microgel particles were functionalized with ^{13}C enriched poly(ethyl methacrylate) brushes. New synthetic pathways were developed in order to enrich not the entire brush with ^{13}C, but only exclusively selected regions. ^{13}C chemical shift anisotropy, an advanced NMR technique, can thus be used in order to gather information about the extended conformations in the ^{13}C enriched regions of the PEMA chains immobilized on the μ-gel-g-PEMA particles.

The third part of this thesis deals with the grafting to of polymeric fullerene materials on silicon substrates. Active ester chemistry was employed in order to prepare the polymeric fullerene materials and graft these materials covalently on amino-functionalized silicon substrates.

Contents

1 Introduction

A growing world population is generating an increasing demand for food, better health care, improved housing and numerous consumer products. The chemical industry has seen an extraordinary growth in the last century in response to this increasing demand. For the 21st century a revolution is expected of the chemical industry. A balance between economic considerations and environmental/social issues has to be found. The term *green chemistry* was coined and stands for producing chemicals while being aware of the environment. This includes reducing waste production, reducing materials/energy/resources consumption, and reducing hazards/costs. *Thin film coatings* and *composites preparation* are two versatile strategies for designing materials that have the potential to meet *green* requirements. The advantages of the two mentioned strategies manifest itself in the following arguments:

- Both techniques allow to reduce the amount of functional material, and thus costs, without sacrificing the desired properties.
- Both techniques provide the ability to control properties without designing new materials by a synergy of two well-know materials.

Throughout the course of this thesis it will be demonstrated how the potential of both techniques was utilized to produce novel complex materials from simple building blocks. In all of the projects in this thesis, the building blocks had a size in the nanometer regime.

In recent years efforts have been intensified in research, development, and commercialization of nanomaterials. The major focus was on nanometer thin coatings and nanoreinforcements for polymer composites. A nanomaterial does not only have physical dimensions in the nanometer range, but also has some unique properties by virtue of its size. This definition goes back to Nobel Laureate Richard Feynman and was presented in a talk given in 1959 at the meeting of the American Physical Society at Caltech [1]. Astonishingly Feynman foresaw in this talk the development of nanomaterials and nanomanufacturing methods, such as nanolithography. Yet Feynman did not anticipate the role of chemistry in the ″science of small things″. Nowadays, chemistry is dominating the engineering of small things, along with electrical engineering and materials science [2]. Chemists have developed numerous tools to control the dimensions of a material in the nanometer range and hence the property enhancements.

Especially in the field of polymer synthesis, rapid progress has been achieved. Missing though, is a complete understanding of the structure-property relationship in order to allow the correlation of the molecular structure with macroscopic properties. Computational techniques such as simulations are employed to assist with the construction of structure-property relationships. Despite these efforts the major problems remain. The processing conditions, like mechanical stresses, thermal history, employed solvents affect the final properties of a material. Imperfections and synthetic errors have an additional influence on the properties and need to be taken into account when deriving a structure-property relationship. The imperfections include the degree of end functionality, efficiency of block copolymerization, degree of polydispersity, and shape of the molecular weight distribution. The observation that polymers with higher polydispersity allow for more flexibility regarding processing serves as a good example for the effect of such imperfections. Without the input from experiments with well-defined macromolecules, prediction of macroscopic material properties will remain difficult. Controlled radical polymerization (CRP) techniques are among the tools for the preparation of well-defined macromolecules. **A**tom **T**ransfer **R**adical **P**olymerization (ATRP) has been on of the most successful CRP techniques and most of the polymers in this thesis have been produced via ATRP. ATRP was selected, because it enables good control of composition, architecture, and functionality of polymers. Thus steps towards a more comprehensive understanding of the structure-property correlation have been possible.

2 Fundamentals

2.1 Thin film coatings

The performance of a material is determined by the bulk properties and the surfaces. Especially solids are often coated with a thin organic film to control the interaction of the material with its environment. Coatings have been applied by man for centuries using materials from natural resources [3]. Coatings serve as a protection against corrosion or other degradation processes in most cases. The focus however has shifted as of recently and thin, organic coatings are being successfully applied to control specific interactions between a material and its environment (see Fig. 2.1).

Interface properties like friction [4], adhesion, and wetting by liquids can be controlled by depositing a thin organic film onto a surface. In the medical field, coatings can improve the biocompatibility of an implant or are helping to avoid the nonspecific adsorption of proteins on a analytical device [5].

Even coatings that have only a few Angstroms in thickness can alter the surface properties so strongly, that the chemical nature of the underlying material is completely hidden. By applying such a thin layer total control over the interactions of a materials with its surroundings can be exerted. The application of thin coating has become of great importance in the field of materials engineering, since it enables optimization of bulk and surface properties separately from one another. Countless cases are known today, where a material can only retain its performance, if the polymer layer controlling the surface properties is intact. A distinct example is the computer hard disk [6]. If uncoated, strong stick-slip behavior and a high friction coefficient upon contact with the head is leading to damage. The debris generated is finally leading the rapid failure of the hard disk. Typically thin coatings with perfluo-

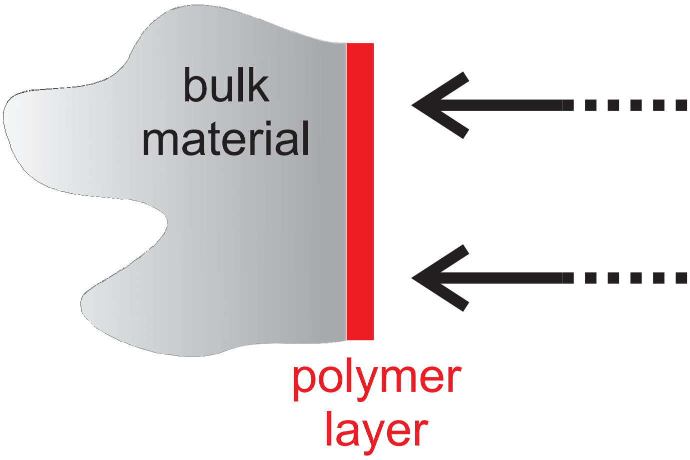

Fig. 2.1: Scheme of a thin polymer coating applied to control the interaction of a material with its environment.

ropolyethers of thicknesses between 2 and 4 nm are used as protection. The mean time to failure of the disk is greatly prolonged by such a thin film, since the wear is reduced dramatically.

As the demand for functional coatings is increasing nowadays, special attention has been devoted to the design of coatings with predictable behavior. A number of ways exist to synthesize materials for coating application. Atom transfer radical polymerization proves to be a well suited method, because it allows control of the composition and architecture of the polymer. Control of the composition and architecture is necessary in order to establish structure-properties relationships.

2.1.1 Atom Transfer Radical Polymerization (ATRP)

In order to understand why ATRP is such a versatile and widely used method, one needs to have a look at alternative polymerization techniques first. Free radical polymerization (FRP) is without doubt the most important method for synthesizing polymers, be it on the industrial level or on the lab scale. Nearly 50% of all polymers are produced nowadays by FRP. The popularity both in research and in industry stems from the fact, that a broad spectrum of monomers can be polymerized in this way. Nearly every alkene can be polymerized using free radical polymerization and a high tolerance for numerous functional groups is given additionally. Moreover, facile copolymerization can be achieved using various monomers. Not to be forgotten is the convenient temperature range in which most polymerizations can be performed. The biggest advantage though, lies in the minimal requirements for purification of the monomers, solvents and reactants. Solely deoxygenation is necessary.

The biggest drawback of FRP is the occurrence of bimolecular termination reactions, viz. recombination and disproportionation. Thus control over molecular weight of the polymers is not easily achieved. Whereas polydispersity of the polymers cannot be controlled at all.

Ionic polymerizations, in comparison, allow control of molecular weight and polydispersity, because termination reactions are negligible. Ionic polymerizations are therefore commonly referred to as *living* polymerizations [7, 8]. Synthesis of more sophisticated polymer structures, such as block and graft copolymers with remarkable properties can be achieved using living polymerization methods. The degree of polymerization (DP_n) can be predetermined by properly adjusting the monomer ($[MM]_0$) to initiator ($[I]$) ratio using following formula.

$$DP_n = \frac{[MM]_0}{[I]} \tag{2.1}$$

The obtained polymers have a narrow molecular weight distribution. A linear increase of molecular weight with conversion is observed as a result of quantitative initiation and absence of termination reactions.

Ionic polymerizations have two drawbacks. One is the high demand on purity of the chemicals, that need to be carefully deoxygenated and dried. The second one is the limited number of monomers that can be polymerized, due to the intolerance towards the majority of functional groups. Hence, controlled radical polymerization techniques have attracted tremendous interest, especially from researchers.

The basis of all controlled radical polymerization techniques is a dynamic equilibration between the propagating free radicals and a kind of dormant

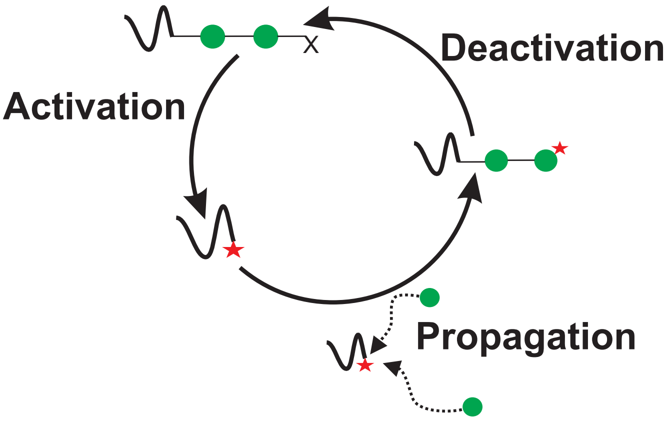

Fig. 2.2: Schematic representation of the exchange between active radical and dormant species in ATRP.

state. A low concentration of free radicals is the result, reducing the probability for the occurrence of termination reactions to less than a few percent of the total number of chains. The controlled radical polymerization techniques are also classified as living radical polymerizations because the produced polymers have a narrow molecular weight distribution, comparable to that of ionic polymerizations. Three controlled radical polymerization techniques are well-established nowadays [9]: (a) *Nitroxide Mediated Polymerization* (NMP) [10–12], (b) *Reversible Addition-Fragmentation Chain Transfer Process* (RAFT) [13–15], and (c) *Atom Transfer Radical Polymerization* (ATRP) [16–18]. Whereas the RAFT process is relying on a degenerative chain transfer process, are ATRP and NMP using a persistent radical effect to establish control over the radical concentration [19]. The focal point of this thesis is on ATRP and thus the details of this polymerization technique will be discussed in the following.

Mechanistic aspects of ATRP

Fig. 2.2 demonstrates how the persistent radical effect is implemented in ATRP. Once a radical is generated, symbolized by the red star, it adds monomers, symbolized by the green dots, in a propagation step, much like in

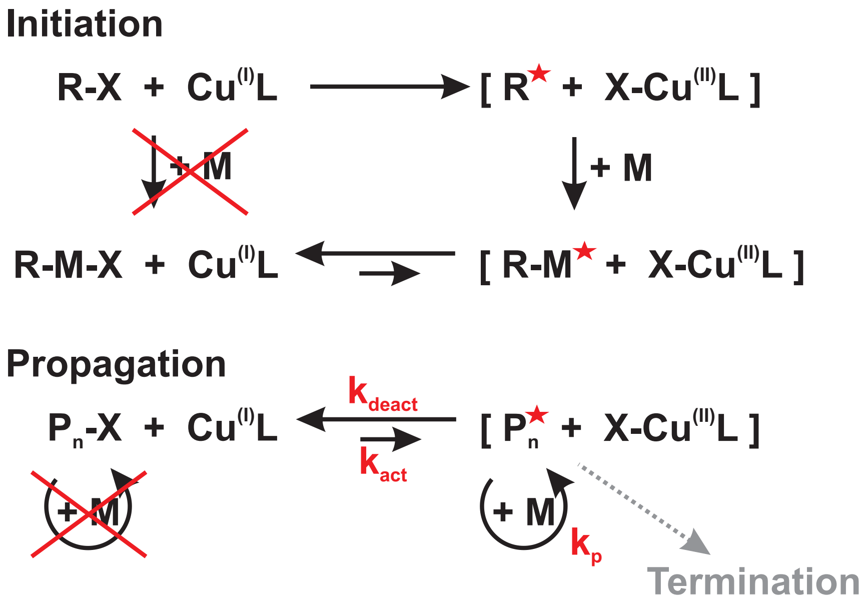

Fig. 2.3: Fundamental steps involved in ATRP and corresponding rate constants.

FRP. The growing radical chain is trapped immediately in a deactivation step by the reaction with a species X. This is in stark contrast to FRP and allows the chains to add only few monomers at a time. After a certain time, an activation step transforms the dormant species back to the radical state and more monomer can be added. Every chain produced by ATRP is passing through such activation - propagation - deactivation - cycle numerous times throughout the course of the polymerization. The advantage of transforming the active chain ends into persistent radicals lies in the fact, that persistent radicals cannot react with each other. Cross-coupling with growing species is thus the only the side-reaction possible for persistent radicals. Despite the short lifetime of active radicals, it cannot be ruled out that two radicals meet. In this case radical-radical termination can occur, generating capping agent X. An accumulation of capping X with reaction time is the result, which is leading to a decrease in concentration of free radicals. The probability of radical-radical termination to occur is thus decreasing with reaction time [20, 21].

The working mechanism of ATRP is depicted in Fig. 2.3. Organic halides

$R - X$ act as initiators and transition metal complexes, such as $Cu^{(I)}L$, act as catalysts. The complex triggers homolytic cleavage of an alkyl halide bond in the initiator and abstracts the halogen atom X, usually chlorine or bromine, in the initiation step. The complex is thus transferred into a higher oxidized species, $X - Cu^{(II)}L$ and a carbon-centered radical $R^{\star}$ is formed. The initiation step is fast and proceeds quantitatively.
$R^{\star}$ adds a small number of monomers M before undergoing reversible deactivation in an equilibrium reaction. The transition metal complex $X - Cu^{(II)}L$ acts as catalyst in the formation of the equilibrium and transfers the halogen atom X to the radical. A dormant state $R - M - X$ is formed and the complex is transformed back to its initial state $Cu^{(I)}L$. As the reaction proceeds and each chain is passing through the activation - propagation - deactivation - cycle over and over again, an equilibrium between a minute amount of growing free radicals $P_n^{\star}$ and a large majority of dormant species $P_n - X$ is established. The dynamic equilibrium can only be established, if the rate constant of the activation step (k_{act}) is smaller than the rate constant of the deactivation step (k_{deact}).

$$k_{act} << k_{deact} \tag{2.2}$$

The rate constant of activation is typically lower by 5-7 orders of magnitude compared to the rate constant of deactivation, whereas the rate constant for propagation k_p is somewhere in between [22]. One important aspect in ATRP is the fact, that kinetics and reaction control depend not only on the persistent radical $X - Cu^{(II)}L$, but also on the activator $Cu^{(I)}L$. Molecular weights are not affected by the concentration of the transition metal complex and are defined by $[M]_0/[R - X]$. The polymerization rate R_p however is proportional to the ratio of concentrations of activator to deactivator $[Cu^{(I)}L]/[X - Cu^{(II)}L]$ and increasing with initiator concentration $[R - X]$.

$$R_p \approx \frac{[Cu^{(I)}L]}{[X - Cu^{(II)}L]} \approx [R - X] \tag{2.3}$$

The synthesis of polymers with low polydispersity requires however a sufficient concentration of deactivator $X - Cu^{(II)}L$. The polydispersity is decreasing with concentration of deactivator $[X - Cu^{(II)}L]$ and with monomer conversion p, but increases with the k_p/k_{deact} ratio.

$$PDI = \frac{M_w}{M_n} \approx p^{-1} \approx [X - Cu^{(II)}L]^{-1} \approx \frac{k_p}{k_{deact}} \approx [R - X] \qquad (2.4)$$

The polydispersity is lower for higher target molecular weights, in other words, lower initiator concentrations $[R - X]$ [23]. Before looking at the basic ATRP components, it is worthwhile to discuss some similarities and differences between FRP and ATRP. The participation of dormant states prolongs the lifetime of a growing chain in ATRP to roughly 1 h compared to a lifetime of roughly 1 s in FRP. A short example illustrates this. The typical lifetime of a propagating chain in FRP is roughly 1000 ms, i.e. ~ 1 s. Chains in ATRP are active only for a short time, lets assume ~ 1 ms. Then transfer to the dormant state takes place, in which they remain for a longer time (~ 1 min). Assuming that each chain is passing through the activation - propagation - deactivation - cycle 1000 times during a polymerization, we get a lifetime of 1000 ms in the active state. The lifetime in the active state is thus comparable to the lifetime in FRP. The whole propagation process in ATRP takes 1000 min. however, in other words, roughly 1 day. The length of the propagation process in ATRP allows to perform various synthetic procedures, such as chain extension and others [24].

A steady state of growing radicals in FRP is formed by a balance of initiation and termination. Initiation is typically slow and initiator is left unconsumed even at the end of the polymerization. In ATRP the steady state of growing radicals is established by the rapid transfer of chains between active and dormant state. Initiation is typically much faster than termination. Thus all chains start growing at the same time and grow more or less to the same length.

Nearly all chains in FRP are dead, whereas the percentage of dead chains in ATRP is commonly lower than 10%.

Basic ATRP components

A variety of monomers has been successfully polymerized by ATRP as the following list demonstrates.

- styrenes
- (meth)acrylates
- (meth)acrylamides
- vinyl pyridine
- acrylonitrile

The list includes the more common monomers [25, 26], but ATRP has been used for many others [18]. Polymerizing monomers carrying functional groups, such as hydroxy, amino, amido, ether, ester, presents no challenge in ATRP. It should be noted however, that the ATRP equilibrium constant (k_{act}/k_{deact}) is determined by the structure of the monomer and the initiator $R - X$. Thus the choice of the monomer determines the catalyst that has to be used. ATRP proved to be very valuable for the preparation of block copolymers. Chain extension of a macromolecular alkyl bromide with a second monomer using CuBr is one possible route to block copolymers. The use of alkyl chloride-type (macro)-initiators and CuCl yields block copolymers with lower polydispersity however [27]. Alkyl chloride-type (macro)-initiators have an ATRP equilibrium constant that is 1-2 orders of magnitude lower than the one of alkyl bromides. C-Cl bonds are activated more slowly, which is the reason for the lower ATRP equilibrium constant. Slower activation leads to a lower rate of propagation with respect to the rate of initiation and thus an increased initiation efficiency from the macroinitiator is observed [28].

An advantage of ATRP can be seen in the broad availability of initiators. Alkyl halides ($R - X$) bearing activating substituents on the α-carbon such as aryl, carbonyl, or allyl groups are typically used in ATRP.

A typical ATRP-initiator is shown in Fig. 2.4. The reactivity of such an initiator is governed by the colored regions [29]. An increase in reactivity

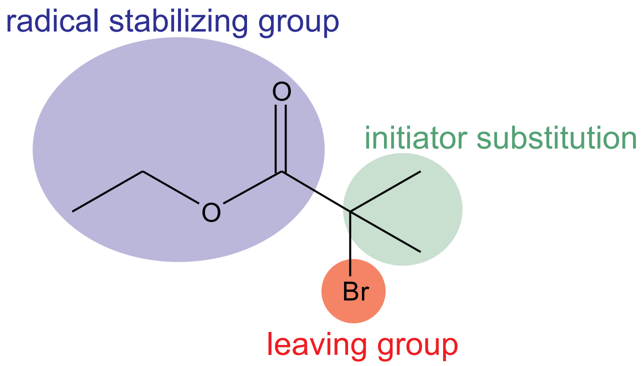

Fig. 2.4: 2-Ethyl α-bromoisobutyrate (2-EiBBr), a typical initiator for ATRP. The colored regions mark the sites determining the reactivity of the initiator.

is observed with increasing initiator substitution (for example: $primary < secondary < tertiary$). The reactivity of the initiator is also linked to the radical stabilizing group and its ability to withdraw electrons (for example: $-C(O)NEt_2 < -Ph \approx -C(O)OR \ll -CN$). The bond dissociation energy ($iodo < bromo < chloro$) of the leaving group has a reciprocal influence on the reactivity.

The most important component of an ATRP system is by far the catalyst, consisting of a transition metal and one or more ligands complexing the metal atom. The catalyst controls the exchange between dormant and active state and therefore determines the position of the ATRP equilibrium. The use of a variety of transition metals in ATRP is documented: Molybdenum [30], Rhenium [31], Ruthenium [17] and Iron [32], Nickel [33] and Palladium [34], and the most efficient one, Copper [16]. The use of Cu has several advantages:

- Two readily accessible oxidation states separated by one electron.
- Reasonable affinity towards halogen.
- Low affinity towards hydrogen.
- Low tendency to complex with polar monomers.

The role of the ligand is solubilizing the metal-salt in the organic environment and to adjust the redox potential for appropriate reactivity and dynamics of

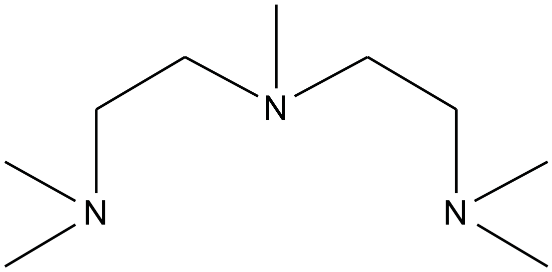

Fig. 2.5: N,N,N′,N″,N″-Pentamethyldiethylenetriamine (PMDETA), a typical polydentate nitrogen-containing ligand for ATRP.

the atom transfer. Polydentate nitrogen-containing ligands are most widely used together with Cu in ATRP [18]. An example for such a ligand is shown in Fig. 2.5.
PMDETA shows a high complexing ability whilst keeping the coordination sphere around the metal expandable upon oxidation [35], allowing the accommodation of a halogen. The activity of a ligand is depending on [36]:

- Linking unit between N atoms ($C4 \ll C3 < C2$) and thus coordination angle.
- Topology of the ligand ($cyclic \approx linear < branched$).
- Nature of the ligand ($arylamine < alkylamine \approx pyridine$) [37,38].
- Steric effects.

2.1.2 Coating Techniques

ATRP is a well-suited method to produce tailor-made materials for a coating application. Producing the polymer however is just one step towards a coating. The choice of the coating technique is of equal importance [39]. Coating techniques are divided into two categories, depending on the interactions between coating and substrate. The interactions can be of physical [40–42] or chemical nature. Chemical bonds between substrate and coating are formed in the latter case, leading to irreversible anchoring of the coating. Physical interactions are by far not as strong as chemical interactions. The physical properties of a coating and its long-term stability are thus determined by the choice of coating technique. Moreover has the choice of coating technique an influence on the final film thickness.

Coating techniques that are of industrial relevance mainly rely on physical interactions between coating substrate. Examples for such relevant techniques are:

- Painting.
- Spray coating.
- Dip coating.
- Spin coating.
- Doctor blading.

All the above-mentioned techniques share solvent evaporation as a common basis. Careful control of the deposition conditions allow to reproducibly produce homogeneous layers with well-defined thickness nevertheless.

As an alternative to these simple coating procedures emerged several techniques that are more sophisticated. An examples for such a technique is the deposition of a multilayer of two oppositely charged polyelectrolytes, typically called the Layer-by-Layer technique [43]. A simplified version of this technique is the deposition of monomolecular layers of homo- or block-copolymers [40] from solution. The Langmuir-Blodgett technique [44] is by far the technologically most advanced technique and requires the use of a more complicated set-up. The more sophisticated techniques allow precise control of film thickness and internal film structure.

The techniques discussed thus far rely on physical interactions between deposited molecules and substrate. Failure of adhesion in hostile environments is an issue however and leads to destruction of the coating. Four mechanisms have been identified leading to the destruction of physically absorbed coatings:

- Desorption.
- Displacement.
- Dewetting.
- Delamination.

Desorption is a common failure mechanism upon exposure to solvents capable of dissolving the coating. The solvent molecules are competing with coating molecules for surface sites. Charged substrates present a problematic case, since they exhibit a strong affinity towards water. The desorption mechanism is a low molecular weight case of the displacement mechanism. Contaminants that have stronger interactions with the substrate compared to the coating molecules are displacing the coating molecules on the surface. Polyelectrolytes are a common examples for such a contaminant. The prerequisite for dewetting to occur is a higher surface tension of the coating material compared to that of the substrate. Once the coating molecules reach an equilibrium, dewetting can be observed. Heating a polymer film above the T_g or adsorption of a plasticizer can be the trigger for dewetting. In contrast to that can delamination be observed for films in the glassy state. The entire film can peel off, if mechanical stress is developing at the interface. Mechanical stress can be generated by external stimuli. The external stimuli can be either a temperature swings or swelling. Both can lead to different expansion/contraction of the coating and substrate.

One common way to prevent failure of adhesion is to switch from physical interactions between coating and substrate to chemical interactions. Films with long-term stability in hostile environments can be produced by creating a covalent bond between coating molecules and substrate. Creating these covalent bonds requires more complicated coating techniques. Side reactions have to be prevented and it has to be ensured that the surface reaction proceeds with high yield.

The preparation of self-assembled monolayers (SAM) [45] is one way to produce coatings that are covalently anchored. Small molecules with reactive end groups are typically used. The surface-attachment stops once all surface sites are consumed or no longer accessible and the reaction is thus selflimiting. The most dominant example of such a SAM are silanes on oxide surfaces, or thiols on noble metal surfaces. If molecules carrying a functionality at the tail end are used, novel surface properties can be generated. Such a functionality could be a fluorocarbon segment. A hydrophilic surface covered with a SAM carrying fluorocarbon segments can thus be transformed into a hydrophobic one exhibiting water repellent properties [46, 47]. A combination of soft lithography with the preparation of a SAM can be used to generate a spatial 2D arrangements of functional groups [48].

The preparation of SAMs has one limitation with regard to the surface density of functional groups. The maximum density that can be achieved is given by the surface area cross-section of the assembled unit. In the majority of cases the density is lower though, because functional sites become blocked by neighbors at high densities. A 3D-arrangement of functional groups is the solution to this problem. Using polymer chains carrying functional groups along the chain, coatings with a high cross-sectional densities of functional groups can be produced.

2.1.3 Surface-attached polymers

Most approaches for producing surface-attached polymers rely on a principle derived from the preparation of SAMs. Polymers carrying an anchor group at the chain end or somewhere at a side chain are used. The anchor groups react with chemical moieties on the surface, in analogy to the preparation of SAMs. Synthesis of (end)functionalized polymers is not trivial from a chemical point of view, but the chemistry of the attachment reaction is rather simple and well-established due to the work conducted on SAMs. Attachment of the polymers to the surface at one point of the chain is achieved by using terminally functionalized polymers. Multiple attachment points can be created by using side-chain anchor groups. Multiple attachment points thus give polymers layers with a more flat conformation of the individual chains. Surface-attached monolayers of polymer molecules are produced by this approach generally referred to as *grafting to* [49, 50]. A schematic illustration can be found in Fig. 2.6 on the left. The structures that can be obtained by

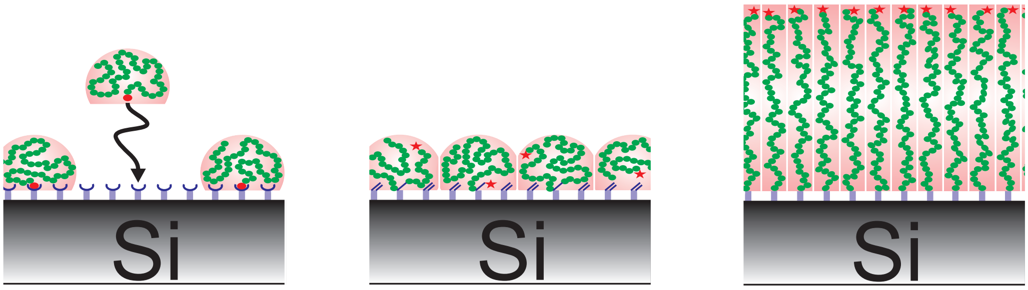

Fig. 2.6: Schematic illustration of different techniques available for the attachment of polymers to surfaces. Grafting to (left). Grafting by reaction of growing chains with surface-bound monomeric units (middle). Grafting from / Surface-initiated polymerization (right).

this procedure are rather limited. Polymers carrying functional groups that can compete with the anchor group for surface sites cannot be grafted using the grafting to procedure. Very common is the use of chlorosilyl anchoring groups and these do not tolerate amine-, hydroxyl- or carboxy functionalities. Conducting a polymerization reaction in the presence of a surface functionalized with monomeric units is also regarded as grafting to. The procedure is schematically illustrated in the image found in the center of Fig. 2.6. Initiator molecules start the polymerization in solution and free monomeric units are consumed in a first step. An attack of such a macroradical on one or more surface-bound monomeric units can occur in a second step. The surface-bound monomeric unit is thus incorporated into the backbone and the growing chain is attached to the surface. Again free monomeric units can be added, as the reaction proceeds, and the chain grows away from the surface. The bottleneck of the reaction is the attack of the macroradical on the surface-bound monomers in the second step [51].

Both mentioned grafting to procedures share a limitation. The film thicknesses that can be obtained by chemisorption from solution are typically limited to 5 nm. The origin of the limitation is both kinetic and entropic in nature. A kinetic hindrance of attachment can be observed with increasing reaction time. The concentration of polymers at the interface is rapidly exceeding the concentration in solution with increasing coverage of the surface. Additional chains have to overcome a concentration gradient in order to reach the surface and become attached [52]. The concentration gradient increases with increasing grafting density and slows diffusion towards the surface. The increasing diffusion barrier directly hinders attachment. A leveling off in the rate of immobilization is observed and additional polymer is attached at an extremely low rate, as the reaction proceeds. Theoretical considerations predict that additional grafting takes place on a logarithmic time scale once the attached coils begin to overlap [49, 50]. Experimental evidence has been acquired confirming the predictions. Time frames of thousands of years are inevitable if a few nanometers of polymer are to be added to a layer of low grafting density. Thermodynamic reasons are additionally opposing the attachment of chains to already covered substrates. Coils are starting to overlap once the substrate is fully covered. Unfavorable segment-segment interactions are the result of the overlap, leading to deformation of the coils. Every chain, which is about to be attached to such a covered substrate, has to change its conformation from a coil to a more stretched shape. This loss of chain entropy has to be compensated by the energy released by forming a chemical bond between substrate and polymer chain. Smaller distances between grafting points leads to bigger chain deformations. The entropic penalty for attaching another chain is thus increasing. The gain in enthalpy by establishing a chemical bond is unchanged however.

Grafting to procedures typically produce polymer layers with a distance between anchoring sites larger than the dimension of the individual polymer coil. Segments belonging the individual chains thus do not interact. Each single chain behaves like a polymer coil attached by one end to a surface. This situation is illustrated on the left in Fig. 2.7. The term mushroom conformation is used to describe grafted chains exhibiting such a conformation [53].

By properly adjusting the reaction conditions and the concentration of polymer in solution of a grafting to reaction one can produce a polymer layer with slightly overlapping polymer coils. This situation is illustrated in the image found in the center of Fig. 2.7. Densely grafted layers cannot be prepared by a grafting to approach. The next section is dealing with the synthesis and theoretical description of such densely grafted (brush-like) layers.

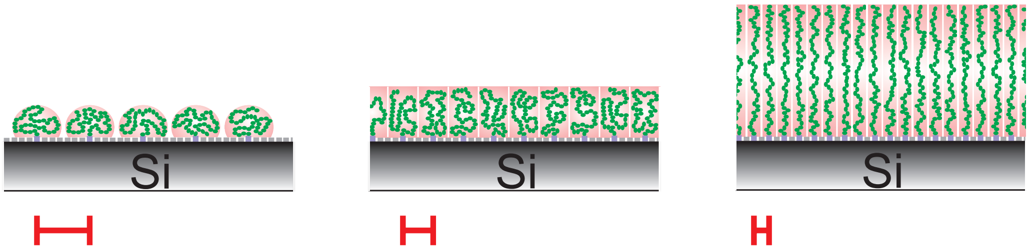

Fig. 2.7: Schematic illustration of different conformations that surface-attached polymers can exhibit, depending on the distance between grafting sites (red bars). Mushroom conformation (left). Intermediate (middle). Brush conformation (right).

2.2 Polymer Brushes

Polymer chains chemically grafted to a surface in such a way that the distance between grafting site is low enough for the chains to become crowded are commonly referred to as a *polymer brush*. As result of the crowding a stretching of the chains perpendicular to the surface is observed. The stretching is the reason for the much higher film thicknesses observed for polymer brushes compared to brushes in the mushroom regime, even if they have the same degree of polymerization. This relationship between brush conformation, grafting density and film thickness is depicted in Fig. 2.7 [40,54,55].

2.2.1 "Grafting from" - Surface-initiated polymerization

Surface-attached polymers with such high grafting densities that lead to strong stretching of the chains can be produced by a *grafting from* procedure. A schematic illustration of grafting from can be found in Fig. 2.6 on the right. A small molecule is self-assembled on the surface in this technique. The small molecule has an anchoring group and a group capable of initiating a polymerization reaction. The chain growth is initiated from these molecules subsequently. The diffusion of monomers to the primary radicals, or later on growing chain ends, is not limited by the already grafted chains. Virtually every known polymerization protocol, ranging from polycondensation to chain growth reactions, has been carried out on surfaces using the grafting

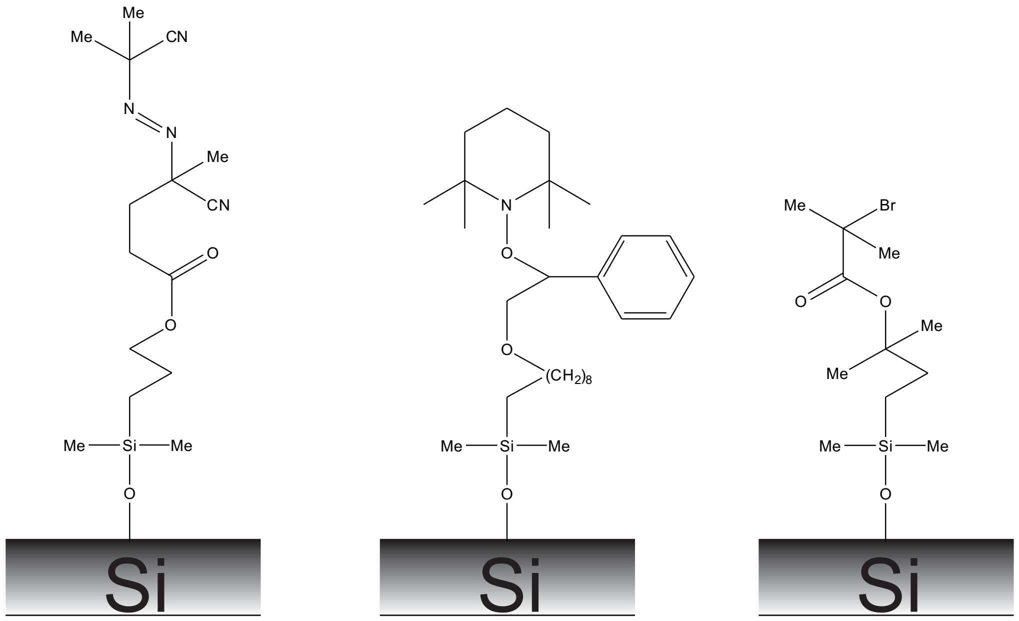

Fig. 2.8: Selected systems for surface-initiated polymerization following a free radical protocol (left) [53], a nitrogen mediated protocol (middle) [56], and an atom transfer protocol (right) [57].

from procedure. The variety of polymerization protocols allows to generate polymer brushes from almost any monomer. No limitations were found for surface-initiated polymerizations regarding the type of surfaces (inorganic, organic) or topologies (planar, curved, irregular) that can be used. Three prominent examples for surface-attached initiators were therefore selected and are shown in Fig. 2.8.

Rühe et al. [53,58,59] successfully used surface-initiated free radical polymerization (SI-FRP) to prepare films with thicknesses of more than 2200 nm with a distance between anchoring points below 3 nm. The initiator that they used is depicted on the left in Fig. 2.8. Poor control over chain length and polydispersity of the brushes is the major drawback of SI-FRP. Longer chains in such a polydisperse brush will form an outer fringe with relatively low segmental density. The properties of the higher density brush near the surface are thus masked by the fringe. Living systems with rapid initiation enable control over the brush parameters [60]. Surface-initiated graft polymerizations using controlled living radical polymerization (LRP) techniques have garnered tremendous interest among researchers. SI-LRP techniques provide simple, yet robust, synthetic routes to well-defined (co)polymer brushes. A common approach is to immobilize a conventional radical initiator on the surface, such as the one shown on the left in Fig. 2.8 and adding a free capping agent to the solution (reverse LRP). RAFT-mediated grafting from is mainly conducted in this reverse mode [61]. Immobilizing the dormant species on the surface and adding a free initiator to the solution phase seems to be the more promising route towards well-defined polymer brushes [62]. Fig. 2.8 shows two examples of surface-immobilized dormant species including an alkoxyamine for NMP (middle) and a haloester-compound for ATRP (left).

One has to be aware of the fact that a surface-initiated polymerization has different characteristics than those conducted in solution. The reason for the different characteristics are the crowding of the chains and the tethering of the initiating/dormant species. The question arises, especially for SI-LRP techniques, whether the initiation is efficient on the surface. Among the most important brush parameters is the grafting density. The efficiency of the initiation is thus the dominant factor in determining the grafting density. Another aspect that has to be considered, is if the crowding of the chains has an effect on the reaction rates. The local concentration of reactants near the growing chain ends will differ from those in solution. Intermolecular reactions between the tethered radicals will become more likely, leading to an increase in bimolecular termination and chain transfer on the surface. The situation is further complicated by the limited surface area, that flat substrates present. The concentration of initiating/dormant species is therefore low, which could lead to poor reaction control.

One way to explore these issues, is to compare the chain length and polydispersity of grafted and free chains produced in one reaction. Free initiator can be added to the reaction solution in order to produce free polymer. Hence the reaction proceeds simultaneously in solution and on the surface.

The focal point of this thesis is on SI-ATRP and thus the details of this polymerization technique will be discussed in the following.

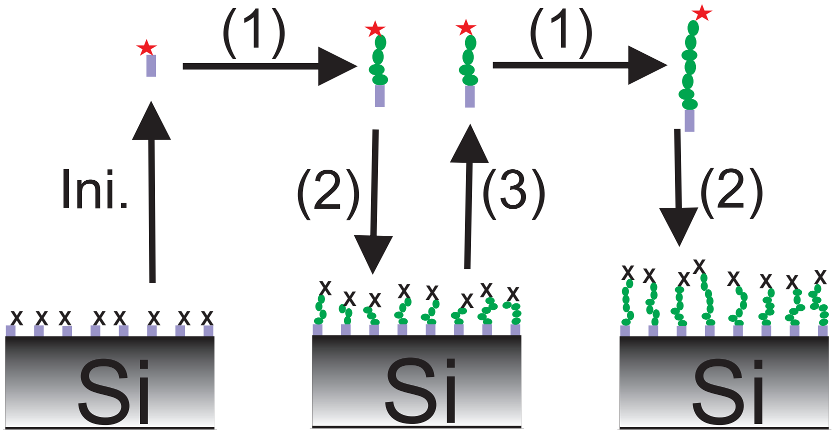

Fig. 2.9: Scheme of surface-initiated atom transfer polymerization illustrating the: (Ini.) initiation step, 1.) propagation step, 2.) deactivation step, 3.) activation step.

Surface-initiated ATRP

Ejaz et al. were the first to conduct SI-ATRP on a flat substrate successfully [63]. Since this initial report, SI-ATRP has been conducted on a variety of other materials [64], including fine particles and porous materials. The SI-ATRP process is schematically illustrated in Fig. 2.9. An activator, such as an organic copper complex, abstracts an halogen atom of the immobilized initiating species (Ini.) or dormant species (3). The radical adds a small number of monomers in the propagation step (1), before it is capped in a deactivation step, forming a dormant species (2). Each chain is passing through this activation - propagation - deactivation - cycle repeatedly as the reaction proceeds. All chains seem to grow simultaneously and thus controlled, when examined on a longer time scale. This is in stark contrast to a SI-FRP reaction. Once a radical is formed on the surface, it grows to a high-molecular tethered polymer. An increase in the number of grafted chains is observed, as the reaction proceeds.

The concentration of initiating species in SI-ATRP from flat surfaces is rather low, as pointed out previously. The main challenge is thus to increase the persistent radical/deactivator concentration after transfer of the halogen atom to the copper catalyst. Otherwise uncontrolled chain growth can occur, since the number of deactivator species is too low to reversibly trap active chains. Two alternative approaches have been designed in order to increase the persistent radical/deactivator concentration. One approach addresses the challenge through the addition of persistent radicals/deactivator, whereas the other approach is relying on the addition of sacrificial initiator.

The addition of radical deactivating agents, such as Cu(II)halides, at the beginning of the reaction allows to control SI-ATRP. The deactivating agent facilitates rapid trapping of active radicals, as predicted from the persistent radical effect [20, 21]. The approach was successfully implemented for the first time by Matyjaszewski et al. [65]. A linear increase of amount of grafted polymer with polymerization time was observed, which is a good indication for the living nature of the SI-ATRP reaction and a constant grafting density. The publication by Matyjaszewski indicates however, that it is not sufficient to add a deactivating agent alone. Control of the Cu(I) concentration is necessary in addition. They observed excessive termination reactions among the tethered radicals even in the presence of a deactivating agent, as long as the overall concentration of Cu(I) was too high. Wirth et al. overcame this challenge by diluting the catalyst using higher concentrations of monomer [66].

The alternative approach to the addition of deactivating agents is the addition of sacrificial initiator. Untethered small initiator molecules are added to the ATRP mixture containing the functionalized substrate at the beginning of the reaction. The result is that the polymerization proceeds simultaneously on the surface and in the solution. This approach offers a number of benefits regarding both synthesis and characterization of the brushes, as Ejaz et al. [63] and Husseman et al. [56] stated. A sufficient concentration of persistent radicals/deactivator is formed in systems with free initiator by termination of radicals formed in the solution, in analogy to ATRP. One of the advantages of adding sacrificial initiator can be seen in the fact that the degree of polymerization of the tethered chains is dominated by the initial concentration of the sacrificial initiator. Another major advantage is that the free polymer produced by the sacrificial initiator can be analyzed with standard techniques, e.g. gel permeation chromatography (GPC). The determination of monomer conversion and chain length, as well as chain length distribution, of the polymers in the system is thus facilitated. One of the issues concerning SI-LRP reactions is whether the reaction proceeds in a similar fashion both on the surface and in solution, as stated previously. Several research groups have compared the chain length and polydispersity of grafted and free chains produced in a SI-ATRP reaction in order to resolve this fundamental question [56,67–69]. These research groups compared free polymer grown in solution to polymer grown on silica particles by subsequently cleaving off the polymer from the particles. A good agreement in molecular weight and polydispersity index was found. The agreement was verified using various particle sizes, suggesting that the curvature does not affect polymer growth. No such data is available for SI-ATRP on flat substrates. Koylu et al. attached a photopolymer film containing ATRP initiating sites on a silicon substrate and conducted SI-ATRP using sacrificial initiator [70]. Analysis of the free polymer and the cleaved polymer resulted in a higher molecular weight of the cleaved brushes compared to the free polymer. Furthermore did they observe an increase in the difference of molecular weight between free and cleaved polymer with increasing molecular weight. Koylu et al. thus presented first evidence, that it cannot be universally assumed that the growth kinetics of polymer brushes and polymers grown from free initiator in solution are the same. One should be careful though to compare the results obtained by Koylu et al. directly to results obtained from a monolayer of initiating sites. The systems are too different in nature, since Koylu et al. used a photopolymer film containing ATRP initiating sites. More data for SI-ATRP on flat substrates is not available. Devaux et al. succeeded to compare the molar mass and polydispersity of cleaved chains to polymer grown in solution for SI-NMP on flat silica substrates [71]. Both molar mass and polydispersity of free polymer and cleaved polymer were similar. One has to keep in mind, that the surface area of flat substrates and thus the amount of grafted polymer is in most cases too low to conduct reliable analysis. A short example illustrates this. The total amount of grafted polymer is as low as 0.5 ng for a wafer the size of 2 times 2 cm. The value was obtained assuming a grafting density of 0.4 $chains/nm^2$ and a molecular weight of 30000 g/mol for the polymer brushes. Even if the entire amount of 0.5 ng would be recovered after cleavage, it would barely be enough to be detectable in GPC.

Ejaz et al. [63] were able to produce PMMA brushes with a grafting density of 0.8 $chains/nm^2$ from a initiator monolayer created with the Langmuir-Blodgett technique. The question arises why it is possible to obtain brushes with such a high grafting density. It is known from ATRP carried out in solution that the initiation efficiency is essentially 100 %. This conclusion can be drawn, since each chain is passing through a activation - propagation - deactivation - cycle numerous times without termination. The initiation step is essentially one of these activation steps [72,73]. Measurements of the grafting density Γ_i of the initiating dormant species have revealed however, that Γ_i is much higher than the grafting density of the polymer brushes Γ. SI-ATRP seems to show a lower initiation efficiency compared to ATRP in solution, where 100 % of the initiating moieties start a polymer chain.

The obvious explanation is suggesting that surface bound radicals are close together and radical-radical termination is the dominant reaction at the surface. The surviving chains would be the ones forming the polymer brush. A comparison of experimental data obtained by several research groups reveals however that the grafting density of brushes seems to be independent of polymerization conditions [56,63,74–76]. In other words, the concentration of radicals is not the determining factor for the grafting density. The results were obtained independently for different surfaces geometries (flat, convex) and materials (silicate, gold) using different types of initiating species. An increased probability for radical-radical termination at the surface can thus be ruled out as explanation for the discrepancy in Γ_i and Γ.

Tsujii et al. [77] offer an explanation for the reduced initiation efficiency in SI-ATRP based on an excluded volume argument. The cross-sectional area per monomer unit a^2 can be calculated using v_0 and b_{eff}.

$$a^2 = v_0/b_{eff} \tag{2.5}$$

The cross-sectional area a^2 is represented by the pink area on the surface and the grey area inside a monomeric unit on the left in Fig. 2.10. v_0 describes the molecular volume per monomer unit as estimated from the density of

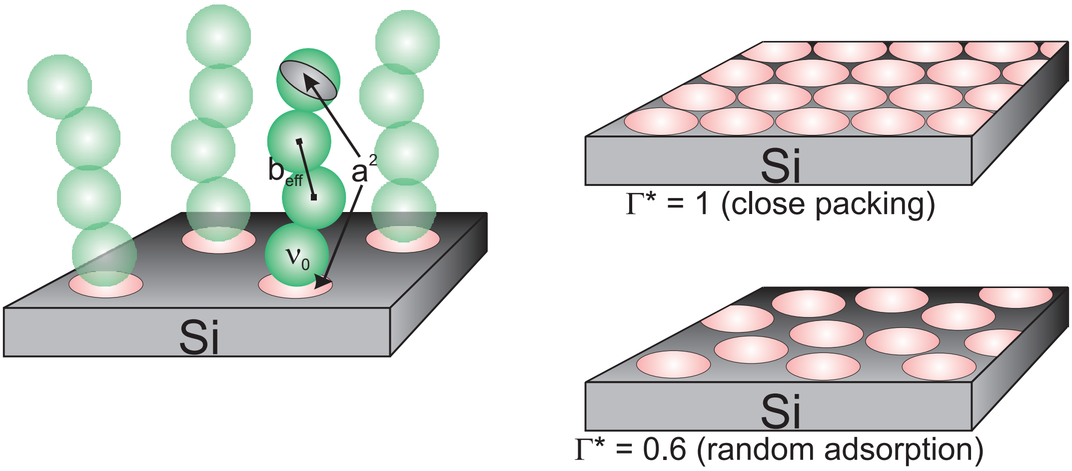

Fig. 2.10: Scheme representing the effect of the excluded volume of monomers on the initiation efficiency in SI-ATRP.

monomer in the bulk. A monomeric unit is represented by a green sphere in Fig. 2.10. b_{eff} is the effective bond length and represents the distance between the center of mass of two monomeric units in a chain. A typical value for the effective bond length in the case of vinyl monomeric units is $b_{eff} = 0.25nm$ [78]. The cross-sectional area per monomer unit a^2 can be used together with the experimentally observed value for the grafting density Γ in order to calculate a dimensionless grafting density $\Gamma^\star$.

$$\Gamma^\star = a^2 * \Gamma \tag{2.6}$$

For a close packing of physically completely stretched chains (all-trans conformation) $\Gamma^\star$ would reach a value of 1. The close packing of chains is depicted in the scheme on the upper right in Fig. 2.10. Using the experimentally observed values for the grafting density Γ of 0.5 *to* 0.8 $chains/nm^2$ Tsujii et al. calculated values of $\Gamma^\star$ ranging from 0.4 *to* 0.6. A simulation of the random and irreversible adsorption of spheres on a flat substrate returned exactly a value for the average surface coverage of $\Gamma^\star = 0.6$. A surface coverage of $\Gamma^\star = 0.6$ is depicted in the scheme on the lower right in Fig. 2.10. The simple considerations by Tsujii et al. seem to confirm what Matyjaszewski et al. [65] and Shah et al. [76] have speculated on. Steric factors inhibit polymer growth from every initiator molecule in a SAM immobilized on a flat substrate. Shah et al. [76], as well as Kim et al. [79], succeeded in calculating the average cross-sectional area A_x of a chain within a brush directly from the brush molecular weight M, the corresponding brush thickness d, and the bulk density of the polymer ρ.

$$A_x = \frac{M}{t * \rho * N_A} \tag{2.7}$$

The value of $A_x = 180 - 200\ \mathring{A}^2$ obtained was much higher than the surface area of an initiator molecule ($\sim 20\ \mathring{A}^2$), as measured in a Langmuir through. The grafting efficiency has to be roughly 10 % therefore. In other words, one out of ten initiator molecules is expected to initiate polymer growth. Jordan et al. conducted surface-initiated anionic polymerization and found out that one polymer brush was formed per 17 initiator molecules [80]. Bimolecular termination reactions cannot occur in anionic polymerization, so it seems very likely that steric hinderance is the reason for the low initiation efficiency in surface-initiating polymerizations.

An approach to gather more information about the growth mechanism of polymer brushes under SI-ATRP conditions has been presented by Yamamoto et al [81]. Changes in grafting density of the initiator Γ_i, as estimated from FT-IR measurements, were achieved by photodecomposition of a dense monolayer using UV-light. Longer irradiation times resulted in lower Γ_i. No changes in brush grafting density were observed for short irradiation times. The decrease in Γ_i must have lead to an increase in initiation efficiency, which was as low as 20 % for the unirradiated sample due to steric reasons. The initiation efficiency reached 100 % once the grafting density of the initiator reached the maximum value of brush grafting density ($\Gamma_i = \Gamma$). Longer irradiation times resulted in a decrease of brush grafting density as a function of a decrease in grafting density of the initiator. Difficulties in determining Γ_i for long irradiation times inspired several research groups to develop a different approach to control Γ_i. Blending of intiator molecules with ATRP-inactive molecules and subsequent deposition allows to prepare monolayers with varying Γ_i. Ejaz et al. [82] did not observe changes in grafting density, and hence layer thickness, upon incorporation of up to 40% of an inert molecule into the monolayer. The dilution of the initiator molecules did not reach the maximum value of brush grafting density in this case. In other words, the initiation efficiency was increasing up dilution, but did not reach the maximum value of 100 %. Ejaz et al. were not able to prepare monolayers with higher content than 40 % of inert molecules. Jones et al. on the other hand were able to prepare monolayers with varying content of initiator molecules ranging from 0 *to* 100 %. The obtained results differ from those obtained by the aforementioned authors. A direct proportionality between film thickness and initiator density was observed by Jones et al. The film thickness maintained from a monolayer with 10 % initiator content, for example, reached 1/10 of the film thickness maintained from a monolayer with 100 % initiator content. Dilution of the initiator lead directly to larger distances between polymer molecules and not to changes in initiation efficiency. The system used by Jones et al. cannot be compared to the ones used by Yamamoto et al. and Ejaz et al. however. Jones et al. did not use sacrificial initiator nor deactivating agents and worked in aqueous solution. It can be doubted therefore, that the polymerization was well-controlled in the beginning, since the concentration of initiating species was too low for that. Under these circumstances one can understand the observation by Jones et al., that initiation at the surface was not quantitative and independent of SAM composition.

Many research groups have investigated the effect of varying initiator density on the grafting density of the brushes, as illustrated above. The grafting density is one of the major factors determining not only conformation of the polymer brushes, but also their unique physical properties. The so-called autophobic behavior is an example for such a unique property. Applying a free polymer to a material coated with a surface-attached polymer layer leads to dewetting, even if the free and grafted chains are chemically identical. The grafting density of the surface-attached layer needs to exceed a certain threshold value in order for autophobic behavior to occur. Above this threshold value dewetting is observed once the molecular weight of the free polymer is higher than that of the grafted chains [81–84].

2.2.2 Theory of Polymer Brushes - flat interfaces

A theoretical description of polymer brushes is necessary, in order to understand the relationship between the structure and the properties of polymer brushes. The goal of this Section is to give a brief outline of brush theory based on the two reviews by Milner [85] and Halpering et al. [40].

Attaching one end of polymer chains to a surface at distances low enough to cause crowding leads to unfavorable segment-segment interactions. The chains minimize these excluded volume interactions by stretching away from the surface. The deformation, in turn, reduces the number of possible conformations that the polymer chains can exhibit, which is equal to a loss of chain entropy. Therefore the stretched chains are in an equilibrium with higher energy level, compared to the equilibrium conformation with the lowest energy level, which is the random coil conformation. A retracting force is acting on the stretched chains, trying to restore the random coil conformation, much like in a stretched piece of rubber. Thus the deformation is a result of the competition between the interaction energy F_{int} of polymer segments and the entropic elastic energy of the chain F_{el}. Both terms, F_{int} and F_{el}, contribute to the free energy of a polymer brush [86].

$$F = F_{int} + F_{el} \tag{2.8}$$

This energy balance argument is similar to the one used by Flory to define the Flory exponent [87] describing the swelling of a free chain in a good solvent. When describing a polymer brush, the following parameters are typically taken into account.

- The segment density profile φ as a function of the distance z from the surface.
- The brush height d as a function of the grafting density Γ (chains per unit area).

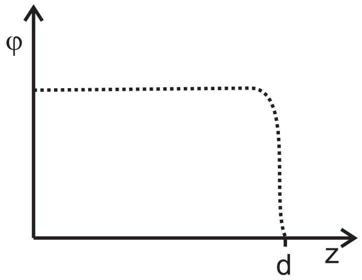

Fig. 2.11: Schematic step-like segment density profile as used in the Alexander model.

- The number of segments N in the tethered chains.
- The solvent quality.

Alexander was the first to study the scaling properties of end-tethered chains [88]. Two assumptions were made by Alexander in order to simplify the expressions of the two contributions to the free energy of a polymer brush. (1) The segment density profile has a step-like shape (depicted in Fig. 2.11), meaning that the density of the segments is constant within the layer up to a height d.

$$\varphi \approx \frac{N * a^3}{l^2 * d} \tag{2.9}$$

The meaning of $\approx$ within this chapter is "equal to within numerical factors of order one". a is the diameter of a segment and thus $N * a$ gives the conventional contour length of the chain (maximum end-to-end distance of a physically completely stretched chain in all-trans conformation). l is a measure of the distance between the anchoring points of neighboring chains.

(2) All chains are uniformly stretched, thus all chains ends are located in a single plane at distance d from the surface. The latter assumption yields simplified expression for F_{el}, whereas the first assumption allows to simplify the expression for F_{int}. In the limit of relatively low grafting densities, the layer of end-grafted polymer chains can be viewed as a semi-dilute solution. This semi-dilute solution can be characterized by a correlation length $\xi \sim \varphi^{-3/4}$ and has an interaction free energy density of kT/ξ^3. Alexander divided each

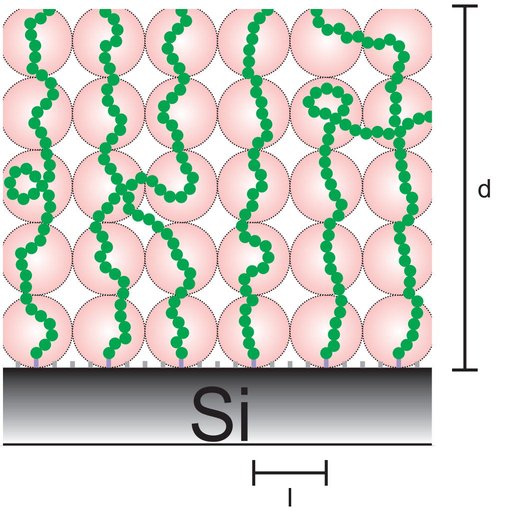

Fig. 2.12: Illustration of the Alexander model for the description of a polymer brush in the semi-dilute regime. The circles indicate the excluded volume blobs.

chain into a string of blobs with uniform size ξ, as shown in Fig. 2.12, and assigned each blob a free energy of kT.

The number of monomers per blob g is given by $g \approx (\xi/a)^{5/3}$. Since the interaction energy F_{int}/kT of polymer segments is related to the number of blobs per chain, the following expression can be deduced.

$$\frac{F_{int}}{kT} \approx \frac{N}{g} \approx N * (\xi/a)^{-5/3} \approx N * \varphi^{5/4} \approx \varphi^{9/4} * l^2 * \frac{d}{a^3} \tag{2.10}$$

Ferry [89] and Noda et al. [90] independently found experimental evidence for this form of the interaction energy.

The nonideal character of the excluded volume chains has also an effect on the entropic elastic energy F_{el}. The blob model takes this into account by describing the chains in the semi-dilute solution as Gaussian at large scales and the subunits as excluded volume blobs. The entropic elastic energy for a Gaussian chain of blobs can be expressed by $F_{el} = d^2/R^2$ with a radius of the chain given by $R \approx (N/g)^{1/2} * \xi \approx N^{1/2} * \xi^{-1/8}$. Daoud et al. [91] were able prove this concentration-dependent coil contraction experimentally.

The conclusion from this considerations is that the free energy of a polymer chain in a brush can be expressed by:

$$\frac{F_{scaling}}{kT} \approx \frac{l^2 * d}{a^3} * \varphi^{9/4} + \frac{d^2}{N * a^2} * \varphi^{1/4} \tag{2.11}$$

Furthermore Alexander used scaling arguments to deduce a dependence of brush height d on grafting density Γ and the number of segments N in the grafted chains, viz. the molecular weight. The average distance l between anchoring points is given by:

$$l = a * \Gamma^{-1/2} \tag{2.12}$$

Essentially this is a different expression for the blob size ξ using the grafting density Γ. Using the approximation for the number monomers per blob g introduced above, l can be rewritten.

$$l = a * g^{3/5} \tag{2.13}$$

The segment density φ can be rewritten to be more practicable using l, since the space inside the brush is filled by the blobs.

$$\varphi \approx \frac{N * a^3}{l^3} \tag{2.14}$$

Combining Eq. 2.14 with Eq. 2.12 allows to relate the segment density φ to the grafting density Γ,

$$\varphi \approx \Gamma^{2/3} \tag{2.15}$$

Given that the volume of one chain with N segments is $d * l^2$, one finds:

$$d \approx N * a * \Gamma^x \tag{2.16}$$

The exponent x, called the Flory exponent, describes the solvent quality and varies from $\frac{1}{3}$ for a good solvent to $\frac{1}{2}$ and 1 for a Θ-solvent and a poor solvent respectively.

Regardless of the exponent, it should be noted that the brush height d depends linearly on the number of segments N, which is a measure of the molecular weight of the polymer chain. This linear dependency is much stronger compared to the size-dependency on molecular weight of a free polymer chain in solution. For an ideal chain (Θ-solvent) the radius of gyration scales with $R_g \sim N^{1/2}$ and for a chain in a chain in a good solvent with $R_g \sim N^{3/5}$.

Connecting Eq. 2.16 with the radius of gyration R_g that an isolated chain has, according to Flory [87], demonstrates the stretching of the end-tethered chains.

$$\frac{d}{R_g} = \left(\frac{R_g}{l}\right)^{2/3} \tag{2.17}$$

The key feature of Eq. 2.17 is the direct relationship between the degree of stretching $\frac{d}{R_g}$ and the ratio of the distance between anchoring points l and the radius of gyration R_g to the power of $\frac{2}{3}$.

The validity of Eq. 2.15 becomes questionable in the case of a fully close-packed brush, where the surface is fully covered with anchoring site. The grafting density Γ would turn unity in this case and therefore the volume fraction inside the brush φ would turn unity as well. A volume fraction of unity leads to a breakdown of the assumption that the layer of end-tethered chain behaves like a semi-dilute solution. Thus one deals with a concentrated solution, when studying layers with high grafting densities. Above a crossover value in segment density of $\varphi^\star \approx \nu/a^3$, as given by Noda et al. [90], a solution is defined as concentrated. ν is the excluded volume parameter. A key feature of a concentrated solution are weak fluctuations in concentration, hence mean-field theories can be applied to describe them. Flory and Huggins [87] linked the excluded volume parameter ν to the Flory-Huggins interaction parameter χ.

$$\nu = a^3(1 - 2\chi) \tag{2.18}$$

The values of χ range from $1/2$ at the theta point to 0 in the athermal limit. With the help of Eq. 2.18 one can estimate the concentration at which a solution becomes concentrated. Noda et al. [90] measured a value of 0.4 for the Flory-Huggins interaction parameter χ using a poly(α-methylstyrenes) in toluene, a good solvent, at 25 °C . On account of this one can assume a polymer solution to be concentrated when the segment density reaches tens of per cent.

deGennes [86] was able to derive a relationship between the brush height d and the number of segments N for brushes in the concentrated regime, similar to Eq. 2.16 for the semi-dilute case. As stated above, deGennes used an energy balance argument to describe the free energy of a polymer brush (see Eq. 2.8). Similar to Alexander, deGennes used Gaussian chain statistics to relate the entropic elastic energy of the chain F_{el} to the film thickness d.

$$\frac{F_{el}}{kT} = \frac{d^2}{N * a^2} \tag{2.19}$$

deGennes emphasized the solvent quality by including the excluded volume parameter ν in his description of the interaction energy F_{int}/kT:

$$\frac{F_{int}}{kT} \approx \nu * \varphi^2 * l^2 * \frac{d}{a^3} \tag{2.20}$$

Thus deGennes obtained the following approximation for the free energy per chain in units of the thermal energy kT:

$$\frac{F_{Flory}}{kT} \approx \nu * \varphi^2 * l^2 * \frac{d}{a^3} + \frac{d^2}{N * a^2} \tag{2.21}$$

The free energy in Eq. 2.21 carries the subscript Flory, because deGennes derived it using a Flory approximation. Minimization of Eq. 2.21 with respect to the film thickness d yields:

$$d \approx N * (\nu * \Gamma)^x \tag{2.22}$$

A comparison of Eq. 2.22 to Eq. 2.16 shows, that both predict the same linear dependence of the brush height d on the molecular weight. Both equations yield in addition a dependence of the brush height on the grafting density to the power of the Flory exponent (Γ^x). In summary, the deGennes model emphasizes the role of the solvent quality, since it includes an excluded volume parameter ν in predicting the film thickness of a polymer brush. This

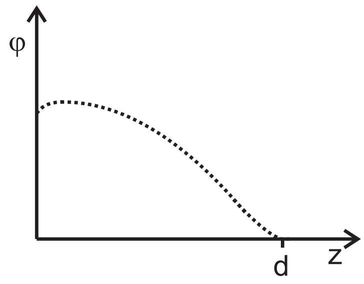

Fig. 2.13: Schematic parabola-like segment density profile as calculated by SCF-theory [42].

seems to be reasonable, inasmuch as the degree of brush swelling increases with increasing solvent quality.

The first experimental confirmation of the Alexander-deGennes model came in 1991, when Auroy et al. [92] measured the thickness of poly(dimethylsiloxane) chains covalently end-grafted via ether bonds on porous silica as a function of the molecular weight. Thus the simple Alexander-deGennes model was successfully used to predict the experimentally observed scaling behavior.

The disadvantage of the Alexander-deGennes model are the strong restrictions on configurations that the chains within a brush can possibly exhibit. The restrictions are the uniformity of the segment density and the fixed location of all chain ends at the same distance from the surface. Hence more sophisticated models were developed calculating the segment density profile, as well as the chain end distribution. The basis of these sophisticated models is the basic mean-field assumption, that any stretched chain in a relative dense brush interacts rather with its neighbors than with itself. Thus a self-consistent field (SCF) [93, 94] approach was applied to describe the chain configurations. A numerical implementation of the SCF-approach was presented by Cosgrove et al. [95].

The major result of the numerical implementation is a segment density profile as schematically shown in Fig. 2.13. At short distances from the surface the segment density rises sharply before reaching a maximum. Beyond the maximum the segment density falls following roughly a parabolic shape given by

$\varphi \sim -z^2$ with increasing distances from the surface. At the periphery an exponential tail region can be identified. The depletion region at the surface is found only in those cases where the polymer does not absorb on the surface. In the case of strong absorption of the polymer on the surface, depletion at the surface is not observed. Wijmans et al. [96] showed that the exponential tail region of the profile disappears with higher molecular weight chains.

An explanation for the parabolic profile came from an analytical solution to the SCF-approach independently developed by Milner et al. [97, 98] and Zhulina et al. [99]. The key idea behind the work of Milner and Zhulina was taken from the Alexander-deGennes model. The chains repel each other, leading to stretching, which in turn reduces the number of configurations that the chains can exhibit. In this view the most probable configuration is one, where the chains fluctuate around a dominant, stretched trajectory. A single-chain partition function Z_{SC} can describe each possible trajectory of a grafted chain as a sum of Boltzmann factors. Using continuum equations to express the trajectories as $r(t)$ with r representing the position of the monomer with unit number t in space, one receives the following for the partition function:

$$Z_{SC} = \sum_{\{r(t)\}} \exp(-S_k) \tag{2.23}$$

The sum is taken over all possible chain configuration $r(t)$ with S_k given by

$$S_i = \int \left[\frac{1}{2} \left(\frac{dr_i}{dt} \right)^2 - U(r(t)) \right] dt \tag{2.24}$$

for each of those configurations. $U(r)$ is referred to as the effective mean-field potential. In analogy to the Alexander-deGennes model the free energy is given by the sum of the stretching energy and the effective mean-field potential $U(r)$. The configuration that minimizes Eq. S is dominating the partition function (Eq. 2.23). If the index t is taking the role of time, Eq. 2.23 and 2.24 become analogous to the path integral formulation of quantum mechanics. Thus the dominant configuration of a stretched chain can be described by a trajectory of a classical particle with large momentum. The function S_i corresponds to the action and the stretching energy resembles the kinetic energy of a particle. The path taken by a particle in the classical limit of quantum mechanics, is the one that minimizes the action. In analogy to Newtons second law of motion, one can define the equation of motion for polymer chain trajectories.

$$\frac{d^2r}{dt^2} = -\nabla U \tag{2.25}$$

Initially Semenov [40] had developed this analogy to quantum mechanics in 1985. Boundary conditions are required in order to solve the differential equation. One end of every chain has be located at the wall, the location of the free chain end is not know however. What is known though, is that local stretching at the chain end is zero if external forces are absent. To stay with the mechanical analogy, chains correspond to particles dropped from rest at a certain distance from the wall. The particles move through the potential to the wall, arriving at the wall after a time corresponding to the degree of polymerization of the chains. Thus the initial rest position is located at the position of the chain ends, the bottom of the well is located at the wall, and the role of time is taken by index number t of each monomer. In other words, the path of the particle is laid out by the chain by adding a monomer per each unit of time. Assuming that all chains have the same length, their trajectories have to reach the wall at the same time, independent of starting position. With the help of this information one can mathematically describe the self-consistent potential. It needs to be a so-called equal time potential, meaning that a particle dropped at arbitrary positions arrive at the origin at the same time. From symmetry considerations one can learn additionally that the potential is exclusively a function of distance z from the wall. The potential of a simple harmonic oscillator has all these properties, since the period of a harmonic oscillator is independent of its amplitude. The potential is essentially a quadratic one, given by:

$$U(z) = Bz^2 - A \tag{2.26}$$

The constant B is related to the chain length via the number of segments N. N corresponds to the time that passes until a particle reaches the origin, which is one quarter of the period of a harmonic oscillator.

$$B = \frac{\pi^2}{8N^2} \tag{2.27}$$

In order to define A, a relationship between the potential and the segment density φ is necessary. For a concentrated solution this relationship is $U(\varphi) = -\nu\varphi$ with the excluded volume parameter ν. Based on this relationship a conversion of the potential in Eq. 2.26 into a segment density profile is possible. In this sense, A can be fixed using the requirement, that an integration over the segment density profile results in the coverage. Thus the final result for the segment density profile is

$$\varphi(z) = \frac{B}{\nu} * (d^2 - z^2) \tag{2.28}$$

The brush height d for a good solvent is given by

$$d = \left(\frac{12}{\pi^2}\right)^{\frac{1}{3}} * N * (\nu * \Gamma)^{\frac{1}{3}} \tag{2.29}$$

Experimental results confirm the findings maintained from SCF-theory. For example, Auroy et al. [100] did small-angle neutron scattering on porous silica with end-grafted polystyrene chains.

In summary, the analytical SCF-theory yields the same functional dependence of brush height d as the simple energy balance argument that was used by deGennes to derive Eq. 2.22. The analytical SCF-theory provides the same scaling properties as the Alexander-deGennes model, especially regarding the average layer thickness. This is very strong support of the Alexander-deGennes model, with one subtle difference: the basis of the analytical SCF-theory are local properties along a chain, whereas the Alexander-deGennes model takes properties averaged over the whole chain into account. The analytical SCF-theory provides additionally a detailed explanation for the parabolic segment density profile (see Fig. 2.13) found by Cosgrove et al. using a numerical SCF-theory. The parabolic shape of the segment density profile however is not universal. With increasing grafting density the parabolic shape is changing more and more into the step-like shape, which was part of

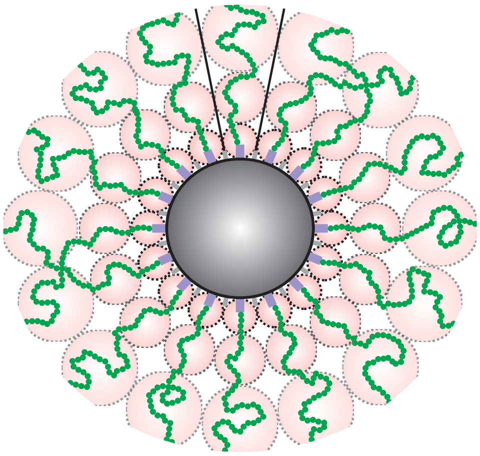

Fig. 2.14: Illustration of the Alexander model for the description of a polymer brush attached to a curved substrate. The circles indicate the excluded volume blobs, which expand in size with distance from substrate.

the Alexander-deGennes model (see Fig. 2.11).

The validity of the SCF-theory reaches its limit for very high grafting densities. Three body interactions develop in brushes with very high grafting densities [101], which cannot be taken into account by the SCF-theory.

2.2.3 Theory of Polymer Brushes - curved interfaces

The Alexander-deGennes model cannot directly be applied to curved grafted brushes since the basic assumption that the model makes is a step-like segment density profile. The segment density profile for spherical geometries however is decreasing monotonically with distance from the substrate. The reason is the growing volume accessible to the individual chains as the distance from the grafting site increases. The global scaling features for polymer chains grafted to curved substrates can be derived from the Alexander-deGennes model nevertheless.

The Alexander-deGennes model makes the assumption that chains attached to a flat substrate are confined into cylindrical regions with radius l and with height d, as shown in Fig. 2.12. The radius of the cylinder l is equal to the size of a blob ξ and each chain therefore is represented by a stack of blobs with overall height d. A film made up of end-tethered polymer chains can be divided into a multilayer of blobs, with each chain contributing a blob per layer. This multilayer structure of blobs can be transferred to polymer chains attached to a curved substrate, as shown schematically in Fig. 2.14. The major difference is, that the chains are confined to a conical region and not a cylindrical one. The consequence is, that blobs belonging to the same layer have the same size ξ. Blobs belonging to different layers however differ in size. Blobs become bigger with increasing distance from the surface. This satisfies the assumption of the Alexander-deGennes model, that all chains are uniformly stretched.

Analysis of the scaling behavior is in the case of curved substrates straightforward and can be achieved relying on geometrical considerations, circumventing the free energy minimization known for brushes on flat substrates. Daoud and Cotton [102] pioneered the geometrical analysis of polymer brushes on spherical substrates. Daoud and Cotton located all blobs with the same distance from the grafting sites in a shell with surface area S. S can be calculated by $S \approx f * \xi^2$ using the total number of grafting sites f on the substrate. This corresponds with the result from the Alexander-deGennes model for flat substrates, since in this case all shells have the same surface area and thus the blob size ξ is given by $\xi \approx (S/f)^{(1/2)} \approx l$ (compare to Eq. 2.12). For curved substrates one needs to take into account though, that the blob size ξ depends on the distance z from the substrate. The same dependence on z is also found for the surface area of the shells $S \sim z^2$, leading to $\xi \approx (z/f)^{(1/2)}$. Thus the whole problem is reduced to finding an expression for $\xi(z)$.

A calculation of the segment density profile $\varphi(z)$ is possible by using

$$\varphi(z) \approx \left(\frac{a}{\xi}\right)^{4/3} \tag{2.30}$$

since for good solvents the blob size ξ is related to the segment density via $\xi(z) \sim \varphi^{-3/4}$. Assuming that an integral over the segment density profile includes all monomers in the layer allows to determine the average thickness d of a polymer layer attached to a curved substrate.

$$N \approx \int_{R_{in}}^{R_{in}+L} \left(\frac{\xi}{a}\right)^{5/3} * \xi^{-1} dr \tag{2.31}$$

N is the total number of monomers in a chain, whereas R_{in} is the radial position of the surface. dr/ξ and $\left(\frac{\xi}{a}\right)^{5/3}$ are measures for the number of blobs and the number of monomers per blob, respectively. The kT-per-blob ansatz yields the free energy per chain

$$\frac{F_{scaling}}{kT} \approx \int_{R_{in}}^{R_{in}+L} \xi^{-1} dr \tag{2.32}$$

The following table shows a comparison of the predictions made by the Alexander-deGennes model for brushes on flat substrates to the Daoud-Cotton model for brushes on curved substrates.

Table 2.1: Scaling behavior of free energy $F_{scaling}$, film thickness d, and segment density φ with tethering density and chain length for brushes on flat/curved substrates in good solvents.

Geometry	Blob size ξ	φ	d/a	$F_{scaling}/kT$
flat	1	$(a/l)^{(4/3)}$	$N(a/l)^{2/3}$	$N(a/l)^{5/3}$
curved	$(z/f)^{(1/2)}$	$f^{2/3}(a/z)^{4/3}$	$f^{1/5}N^{3/5}$	$f^{1/2}ln(R_{in}+d)/R_{in}$

2.3 Nanocomposites

The expression composite appeared in the early twentieth century for the first time [103]. Generally it is used to describe the union of two or more diverse materials. The union of the materials has superior qualities to those exhibited by the individual constituents.

Nature has always been a source of inspiration, as it is in the case of composite materials [104]. Plants and animals contain highly advanced macromolecular composites. The connective tissues in mammals serve as a good example. Collagen, a fibrous protein, is used very efficiently both in hard and soft connective tissues [105]. In bones collagen serves as binder for the inorganic hydroxyapatite, stiffening the structure in this way. Collagen fibres in soft connective tissues are glued together by a matrix of a gel-like proteoglycan. Tendons, the elastomeric cable between muscles and bones, are made of such a glued-fibre structure.

The first more scientific study of a composite materials dates back to the 1860s. Different materials were added to vulcanized rubber in order to enhance its mechanical properties. Carbon black significantly enhanced the properties of rubber due to its high surface area, surface energy, and mechanical properties. Therefore one can argue that rubber reinforced with carbon black was the first primitive nanocomposite [106].

The term nanocomposite however did not appear in scientific literature until the 1980s and was used for ceramic-based materials [107]. In 1991 the term nanocomposite was mentioned for the first time in relation to a polymer matrix in a full paper, dealing with the preparation of copper nanoparticles in a poly(2-vinylpyridine) matrix [108]. The questions arise what the definition of a nanocomposite is and what the origin for the unique properties is.

In general, a nanocomposite is defined as a material resulting from the association of particles with at least one dimension in the nanometer regime, organized in a continuous phase [109]. In the frame of this thesis, the continuous phase is considered to be an organic polymer. This implies that the filler sizes approaches the length scale of a polymer coil. Unique interactions are the result [110]. Thus one needs to understand the properties of the individual constituents in a polymer nanocomposite, such as the polymer matrix and the nanoscale filler, in order to understand the behavior of the composite. Parameters like the chemistry and the morphology of the polymer, as well as the surface, the size and the shape of the filler have to be considered.

The polymer matrix is the major component in a composite, judging by volume. Polymers with a wide range of properties can by produced, depending on chemistry, molecular architecture, and processing history. Processing and architecture of a polymer are determined in big parts by the choice of the synthesis method (e.g. free radical, anionic, controlled living polymerization) [111]. The choice of synthetic route determines the polydispersity, remaining initiator content, content of chain transfer agents, and content of chain termination agents. By controlling the chemistry one can adjust the factors contributing to the free energy of the composite. The contributions to the free energy of a composite are the entropic interaction among nanofillers, excluded volume interactions, and the interactions between polymer chains and nanofillers [110, 112]. Especially the enthalpic interactions between the polymer chains and nanofillers can be influenced by the chemistry of the polymer.

The minor component in a composite is the filler. The filler shape and the size have to be considered [113]. Three types of composites can be distinguished by the number of spatial dimensions of the particles in the nanometer range. Nanoparticles appear as sheets if just one dimension is in the nanometer range. The thickness is typically 1 nm, but length and width range from hundreds to thousands of nanometers. Clays, such as naturally occurring layered (alumino)silicates, starch-based platelets, graphite nanosheets, and numerous other synthetic layered particles (e.g. layered double hydroxides, zirconium phosphates) belong to this family of 2D nanoparticles. Among all available nanoparticles, these sheet-like particles have been most widely investigated, due to their high abundance in nature [114].

Nanotubes or whiskers are categorized as 1D nanoparticles. Two dimensions are in the nanometer range, while the third one is longer, resulting in elongated structures. Among the 1D nanoparticles carbon nanotubes [115, 116] and cellulose/chitin whiskers have attracted the most interest [117, 118].

Isometric nanoparticles have three dimensions in the order of a few nanometers. Prominent examples are metallic particles (gold, silver, etc.) [119], oxides (silica, titanium dioxide, etc.) [120, 121], metal compounds (CdS, CdSe, etc.) [104], and even carbonaceous (carbon black, fullerenes) [122].

The question is though, what influence the shape of the nanoparticles has on the properties of the polymer nanocomposite. The general motivation of adding nanoparticles to polymers is the high surface-to-volume ratio of the particles. For cylindrical particles of radius r and length L the surface-to-volume ratio A_c/V_c is given by eq. 2.33.

$$\frac{A_c}{V_c} = \frac{2\pi r^2 + 2\pi r L}{\pi r^2 L} = \frac{2}{r} + \frac{2}{L} \tag{2.33}$$

For a spherical particle with radius r one gets the following relation for the surface-to-volume ration A_s/V_s:

$$\frac{A_s}{V_s} = \frac{4\pi r^2}{4/3\pi r^3} = \frac{3}{r} \tag{2.34}$$

A comparison of the surface-to-volume ratios of a spherical filler A_s/V_s to a cylindrical filler A_c/V_c yields:

$$\frac{A_s/V_s}{A_c/V_c} = \frac{3}{2(1 + r/L)} \tag{2.35}$$

Eq. 2.35 demonstrates that plates ($r > L$) and short rods ($L < 2.0r$) have a higher surface-to-volume ratio in comparison to spherical particles. Long fibers ($L > 2.0r$) however have a smaller surface-to-volume ratio than spherical fillers. Therefore plate geometries, like clay sheets, are definitely at advantage judging by the surface-to-volume ratio. Yet the surface-to-volume ratio is not the only factor that has to be considered when designing a polymer nanocomposite. Using rigid cylindrical fillers one is always facing the difficulty of dispersing them in an isotropic manner. From the field of colloidal dispersions it is known, that the excluded volume effect and the ease of packing non-spherical objects are the reasons for the difficulty in dispersing rigid fillers [123]. The excluded volume refers to the idea that two hard objects cannot occupy the same space at the same time. A repulsive force is acting between the objects due to the entropy. The conclusion from the concept of excluded volume is that the ability to isotropically disperse long cylinders, or in general high-aspect ratio objects, decreases as their aspect ratio L/r increases. Ordered phases, known from liquid crystals, can develop even at low volume fractions of fillers.

From here on further discussions of polymer nanocomposites containing fillers with other geometries than spherical will be omitted, since this would go beyond the scope of this thesis.

Besides the shape, the size of the filler has a major influence on the surface-to-volume ratio. The calculation of the surface-to-volume ratio is straightforward for isometric particles as shown above in eq. 2.34. The equation demonstrates the relationship between the surface area A_s per volume V_s and the radius of the spheres, in other words their size. A decrease in spherical radius r results in an increase in surface area to volume. The total quantity of interfacial area within the nanocomposite can also be taken into account by relating the filler volume fraction ϕ to the total interfacial area-to-volume ratio $A_{i,total}/V_{total}$.

$$\frac{A_{i,total}}{V_{total}} = \frac{3\phi}{r} \tag{2.36}$$

One can draw the following conclusion from this relation. An increase in total interfacial area $A_{i,total}$ can be accomplished by decreasing the filler radius r, when keeping the volume fraction ϕ constant. More chain/filler interactions are the result, which is beneficial to the performance of a composite. Several production pathways have been designed to achieve an isotropic dispersion of nanoparticles in a polymer matrix [124]. Depending on the properties of the nanoparticles (i.e. state of aggregation, chemical nature, surface reactivity, ...) and the polymer matrix (solubility, reactivity towards the nanoparticle surface, ...) a pathway needs to be selected. A classification into three general categories is possible despite the multitude of nanoparticles and polymers used in the preparation of composites.

Mixing a solution of a polymer (or the molten polymer) with nanoparticles (or a suspension of them) is the straightforward pathway. Engineers have developed numerous devices, such as mixers or extruders [125, 126], to achieve melt blending. The devices allow to apply shear to the polymer melt and thus the particles are dispersed. In many cases shearing of the polymer melt is not enough to overcome particle-particle interactions and achieve a good dispersion [127]. A common method is the chemical modification of the particle surface to lower the surface energy of the particles, that is usually high. Surface agents and even polymer chains have been used to modify the particle surface. Examples where this approach is successfully implemented range from composites made of silica particles, to composites made of calcium carbonate particles, and composites made of carbon black. Especially surface modifications using the grafting from process have achieved tremendous interest [128–131]. Grafting onto can also be achieved during melt blending [132].

By the preparation of particles in the polymer matrix a good dispersion can be achieved. This method is not as versatile as mixing of the polymer and the particles, nevertheless countless examples can be found in literature. Not only dispersions of metal nanoparticles (Au, Ag, Cu, etc.) [119,133] have been produced in this fashion, but also dispersions of metal oxides [120, 121], and others [104]. Typically a mixture of metal salt or metal complex with a polymer is prepared and then the particles are produced by the reduction of the precursor.

To the third category belong methods that allow to create the polymer matrix around the particles [134, 135]. A dispersion of the particles in the monomer or a solution of the monomer is the prerequisite for these methods to be successful. The common approach to make the particles soluble in the monomer is to modify the particle surface with surface agents. The problem however is that such systems are not in the thermodynamic equilibrium. The particles are only kinetically trapped in the matrix and changes in temperature might affect the dispersion [136].

When looking at the three categories of preparation, one realizes the importance of the interfacial region between filler and polymer. All forces acting on the matrix are transmitted to the filler via the interface. Without favorable interactions of the filler with the matrix and minimal inter-filler interactions a nanocomposite does not exhibit the unique properties that are desirable. This is directly related to the fact that favorable interactions are necessary to isotropically disperse nanoparticles in a polymer matrix. Small molecules and polymer ligands are typically used to modify the surface of the filler.
The aim of this thesis was to gather more insight on how polymer ligands, in other words polymers end-grafted to the surface of the filler, interact with the matrix.

3 ”Grafting from” - Polymer brushes on flat substrates

The focus of this chapter is on the fabrication of polymer brushes on flat substrates, viz. silicon wafers and silicon microcantilever arrays.
A new technique for patterning polymer brushes on the micrometer scale will be presented in which an inkjet printer was used to deposit droplets of acid on a surface-immobilized initiator for atom transfer radical polymerization (ATRP). The acid cleaved an ester bond in the ATRP initiator in a saponification reaction. As a result, the ATRP initiator was rendered inactive. To control the degree of defunctionalization, a new initiator containing a weak ester bond was derived from a tertiary alcohol. Comparison to an established ATRP initiator, derived from a primary alcohol, showed that the novel initiator was defunctionalized with a higher efficiency. Control of the reaction time allowed to partially defunctionalize the initiator molecules, leading to control of grafting densities within the written patterns.
Transfering this technique to silicon microcantilever arrays allowed for the preparation of polymer brushes on selected microcantilevers. In closing, two examples will be given, what the applications of cantilever arrays functionalized with polymer brushes are.

The chapter is based in parts on the publication: Sebastian G. J. Emmerling, Laura B. N. Langer, Sascha A. Pihan, Philipp Lellig, and Jochen S. Gutmann, *Patterning of a Surface Immobilized ATRP Initiator with an Inkjet Printer*. Macromolecules **2010**, http://dx.doi.org/10.1021/ma902836n.

3.1 Patterning of a surface immobilized ATRP initiator with an inkjet printer

3.1.1 Introduction

Fabrication of polymer brush patterns over large areas remains a demanding task, despite recent achievements using photolithography [137] and microcontact printing (µ-CP) [138, 139]. A combination of templating techniques and polymer brush synthesis techniques to amplify the patterns is essential [39]. In this chapter a versatile fabrication method to pattern polymer brushes on the micrometer scale will be introduced. This process focuses on flexibility regarding choice of substrates, control of brush length, and the possibility for automation. Among the existing techniques, µ-CP would be the most suitable, but its automation is not easily achieved. Inkjet printing allows one to circumvent the use of masters and stamps, instead directly writing our patterns on the substrate. Additionally, the new technique enabled the fabrication of gradients in grafting densities over large areas.

Soon after the initial interest in polymer brushes, researchers no longer solely focused on covering entire surfaces with polymer brushes. In 1995 Rühe and co-workers published three different methods for achieving lateral patterning of a polymer coating [140]. Rühe’s group recognized from the beginning the potential application for these patterned surfaces that control the adhesion of biological cells to solid substrates [141]. Research is still focusing on biological applications in this area [142]. Photolithography has also been investigated for patterning by the Hawker group [143]. In addition to deep and near-UV irradiation, electron beams [137] have been deployed. Both these approaches require the use of shadowing masks if larger areas are to be patterned. This is a drawback to keeping production costs low. The major advantage of using shadowing masks, however, is the resolution in the nanometer range. Alongside the development of photolithography and e-beam (chemical) lithography (EBL), various other lithography techniques for pattern formation have been developed. This is highlighted in a recent review [144]. Under the term scanning probe lithography (SPL) are grouped techniques like nanoshaving [145] and dip-pen nanolithography [146]. As the name suggests, these techniques rely on the use of atomic force microscopes (AFM) to manipulate SAMs. The popularity of SPL-techniques stem from the fact that they are technologically simpler compared to EBL, while maintaining a resolution close to that of EBL. When it comes to patterning of large areas, SPL techniques are at disadvantage. This could potentially be mitigated by the use of cantilever arrays.

Soft lithography has attracted by far the most interest among all techniques available for creating laterally structured brushes. Developed in the 1990s by Whitesides and co-workers [48, 147], soft lithography using polymer stamps to deliver patterns was utilized to create initiator functionalized micropatterns for SIP. This technique is also known as µ-CP. A thiol containing an initiator moiety for ring-opening polymerization (ROP) [148] or ATRP [75, 76, 149, 150] is delivered with a stamp onto a gold-covered substrate. Then the uncovered regions are backfilled with a nonfunctional thiol or vice versa. Huck and co-workers [151] developed this approach further by repeating cycles of printing initiator thiols, ATRP thereof, and passivating the living chain ends by nucleophilic substitution with NaN_3. After performing three repeat cycles and one backfilling step, they obtained laterally distinctive multicomponent polymer brushes. Inherent difficulties of this approach include the preparation and handling of the gold films, a potential edge roughness of the written patterns [152], and delamination.

Working with oxidized silicon layers can circumvent some of these problems. First of all, the Si-O bond dissociation energy of 96-133 kcal/mol is higher than the Au-S bond energy at 30-40 kcal/mol. Hence, by using silane/silica chemistry, the layers stay anchored even above 70 °C where Au-S bonds become unstable [153]. However, few publications on the subject of µ-CP and SIP on SiO_2 can be found [154–156]. We attribute this to difficulties in the reproducible formation of organosilane monolayer patterns by µ-CP for SIP. Indeed, all cited procedures require several steps to create patterns of initiator silanes instead of direct deposition of initiator silanes.

A route to circumvent the above-stated problems with µ-CP and SIP on silicon surfaces by a direct and easy one-step approach is described in this

Section of the thesis. Patterns were not generated by µ-CP, but by the use of a computer-assisted drop-on-demand inkjet system and amplify these by ATRP of methyl methacrylate (MMA). The major advantage offered by inkjet printing is the ability to write patterns directly onto substrates, eliminating the use of masks or masters, combined with a resolution of hundreds of nm [157–162].

Furthermore, the computer control of inkjet printers enables fully automated and high throughput manufacturing of patterned materials. This prompted Sankhe et al. [163] to combine inkjet printing with ATRP to produce patterned polymer surfaces. Their work, however, is limited to gold/thiol chemistry, as they print a bromine-containing thiol for ATRP and backfill with a non-ATRP active thiol (or vice versa). Controlling the reaction parameters of the backfilling step proved to be critical, since the printed thiol monolayer was otherwise replaced by the backfilling thiol.

A one-step approach to create patterns with a focus on silicon/silane chemistry is described in this Section of the thesis, since silane layers on silicon are thermally more stable compared to thiol layers on gold. Nevertheless, our approach is also applicable to gold/thiol chemistry. Contrary to Sankhe et al., the entire surface of the wafer was covered with a silane monolayer of an ATRP initiator and the inkjet printer was used to chemically alter this monolayer. The ATRP initiator contains a hydrolytically labile bromoester functionality (see Scheme 1, bold bond). Acids were printed in order to cleave the molecule at this point and pattern the initiator SAM in this way. After cleavage, the surface contains fewer bromo functionalities in the contact areas that participate in ATRP. The thickness of poly(methyl methacrylate) (PMMA) brushes that grew in the contact areas was thus reduced. The observed changes in film thickness in the contact areas are related to changes in grafting density as an effect of the cleavage of a fraction of ATRP initiators. The results obtained with a common ATRP initiator [164] (depicted in Fig. 3.1, structure (2)) led us to the synthesis of a more labile ATRP initiator (depicted in Fig. 3.1, structure (1)). The novel initiator also contains a bromoester functionality but is derived from a tertiary alcohol. In this initiator the ester bond was much more labile and easier to cleave, allowing us to

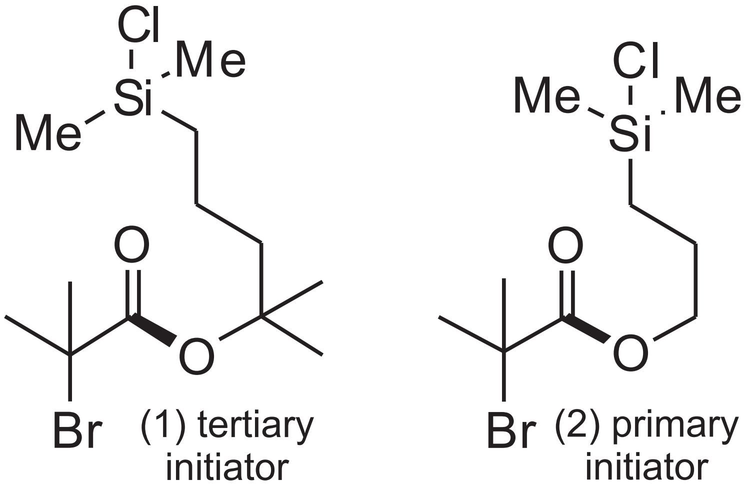

Fig. 3.1: Structures of 4-(Chlorodimethylsilyl)-2-methylbutan-2-yl 2-bromo-2-methylpropanoate (1) and
3-(Chlorodimethylsilyl)propyl 2-bromo-2-methylpropanoate (2).
SI-ATRP initiators deployed for ″grafting from″ of MMA on silicon wafers in this study. The ester bond (bold) in both initiators can be cleaved under acidic conditions.

suppress brush growth completely.

Two aspects of the saponification reaction of the SI-ATRP initiator are discussed in this study. First, the usefulness of hydrochloric acid or sulfuric acid in saponification of the initiator monolayer and its concentration dependence was investigated. To obtain results independent of inital SAM preparation, we used the inkjet printer to screen these parameters on one substrate. Second, the time dependence of the saponification reaction was investigated by controlling the contact time between acid and initiator. In this way a gradual variation of grafting density from the brush regime to the mushroom regime [86] over the area of a silicon piece the size of 2.3 x 3 cm was achieved using a dip-coater.

3.1.2 Syntheses

Synthesis of the SI-ATRP initiator derived from the tertiary alcohol 2-methyl-4-penten-2-ol

The synthesis of the tertiary SI-ATRP initiator is comprised of three steps, as depicted in Fig. 3.2.

First step: Synthesis of 2-methyl-4-penten-2-ol
The Barbier-Grignard reaction [165] was used for the synthesis of the tertiary alcohol. The reaction was carried out in a two-neck round-bottom flask equipped with a pressure-equalizing dropping funnel, a condenser and a magnetic stir bar. Allylmagnesium bromide (in Et_2O; 200 mL; 0.2 mol) was placed in the flask in a protective argon atmosphere and cooled using an ice bath. Under stirring, acetone (14.7 mL; 0.2 mol) was added dropwise (30 min) to the bromide using a dropping funnel while maintaining the temperature at 0 °C . After the addition was completed, the solution was refluxed for 1 h. While cooling, 70 mL of Milli-Q water was added dropwise (20 min), generating a white solid residue. The temperature was kept around 0 °C , and 60 mL of half-concentrated HCl was added dropwise (5 min). The white residue was dissolved and the pH set to 2. For further work-up the solution was transferred to a separatory funnel. The aqueous phase was separated and washed twice with diethyl ether. These ether extracts were combined with the organic phase, washed with little water, dried ($MgSO_4$), and finally evaporated under reduced pressure to yield the crude alcohol. The final product (12.58 g; 62.8 %; lit. [165] 34%) was attained by fractional destillation and had a boiling point of 117 °C (lit. [166] 119.5 °C).
Characterization:
^{1}H NMR [165] ($CDCl_3$, 250 MHz) δ (ppm): 5.83 (d, 1H, **=CH-**); 5.09 (m, 2H, **=CH**$_2$); 2.15 (d, 2H, **-CH$_2$-**); 1.79 (s, 1H, **-OH**); 1.18 (s, 6H, **C-(CH$_3$)$_2$**).

Second step: Synthesis of 2-methylpent-4-en-2-yl 2-bromo-2-methylpropanoate
The pyridine method of Einhorn [167] was used for the synthesis of the es-

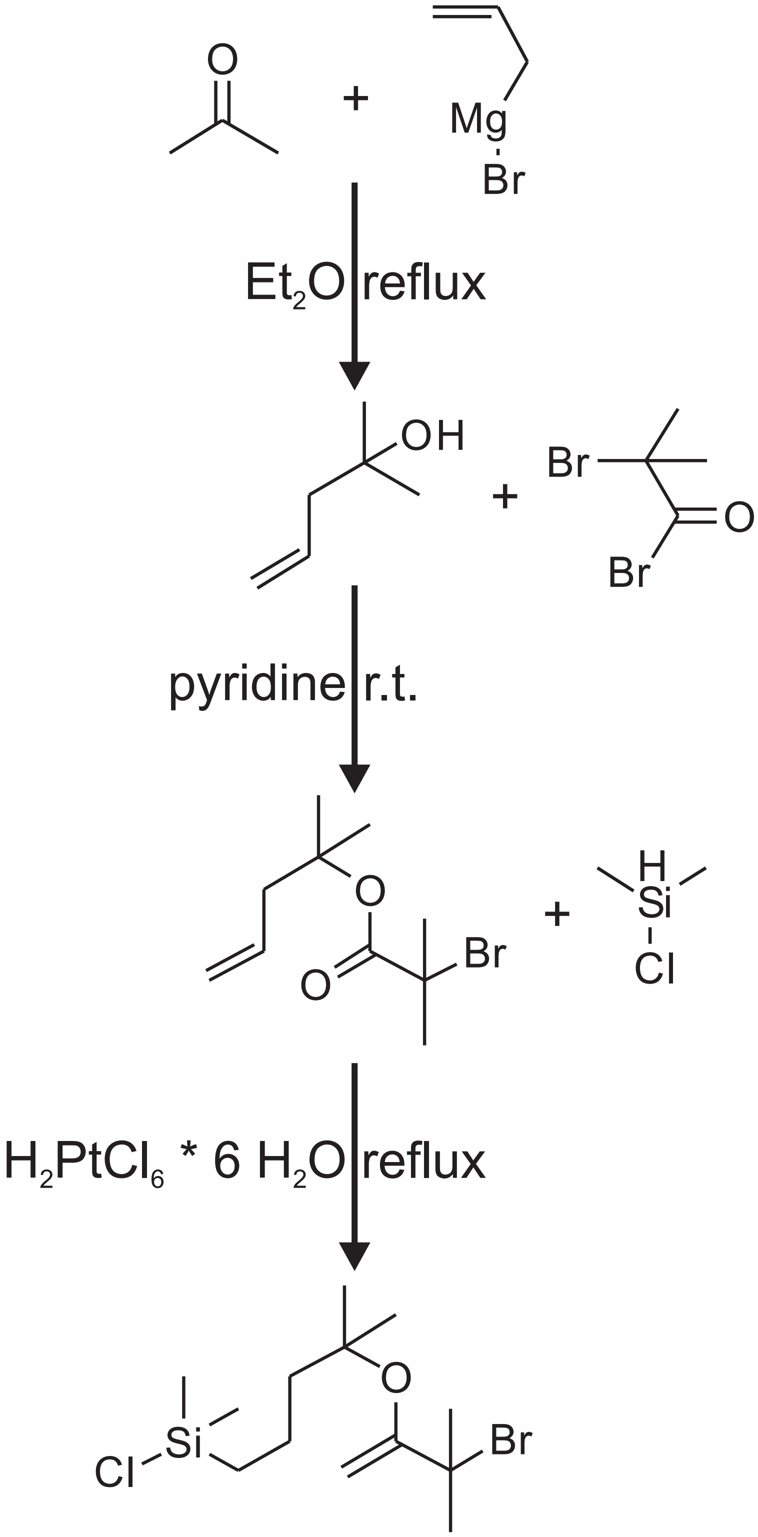

Fig. 3.2: Synthesis of the tertiary SI-ATRP initiator.

ter. Pyridine (102 mL; 1.26 mol) and 2-methyl-4-penten-2-ol (12.58 g; 0.126 mol) were placed in a protective argon atmosphere in a two-neck round-bottom flask equipped with a pressure-equalizing dropping funnel, a condenser, and a magnetic stir bar. While cooling the flask with an ice bath, 2-bromoisobutyryl bromide (16 mL; 0.126 mol) was added slowly (25 min), forming a yellow precipitate. After heating in a water bath for 15 min, agitation was continued overnight under ambient conditions. The suspension was poured into ice water, and the pH was lowered from 6 to 2 by slow addition of concentrated HCl. The precipitate was dissolved, leaving a clear yellow solution. For further processing, the solution was transferred to a separatory funnel, and the crude product extracted by washing three times with dichloromethane. This slightly acidic organic phase was neutralized by washing with an aqueous solution of hydrogen carbonate (2x). Residual salt was removed by washing with water, and then the solution was dried over $MgSO_4$. The solvent was removed under reduced pressure, and subsequently vacuum distillation (0.1 mbar) of the yellow oil yielded the ester (23 g; 73.3 %) with a boiling point of 80 °C as a colorless liquid.
Characterization:
^{1}H NMR ($CDCl_3$, 250 MHz) δ (ppm): 5.85-5.71 (m, 1H, **=CH-**); 5.1-5.03 (m, 2H, **=CH_2**); 2.54-2.51 (d, 2H, **-CH_2-**); 1.85 (s, 6H, **-C(CH_3)$_2$-Br**); 1.45 (s, 6H, **C-(CH_3)$_2$-O-**).

Third step: Synthesis of 4-(chlorodimethylsilyl)-2-methylbutan-2-yl 2-bromo-2-methylpropanoate
The chlorosilane endgroup was generated in a hydrosilylation [168] reaction using hydrogen-hexachloroplatinate(IV) hexahydrate. In this step moisture-free conditions are of uttermost importance, since the chlorosilane group in the final product is easily hydrolyzed. To ensure this, the experiment was conducted in a dry argon atmosphere. The reaction was carried out in a Schlenk tube with a condenser and a magnetic stir bar. First a catalytic amount of hydrogen-hexachloroplatinate(IV) hexahydrate was placed in the tube and melted with the use of a blow-drier. The released water was purged by dry argon. Subsequently, 2-methyl-pent-4-en-2-yl 2-bromo-

2-methylpropanoate(8 g; 0.03 mol), as well as chlorodimethylsilane (30 mL; 0,27 mol) was added, forming a white residue. After refluxing overnight a clear red liquid had formed. By distillation under normal pressure the excess chlorosilane was removed. Finally, vacuum distillation (0.1 mbar) allowed us to obtain the clean product (9.54 g; 96.4 %) as a colorless oil (bp 110 °C). Degradation by moisture during storage was prevented by placing the initiator under an argon atmosphere over silica gel in a desiccator.
Characterization:
^{1}H NMR ($CDCl_3$, 250 MHz) δ (ppm): 1.87 (s, 6H, **-C(CH$_3$)$_2$-Br**); 1.53-1.41 (m, 10H, **O-C(CH$_3$)$_2$-CH$_2$-CH$_2$-**); 0.85-0.78 (m, 2H, **-Si-CH$_2$-**); 0.4 (s, 6H, **-SI-(CH$_3$)$_2$-Cl**).

Synthesis of the SI-ATRP initiator derived from the primary alcohol prop-2-en-1-ol

The initiator 3-(chlorodimethylsilyl)propyl 2-bromo-2-methylpropanoate (structure (2) in Fig. 3.1) was synthesized according to Ramakrishnan et al. [74]. However, we opted to do the hydrosilylation step following the above described approach for the tertiary initiator with hydrogen-hexachloroplatinate(IV) hexahydrate. Distillation under reduced pressure was carried out to obtain the pure product, which was stored in an argon atmosphere over silica gel in a desiccator.

3.1.3 Application of acids with the inkjet printer

In a typical dispense experiment, a silicon wafer covered with a monolayer of ATRP initiator was mounted onto the working plate of the inkjet printer. The printing nozzle was loaded with either concentrated HCl or one of the different concentrations of H_2SO_4.
As depicted in Fig. 3.3 *(a)*, single droplets (volume 0.35-0.4 nL) were deposited and arranged in lines. This was completed within seconds. After spreading, the typical droplet size was below 100 µm (see Fig. 3.5). Individual droplets were placed around 300 µm apart from each other. The distance

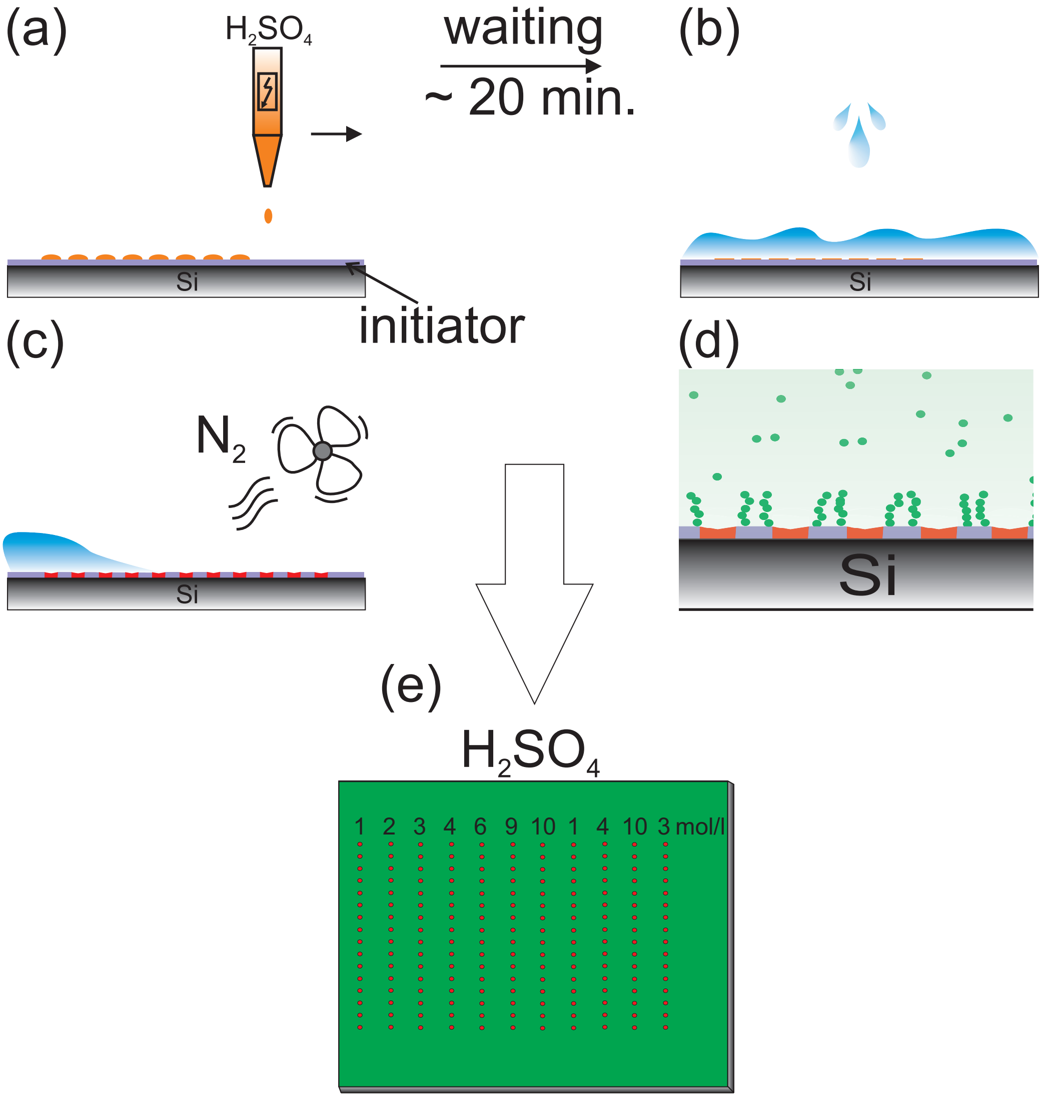

Fig. 3.3: Sample preparation by **(a)** Printing the acid with a commercially available inkjet printer, **(b)** Washing, **(c)** Drying the sample in a stream of nitrogen, **(d)** ATRP of MMA, and **(e)** Top view of sample prepared by printing various concentrations of H_2SO_4.

between lines was about 1 mm. The average contact time between the surface and the acid was 20 min, after which the wafer was taken out of the printer and washed with plenty of Milli-Q water (Fig. 3.3 *(b)*). This was done to remove the applied acid and the generated bromoisobutyric acid. Subsequently, the wafer was blown dry in a stream of nitrogen (Fig. 3.3 *(c)*). In the final step, the PMMA brushes were grown on the surface of the wafer. Reaction details are given in the next paragraph and in Fig. 3.4. In the areas, where the acid previously had been in contact with the surface, grafting density was lowered. For some concentrations of acid brush growth was completely suppressed. The red areas in Fig. 3.3 *(d)* represent these contact areas, and the green dots represent the monomer. Fig. 3.3 *(e)* illustrates the top view of the samples prepared for an in-depth study of different concentrations of H_2SO_4. For this purpose two lines of 10, 4, 3, 1 mol/L H_2SO_4 were printed, along with a line of 9, 6, 2 mol/L. Data of samples prepared in this fashion are displayed in Fig. 3.9 and 3.10. Not shown in Fig. 3.3 are the samples that were prepared in order to compare the effect of concentrated HCl and different concentrations of H_2SO_4 on the ester bond in the initiator molecules. Overall, droplets of concentrated HCl were arranged in three lines. In addition, two lines of 10 and 1 mol/L H_2SO_4 each were printed, along with one line of 6 and 3 mol/L H_2SO_4 and a line of Milli-Q water. The data obtained from these samples are presented in Fig. 3.7 and 3.8.

3.1.4 Application of acids for investigation of time dependence of saponification reaction

Two different approaches were taken to investigate the effect of contact time between H_2SO_4 and both of the initiator SAMs. First of all, were samples with the inkjet printer created that allowed the comparison of the effect of contact time between three different concentrations of H_2SO_4 (1, 0.5, and 0.1 mol/L) on the initiator molecules. The samples were cooled to 10 °C in order to slow the saponification reaction. A line of droplets for each concentration was printed every 4 min. 32 min after deposition of the first line, the last line was printed, and after an additional 4 min the wafer was washed and

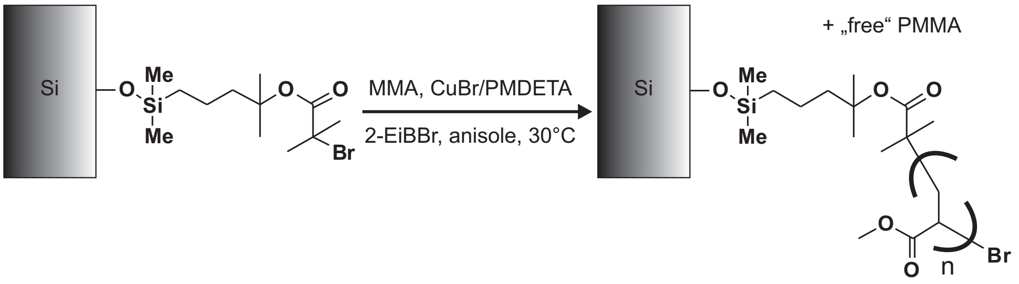

Fig. 3.4: Reaction scheme of SI-ATRP of MMA with tertiary initiator covalently anchored on a silicon surface. The sacrificial initiator 2-EiBBr generated free polymer.

the polymerization started. The data obtained from these samples are represented in Fig. 3.12.

In the second approach we utilized a dip-coater. The use of a dip-coater allowed us to create a gradient in grafting density over the area of a whole wafer. Additionally, evaporation plays no role in dip-coating, whereas the small droplets in inkjet printing evaporate rapidly. Two wafers, one coated with the tertiary initiator and one with the primary, were fixed on the dip-coater. These wafers were totally immersed in a solution of 1 mol/L and 5 mol/L H_2SO_4 respectively, except for an area 3 mm in width. Starting after 2 min, the wafers were pulled out of the solution with a speed of 1.5 mm/min. The data obtained from these samples are presented in Fig. 3.13 and 3.14.

3.1.5 SI-ATRP of MMA

The wafers were cleaned and the ATRP-initiators immobilized as described in Section 3.1.17. Subsequently SI-ATRP was carried out as depicted in Fig. 3.4. The wafers were immersed in a solution containing the solvent (anisole), the monomer (MMA), the ligand (PMDETA), CuBr and the sacrificial initiator 2-EiBBr. The polymerizations were conducted at room temperature (30 °C) ensuring reaction control. Exact procedure and reaction details can be found in Section 3.1.17. After the polymerization was stopped, the wafers were washed and the film thickness measured by ellipsometry. Free polymer was recovered and subjected to GPC analysis. Molecular weights and grafting

densities of each polymerization are given in the respective Sections. A plot showing the linear dependency of film thickness on molecular weight of the free polymer (Fig. 3.18) and the average grafting density for both starters (Fig. 3.19) are discussed in Section 3.1.15.
If the data of wafers covered with tertiary initiator are compared to the data of wafers covered with primary initiator, the PMMA brushes on both wafers were typically grown in the same solution, ensuring the same molecular weight of polymer molecules.

3.1.6 Data acquisition and treatment

PMMA film thicknesses given throughout this publication were acquired with an imaging ellipsometer. This technique allowed to select certain regions of interest, where the film thickness can be measured. This is sketched in Figure 3.5. All objects were imaged distorted along the incoming beam (indicated by the white arrow) due to a viewing angle of 60 degrees. A spherical droplet is thus imaged as an ellipse. For information on the calculation of the feature size on the sample surface in vertical direction, see Section 3.1.17.
The dark 60 µm wide (horizontal direction) feature was generated by spotting a droplet of acid on the initiator layer prior to polymerization. Little or no polymer grew in this contact area. Therefore, the change in polarization of these areas with thinner films is clearly distinguishable from the polarization of the light induced by the surrounding thicker films.
By *contact area* (34 x 27 µm/horizontal x vertical size) we refer to the region of interest that was located within one of the patterns. Within the distance of 50-100 µm of the pattern we placed a region of interest labeled *nearby* (292 x 274 µm/horizontal x vertical size).
A representative value taken as a *reference thickness* (390 x 300 µm/horizontal x vertical size) was obtained from positions on the wafer that were at least 1 mm away from any dispensed droplet. In these areas the recorded data were not affected by acid. Spraying due to the formation of satellite droplets may occur in inkjet printing as well as spreading of the liquid on the surface [169]. Both these effects could have potentially influenced the *nearby* film thickness.

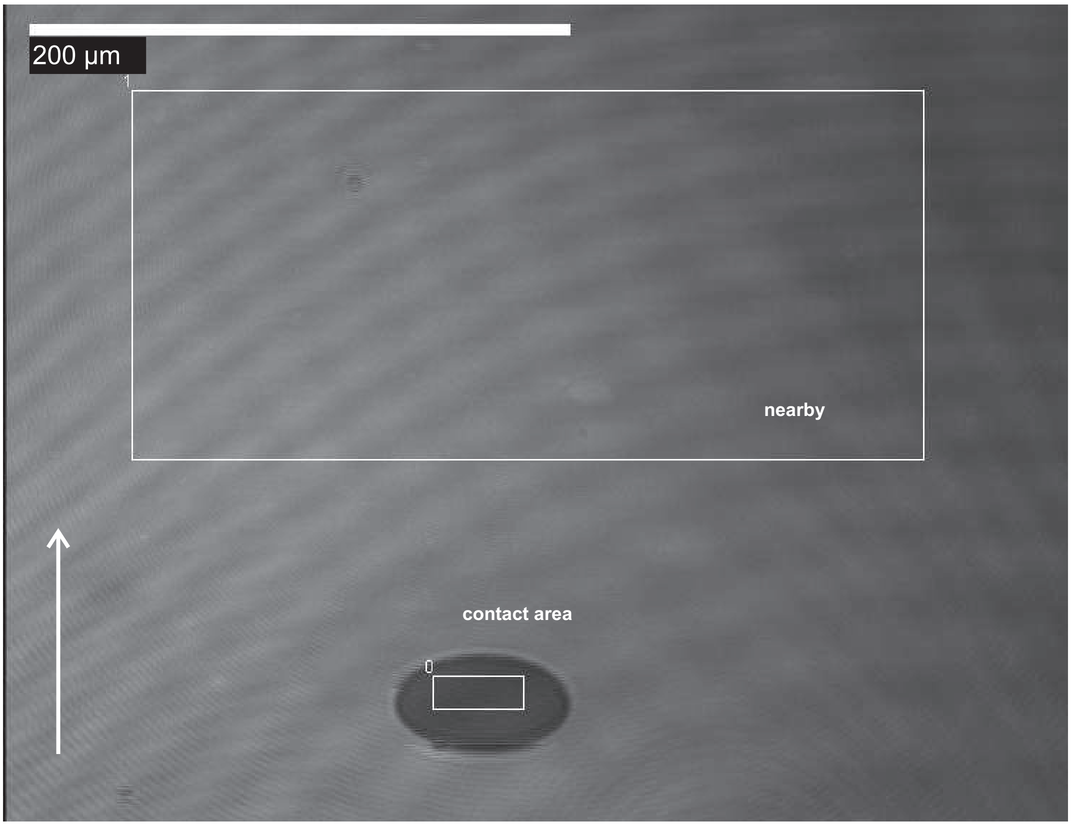

Fig. 3.5: Typical image of data acquisition with the imaging ellipsometer on a sample of patterned PMMA brushes. The white rectangles mark the regions of interest, where the film thickness was acquired. The spherical drop is imaged as elliptical in shape because the image was taken under a viewing angle of 60 degrees. The white arrow indicates viewing direction of the optical system.

On average, we measured eight points on the sample away from patterns to calculate the mean value and plotted it as the *reference thickness*. The standard deviation was in all cases lower than the error that resulted from the modeling of the ellipsometric angles. Therefore, we chose the error of the modeling (± 1 nm) as error bars. We proceeded like this when comparing the data for the two kinds of acids (Fig. 3.7) as well as for the comparison between the different concentrations of H_2SO_4 (Fig. 3.9). Similarly, mean values for the *contact area* and *nearby* are plotted in Fig. 3.7 and 3.9. On average, four single drops were measured and the mean value calculated. Once again the margin of error from the modeling of the ellipsometric angles was bigger than the standard deviation from the mean value, so the error of the modeling (± 1nm) was chosen as error bars.
Based on the theoretical considerations of Alexander [88] and deGennes [86] the following equation allowed to *estimate* the grafting density Γ of the polymer brushes.

$$\Gamma = \frac{d * \rho}{M_n} N_A \tag{3.1}$$

From Gaussian error propagation an estimation of the grafting density error $\Delta\Gamma$ is possible:

$$\Delta\Gamma = \sqrt{(\frac{\rho}{M_n} N_A \Delta d)^2 + (-\frac{d * \rho}{M_n^2} N_A \Delta M_n)^2} \tag{3.2}$$

N_A is Avogadros constant $6.02*10^{23}$ mol^{-1} and ρ is in this case the density of the PMMA brushes. This value was assumed to be close to the bulk density of PMMA at $1.119*10^{-21}$ g/nm^3, neglecting effects like solvation. d stands for the film thickness measured in nm. M_n is the molecular weight of the polymer brushes *estimated* from the molecular weight of the free polymer measured by GPC. For the error of the film thickness $\Delta d = 1\ nm$ was chosen, which is the error of the modeling. The error of the molecular weight ΔM_n was set to 5 % of the measured molecular weight. The absolute numbers provided by this formula can only serve as a rough guide, but comparison of brushes relative to one another should be possible.

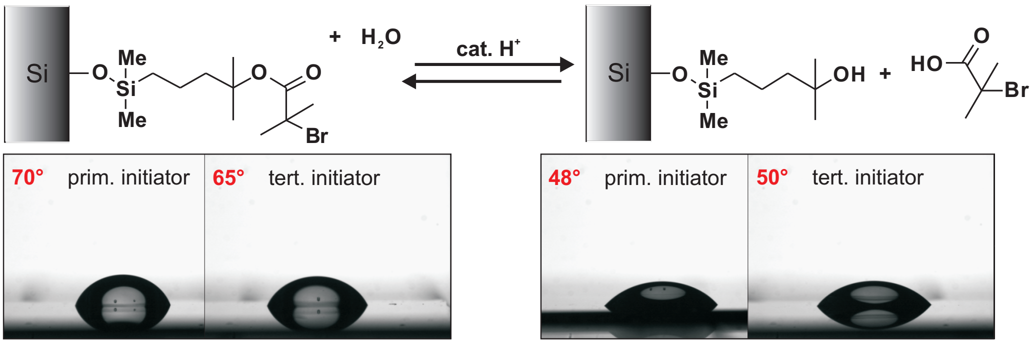

Fig. 3.6: Saponification of surface-immobilized ATRP initiator with catalytic amount of acid. The error of the contact angles is ± 10 degrees.

In addition to plotting the data against absolute film thickness, the data was additionally plotted as relative thickness with respect to the *reference thickness*. Trends in the data are at times more articulated using the relative thickness, since the absolute thickness varies from sample to sample. Several factors, among them the polymerization time and the conversion, are the reason for this. This was the motivation for plotting the data in Fig. 3.12, 3.13, and 3.14 exclusively as relative thickness.

3.1.7 Contact angles: Determination of surface properties after contact with acid

The basic principle underlying this research is the saponification reaction of surface-immobilized ATRP initiator molecules. Ordinarily, saponification is done on mobile molecules in solution and not on molecules immobilized on a surface. The first step was therefore to prove that saponification of surface-immobilized molecules is feasible. Static contact angle measurements were preformed to examine the change in surface energy after the saponification. As depicted in the upper part of Fig. 3.6, quantitative saponification of the tertiary initiator leaves a tertiary alcohol on the surface. The free bromoisobutyric acid can be washed away in the cleaning step. Two wafers were covered with the initiator molecules and contact angles of 70 ± 10 degrees for the primary initiator (compared to 77 degrees from an earlier publication of our group [170]) and 65 ± 10 degrees for the tertiary initiator on the freshly prepared samples measured. The samples were processed further by immersing them halfway into 1 mol/L H_2SO_4 for 40 min to allow the saponification to proceed. A cleaning step - washing with Milli-Q water and extraction with DCM overnight - was performed to remove any residual free bromoisobutyric acid from the surface. No changes in contact angles were observed on the parts of the samples that had not been in contact with the acid. In the contact area we observed a decrease to 48 ± 10 degrees in the case of the primary initiator and 50 ± 10 degrees for the tertiary one. Miyake et al. [171] reported a contact angle for a hydroxyl terminated SAM of 55 degrees, which is within the error of our observation. This indicates that saponification reactions on surface-immobilized molecules are possible.

3.1.8 Comparison of effectiveness of hydrochloric acid and sulfuric acid in saponification

In general, saponification is an equilibrium reaction. The reaction conditions must be adjusted in such a way that the equilibrium is located on the side of the product. In this present case the product is the alcohol on the surface and the free bromo isobutyric acid (see Fig. 3.6). The parameters determining the position of the equilibrium are the type of acid used and the amount of water available. With the use of the inkjet printer it was possible to screen these parameters simultaneously. In a first attempt two different types of acid, concentrated HCl and four concentrations of H_2SO_4 (Fig. 3.7) were compared. Direct techniques to measure the density of active initiator molecules in an area as small as 60 µm were not available. Therefore the film thickness was measured and related to changes in grafting density.

The more cleaved ester bonds were generated with the acid, less molecules remained on the surface that still carried bromo functionalities. In turn, this means a reduction in grafting density, resulting in a lower film thickness for a given molecular weight. The effect of the various acids on the tertiary initiator (upper diagram in Fig. 3.7) will be discussed first. After treatment with

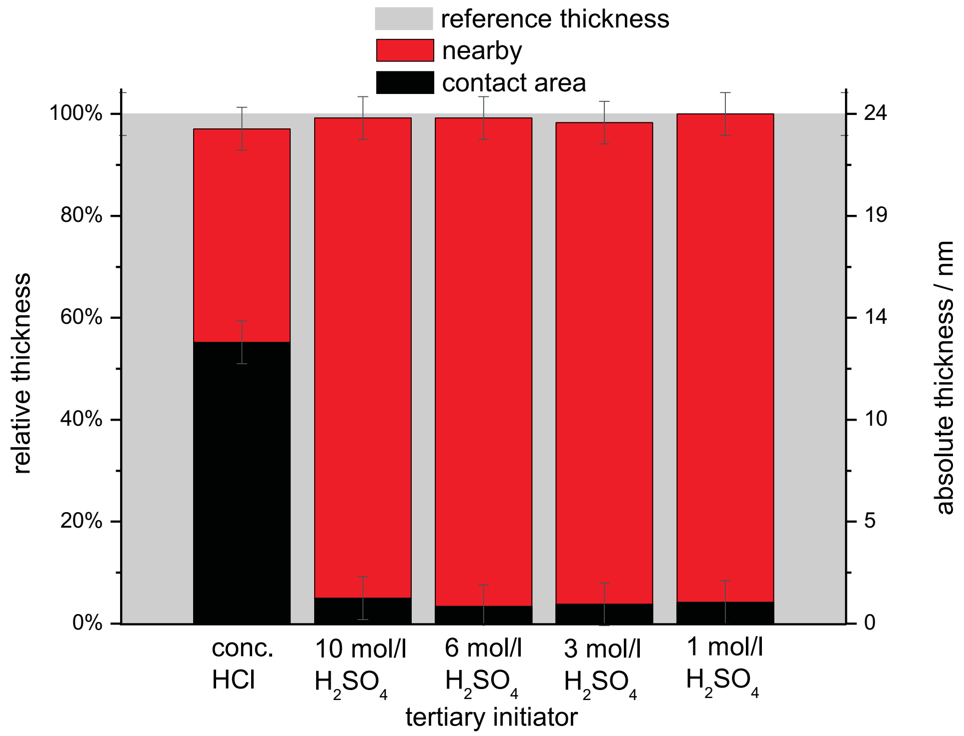

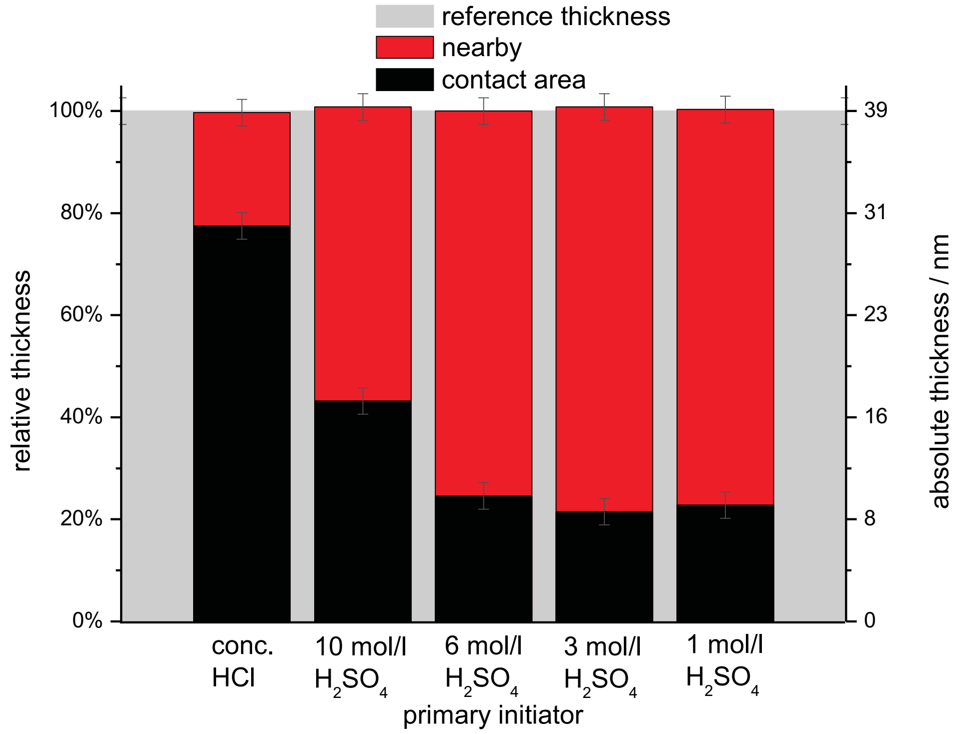

Fig. 3.7: Effect of concentrated HCl and various concentrations of H_2SO_4 on the film thickness of PMMA brushes.

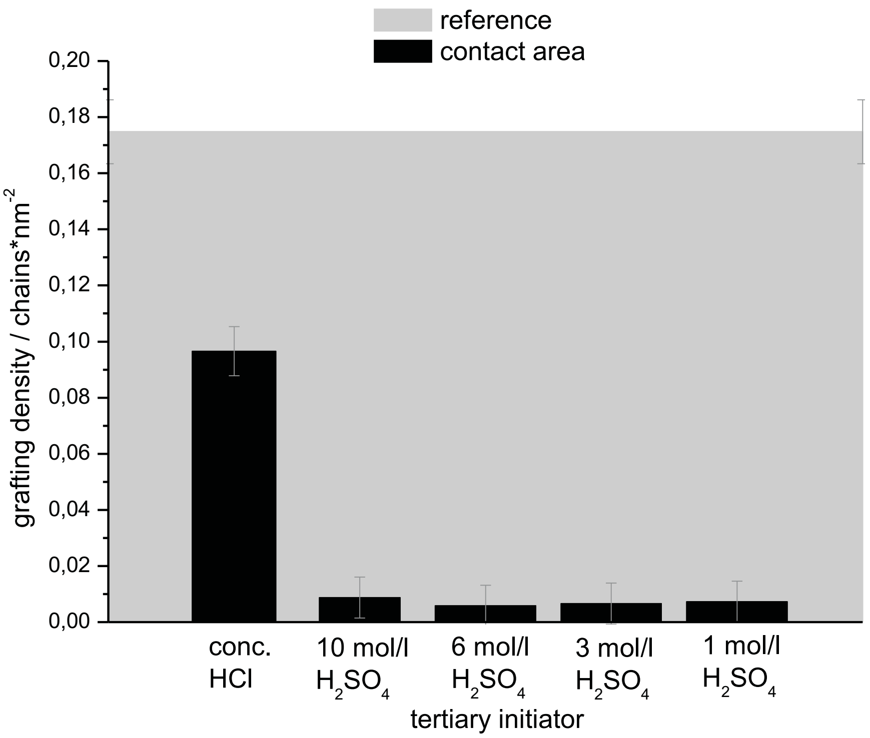

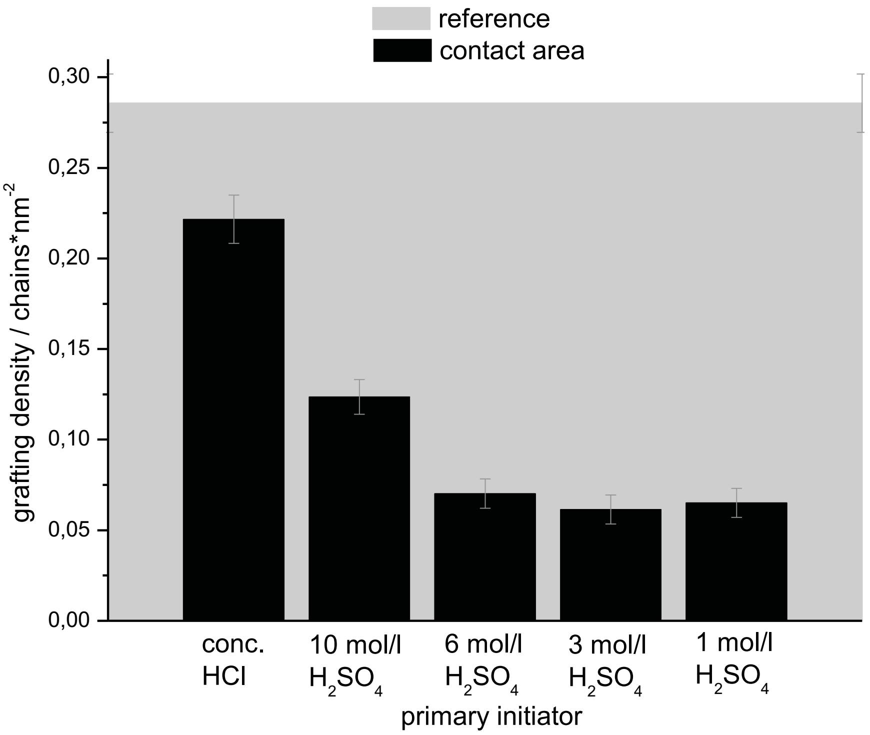

Fig. 3.8: Effect of concentrated HCl and various concentrations of H_2SO_4 on the grafting density.

any of the four concentrations of H_2SO_4, no polymer is found within the margin of error ($> 1.2 \pm 1$ nm in every case). In contrast, the film thickness after treatment with concentrated HCl is still 13 nm, which is approximately 55 % of the reference thickness. Similar observations concerning the effect of concentrated HCl can be made in the case of the primary initiator (lower diagram in Fig. 3.7). Film thickness after treatment with concentrated HCl is only reduced to 30 nm (75 %), whereas on the other hand 6, 3 and 1 mol/L H_2SO_4 reduce the film thickness to 9 nm. This corresponds to 25 % of the reference film thickness. 10 mol/L H_2SO_4 shows a significant discrepancy compared to the other H_2SO_4 concentrations. In this case the film thickness was only reduced to 45 % (16 nm). The motivation for the synthesis of the tertiary initiator was the hydrolytically more labile ester bond in this molecule, which should be easier to cleave. Indeed, for all concentrations of H_2SO_4 and for the HCl, the comparison of relative film thickness of the two initiators show a decrease in relative thickness by 20 % or even up to 40 % for the 10 mol/L H_2SO_4 in the case of the tertiary initiator. This demonstrates the increased lability of the ester bond in the tertiary initiator. The tertiary initiator combined with diluted H_2SO_4 of 6, 3 or 1 mol/L concentration suppresses polymer growth completely within the margin of error. Yet the primary initiator is interesting to use, when tuning of grafting density is desired.

An explanation for the difference between concentrated HCl and all of the chosen concentrations of H_2SO_4 is the high volatility of concentrated HCl. HCl has a boiling point of 45 °C [172] (38 %), unlike concentrated sulfuric acid, which is nonvolatile with a boiling point of 300-320 °C [173] (96 %). The high surface-to-volume ratio of inkjet-printed microdroplets leads to extremely rapid evaporation, even for liquids with boiling points of 200 °C (vapor pressure around 10^{-1} mm Hg). Micro droplets of liquids with high boiling point around 200 °C evaporate approximately within 1 minute [160]. The more quantitative observations are consistent with this argument of volatility. Immediately after deposition the drops of Milli-Q water or concentrated HCl were evaporated. This behavior of HCl is expected, since it is a gas dissolved in water. By contrast, the drops of diluted H_2SO_4 were still present after 20 min, although they seemed to shrink to some extent after deposition due to the loss of water. More details about the evaporation process can be found in Section 3.1.14.

The number average molecular weight and the polydispersity of the free polymer was $M_n = 97900 g/mol$, $PDI = 1.2$, as measured by GPC.

From the molecular weight an estimation of the grafting densities in the contact areas and the reference thickness was possible, as shown in Fig. 3.8. The value obtained from the reference areas (gray box) at 0.17 ± 0.01 chains/nm^2 in the case of the tertiary initiator, and 0.29 ± 0.02 chains/nm^2 for the primary initiator are within the error of the average values of 0.11 ± 0.03 and 0.26 ± 0.04 chains/nm^2, as presented in Fig. 3.19.

Treatment of the tertiary initiator with 6, 3, and 1 mol/L of H_2SO_4 resulted in a grafting density of 0.007 ± 0.007 chains/nm^2. Therefore it can be concluded, that no polymer grew in the areas that had been in contact with 6, 3, and 1 mol/L H_2SO_4. On the other hand a value of 0.09 ± 0.009 chains/nm^2 for the concentrated HCl was estimated. This value is approximately 55% of the value found for the reference area at 0.17 ± 0.01 chains/nm^2.

The effect of concentrated HCl on the primary initiator was similar. The grafting density was reduced down to 75 % at 0.22 ± 0.01 chains/nm^2. 10 mol/L H_2SO_4 was more effective yielding a grafting density of 0.12 ± 0.01 chains/nm^2 (45 %). Even more effective were 6, 3 and 1 mol/L of H_2SO_4, where the grafting density went down to 0.07 ± 0.008 chains/n^2 (25 %).

3.1.9 Comparison of effectiveness of different concentrations of sulfuric acid in saponification

Next it was investigated in more detail why 10 mol/L H_2SO_4 was not as effective as lower concentrations, at least in the case of the primary initiator. The hypothesis is that the water content is solely responsible for the position of the equilibrium of the saponification reaction.

Regardless of the concentration of H_2SO_4 plotted on the tertiary initiator, the remaining film thickness is below 5 % of the original thickness (upper diagram, Fig. 3.9). With all concentrations of 10 to 1 mol/L of H_2SO_4 and a contact time of 20 min, brush growth from the tertiary initiator can be sup-

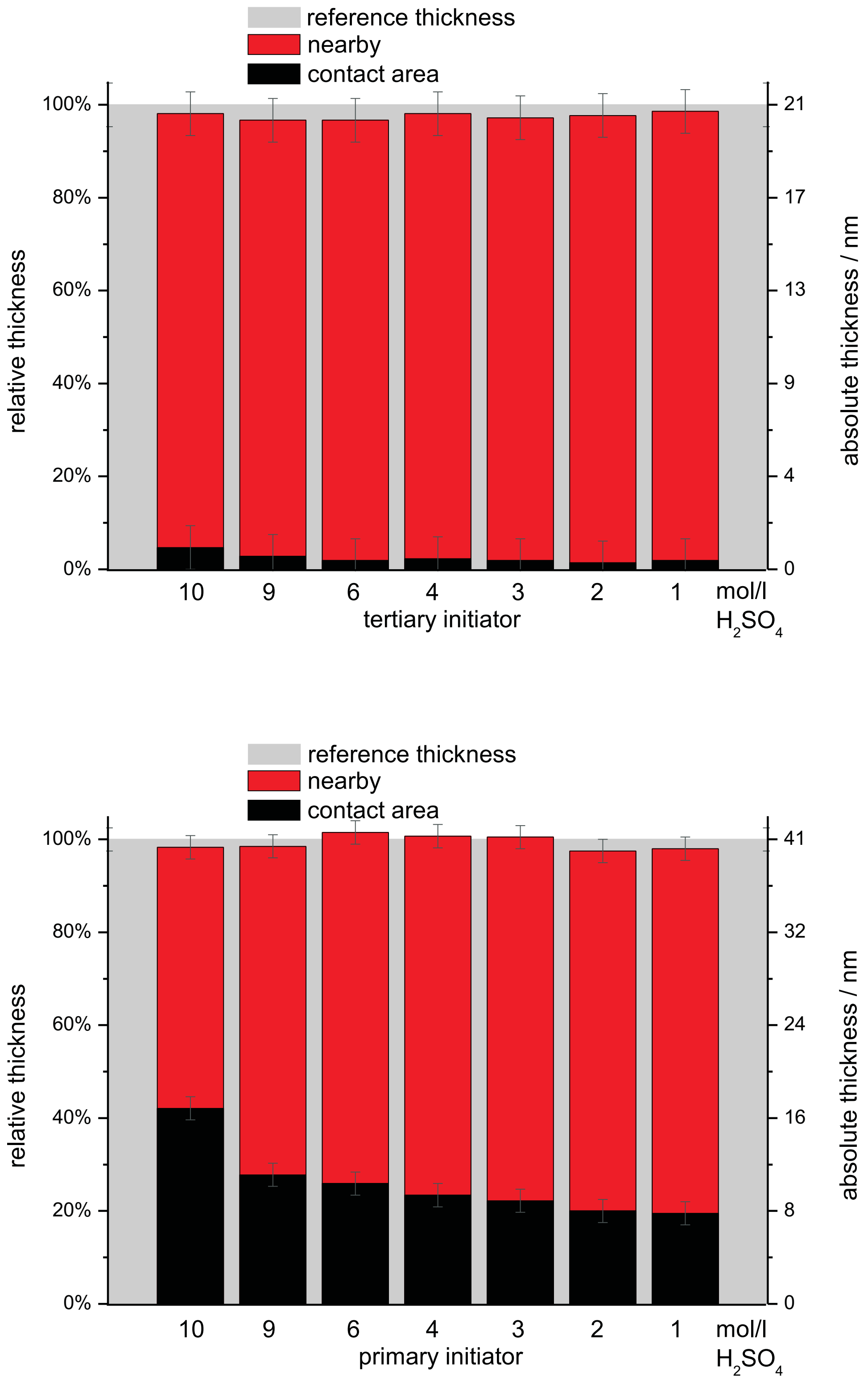

Fig. 3.9: Effect of various concentrations of H_2SO_4 on the film thickness of PMMA grown via SI-ATRP.

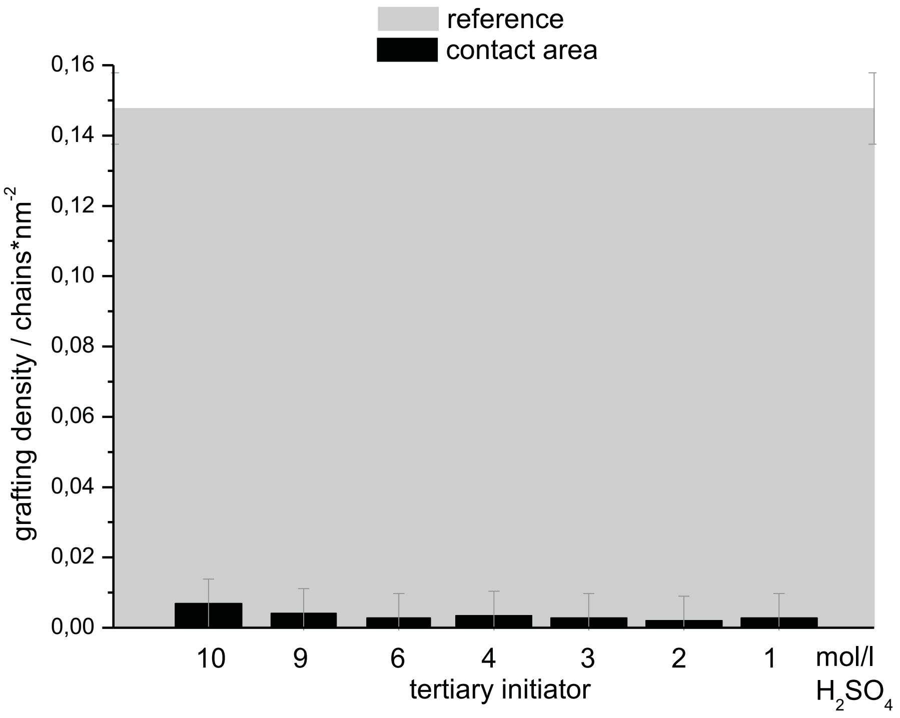

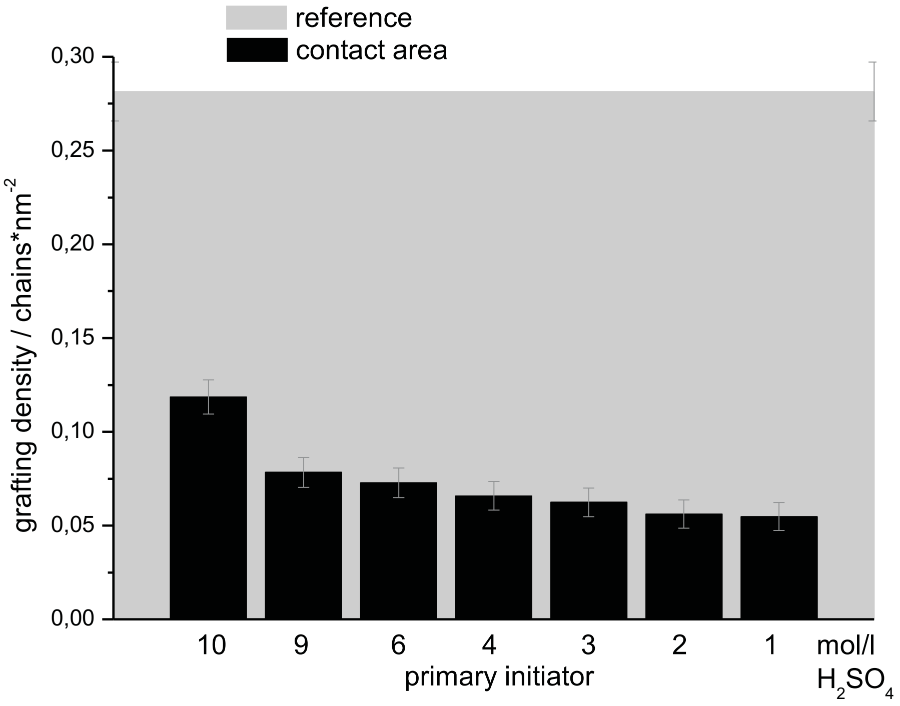

Fig. 3.10: Effect of various concentrations of H_2SO_4 on grafting density.

pressed within the margin of error. For the primary initiator - lower diagram Fig. 3.9 - the trend to lower thickness with lower concentration of deployed H_2SO_4 is clear-cut. In none of the used concentrations does the thickness go below 20 %. So the comparison of the relative film thickness in the contact area between the two initiators for all the different concentrations of H_2SO_4 supports the conclusion that was drawn from Fig. 3.7. The ester bond is more labile in the tertiary initiator. This effect is independently observed from the value of absolute film thickness, as a comparison of Fig. 3.7 and Fig. 3.9 shows.

The data for both initiators is congruent regarding the effectiveness in saponification of 10 mol/L H_2SO_4. It is lower than all of the more dilute concentrations. This effect is more pronounced for the primary initiator but is in principle also observed for the tertiary initiator. The equilibrium in the saponification reaction (Fig. 3.6) can be shifted solely by supplying water; protons are just needed as a catalyst. With higher water content, the equilibrium is shifted more and more to the desired side of the alcohol on the surface and the free bromoisobutyric acid. For the tertiary initiator the water content does not seem to be as crucial. This is due to the fact that the ester bond is more labile and breaks easier from the start. The compliance between the reference thickness (gray) and the nearby (red) again indicates that the droplets did not splash upon contact with the surface (Fig. 3.9).

The number average molecular weight and the polydispersity of the free polymer was $M_n = 103300 g/mol, PDI = 1.17$, as measured by GPC.

From the molecular weight an estimation of the grafting densities in the contact areas and the reference thickness was possible, as shown in Fig. 3.10. The value obtained from the reference areas (gray box) at 0.15 ± 0.01 chains/nm^2 in the case of the tertiary initiator, and 0.28 ± 0.02 chains/nm^2 for the primary initiator are within the error of the average values of 0.11 ± 0.03 and 0.26 ± 0.04 chains/nm^2, as presented in Fig. 3.19.

Treatment of the tertiary initiator with any of the chosen concentrations of H_2SO_4 resulted in a grafting density below the error at ± 0.007 chains/nm^2. Therefore it can be concluded, that polymer growth was completely suppressed in the areas that had been in contact with 10 - 1 mol/L of H_2SO_4

for 20 min.
For the primary initiator a trend to lower grafting densities with lower concentration of deployed H_2SO_4 is clear-cut. A value below 0.05 ± 0.007 chains/nm^2 (20 %) however, was not observed. This supports the findings, that the ester bond in the tertiary initiator is more labile and that more dilute concentrations of H_2SO_4 are more effective in saponification.

3.1.10 Fabrication of the MPIP-Logo

After finding the optimum conditions for suppressing polymer growth completely, a test of the potential of our method for printing more complex designs was conducted. Since imaging a pattern several hundreds of micrometers in size was not possible with the use of the imaging ellipsometer, we printed a pattern with 1 mm in size. With the use of an optical microscope we were able to image this pattern. In Fig. 3.11 the pattern is shown on the right side. It resembles the logo of our institute, which is shown on the left. The pattern was formed by printing 1 mol/L H_2SO_4 on the tertiary starter. The film thickness is 8.6 ± 1 nm as measured by ellipsometry. Polymerization did not occur in the regions where sulfuric acid had been printed. In these regions the film thickness is $> 1.2 \pm 1$ nm. The former contact areas appear lighter in the optical microscope image because we measured under moist conditions. The moisture generated a contact angle contrast between the more hydrophobic regions where polymer was grown and the more hydrophilic regions where the initiator was destroyed.
The number average molecular weight and the polydispersity of the free polymer was $M_n = 56000 g/mol$, $PDI = 1.18$, as measured by GPC.

3.1.11 Time dependence of saponification reaction from inkjet printing

In the preceding Sections it was shown, that the tuning of grafting densities is possible by applying either HCl or H_2SO_4 in different concentrations. However, it would be much more convenient to tune the grafting density by

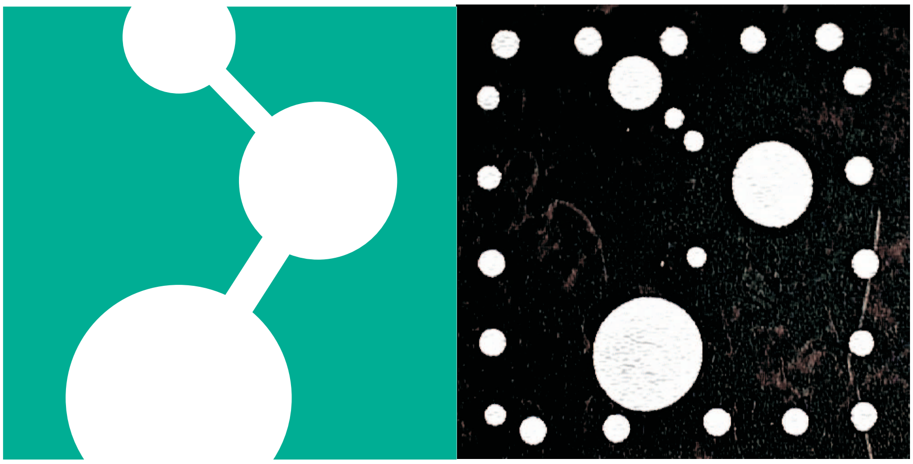

Fig. 3.11: The logo of our institute is shown on the left. On the right side is the pattern after polymerization with PMMA shown. The light regions correspond to no polymer growth, while the regions where polymer was grown, appear darker. The image was taken with an optical microscope.

controlling the contact time between the acid and ATRP initiator. Hence, the time dependence of the saponification reaction was investigated. 1 mol/L H_2SO_4 in contact with the surface leads to almost complete defunctionalization of the tertiary initiator. Water evaporation was slowed down by cooling the samples to 10 °C . Cooling slowed down the reaction and lower acid concentrations of 0.5 and 0.1 mol/L H_2SO_4 were investigated.

The data in Fig. 3.12 are plotted as relative thickness against contact time. We measured the film thickness in four contact areas, plotted the mean value of those, and chose the error of the modeling as error bars (± 1 nm). In the upper diagram of Fig. 3.12 there is a gradual decrease in relative brush thickness with contact time for the tertiary initiator. The same holds true in the case of the primary initiator (lower diagram Fig. 3.12), but the curve levels off after 20 min within the margin of error. In addition, the data for both initiators show no difference regarding the three concentrations. Given that the water content matters, and not the amount of protons, any concentration below 10 mol/L H_2SO_4 has enough water to shift the equilibrium of the saponification to the product side before the water is evaporated.

When comparing the final thickness for 1 mol/L H_2SO_4 from Fig. 3.9 to Fig.

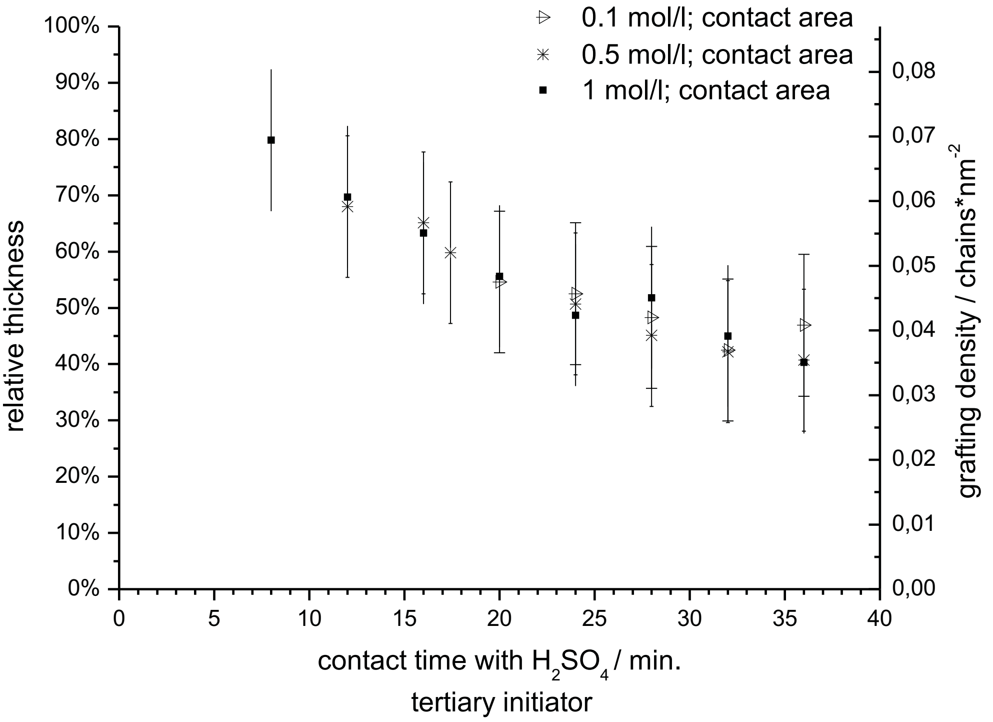

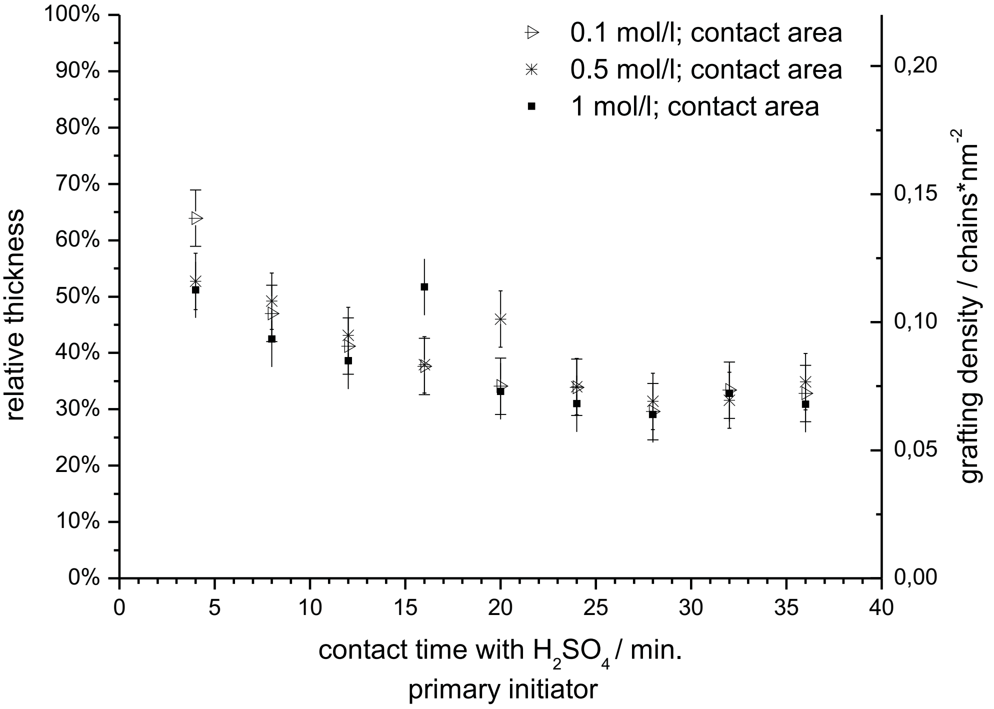

Fig. 3.12: Time dependence of the saponification reaction from inkjet printing. For each concentration a line of droplets was deposited every 4 min. Error bars with long end-caps belong to the data of the 0.1 mol/L sulfuric acid. Error bars with medium end-caps belong to 0.5 mol/L. Error bars with no end-caps indicate data related to 1 mol/L.

3.12 for both initiators it is clear that they do not reach the same level, even though the contact time was twice as long. The sample preparation was altered in the case of the time dependency by cooling the samples to 10 °C . Cooling of the samples slows down the evaporation of water out of the microdroplets, while heating enhances evaporation [158]. This supports the hypothesis that the initial water content of the microdroplet matters. That was the reason why the film thickness decreased with decreasing concentration of H_2SO_4. Then the evaporation of water from the microdroplet set in and the concentration of H_2SO_4 started to increase. This seems to drive the saponification reaction to completion. Due to the cooling of the substrate, the evaporation of the water from the micro droplet was changed. As a result, a lower fraction of ester molecules was cleaved on the time scale under investigation.

The number average molecular weight and the polydispersity of the free polymer was $M_n = 65100 g/mol$, $PDI = 1.16$, as measured by GPC. From the molecular weight an estimation of the grafting densities was possible.

The grafting density obtained from the area that had not been in contact with acid is 0.09 ± 0.01 chains/nm^2 in the case of the tertiary initiator, and 0.22 ± 0.02 chains/nm^2 for the primary initiator. The values are within the error of the average values of 0.11 ± 0.03 and 0.26 ± 0.04 chains/nm^2, as presented in Fig. 3.19.

A gradual decrease of grafting density with increasing contact time is observed for both initiators. Values of 0.03 ± 0.01 for the tertiary initiator and 0.07 ± 0.01 chains/nm^2 for the primary initiator are reached at 35 min. Both these values are higher, compared to what was observed in Fig. 3.10 for 1 mol/L H_2SO_4 at 20 min. As elucidated above, the samples were cooled, so the saponification did not proceed with the same efficiency.

3.1.12 Time dependence from dip-coating/Creation of a gradient in grafting density over the area of a whole wafer

To study the efficiency of the saponification reaction independent of droplet evaporation a dip-coater was used and the samples gradually pulled out of a solution of 5 and 1 mol/L H_2SO_4. This approach allowed to tune the grafting density from brush regime to mushroom regime over larger areas, which is desirable when studying the dependence of brush height on grafting density [55, 81]. The data in Fig. 3.13 and 3.14 are plotted as relative thickness against contact time. As the point of reference for each initiator (100% relative thickness) the 3 mm wide area that had not been immersed in H_2SO_4 was selected. Measurements of the film thickness were taken at four different areas; the mean value of this was plotted and the error of the modeling was chosen as error bars (± 1 nm).

In Fig. 3.13 the data of the dip-coating using 1 mol/L H_2SO_4 are shown. With longer contact time the film thickness was reduced for both initiators. In analogy to the data in Fig. 3.12 the film thickness in the case of the primary initiator reaches a steady state after 20 min. No steady state is reached for the tertiary initiator, at least not within the contact times under investigation. As is noticeable, the film thickness can be tuned all the way down to 55 % for the primary initiator and 30 % for the tertiary initiator. Compared to the data from inkjet printing of 1 mol/L H_2SO_4 (Fig. 3.9) where levels of 25 % for the primary initiator and 5 % for the tertiary initiator were reached, the values here are much higher. When using the dip-coater and 20 mL of acid, evaporation plays no role. Thus, the reaction proceeds in a different way, and therefore the saponification reaction did not reach the same conversion as in printing.

The number average molecular weight and the polydispersity of the free polymer was $M_n = 17500 g/mol$, $PDI = 1.05$, as measured by GPC. From the molecular weight an estimation of the grafting densities was possible.

The grafting density obtained from the area that had not been in contact with acid is 0.13 ± 0.04 chains/nm^2 in the case of the tertiary initiator, and 0.19 ±

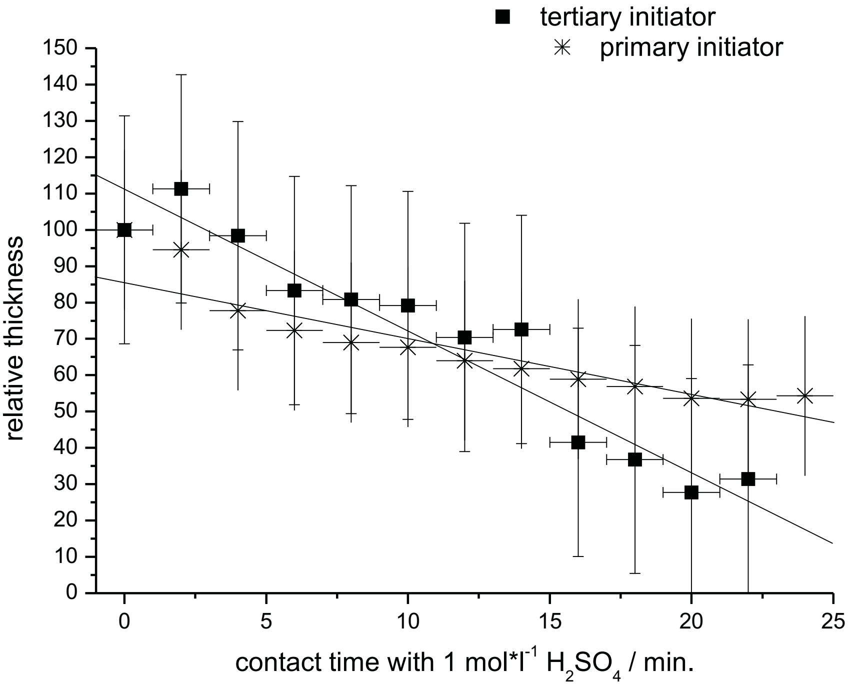

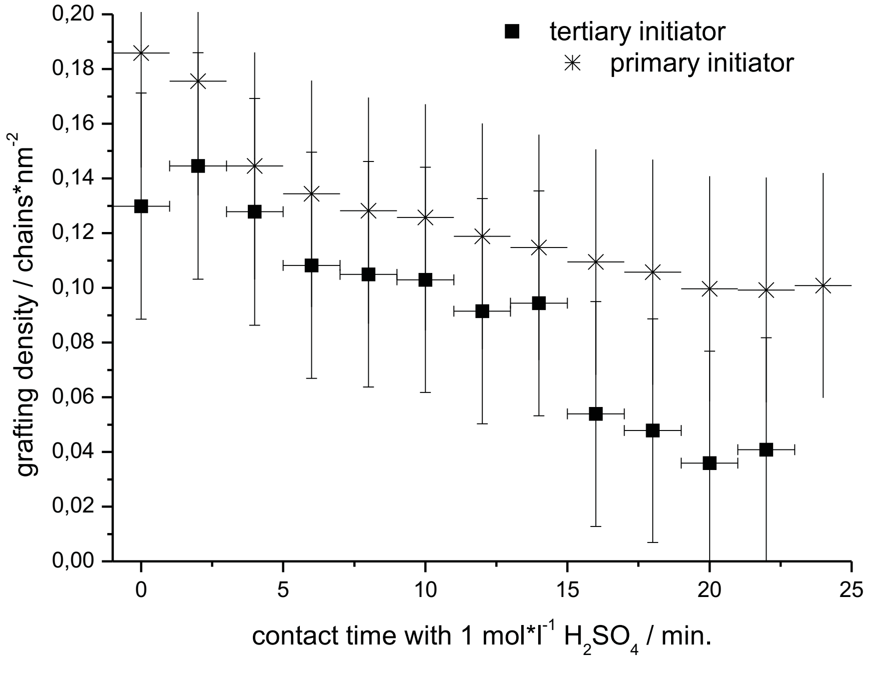

Fig. 3.13: Time-dependence of the saponification reaction from dip-coating. The wafers were pulled out of a solution of 1 mol/L H_2SO_4 with a speed of 1.5 mm/min using a dip-coater. Solid lines are guides to the eye. Error bars of the primary starter have no end-caps.

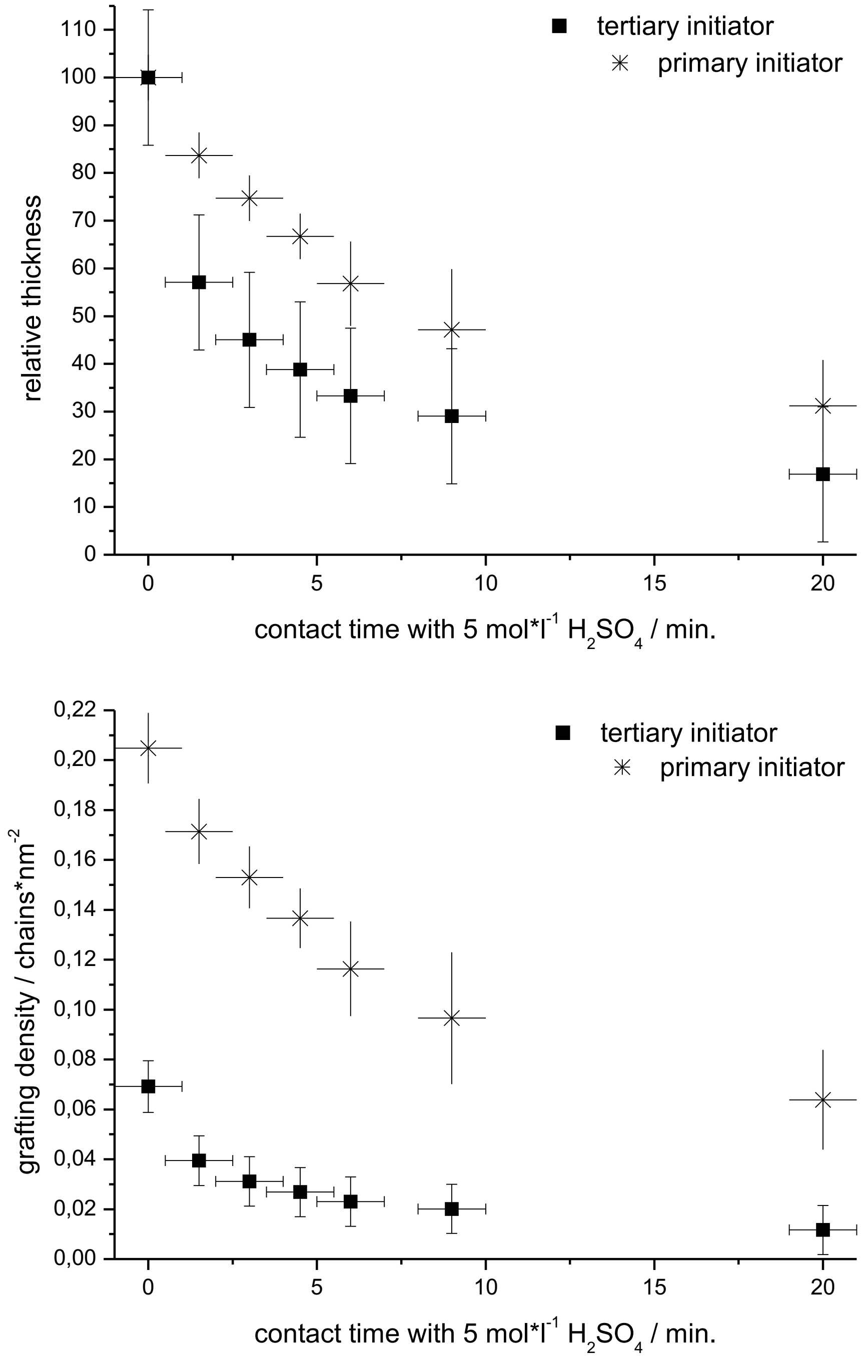

Fig. 3.14: Time-dependence of the saponification reaction from dip-coating. The wafers were pulled out of a solution of 5 mol/L H_2SO_4 with a speed of 1.5 mm/min using a dip-coater. Solid lines are guides to the eye. Error bars of the primary starter have no end-caps.

0.04 chains/nm^2 for the primary initiator. The values are within the error of the average values of 0.11 ± 0.03 and 0.26 ± 0.04 chains/nm^2, as presented in Fig. 3.19.

A reduction in grafting density down to 0.04 ± 0.04 for the tertiary initiator and 0.1 ± 0.04 in the case of the primary initiator is observed. These values are slightly higher than the values from ink printing of 1 mol/l H_2SO_4 (Fig. 3.9). A value of grafting density of the tertiary initiator below the error at ± 0.007 chains/nm^2 and 0.05 ± 0.007 chains/nm^2 was observed for the primary initiator. But as elucidated above evaporation plays no role in the dip-coating experiments, so the saponification proceeds in a different way.

In Fig. 3.14 the data from dip-coating using 5 mol/L H_2SO_4 are presented. With longer contact time the film thickness was reduced for both initiators. In contrast to the data obtained using 1 mol/l H_2SO_4 (Fig.3.13) for the dipping a steady state in film thickness was reached for both initiators at 20 min. It appears that the equilibrium of the saponification reaction was established after 10 min. Beyond that time no further change in film thickness was observed. The final value in film thickness is 16 % for the tertiary initiator and 30 % for the primary one. These values are half the values obtained using 1 mol/l H_2SO_4 for dipping (Fig.3.13). The obtained value is even comparable to the result from inkjet printing 1 mol/L H_2SO_4 (Fig. 3.9) on the primary initiator at 25 %.

The number average molecular weight and the polydispersity of the free polymer was $M_n = 73100 g/mol$, $PDI = 1.35$, as measured by GPC. From the molecular weight an estimation of the grafting densities was possible.

The grafting density obtained from the area that had not been in contact with acid is 0.07 ± 0.01 chains/nm^2 in the case of the tertiary initiator, and 0.2 ± 0.01 chains/nm^2 for the primary initiator. The values are within the error of the average values of 0.11 ± 0.03 and 0.26 ± 0.04 chains/nm^2, as presented in Fig. 3.19.

A reduction in grafting density down to 0.07 ± 0.01 for the tertiary initiator and 0.06 ± 0.02 in the case of the primary initiator is observed. These values are similar to the values obtained using 1 mol/L H_2SO_4 for dip-coating. In the case of the primary initiator is the final grafting density comparable

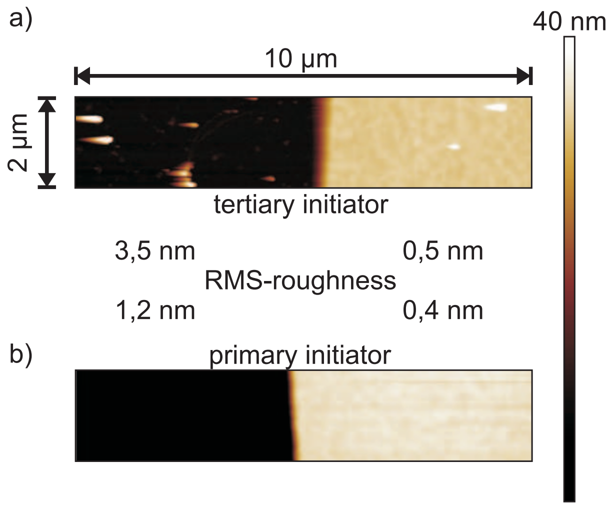

Fig. 3.15: AFM height images and roughness on the rim of the contact area after the polymerization.

to the one obtained from printing 1 mol/L H_2SO_4 (Fig. 3.9) at 0.05 ± 0.007 chains/nm^2.

3.1.13 AFM studies of contact areas

After testing the effect of acid on the SI-ATRP initiators the last step was to study in detail the ink behavior on the substrate. A crucial step in ink-printing is the moment a droplet hits the solid substrate and comes to rest. Thus, the features were checked for uniformity and roughness using an AFM. The AFM images in Fig. 3.15 were taken on the rim of the former contact area between 1 mol/L H_2SO_4 and a) the tertiary initiator and b) the primary initiator. In both images a sharp step is clearly distinguishable. The step separates the former contact between initiator molecules and the acid from the surrounding PMMA brushes. Concerning the RMS roughness of the surrounding PMMA layers we obtained 0.5 nm for the tertiary initiator and 0.4 nm for the primary one. Ramakrishnan et al. [74] published a roughness of 0.5 nm for the PMMA layer from X-ray reflectivity measurements in the case of the primary initiator. The agreement between the roughness of the PMMA

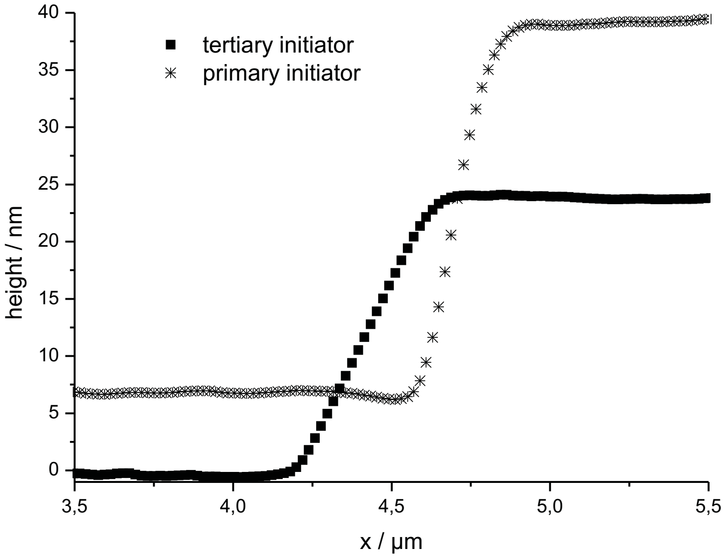

Fig. 3.16: Cross-sections from AFM height images indicating the structure and the height of the rim.

brushes around the pattern between the two tested ATRP-initiators and the roughness from literature demonstrates that the acid did not have any effect on the surrounding areas and in turn catalyzed the saponification reaction only in the printed areas.

The cross sections in Fig. 3.16 substantiate the findings from the height images. A sharp step separates the contact area from the surroundings. However, a difference in slope between the two initiators can be identified. Within 0.6 µm the transition from the former contact area to unaffected areas is complete in the case of the tertiary initiator. The transition for the primary initiator is completed within 0.4 µm. In the transition areas the change in film thickness is a result of the change in the grafting density of brushes. The difference in slope that was observed has its origin in the combination of droplet evaporation and ester bond lability. For the tertiary starter the evaporation sets in while the saponification proceeds and the droplet shrinks in size. In the case of the primary starter saponification is slow, and therefore the greater part of the saponification takes place after the shrinking of the droplet has proceeded.

The heights of the rim indicated in the cross sections (Fig. 3.16) from AFM are compared to the ellipsometry data. Given that AFM can only measure relative height differences, the reference thickness from ellipsometry measurement was chosen as the highest point of the cross section. For the tertiary initiator (filled squares) AFM gave a height of the rim of 24 nm, which is in good comparison to 23 ± 1 nm calculated from ellipsometry data. In the case of the primary initiator (stars) ellipsometry yielded a height of 31 ± 1 nm, compared to 33 nm from AFM.

3.1.14 Evaporation of acids

The reasoning for explaining the differences between small drops of HCl and H_2SO_4 in saponification was so far more quantitative in nature. The lower effectiveness of HCl, compared to H_2SO_4, was attributed to the immediate evaporation of the HCl microdrops after deposition. The microdrops of H_2SO_4, did not evaporate completely, but shrunk in size due to the loss of water. A more qualitative study of these evaporation processes is presented in this Section. The measurements were carried out in collaboration with Chuanjun Liu.

A modified reversed particle interaction apparatus was used [174]. It was equipped with an inkjet nozzle for microdrop deposition on a rectangular silicon microcantilever. The cantilever was actively excited by applying a voltage pulse, enhancing the amplitude of oscillations. The resonance frequency was monitored with an optical lever technique at every stage of the evaporation. From the measured resonance frequency at a certain time i calculation of the drop mass m_i was possible, using the following equation:

$$m_i = \frac{K\left(f_0^2 - f_i^2\right)}{4\pi^2 f_0^2 f_i^2} \tag{3.3}$$

where K is the spring constant of the cantilever, f_0 / f_i the measured frequency prior drop deposition / at time i. For more details about the mathematical formalism and the equipment see Section 7.10.

The drop contours were additionally visualized with a camera system.

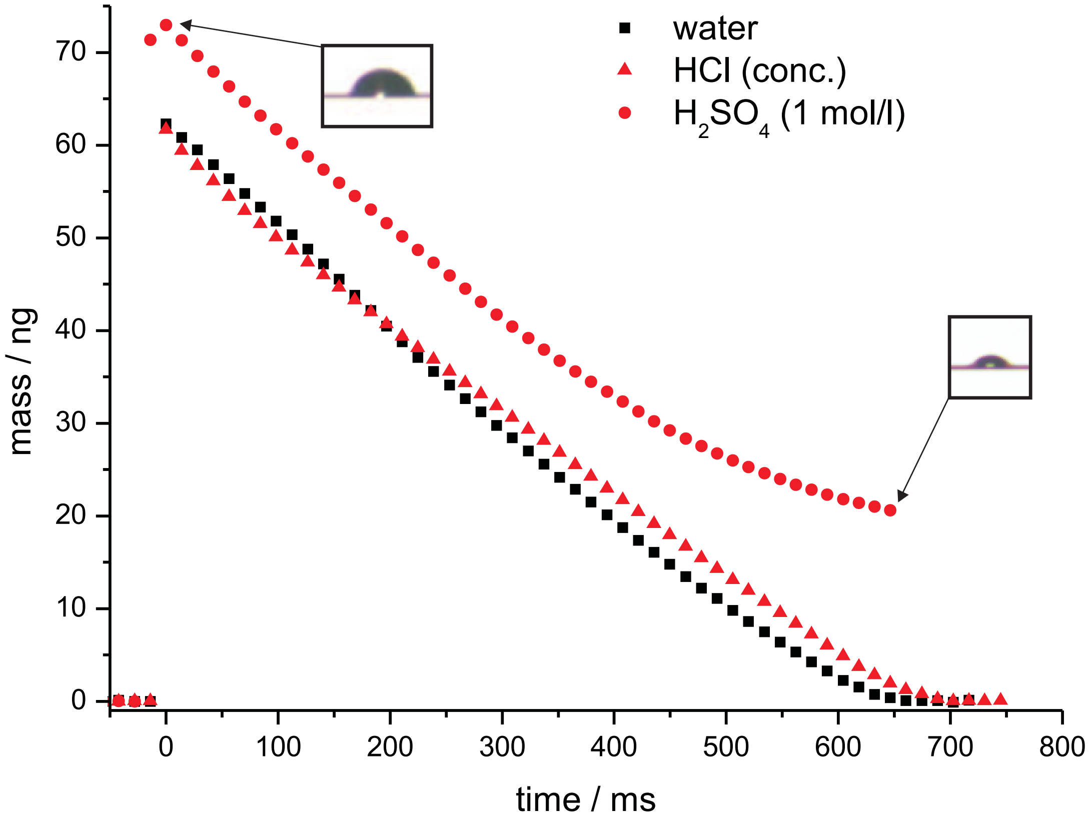

Fig. 3.17: Drop mass of water, concentrated HCl, and 1 mol/L H_2SO_4 vs time during evaporation. The small insets show the size of the H_2SO_4 drop at deposition (time = 0 ms) and at the end of observation (time = 650 ms).

In Fig. 3.17 the calculated mass for a drop of water (black squares) is shown. The drop had an initial mass of $m_0 \sim 62$ ng and monotonically decrease in mass. At roughly 650 ms the drop was completely evaporated.

For a drop of concentrated HCl (red triangles) with similar mass ($m_0 \sim 62$ ng) the behavior resembled that of the water drop. After a monotonic decrease the evaporation was completed at roughly 650 ms.

The initial drop mass was slightly higher at $m_0 \sim 73$ ng in the case of H_2SO_4 (red circles). The evaporation proceeded monotonically roughly up to 300 ms with a similar slope as in the case of water. Beyond 300 ms the evaporation slows down and the curve levels off. The evaporation was not totally completed within the time under observation, but a final drop mass of 20 ng can be estimated. The small insets demonstrate the decrease in drop size from deposition (time = 0 ms) to the end of the observation (time = 650 ms). Based on the pictures of the drop and assuming a spherical cap geometry, the volume of the drop at initial and final stage was estimated using eq. 3.4.

$$V_i = \frac{1}{6}\pi h_i \left(3a_i^2 + h_i^2\right) \tag{3.4}$$

Combining volume and mass, an estimation of the H_2SO_4 density was possible. At deposition the density was close to 1.2 g/cm^3, which means the concentration was rather 5 mol/L (38 weight-%, 1.28 g/cm^3) than 1 mol/L. This a realistic value, because evaporation starts at the inkjet noozle, even before the drop is deposited. In the final stage of evaporation a density of 1.7 g/cm^3 was estimated. This is close to the value of concentrated H_2SO_4 (96 weight-%, 18 mol/L, 1.84 g/cm^3 [175]). So the evaporation of water out of a microdroplet of H_2SO_4 ends with concentrated H_2SO_4, where all the remaining water is bound to the acid.

From these experiments it can be concluded, that the saponification reaction of the ATRP initiator monolayer proceeds within 600 ms. After this time HCl is completely evaporated and H_2SO_4 has reached a concentrated state.

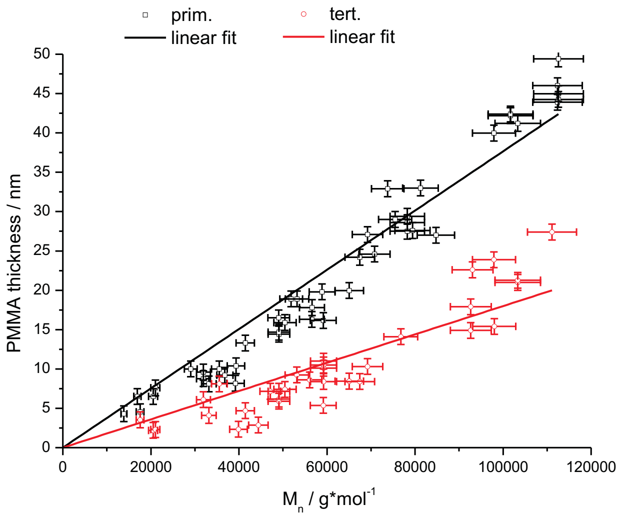

Fig. 3.18: Correlation of PMMA film thickness with the molecular weight M_n of free PMMA produced by the sacrificial initiator in solution. Solid lines show the linear fit.

3.1.15 Correlation of film thickness and grafting density with molecular weight of free polymer

So far it was demonstrated, that patterning and tuning of grafting densities is possible by saponification. SI-ATRP was chosen to amplify the patterns and gradients in grafting density. A well-known system, the primary initiator, was compared to a novel tertiary one. For the primary initiator it is known, that under the described reaction conditions, good control of the polymerization process is achieved [74, 164]. This entails a linear relationship between film thickness d and molecular weight M_n of the free polymer.

$$d \sim M_n \tag{3.5}$$

In order to verify this for the novel starter a series of polymerization was conducted, always polymerizing a wafer with primary initiator together with a wafer containing the tertiary initiator. Molecular weights of up to M_n = 120000 g/mol were obtained and the corresponding film thickness measured. The data are shown in Fig. 3.18.

As expected from literature, the primary initiator (black squares) shows a

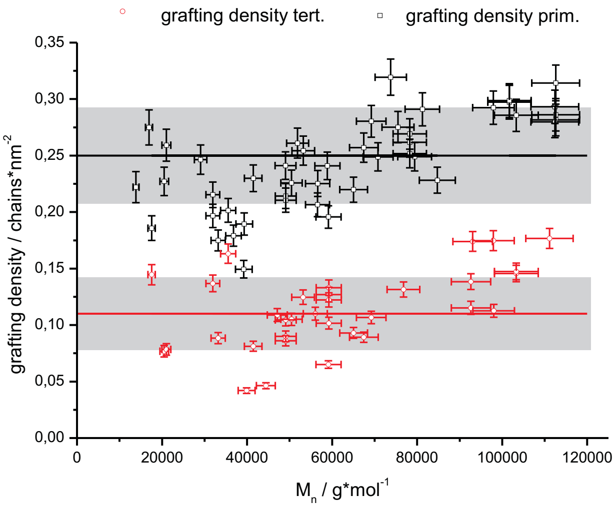

Fig. 3.19: Correlation of the calculated grafting density with the molecular weight M_n of free PMMA produced by the sacrifical initiator in solution. Solid lines show the average grafting density. The shaded regions are related to the standard deviation from the average value.

linear dependency of film thickness on M_n. The black solid shows the linear fit. This behavior is also observed in the case of the tertiary initiator (red circles, red solid line). The assumption that the M_n of the grafted polymer is *proportional* to that of the free polymer, can be made for both initiators. The major difference between both initiators however, is the slope in the plot of film thickness vs M_n. The slope is lower in the case of the tertiary initiator. This is also demonstrated by the lower growth rate (slope^{-1}) in the case of the tertiary starter. For the tertiary starter the M_n has to increase by roughly 5500 g/mol for increase in film thickness of 1 nm. For the primary starter it only takes 2600 g/mol per 1 nm.

As shown in the preceding Sections, the grafting density can be *estimated* from the molecular weight of the surface-attached chains and the film thickness (Section 3.5, eq. 3.1). For each polymerization in Fig. 3.18 this was done and the data are shown in Fig. 3.19.

In all cases the grafting density in the case of the tertiary initiator (red circles) was lower compared to the primary initiator (black squares). The vicinity of the ATRP-initiating site is exactly the same in both initiators. The additional methyl groups in the tertiary initiator are four atoms away from the initiator site. So the initiator efficiency should not be affected by the methyl groups. As literature suggests [83] the difference in grafting density of the two initiator molecules is likely related to a difference in packing density of the initiators. The additional methyl groups might be the reason for a bigger distance between initiators in a monolayer of the tertiary initiator. Further experiments would be necessary though, to clarify this point.

An average value of 0.11 ± 0.03 chains/nm^2 (red solid line) was obtained for the tertiary initiator and a value of 0.26 ± 0.04 chains/nm^2 for the primary initiator (black solid line). The shaded regions are related to the standard deviation from the average value. Ramakrishnan et al. [74] estimated an average grafting density of 0.25 chains/nm^2 for the primary initiator. This is in agreement with our value. From the constancy of grafting density over the range of molecular weights under investigation it can be concluded, that the rate of exchange between the active and dormant chains was fast. This means in turn, that all chains grew more or less at the same rate and that the number of growing chains remained constant.

3.1.16 Stability of initiator SAMs

For the study of the lability of the ester bond in saponification freshly prepared wafers with a monolayer of initiator were used. As presented in the above Sections, a catalytic amount of protons is sufficient for the saponification to proceed. Preparation of a fresh monolayer for each experiment is tedious. Therefore the stability of the initiator monolayer upon storage under ambient conditions for several days was studied. In Fig. 3.20 are the data for both initiators presented.

Freshly prepared samples are compared to samples with an age of 40 days at maximum. As can be seen, there is no dependence of PMMA film thickness on the age of the initiator SAM. The film thickness scatters however by 5 to 8 nm. Since all samples were polymerized in one reactor, factors like conversion or polymerization time can be ruled out as the reason for this deviation. Most likely the reproducibility of monolayer fabrication is the reason for the

Fig. 3.20: Film thickness produced by initiator SAM as function of SAM age.

deviation.

3.1.17 Experimental

Cleaning of silicon wafers

Dust was blown off the 2.3 x 3 cm big wafer in a nitrogen stream. Organic impurities were removed by immersing the wafer in dichloromethane and placing it in an ultrasound bath for 10 min followed by base cleaning. The wafer was placed in a mixture of NH_3 (4 mL, 32%), H_2O_2 (4 mL, 35%), and Milli-Q water (50 mL) at 80 - 85 °C , for 20 min. Finally, the wafer was washed twice with Milli-Q water, desiccated in nitrogen current, and used immediately.

Immobilization of ATRP initiators

Moisture-free conditions and dry chemicals are of importance in this step since both initiators are easily hydrolyzed. The wafer was mounted in a modified Schlenk tube; toluene (25 mL), triethylamine (0.2 mL, 1.435 mmol), and one of the initiators (0.2 mL) was added in a dry argon counter flow. After stirring for 20 h, a suspension formed. The formation of the insoluble salt (TEA*HCl) indicated the successful functionalization of the wafer surface. The resulting silanated wafer was washed with Milli-Q water (2x) and then placed in a Soxhlet apparatus with dichloromethane overnight to remove any traces of salt and physisorbed initiator molecules.

SI-ATRP of MMA

Surface-initiated ATRP was carried out in a modified Schlenk tube containing the freshly functionalized wafers and a magnetic stir bar. Oxygen-free conditions were ensured by working in an argon atmosphere and by flushing anisole (10 mL) and MMA (10 mL, 0.09 mol) with argon prior to use. Under argon counter flow, CuBr (13.4 mg, 0.09 mmol), anisole, MMA and PMDETA (19.6 L, 0.09 mmol) were added to the tube. The active copper complex formed during stirring for 10 min. The slightly green tint of the solution is caused by traces of Cu(II). Subsequent to the addition of the free initiator 2-EiBBr (13.8 L, 0.09 mmol), the holder was capped with a stopper, and three freeze-pump-thaw cycles were executed. During the course of heating overnight at 30 °C the polymerization proceeded and finally was stopped by exposing the solution to air. The wafers were taken out, washed with dichloromethane and then extracted with dichloromethane overnight in a Soxhlet apparatus to remove the free polymer. The free polymer generated by the sacrificial initiator was purified by stirring with DOWEX MSC macroporous ionic exchange resin and recovered by precipitation into methanol. Inclusion of anisole made it necessary to re-dissolve the polymer in THF and precipitate it again in methanol. Finally the polymer was dried in vacuum.

Optical distortion in imaging ellipsometry

In vertical direction (along the beam, indicated by white arrow in Fig. 3.5) features appear smaller than they are on the sample surface due to the optical distortion. Size of all features, including drops and regions of regions of interest were corrected to take account of this. Based on geometrical considerations (Fig. 3.21), eq. 3.6 was derived.

$$S = \frac{L}{\sin \alpha} \tag{3.6}$$

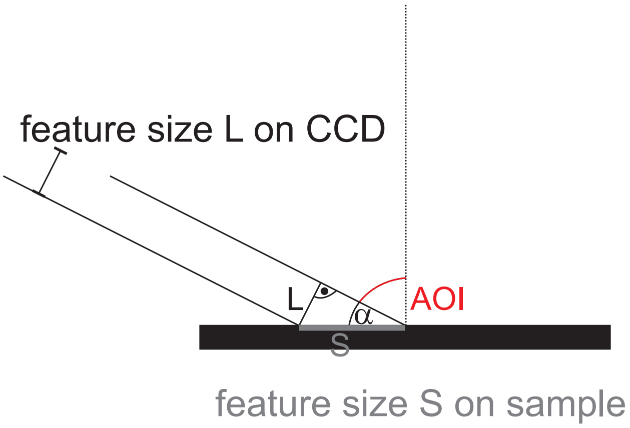

Fig. 3.21: Under the viewing angle of 60 degrees features with size *S* on the sample surface distorted and thus smaller in vertical direction (along the beam). Representation of geometry for the correction of this distortion.

For α half the angle of incidence (60 degree) was used, L stands for the feature size on the CCD, and S is the corrected feature size.
So the feature size L on the CCD has to be multiplied by a factor of 2, in order to get the actual feature size S.

Instrumentation

The Nano-Plotter© NP 2.0 was used to dispense droplets of acid onto the silicon surface covered with a monolayer of ATRP initiator. For more details see Section 7.1. During time-dependent saponification experiments the temperature of the work plate was set to 10 °C . All other printing experiments were conducted at room temperature (20 °C).

The imaging ellipsometer EP3 was used to determine the thickness of the polymer brush layer. For more details see Section 7.2. The calculation of PMMA thickness was conducted using a multilayer model (Air, PMMA, initiator monolayer/SiO_2, amorphous Si) [176]. With the chosen model, the error for reported layer thickness was calculated as ± 1 nm.

A reversed particle interaction apparatus was used to follow the drop evaporation on the microcantilevers. For more details see Section 7.10.

Analysis of the bulk PMMA was carried out with the gel permeation chromatography (GPC) set-up described in Section 7.4.

Proton nuclear magnetic resonance (^{1}H NMR) spectra were recorded with the spectrometer described in Section 7.5.

Contact angle measurements were conducted using a Krüss DSA10-MK2 tensiometer. Millipore water was used as liquid and the static contact angles were recorded at room temperature.

AFM under ambient conditions was carried out with a Dimension 3100 setup connected to a NanoScopeV controller. Silicon cantilevers (OMCL-AC 160 TS-W2, Olympus, Japan) with a tip radius of $\sim$10 nm were used in the tapping mode with a resonance frequency near 300 kHz. Images were recorded in retrace line direction.

Materials

Allymagnesium bromide (1.0 M in diethyl ether, Aldrich), 2-bromoisobutyryl bromide (97%, Alfa), pyridine (99%, Aldrich), chlorodimethylsilane (95%, Fluka), dihydrogen hexachloroplatinate(IV) hexahydrate (99,9% metals basis, Alfa), ethyl α-bromoisobutyrate (97%, Fluka), toluene (anhydrous 99,8%, Aldrich), sulfuric acid (purum p.a. 95-97%, Fluka) and hydrochloric acid (37%, Aldrich) were used as received.
Copper bromide (98%, Aldrich) was purified by boiling it for a short time in a mixture of 50:50 v/v Millipore water/glacial acetic acid and thereafter filtered off. This was followed by rinsing the precipitate with water, ethanol, diethyl ether, and finally it was dried under reduced pressure for 24h [177].
MMA (99%, Acros) was purified by passing it through an alumina column, distilled under reduced pressure from CaH_2, and stored under argon at -

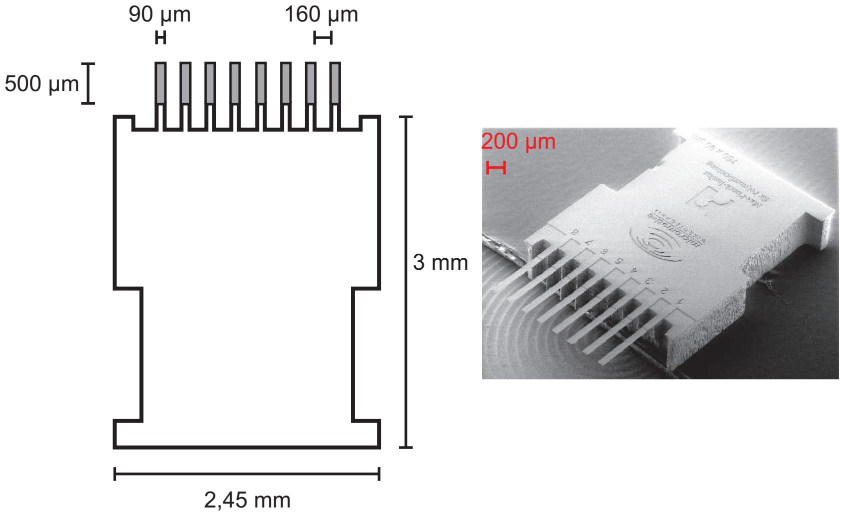

Fig. 3.22: Scheme (left) presenting the dimensions of a Octosensis micromechanical cantilever array chip with cantilever length of 500 µm. Scanning electron micrograph (right) of the chip.

20 °C .
N,N,N′,N′,N″-Pentamethyldiethylenetriamine (PMDETA) (99%, Aldrich) was purified by distillation under reduced pressure and triethylamine by distillation from CaH_2 in an argon atmosphere.

3.2 Polymer brushes on microcantilevers

The fabrication and characterization of polymer brushes on microcantilever arrays will be presented in the following. The approach was adapted from an earlier publication of our group [177]. The reaction details and the exact procedure can be found in Section 3.2.3.
The cantilever arrays used for SI-ATRP were Octosensis arrays with dimensions as depicted in Fig. 3.22. Each array is comprised of eight rectangular cantilevers with varying length and a thickness between 1 to 5 µm depending on the application.

3.2.1 Polymer brushes as asymmetric coatings

In 1991, Thomas Thundat observed bending of an AFM cantilever induced by water vapor adsorption [178]. From there on, the phenomenon attracted more and more interest [179]. To this day, physical [180–182], chemical [183, 184], and biological sensors [185–187] based on cantilever bending have been developed by researchers worldwide. State of the art sensors based on MCs are comprised of a cantilever array with up to eight individual cantilevers. A combination of uncoated reference MCs and MCs with a sensitive coating allow for the correction of the bending data for unspecific signals [188].

Readout of the bending is typically done using the beam deflection method, know from SPM [189, 190]. A laser beam is focused on the free end of the cantilever and deflected to a detector. Bending of the cantilever changes the position of the spot on the detector. One drawback of this method is, that the laser focus needs to be adjusted if solvents of different refractive indices are used [191].

Imaging interferometric techniques can be used alternatively [192]. The setup is deduced from a Michelson interferometer and measures the interference between light reflected from the MC surface with reflections from a reference mirror. Thereof a 3-D topography image of the MC can be deduced. The advantage of this method is, that not only changes in bending of the cantilever can be measured, as in the deflection method. The initial bending of the cantilever can be measured.

Depending on the application three different modes of operation are possible. Upon deposition of a thin metallic layer on one of side of a cantilever, changes in temperature cause the cantilever to bend [180, 184, 193]. The bimetallic effect is the reason for the bending. The cantilever material, typically silicon has a linear expansion coefficient differing from the expansion coefficient of the coating. Changes in temperature can be monitored precisely, thus this mode of operation is called the heat mode.

Cantilevers actively excited by applying voltage pulses show a change in resonance frequency on adsorption of mass on the cantilever. The calculation of the mass is possible using the change in resonance frequency [174, 182, 194].

This operational mode is called dynamic mode and was used to monitor the evaporation process of the acids in Section 3.1.14.

The prerequisite for the static mode of operation is an asymmetric coating of the MC. An asymmetric coating is essentially a coating applied to one side of the cantilever. The mechanical response, i.e. changes in surface stress of this layer, to the adsorption of molecules leads to a static bending of the MC [181,185,186,191].

A selective coating of one side of the MC with a homogenous film is of importance to obtain reproducible results. In addition, one has ensure that only the sensing MCs in an array are coated, but not the reference MCs. Several strategies have been developed to produce an asymmetric coating on selected cantilevers, as these reviews highlight [179,195,196]. Among them are rather simple techniques such as spray coating [197], as well as painting with dimension-matched glass capillaries [193, 198]. More elaborate techniques include thermal or electron-beam assisted evaporation of materials [199] using masks, and inkjet printing [200–202]. The aforementioned techniques however are not suitable to produce well-defined chemically adsorbed polymer films with thicknesses above 5 nm. Surface-initiated polymerization techniques, like SI-ATRP, are suitable to produce covalently bound polymer molecules with control over film thickness. In order to produce an asymmetric coating on a cantilever, SI-ATRP needs to be restricted to one side of the cantilever. Bumbu et al. [177,191] solved this problem in the following way. A passivating layer of gold was deposited on one side of the cantilever and then the non-protected site of the cantilever was funtionalized with an initiator suitable for SI-ATRP. After the polymerization they obtained densely grafted polymer brushes on one side of the cantilever. Upon removal of the protective gold layer with I_2/KI, they were able to monitor brush swelling in different solvents. One drawback of the method relying on a passivating layer is, that gold layer needs to cover the surface during the immobilization of the initiator, but should come off completely during the removal. Any residuals of the passivating layer or a passivating layer not completely covering the MC can influence the bending dramatically, as Wolkenhauer et al. [203] showed.

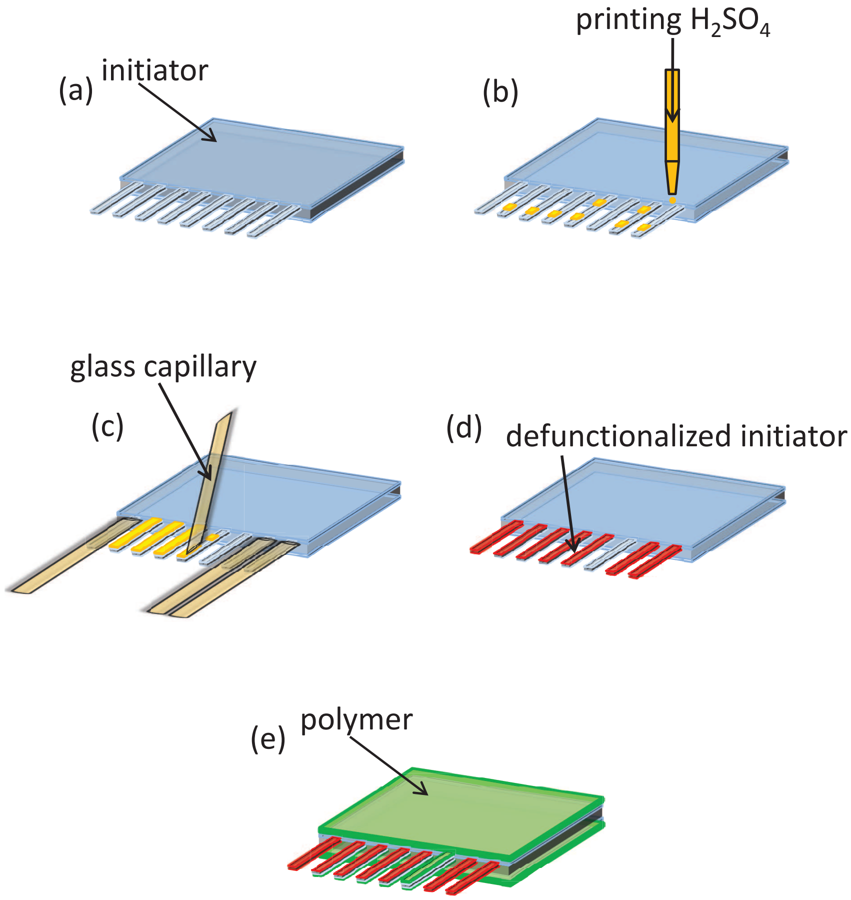

Fig. 3.23: Site selective coating of a microcantilever array via SI-ATRP. (a) Cantilever array with immobilized initiator. (b) Printing the acid with a commercially available inkjet printer on the topside of selected cantilevers. (c) Defunctionalizing the reference cantilevers in glass capillaries with acid and spreading the acid on the topside of the printed cantilevers with a glass capillary. Washing and drying. (d) Cantilever array with defunctionalized initiator monolayer. (e) SI-ATRP of MMA.

In the following an alternative approach to achieve an asymmetric coating of a microcantilever via SI-ATRP ia presented. The approach is based on the saponification of a surface-immobilized ATRP initiator. As presented above, 1 mol/L H_2SO_4 in contact with the novel tertiary initiator leads to complete suppression of brush growth. This system of initiator and acid was thus chosen. The task at hand was to cover one side of a cantilever completely with acid. Inkjet printing alone was not sufficient, because the droplets deposited did not form a film. The contact angle of 65 degrees (see Fig. 3.6) prevented the acid from wetting the surface of a cantilever completely. Thus a combination of inkjet printing and painting with glass capillaries was designed. This combination is depicted in Fig. 3.23. In step *(a)* the array was completely covered with the tertiary initiator (blue). The inkjet printer was used to deposit the acid (orange) on the topside of selected cantilevers in step *(b)*. Two drops were deposited on cantilever 2 and 4, one drop on cantilever 5, 6, and 7. No drops were deposited on cantilever 3 and 8, as the image in Fig. 3.24 shows. The defunctionalization of the initiator on the bottomside of the designated reference cantilevers was carried out in step *(c)*. Cantilever 1, 2 and 8 were positioned inside glass capillaries filled with acid. Another glass capillary was brought into contact with the topside of the designated sensing cantilevers (4 through 7) in order to spread the drops of acid mechanically. After extracting the array with DCM, the initiator was defunctionalized (red) on both sides of cantilever 1, 2 and 8. The initiator on cantilever 3 was left unaffected on both sides, because no acid was deposited. On cantilever 4 through 7 the initiator on the topside was defunctionalized. This is depicted in Fig. 3.23 *(d)*. Subsequently the SI-ATRP was carried out and polymer grew only in the areas that had not been in contact with the acid, as expected. The imaging ellipsometer was used to measure the PEMA film thickness on the top- and bottomside of the cantilevers. The data can be found in Tab. 3.1 and a schematic representation of PMMA film location on each side of the individual cantilever.

The sensing cantilevers 4 through 7 showed the desired asymmetric coating (Fig. 3.25). The coating was exclusively located on the bottomside of the cantilevers, that had not been printed or painted with the glass capillary. Polymer growth on the topside was totally suppressed. A film thickness of 0.5 to

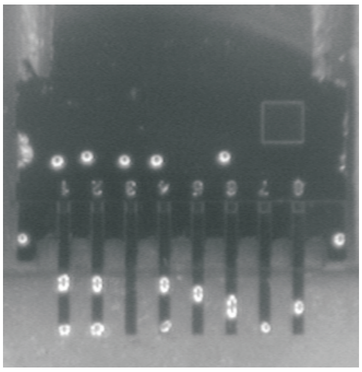

Fig. 3.24: Typical image of inkjet printing of 1 mol/l H_2SO_4 on individual cantilevers. The drops of acid appear as white features on the cantilever and the chip.

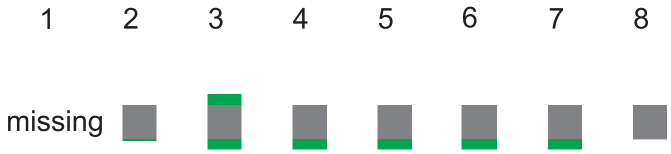

Fig. 3.25: Schematic representation of PMMA film location on each side of the individual cantilever (array OS-S 500 #042). Cantilever 1 broke during the synthesis.

Table 3.1: PEMA brush thickness in nm on top- and downside of microcantilever array OS-S 500 #042.

topside	**thickness nm**	**downside**	**thickness nm**
Chip	10.3		12.7
Cantilever 1	missing		missing
Cantilever 2	1.3		2.1
Cantilever 3	10.1		9.4
Cantilever 4	0.9		9.0
Cantilever 5	0.5		8.2
Cantilever 6	1.0		8.2
Cantilever 7	0.9		8.3
Cantilever 8	0.9		1.2

1 ± 1 nm was measured. On the bottomside a polymer thickness of 8.2 to 9 ± 1 nm was measured (Tab. 3.1). This is within the error of the bottomside thickness measured on cantilever 3 at 9.4 ± 1 nm. Cantilever 3 is a reference cantilever and neither the bottomside nor the topside had been in contact with acid. PMMA was thus found on both sides of the cantilever (Fig. 3.25). The film thickness on the topside of cantilever 3 was 10.1 ± 1 nm.

Therefore it can be concluded, that the combination of inkjet printing and glass capillary painting allows unaffected growth of polymer brushes on the downside of cantilevers.

Cantilever 2 and 8 were other designated reference cantilevers. Both of them had been place inside glass capillaries for a predetermined time. Neither of the cantilevers showed a significant PMMA coating on the topside (Fig. 3.25). The measurement of film thickness on the reference cantilevers 2 and 8 gave values of 0.9 to 1.3 ± 1 on the topside. On the downside a value of 1.2 ± 1 nm was measured for cantilever 8. Cantilever 8 had been inside a capillary filled with acid for two hours. The time was sufficient to suppress polymer growth completely within the error. Cantilever 2 had been inside the glass capillary with acid for a shorter time of 45 min. On the downside a thickness of 2.1 ± 1 nm was measured (3.25).

Therefore it can be concluded, that for the preparation of an uncoated reference cantilever a time of 2 hours inside a glass capillary is necessary.

The film thickness measured on the topside of the chip at 10.3 ± 1 nm is in agreement with the value measured on the topside of cantilever 3. The value measured on the downside of the chip is higher at 12.7 ± 1 nm. The image taken with the imaging ellipsometer however revealed, that there was some debris covering the chip.

From the average film thickness (11 ± 1 nm)and the molecular weight ($M_n = 70200 g/mol$) an average grafting density for 0.11 ± 0.01 chains/nm^2 was estimated following eq. 3.1. This is in agreement with the average grafting density for the tertiary initiator of 0.1 ± 0.03 chains/nm^2 in the case of MMA (Section 3.1.15).

The presented combination of inkjet printing and capillary painting can be used to prepare asymmetric coatings of microcantilevers without the use of a passivating gold layer. The preparation of sensing cantilevers with asymmetric coating requires the deposition of acid drops on the topside of the cantilever and spreading of the drops with the use of glass capillaries. Reference cantilevers can either be prepared uncoated/coated on both sides. Reference cantilevers uncoated on both side can obtained by placing them inside a glass capillary filled with acid for 2 hours. Contact with acid needs to avoided for double side coated reference cantilevers.

3.2.2 Polymer brushes as adhesion layer for printing of polymers

Thin organic coating are extensively used to control the interactions of a material with its environment. A prominent example, where a thin organic film is a prerequisite for the function of the whole device, is the computer hard disk [6]. Without a thin film of perfluoropolyether of 2 to 4 nm thickness, the read/write head would damage the disk surface upon contact. Thus the thin film reduces wear and controls the mechanical properties of the disks. Owing to the diminutive amount of material in such a thin film, quantification of mechanical properties is not easily achieved. The micromechanical cantilever method is well suited for accessing the mechanical properties of such thin films. The theory was initially developed by Nicholas [204] and further refined by Whiting and coworkers [205]. The latter group succeeded in verifying the theory using copper and silver thin films on mm-sized cantilevers. The theory allows to connect the frequency shift of a microcantilever upon deposition of a polymer film on the topside to the elastic modulus of the polymer. Fabrication of polymer films on cantilevers is challenging, but can be achieved, for example by inkjet printing of polymer solutions [202] onto the silicon cantilevers. A common problem in inkjet printing is the coffee stain effect [206,207]. So one has to ensure, that the film is homogeneously covering the surface. Otherwise the reproducibility of measurements can become an issue. One possibility to avoid the coffee stain effect is to control the substrate properties [208].

Polymer brushes grown on the surface of a microcantilever are the ideal sub-

Table 3.2: PEMA brush thickness in nm on microcantilevers as adhesion layer for printing of PEMA -batch 1. Cantilever 2 had been missing from the start.

IBM J11	**thickness nm**	**OS-S 750 #052**	**thickness nm**	**OS-S 500 #080**	**thickness nm**
Chip	18.4		6.0		16.6
Cantilever 1	11.8		missing		10.3
Cantilever 2	12.9		11.0		10.5
Cantilever 3	12.5		11.1		10.4
Cantilever 4	12.6		12.5		10.0
Cantilever 5	12.6		12.2		10.2
Cantilever 6	13.5		12.8		10.2
Cantilever 7	14.0		11.9		10.0
Cantilever 8	15.2		12.5		9.0

strate for printing of a polymer with the same chemical nature as the brushes.

The synthesis was carried out two times. From the firs polymerization was free polymer with a number average molecular weight and a polydispersity of $M_n = 43500 g/mol$, $PDI = 1.13$ obtained. In order to determine the thickness of the polymer brushes on the MC an imaging ellipsometer was used. The data can be found in Tab. 3.2.
The variation in film thickness for the arrays with the longer cantilevers (OS-S-750 #052 and OS-S-500 #080) is within the error of the modeling at ± 1 nm. The variation in the case of the array with varying length of cantilevers (IBM J11) is higher at 2.7 nm. This is unusual and can be explained with the small area that is used for the measurement with the imaging ellipsometer. The error of the measurement increases with decreasing measurement area.
The variation in film thickness between the cantilevers and the chip are extraordinarily high for all arrays polymerized in this batch. The images taken with the imaging ellipsometer revealed, that the surface of the chip was covered with debris. The clamping of the arrays in the holder must have prevented the chips from being washed.
From the average film thickness and the molecular weight an average grafting density for 0.21 ± 0.02 chains/nm^2 was estimated following eq. 3.1. This

Table 3.3: PEMA brush thickness in nm on microcantilevers as adhesion layer for printing of PEMA - batch 2. Cantilevers 1 and 2 were broken during the synthesis.

OS-S 750 #034	**thickness nm**	**OS-S 750 #048**	**thickness nm**	**OS-S 750 #031**	**thickness nm**
Chip	26.4		25.8		25.8
Cantilever 1	25.3		missing		24.6
Cantilever 2	25.3		missing		25.2
Cantilever 3	25.3		24.1		25.3
Cantilever 4	25.3		26.0		25.1
Cantilever 5	25.3		26.0		25.2
Cantilever 6	23.4		25.5		23.8
Cantilever 7	25.5		25.1		25.3
Cantilever 8	25.1		24.2		24.7

is in agreement with the average grafting density for the primary initiator of 0.26 ± 0.04 chains/nm^2 in the case of MMA (Section 3.1.15).

In the second run two arrays were polymerized. Free polymer with a number average molecular weight and a polydispersity of $M_n = 62400 g/mol$, $PDI = 1,18$ was obtained. The film thickness as measured with the imaging ellipsometer can be found in Tab. 3.3.

The variation in film thickness between the individual cantilevers and the chip is within the error of the modeling at ± 1 nm. An average PEMA thickness of 25.4 ± 1 nm was calculated. From the average film thickness and the molecular weight an average grafting density of 0.29 ± 0.02 chains/nm^2 was estimated following eq. 3.1. This is in agreement with the average grafting density for the primary initiator of 0.26 ± 0.04 chains/nm^2 in the case of MMA (Section 3.1.15).

Printing of PEMA polymer films on the PEMA brush covered MCs was carried out in collaboration with Sascha Pihan. By printing PEMA polymers with molecular weight smaller than the molecular weight of the brushes homogeneous films were prepared suitable for the determination of mechanical properties. The investigation of the mechanical properties with the use of microcantilevers is part of the SPP1369 Priority Program (Polymer-Solid Contacts: Interfaces and Interphases) funded by the DFG. The mechanical properties of a film on a microcantilever can only be determined if the film is homogeneously covering the cantilever. The PEMA brush layer is an ideal layer for the preparation of homogeneous PEMA films by inkjet printing on the cantilevers, if the molecular weight of brush and free polymer is adjusted properly. The successful synthesis lead to homogeneously printed PEMA films and the mechanical properties of these printed layers are investigated currently by Sascha Pihan. Compared to other widely used mechanical analysis techniques the arrangement of sensors in arrays allows screening material properties and offers an additional advantage. The amount of material required for a conventional mechanical analysis technique is high compared to the amount needed for coating a cantilever.

3.2.3 Diffusion of water into polymer brushes on microcantilevers

Analyzing the diffusion of molecules in and out of a polymer material is attracting more and more interest [209,210]. Water vapor absorbed in a polymer has a strong influence on the properties of this polymer material [211], for example its mechanical stability and its degradation can be changed. Therefore sorption and diffusion of water plays a key role in many applications of polymer materials. One of the most pressing issues is the failure in microelectronic packages due to moisture [210]. Moisture can enter microelectronic packages, because of the small affinity of organic polymers towards water. The affinity is the reason why it is important to determine the degree of water adsorption as well as the diffusion coefficient in polymer coatings, i.e. the quantity and rate of absorption. The measurement of the quantity is more easily achieved, compared to a qualitative determination of the diffusion rate. Two prerequisites have to be met in order to determine the diffusion rate. The technique has to be sensitive to the presence of moisture and needs to have a high time resolution.

A multitude of techniques has been used to study diffusion kinetics of small molecules in amorphous polymers. Among them, gravimetric techniques [212, 213] have been used extensively to measure the diffusion. One drawback of gravimetric techniques however is the relatively low sensitivity. Thus monitoring of mass change with high accuracy is difficult for thin films ($>$ 10 µm).

The quartz crystal microbalance (QCM) has this high accuracy and has therefore become popular for investigating the diffusion of vapor into polymer films [214, 215]. A change in frequency of the single crystal is measured and thereof the mass uptake of the polymer calculated. With the QCM not only the mass uptake of the polymer is detected, but also adsorption of vapor at the surface. Separation of the two contributions to the total mass is challenging. Quantitative evaluation of the mass uptake of the polymer is thus complicated.

Infrared spectroscopy based techniques, like fourier-transform infrared spectroscopy (FT-IR) and attenuated total reflectance (ATR)-FT-IR, can be deployed to follow the transport process in situ only in the case of diffusants with well-defined IR stretching [216–218].

Nuclear magnetic resonance (NMR) has also been deployed for probing the molecular mobility and diffusion in polymers. Relatively large amounts of sample however are needed [219, 220].

Sensors based on micromechanical cantilevers have been used to characterize a wide range of materials and environmental properties [221–224]. The popularity of microcantilevers stems from the fact that they have an extremely high sensitivity to mass changes, to changes in surface stress, and changes in temperature, in addition to their fast response time (less than 1 ms) [223]. Fabrication of polymer films on cantilevers is challenging, but can be achieved, for example by inkjet printing of polymer solutions [202]. A common problem in inkjet printing is the coffee stain effect [206, 207]. So one has to ensure, that the film is homogeneously covering the cantilever surface. Otherwise the reproducibility of measurements can become an issue.

Polymer brushes grown on the surface of a microcantilever can provide a route to homogenous films. The films have a low roughness well below 1 nm, as shown in Section 3.1.13 and can be produced with precise control of final thickness.

If a solvent is deposited on a polymer brush thin film, penetration and up-

Table 3.4: PEMA brush thickness in nm on microcantilevers for measuring the diffusion of water into the brush - batch 1.

OS-S 750 #015	**thickness nm**
Chip	26.2
Cantilever 1	25.4
Cantilever 2	25.2
Cantilever 3	25.3
Cantilever 4	25.0
Cantilever 5	25.3
Cantilever 6	25.4
Cantilever 7	25.3
Cantilever 8	25.3

take of the solvent leads to swelling and a volume increase. In the case of an asymmetric increase of volume, viz. exclusive swelling of the upper surface of cantilever covered with polymer brushes, the cantilever will bend. After the polymer brushes were fabricated using SI-ATRP, the bending of the microcantilevers due to water diffusion into the polymer brush was measured by Chuanjun Liu. A modified reversed particle interaction apparatus was used [174]. For more details about the equipment see Section 7.10. It is equipped with an inkjet nozzle for microdrop deposition on the topside of a microcantilever. Water diffuses into the polymer brush on the cantilever and causes swelling. The time dependence of the bending can be related to the diffusion process of water into the polymer brush. This in turn allows for the determination of the diffusion coefficient.

The coating of the cantilevers was carried out two times. In the polymerization was free polymer with a number average molecular weight and a polydispersity of $M_n = 62400 g/mol$, $PDI = 1.18$ obtained. In order to determine the thickness of the polymer brushes on the MC an imaging ellipsometer was used. The data can be found in Tab. 3.4.

The variation in film thickness between the individual cantilevers and the chip is within the error of the modeling at ± 1 nm. An average PEMA thick-

Table 3.5: PEMA brush thickness in nm on microcantilevers for measuring the diffusion of water into the brush - batch 2. Two cantilevers were missing from the start.

OS-S 500 #003	**thickness nm**	**OS-S 750 #052**	**thickness nm**
Chip	27.8		28.1
Cantilever 1	27.8		27.7
Cantilever 2	28.4		28.2
Cantilever 3	27.7		28.3
Cantilever 4	28.8		28.0
Cantilever 5	28.1		27.9
Cantilever 6	29.3		27.9
Cantilever 7	29.6		missing
Cantilever 8	30.4		missing

ness of 25.6 ± 1 nm was calculated. The error of the modeling was chosen as error bars, because the standard deviation was lower than the modeling error. From the average film thickness and the molecular weight an average grafting density of 0.29 ± 0.02 chains/nm^2 was estimated following eq. 3.1. This is in agreement with the average grafting density for the primary initiator of 0.26 ± 0.04 chains/nm^2 in the case of MMA (Section 3.1.15).

Two arrays were polymerized simultaneously in the second synthesis. Free polymer with a number average molecular weight and a polydispersity of $M_n = 63800 g/mol$, $PDI = 1,15$ was obtained. The film thickness as measured with the imaging ellipsometer can be found in Tab. 3.5.

The variation in film thickness for the array with the longer cantilevers (OS-S-750 #052) is within the error of the modeling at ± 1 nm. The variation in the case of the shorter cantilevers (OS-S-500 #003) is higher at 2.7 nm. This is unusual and can be explained with the small area that is used for the measurement with the imaging ellipsometer. The error of the measurement increases with decreasing measurement area. From the average film thickness and the molecular weight an average grafting density of 0.32 ± 0.02 chains/nm^2 was estimated following eq. 3.1. This is in agreement with the average grafting density for the primary initiator of 0.26 ± 0.04 chains/nm^2 in the case of MMA (Section 3.1.15).

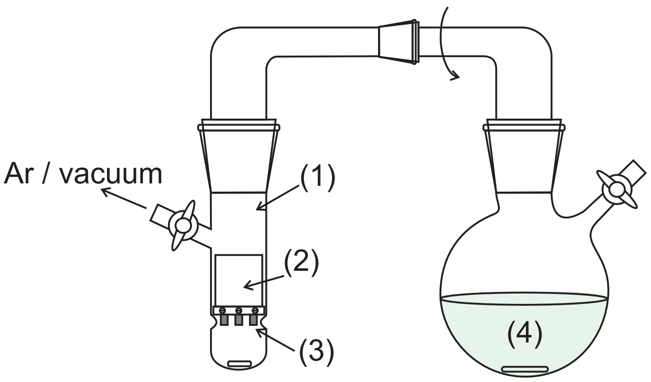

Fig. 3.26: Scheme representing the Schlenk setup deployed for SI-ATRP on micromechanical cantilever arrays (adapted from [177]).

The presented method allows to prepare uniform coatings with control over thickness, suitable for monitoring the diffusion of water into the brushes. Chuanjun Liu is currently using these cantilever in order to determine the diffusion coefficient and the overall water content of PEMA films. Although PEMA is considered to be a hydrophobic polymer, PEMA films contain a minute amount of water and can even be swollen by water, as the first experiments have shown. Cantilevers offer the advantage that the water content and swelling of polymeric films can be probed without relying on elaborated scattering techniques, such as GISAXS or neutron reflectometry, which are typically used [225].

Experimental

The cantilever array was cleaned and made sure that the silicon oxide layer was in a controlled hydration state. This was carried out as described for silicon wafers in Section 3.1.17 with one exception. Ultrasonication breaks the cantilevers, so they were only washed in DCM. The immobilization of the primary SI-ATRP initiator was carried out as described above for wafers. Whereas the synthesis of polymer brushes by SI-ATRP on silicon wafers is carried out in a adapted Schlenk tube, SI-ATRP on microcantilevers requires a more elaborate setup. The common approach of freeze-thawing of the reaction solution cannot be carried out with microcantilevers in the solution. The fragile microcantilevers do not survive the volume change of the solution during freeze-thawing. Freeze-thawing however is necessary to remove the dissolved oxygen from the reaction solution.

Therefore an adapted Schlenk setup was employed, consisting of a Schlenk tube (1) with the special holder (2) for the MCs (3) connected to a Schlenk flask for degassing of the reaction solution (4). The setup is depicted in Fig. 3.26.

SI-ATRP was carried out by placing the freshly functionalized MCs mounted in a special holder in the Schlenk tube together with a magnetic stir bar. The oil pump and the argon line were connected to the holder via a three-way valve. CuBr (13.1 mg, 0.09 mmol) and a magnetic stir bar was placed in the Schlenk flask and the connection between the tube and the flask established. From here on the procedure was continued as described in Section 3.1.17. Because ethyl methacrylate (EMA, 10 mL, 0.08 mmol) was used as monomer in this case, the mixing ratios had to be adjusted slightly (anisole, 10 mL; PMDETA, 19.1 L, 0.09 mmol; 2-EiBBr, 13.4 L, 0.09 mmol). After the three freeze-pump-thaw cyles had been executed, the reaction solution was decanted into the Schlenk tube by rotating the Schlenk flask upside down. Polymerization and purification of the MCs as well as of the free polymer was carried out as described in Section 3.1.17.

The presented method allows to prepare polymer brushes on fragile micromechanical devices, employing mild synthesis conditions. Uniform coatings were produced, with control over thickness and polydispersity of the brushes.

4 ”Grafting from” - Polymer brushes on curved substrates

The focus of this chapter is on the fabrication of polymer brushes on curved substrates, viz. microgel nanoparticles.
The preparation of nanocomposites comprised of polyorganosiloxane microgel particles functionalized with poly(ethyl methacrylate) brushes and linear PEMA chains is described. Brush and PEMA matrix chains had molecular weight above the entanglement molecular weight ($\sim 10k\ g * mol^{-1}$) of PEMA in every case. The inter-particle distance was monitored as function of matrix molecular weight, which was varied between 12k and 269k. Measurement of the inter-particle distance was performed using scanning probe microscopy and grazing incidence small angle X-ray scattering. The matrix molecular weight at which the nanocomposite showed microphase separation was related to abrupt changes in inter-particle distance. Microphase separation occurred when the matrix molecular exceeded the molecular weight of the brushes. The trigger for the microphase separation was a contraction of the polymer brushes, as the measurements of inter-particle distance have revealed. The brushes became impenetrable for the matrix chains upon contraction and thus behaved as hard spheres. The contraction led to a loss of anchoring between particles and matrix, as shown by nanowear tests with an atomic force microscope.

The chapter is based in parts on the publication: Sascha A. Pihan [*], Sebastian G. J. Emmerling [*], Philipp Lellig, Jannis W. Ochsmann, Jichun You, Jan Perlich, Stephan V. Roth, R. Berger and Jochen S. Gutmann, *Entropy controlled*

---

[*] Sascha A. Pihan and Sebastian G. J. Emmerling contributed equally to this work.

miscibility of hairy nanoparticles with like homopolymers, submitted.

4.1 Entropy controlled miscibility of hairy nanoparticles with like homopolymers

4.1.1 Introduction

Current approaches in polymer material design aim at adding new functionalities, reducing the weight of fabricated components and furthermore enhancing mechanical properties of polymeric materials [226]. Engineered materials, such as nanocomposites, are promising candidates to fulfil these conditions [227]. Nanocomposites consist of a nanoscale inorganic filler, which could be a spherical particle with a non-penetrable and smooth surface for example, dispersed in a polymer matrix. The central problem in the preparation of nanocomposite materials is the intrinsic incompatibility between the high energy surface of the inorganic filler and the low energy polymer matrix. The consequence of this incompatibility can be contact aggregation of the filler material leading to macro-phase separation [228, 229]. Asakura et al. created the term *depletion demixing* for this phenomenon and described it theoretically [230]. Entropic effects - colloidal particles are entropically incompatible with linear polymer chains - are the reason for this depletion attraction, as verified experimentally by Bechinger et al. [231].

The situation changes upon modification of the particle surface, which is a typical approach to overcome the intrinsic incompatibility between filler and matrix. Surface modification reduces the energy difference between the constituents of a nanocomposite and homogenous blends can thus be prepared. There are several methods of surface modification reported including silanization [232, 233], surfactant absorption [234] and polymer grafting [39]. The grafting of polymers on the surface of particles has been used for many years in order to stabilize larger colloids [85]. Schärtl et al. [235] and others [133, 236, 237] have shown that grafting polymers can also stabilize nanoparticles. Such polymer grafted nanoparticles can be homogenously dispersed in polymer matrices forming stable suspensions with exceptional mechanical properties [238,239]. Qualitative models [240] were developed based on these findings in order to explain the depletion demixing leading to microphase separation. The explanations about the stabilizing effect of grafted polymers on nanoparticles in polymer melts were derived from theories initially developed for flat substrates. Entropy-driven forces are dominating the brush-melt interactions, if the system is chosen in such a way that the polymer grafted on the surface is of the same chemical nature as the polymer melt wetting the surface [241]. In the case of flat silicon surfaces with end-attached polystyrene brushes, Maas et al. [242] reported on a theoretical wetting diagram which shows two different autophobic wetting transitions. A first order wetting transition at low grafting densities and a second order wetting transition at high grafting densities was predicted. Green et al. were able to map out a similar phase diagram for a nanoparticle suspension experimentally [243]. The system that was used was composed of poly(dimethylsiloxane)-grafted silica spheres dispersed in a PDMS matrix with moderate grafting densities and low core volume fractions. The observed transition between stable and aggregated regions was identified as a first order transition. One can explain the first order transition theoretically by calculating the Gibbs energy G of a homopolymer chain with molecular weight P in contact with a brush of molecular weight N. The Gibbs energy G is a function of the ratio N/P for a given grafting density.

It is clear, however, that the brush conformation, i.e. swollen or contracted, plays a crucial role in the wetting behavior and therefore in the mixing--demixing of a suspension. If the brush is wet by surrounding homopolymer chains these chains must somehow interpenetrate the brush. Thus an *interphase* between the inorganic nanoparticle and the organic polymer matrix is formed (Fig. 4.1). The interphase is determined by the conformation of the brush and influences the distance between neighboring particles.

Based on these considerations, one can envision three different cases for the brush conformation in a system with high grafting density.

a) Polymer-grafted nanoparticles without polymer matrix. The polymer brushes are contracted. Thus the distance between single particles should be

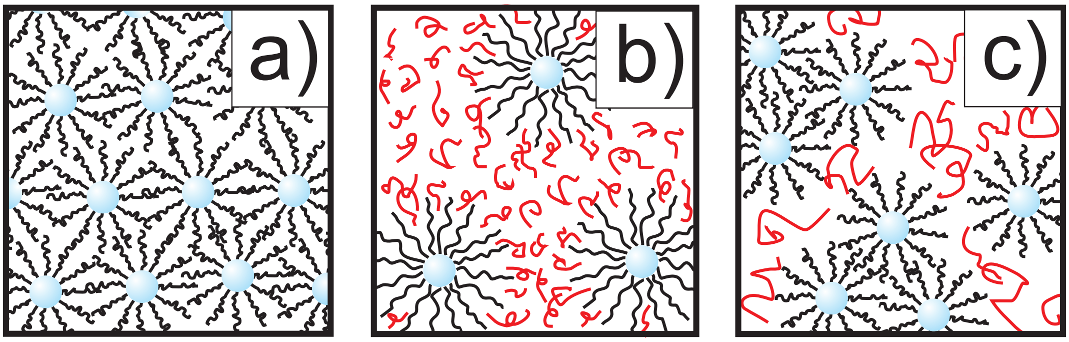

Fig. 4.1: Scheme illustrating the influence of brush conformation on the distance between polymer-grafted nanoparticles: (a) Without polymer matrix. (b) With low molecular weight polymer matrix ($N = P$). (c) With high molecular weight polymer matrix $N/P < 1$.

minimal, as depicted in Fig. 4.1 (a).

b) Polymer-grafted nanoparticles dispersed in a homopolymer matrix with molecular weight lower than that of the brushes ($N/P \sim 1$). The brushes can be wet/swollen by the surrounding homopolymer chains leading to an increase in inter-particle distance, as depicted in Fig. 4.1 (b).

c) Polymer-grafted nanoparticles dispersed in a homopolymer matrix with molecular weight higher than that of the brushes ($N/P < 1$). The homopolymer chains could not wet-swell the brush anymore and thus aggregation of the particles is observed, leading to a reduced inter-particle distance (Fig. 4.1 (c)). The transition between the swollen and contracted state leading to demixing is referred to as the drying/interpenetration limit in literature [243]. The aim of this publication is to demonstrate that the transition in brush conformation between the swollen (wet) and contracted state (dry) can be inferred by means of quantitative measurements of the distance between neighboring particles. Furthermore is the influence of the interphase on the mechanical stability of the nanocomposite studied via nanowear tests. The nanowear tests revealed that the attractive interactions between brushes in a contracted state and a high molecular weight matrix (Fig. 4.1 (c)) are weak compared to brushes swollen by low molecular weight matrix (Fig. 4.1 (b)). Scanning probe microscopy (SPM) was chosen as characterization technique,

along with grazing-incidence small angle x-ray scattering (GISAXS).
SPM and GISAXS are complementary techniques and thus allow to investigate the sample surface, as well as the inner structure. The results of both techniques were combined to sketch a simple model based on the fact, that a contracted brush should capture less space than a swollen brush. This publication can thus be seen as an extension of the investigations carried out by Lindenblatt et al. [238, 240] who analyzed particle spacing based on SAXS (small angle X-ray scattering) measurements. The system employed by Lindenblatt et al. consisted of poly(styrene) (PS) chains grafted onto polyorganosiloxane microgel particles (μgel particles) in a PS matrix. The molecular weight of the PS matrices employed by Lindenblatt et al. was below the entanglement molecular weight.
The same μgel particles were chosen for this study because they can be produced with diameters around 20 nm with narrow size distribution. In contrast though, a system based on PEMA with much a higher grafting density (0.7 $chains * nm^{-2}$) and a much higher brush molecular weight was selected. The molecular weight of the PEMA homopolymer matrix was in all cases above the entanglement molecular weight ($\sim 10k\ g * mol^{-1}$) in order to conduct studies on a more realistic system. Nanoparticle reinforced polymers in applications are certainly entangled.
The μgel particles were functionalized with brushes in a "grafting from" approach using ATRP. The matrix PEMA was also prepared by ATRP. The molecular weight of the matrix was extended to the limit were depletion demixing occurs.

4.1.2 Synthesis

Preparation of PEMA matrix polymers

The matrix PEMA polymers were prepared according to Ramakrishnan et al. [244] in 50 vol-% anisole solution at 32 °C (Fig. 4.2). The solvent (anisole), the monomer (EMA), the ligand (PMDETA), CuBr/CuBr$_2$, the initiator (2-EiBBr) were all mixed together and the polymerization conducted for a preset time. Exact procedure and reaction details (amount of particular reagents, poly-

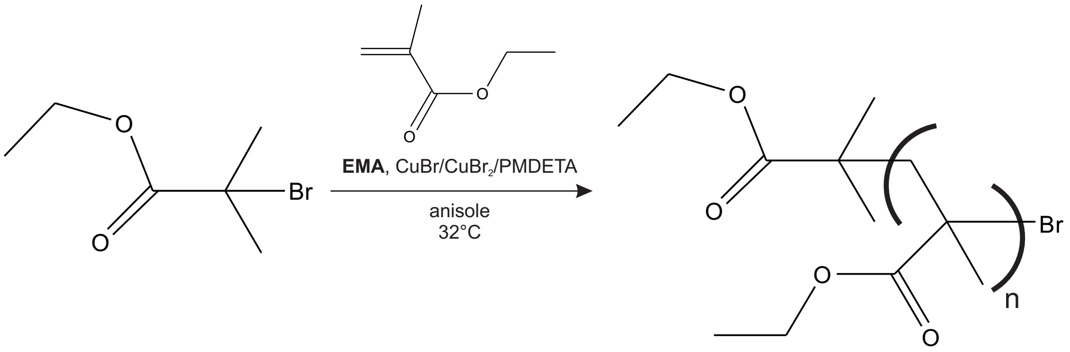

Fig. 4.2: Reaction scheme of ATRP with EMA as monomer, 2-EiBBr as initiator, CuBr/CuBr$_2$ as transition metal, PMDETA as ligand, and anisole as solvent.

Table 4.1: PEMA matrix polymer characteristics determined by GPC/DSC.

Abbreviation	$\mathbf{M_w}$ / $\mathbf{g * mol^{-1}}$	**PDI** / $\mathbf{M_w * M_n^{-1}}$	$\mathbf{T_g}$ / **K**
12k	11700	1.20	340.8
19k	18600	1.15	340.1
36k	36400	1.12	342
75k	75400	1.14	346.2
98k	98400	1.23	344.2
101k	100900	1.21	345.6
140k	139800	1.27	351.3
178k	177800	1.28	352.5
269k	269200	1.11	359.7

merization time) can be found in Section 4.1.6. The polymer was recovered and subjected to GPC and DSC analysis upon termination of the polymerization. One polymer with a molecular weight above $200k\ g * mol^{-1}$ was prepared by living anionic polymerization. In this case sec-buthyllithium/1,1-diphenylethylene in THF at -70 °C was used as the initiator system. MeOH was chosen for termination. The PEMA homopolymers were produced in a controlled fashion as indicated by the narrow polydispersity index (see Table 4.1). The molecular weight was in all cases above the entanglement regime ($M_e = 10k\ g * mol^{-1}$).

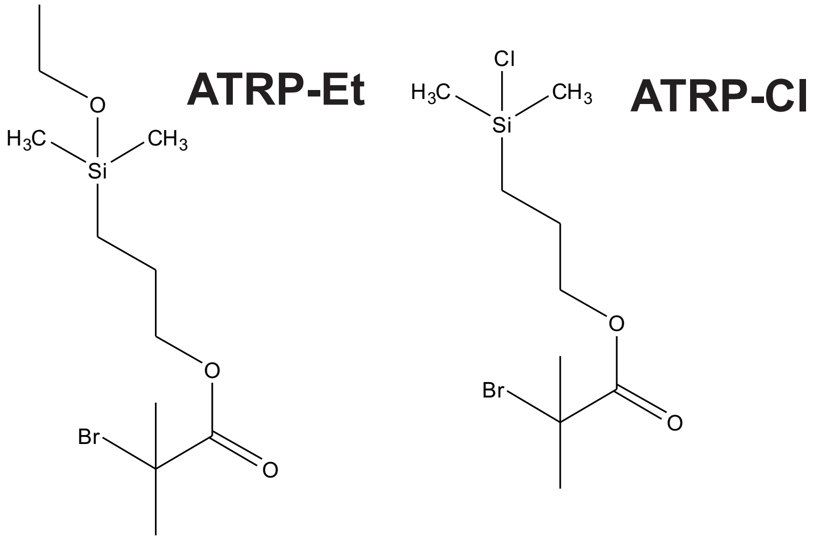

Fig. 4.3: Structures of 3-(ethoxydimethylsilyl)propyl 2-bromo-2-methylpropanoate (ATRP-Et) and 3-(chlorodimethylsilyl)propyl 2-bromo-2-methylpropanoate (ATRP-Cl). SI-ATRP initiators deployed for ″grafting from″ of EMA on μgel nanoparticles.

Synthesis of the silane ATRP-initiators

The ATRP-initiators 3-(chlorodimethylsilyl)propyl 2-bromo-2-methylpropanoate (ATRP-Cl)and 3-(ethoxydimethylsilyl)propyl 2-bromo-2-methylpropanoate (ATRP-Et) were prepared according to Ramakrishnan et al. [74]. The hydrosilylation reaction, however, was carried out with hydrogen-hexachloroplatinate(IV) hexahydrate as described in a recent publication [57].

Microgel synthesis

The synthesis of silsequioxane microgel nanoparticles in microemulsion was introduced in 1994 by Baumann et al. [245]. Benzethonium chloride was employed as surfactant and sodium hydroxide as a basic catalyst. Lindenblatt et al. [240] published an improved synthesis in 2000 introducing dodecylbenzene sulfonic acid (DBA) both as a surfactant and acid catalyst. Our group developed this acid-catalyzed approach further and introduced the synthetic protocol for ATRP-initiator functionalized μgel nanoparticles [246], as shown

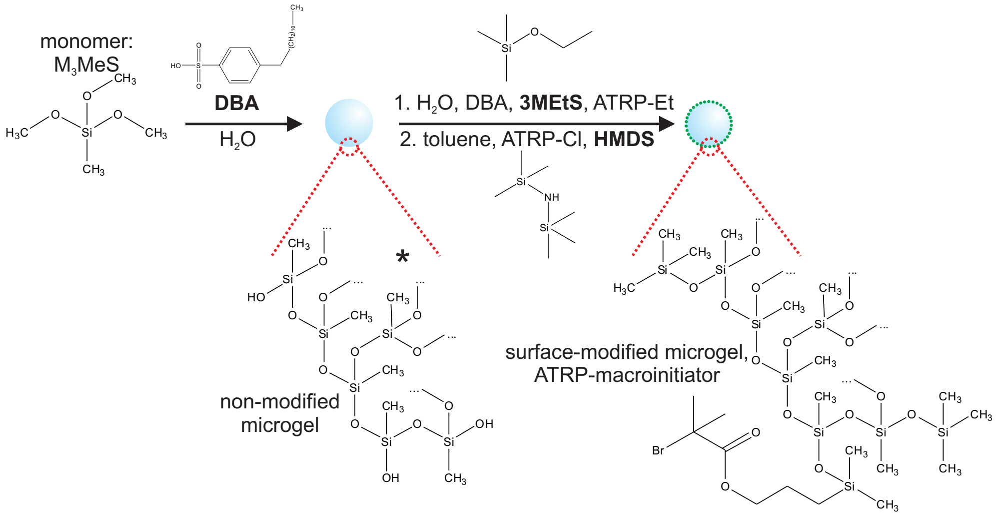

Fig. 4.4: Scheme illustrating the synthesis of the silsesquioxane microgel nanoparticles functionalized with ATRP-initiator.

in Fig. 4.4. A detailed description of the procedure and reaction details can be found in Section 4.1.6.

SI-ATRP polymerization

The procedure for preparation of PEMA-brushes on the μgel particles (Fig. 4.5) was adapted from an earlier publication of our group [246]. However, EMA (Aldrich, 99%) was used as a monomer in this case and the polymerization was conducted at ambient temperatures. A detailed description of the procedure and reaction details can be found in Section 4.1.6.

Cleaving of the grafted PEMA-chains

The core of the μ-gel-g-PEMA particles was dissolved with hydrofluoric acid (Fluka) in order to analyze the molecular weight of PEMA brushes via GPC. Dissolution was accomplished adapting a procedure described by Marutani et al. [247] for PMMA-brushes. Aliquat 336, a phase transfer catalyst, was employed to facilitate core dissolution without hydrolyzing the ester groups of the PEMA. The procedure is depicted in Fig. 4.6. The reaction details can

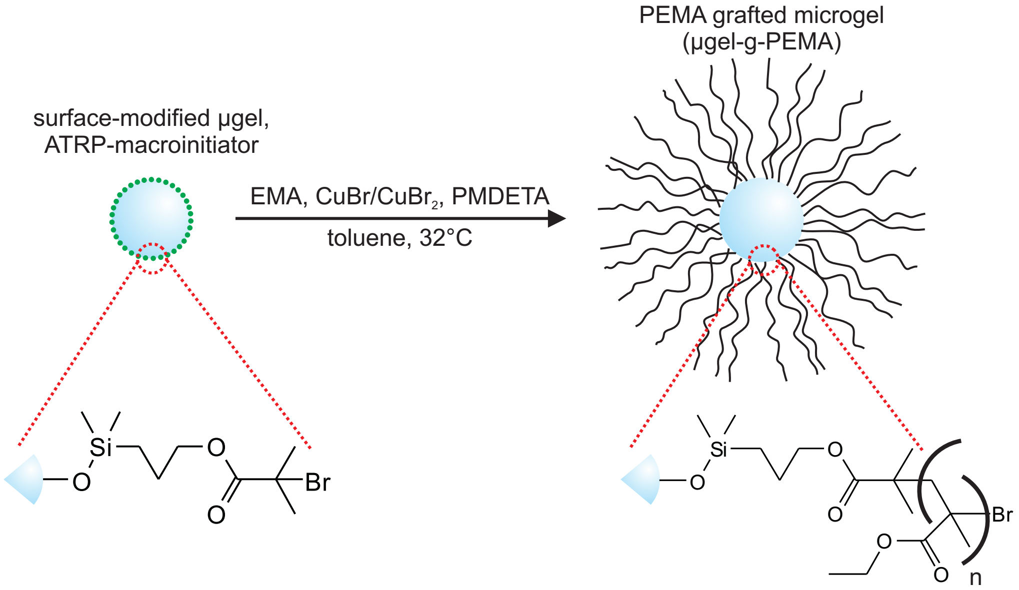

Fig. 4.5: Scheme illustrating the "grafting from" reaction of EMA on μgel nanoparticles.

be found in Section 4.1.6.

4.1.3 Characterization methods and sample preparation

Light Scattering (LS)

The hydrodynamic radius (R_h), the size distribution of μ-gel-g-PEMA particles and the molecular weight of the μgel nanoparticles was determined by light scattering. All experiments were performed at room temperature (25 °C) in toluene. The dilute dispersions had concentrations between 1 and 0.1 g/L and were ultrasonicated for 10 min. prior to the measurements.

Gel Permeation Chromatography (GPC)

The molecular weight of the cleaved/matrix PEMA and the retention volume of the μgel/μ-gel-g-PEMA particles was determined by GPC. All experiments were performed at room temperature (20 °C) in THF.

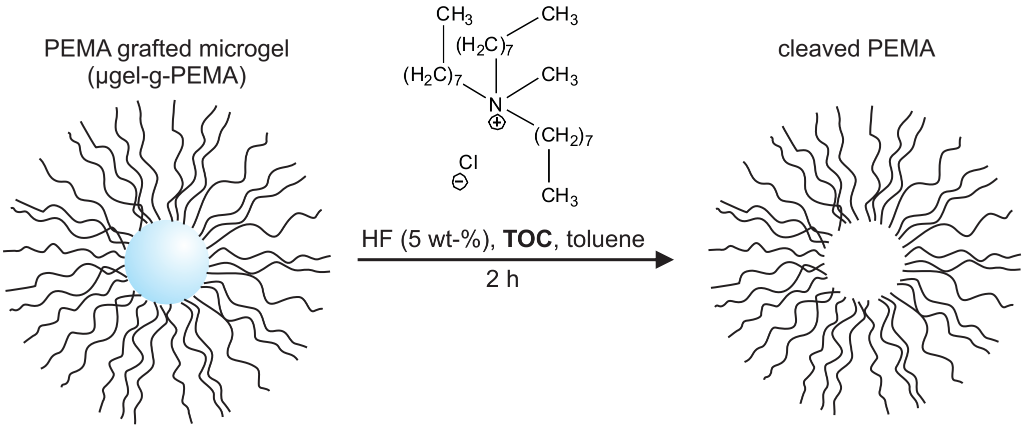

Fig. 4.6: Scheme illustrating the cleavage of grafted PEMA brushes from the μ-gel-g-PEMA nanoparticles by dissolution of the μgel core using HF/phase transfer catalyst.

Thermogravimetric analysis

Thermogravimetric analysis of the μgel and the μ-gel-g-PEMA nanoparticles was carried out in order get an *estimate* of the grafting density of the PEMA-brushes. Analysis of the μ-gel-g-PEMA nanoparticles was conducted twice and the average taken for an estimation of grafted PEMA in wt-% ($PEMA_{TGA}$). To do this, the mass loss of the μgel had to be taken into account.

$$PEMA_{TGA} = \left(1 - \frac{\chi_{\mu-gel-g-PEMA}}{\chi_{\mu gel}}\right) * 100\% \tag{4.1}$$

With $\chi_{\mu gel}$ and $\chi_{\mu-gel-g-PEMA}$, both expressed in wt-%, we have denoted the amount of residue left after TGA of the μgel and μ-gel-g-PEMA respectively. From the total amount of μ-gel-g-PEMA used for TGA we were able to calculate the mass of grafted PEMA in mg. Together with the molecular weight of the brushes obtained by GPC this was converted to the molar amount of grafted PEMA (*mole PEMA*).

$$mole\ PEMA = \frac{PEMA_{TGA}}{M_n} \tag{4.2}$$

A similar approach was taken for the calculation of the molar amount of μgel

($mole\ \mu gel$). The molecular weight of the μgel was taken from static light scattering ($5.6 * 10^6\ g * mol^-1$) and the mass of the μgel calculated by subtracting the mass of grafted PEMA from the total amount of μ-gel-g-PEMA used for TGA.

$$mole\ \mu gel = \frac{\mu gel_{TGA}}{M_w} \tag{4.3}$$

Si-wafer cleaning

The silicon wafers (Si-Mat, CZ) that were used as a substrate for SPM- and GISAXS-measurements were cleaned by treating them in an Argon plasma for 10 min at a pressure of $\sim 2 * 10^{-2}\ mbar$ in a commercial plasma cleaning setup operating at 30 watt plasma power (PDC-002, Harrick Plasma, USA).

Sample preparation for imaging of μgel and μ-gel-g-PEMA particles by SPM

Imaging the particles by means of SPM allowed to analyze the size and shape of the particles. After spin-coating toluene solutions ($1\ \mu g * ml^{-1}$) of μgel or μ-gel-g-PEMA particles on pre-cleaned silicon wafers they were air-dried for at least 1 h prior to measurements.

Scanning Probe Microcopy

The characterization of the μgel and μ-gel-g-PEMA particles was carried out under ambient conditions with a commercial SPM setup (Dimension 3100, Veeco, USA; NanoScopeV controller). Silicon cantilevers (OMCL-AC 160 TS, Olympus, Japan) with a nominal tip radius of ~10 nm and a tip height of 11 μm were used. The measurements were done in tapping mode with a resonant frequency of the cantilevers near 300 kHz.

The images of μ-gel-g-PEMA particles dispersed in a homopolymer matrix were analyzed by applying a straightforward k-nearest neighbor algorithm written in MATLAB. Particle positions were assigned by hand and the Euclidian distance between each particle in the overall image was calculated within this algorithm using Eq. 4.4.

$$NN_j = \sqrt{\left(x_j - x_i\right)^2 - \left(y_j - y_i\right)^2} \tag{4.4}$$

x_j, y_j are the coordinates of the particle of interest and x_i, y_i are the coordinates of every other particle in the image. NN_j indicates an array of all k-nearest neighbors for a particle j in which ($0 < k < n-1$). n is the number of all particles observed. The NN_1-Distance is used as an abbreviation for the first nearest neighbor distance in the following.

Sample Preparation for SPM- and GISAXS-measurements of particle/homopolymer mixtures

The μ-gel-g-PEMA particles were mixed with homopolymers of different molecular weight (see Table 4.1) at core volume fractions (ϕ_c) of 0.26 and 0.49. Toluene (p.a. - grade, VWR) was added and the particle-matrix system diluted to 100 mg/mL. Treatment with ultrasound for 15 min ensured dispersion of the particle-matrix system. All samples for GISAXS-measurements were prepared by spin-coating (2000 rpm, 30 sec) the particle-matrix dispersion on pretreated silicon wafers. The thickness of the films varied between 400 and 600 nm. Samples of the μgel and μ-gel-g-PEMA particles without a homopolymer matrix were prepared in the same fashion.

Grazing Incidence Small Angle X-ray scattering

The GISAXS experiments were carried out at the BW4 beamline of the HASYLAB @ DESY using the μ-focus option. Scattering curves were obtained by taking transverse detector scans of the full 2D scattering pattern in reciprocal scattering plane ($q_{||}$). The transverse cuts were taken at the maximum intensity of the Yoneda peak ($\alpha_c = 0.19\ degree$) [248]. The position of the correlation peak in the scattering curves was directly related to the correlation length between particles. The error of the correlation length was given by the full width half maximum (FWHM) of the correlation peak.

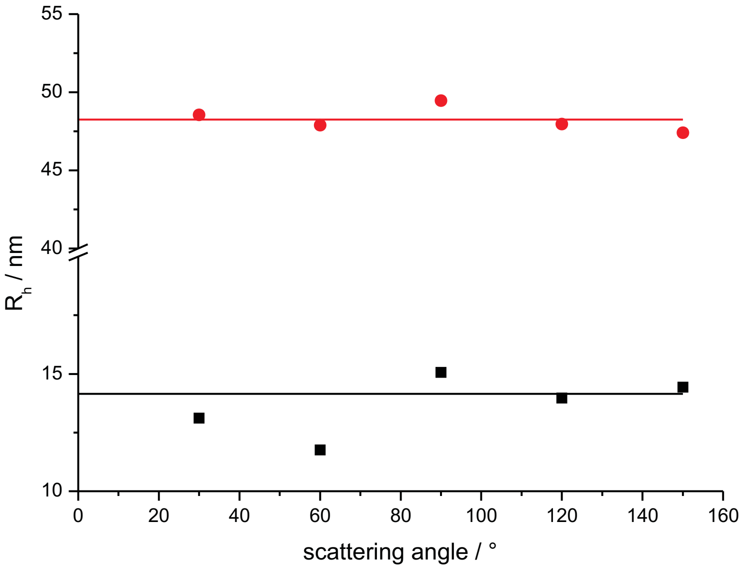

Fig. 4.7: Dynamic light scattering data of μgel (black squares) and μ-gel-g-PEMA (red spheres). Solid lines are indicating the average value obtained from five different scattering angles.

4.1.4 Results and Discussion

Characterization of individual particles

DLS was used to determine the hydrodynamic radius of the μgel nanoparticles ($R_{h(\mu gel)}$). The data is shown in Fig. 4.7 (black squares).
The average value of the data obtained from five different scattering angles (30 - 150 degree in steps of 30 degree), as indicated by the black solid line in Fig. 4.7, gave an hydrodynamic radius $R_{h(\mu gel)}$ of 14 $\pm$ 1 nm. The error bar is the standard deviation of the average value obtained from 5 scattering angles. After growing PEMA chains on the μgel particles an increase in hydrodynamic radius of the μ-gel-g-PEMA particles was found at every scattering angle (red spheres in Fig. 4.7). The average value, as indicated by the red solid line in Fig. 4.7, gave an hydrodynamic radius $R_{h(\mu-gel-g-PEMA)}$ of 48 $\pm$ 2 nm. The brush length was calculated following Eq. 4.5.

$$l_{b(DLS)} = R_{h(\mu-gel-g-PEMA)} - R_{h(\mu gel)} \tag{4.5}$$

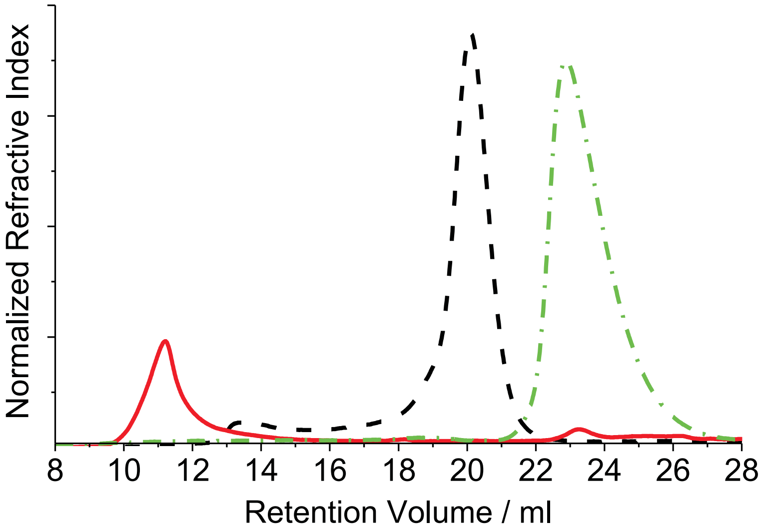

Fig. 4.8: Representative GPC-results for the μgel particles (black dashed line), the μ-gel-g-PEMA particles (red solid line), and the cleaved PEMA brushes (green dash-dotted line).

A brush length $l_{b(DLS)}$ of 34 ± 2 nm was thus obtained in the good solvent toluene.

Characterization of grafted PEMA-chains

The aim of this study was to investigate the brush thickness as a measure of the conformation of grafted polymer brushes as a function of polymer matrix molecular weight. The interactions between matrix polymer and grafted polymer are governed by the respective molecular weights. The determination of brush molecular weight was thus essential. Dissolution of the μgel core with HF was carried out and the free polymer recovered and subjected to GPC measurements (Fig. 4.8, green dash-dotted line). The elution diagram of the cleaved PEMA was compared to the GPC-results of the μgel particles (black dashed line) and the μ-gel-g-PEMA (red solid line). The GPC-data confirm the results obtained by DLS (see Fig. 4.7). The size of the particles increased after polymerization represented by a decrease in retention volume from 20 ml to 11 ml due to the formation of PEMA brushes. Dissolution of the core with diluted HF gave free PEMA with a retention volume of 23 ml. A number average molecular weight M_n = 26100 g/mol, a mass average molecular weight M_w = 37700 g/mol and a polydispersity index PDI = 1.45 of the PEMA brushes after cleaving them from the μgel particles was estimated using the retention volume.

Several questions arose when looking in detail at the GPC curves and comparing them with the DLS data. The elution diagram of the μgel particles (black dashed line) has a shoulder at lower retention volume. A reason for this shoulder could be the presence of aggregates. DLS data did not reveal any hints of aggregates however.

The elution diagram of the μ-gel-g-PEMA particles (red solid line) has a second, but much smaller, peak at a higher retention volume, comparable to that of the cleaved polymer. The formation of unbound polymer during polymerization is the most likely explanation. The peak of the unbound polymer was barely distinguishable from the baseline for some of the GPC measurements. The molecular weight of the unbound polymer and the PDI could not be determined due to the low signal to noise ratio, but the elution volume seems to be exactly the same than the one of the cleaved PEMA (green dash-dotted line). Thus one can conclude that the polymer in solution grew to the same length as the polymer on the surface of the particles.

An interesting question that arises when looking at the GPC data of the cleaved polymer as to why the PDI was as high as 1.45. Such a PDI is unusually high for a controlled reaction and could result in an elevated polydispersity of the μ-gel-g-PEMA particles. A reasonable explanation for the PDI could be that the HF-treatment hydrolyzed some of the ester groups. The carboxylic groups formed during the hydrolysis might change the hydrodynamic radius of the cleaved polymer.

Some of the interesting features in the elution diagrams, that were discussed thus far, can be interpreted using SPM data (see Fig. 4.9). The existence of single, well defined μ-gel-g-PEMA particles was revealed. One aggregate of three particles is also visible in images (c) and (d) of Fig. 4.9. The total number of such aggregates must be low however, since DLS data did not show any hints of aggregates. A small amount of free polymer is making the background in Fig. 4.9 (c) look blurry, but it was barely detectable in GPC and not at all in DLS.

Imaging and characterizing μgel and μ-gel-g-PEMA particles

SPM measurements revealed that the μgel particles as well as the μ-gel-g-PEMA particles were well-distributed over the silicon wafer (Fig. 4.9 (c) and (d)). More than 100 μgel particles were analyzed and a Gaussian distribution was fitted to the histogram of the height distribution (Fig. 4.9 (b), I). The maximum of the fit is at $18 \pm 1\ nm$ which results in a radius of the μgel particles of $r_c = 9 \pm 1\ nm$. The full width half maximum (FWHM) of the cross-sections from the height image were analyzed in order to study the shape of individual particles. The height of a spherical feature should match the FWHM. The nominal tip-diameter ($\sim$ 20 nm, manufacturer specification) was subtracted from the FWHM with the result that the μgel particles had a spherical shape. Some aggregates of μgel particles (Fig. 4.9 (a)) were observed which could explain the shoulder in the GPC curve for the μgel particles (Fig. 4.8, black). A comparison of the DLS ($R_{h(\mu gel)} = 14 \pm 1\ nm$) and SPM ($r_c = 9 \pm 1\ nm$) measurements showed that the hydrodynamic radius was about 5 nm larger than the radius of μgel particles in the dry state. The reason for this discrepancy was swelling of the μgel particles in toluene during the DLS measurement [246].

The height of the μ-gel-g-PEMA particles was $\sim$ 3 nm bigger than the height of the μgel particles, as the histogram II in Fig. 4.9 (b) demonstrates. This increase was attributed to the presence of PEMA brushes underneath and on top of the particles as sketched in Fig. 4.9 (e). The μ-gel-g-PEMA particles appear as heightened dots in the topography image (Fig. 4.9 (c)), whereas the brushes appear as intense disks around the cores in the phase-contrast image (Fig. 4.9 (d)). The small features scattered between the μ-gel-g-PEMA particles was most likely free polymer, which is conform to the observation of a peak at bigger retention volumes in GPC data (Fig. 4.8, red).

The brush shell thickness ($l_{b(SPM)}$) was determined using the radius of the μgel particles of $r_c = 9 \pm 1\ nm$ and the diameter ($D = 144\ \pm 8\ nm$) of the disk of μ-gel-g-PEMA particles (Fig. 4.9 (b), III).

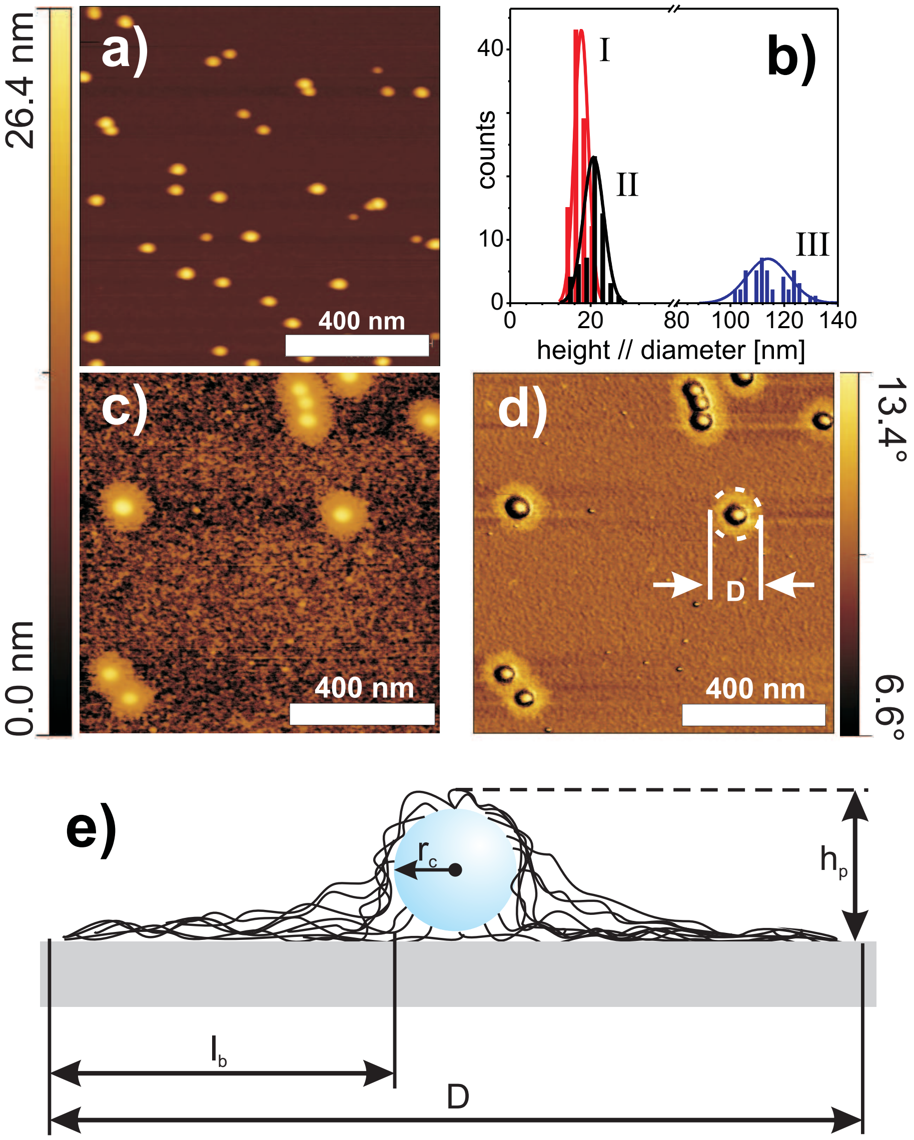

Fig. 4.9: (a) Topography image of μgel particles. (b) Histogram showing the height of μgel particles (red, I), height of μ-gel-g-PEMA (black, II) and diameter D of PEMA disk (blue, III). I and II were obtained from topography images, whereas III was obtained from the phase-contrast image. (c) Topography image of μ-gel-g-PEMA particles on a silicon wafer. (d) Phase-contrast image where the PEMA brushes appear as bright disk with diameter D around the core. (e) Schematic drawing of a μ-gel-g-PEMA particles indicating the dimensions of disk (D) and brushes (l_b). Dimensions not to scale.

$$l_{b(SPM)} = \frac{D}{2} - r_c \tag{4.6}$$

The basis for the calculation of $l_{b(SPM)}$ is the geometric model presented in Fig. 4.9 (e). The brush shell thickness $l_{b(SPM)}$ was thus calculated to be $48 \pm 8\ nm$. Gaussian error propagation was used to calculate the error.

The conventional contour length r_{cont} of a polymer chain with the same degree of polymerization as the PEMA brushes (DP$_w$ = 330 monomeric units) was calculated using Eq. 4.7.

$$r_{cont} = DP_w * b_{eff} \tag{4.7}$$

A value of $r_{cont} = 84nm$ was received using an effective bond length of $b_{eff} = 0.2546nm$ of a vinyl monomeric unit [78]. The conventional contour length is the maximum end-to-end distance of a physically completely stretched chain (all-trans conformation) implying that the PEMA brushes are spread to 57% of the contour length on the silicon wafer. A comparison of the DLS ($l_{b(DLS)} = 34 \pm 2\ nm$) to the SPM ($l_{b(SPM)} = 48 \pm 8\ nm$) data revealed a discrepancy of 15 nm between the swollen state of the brush in DLS measurements and a dry, but spread state in SPM measurements. The brush was thus more stretched on a substrate (e.g. silicon wafer) than in toluene solution (DLS).

Determination of grafting density

The grafting density of grafted PEMA was estimated using Eq. 4.8.

$$\Gamma = \frac{mole\ PEMA}{mole\ \mu gel * particle\ surface} \tag{4.8}$$

$mole\ PEMA = 1.12 * 10^{-7} mol$ and $mole\ \mu gel = 1.5 * 10^{-10} mol$ were obtained from Eq. 4.2 and 4.3 respectively, based on TGA results. The particle surface of 1018 nm^2 was calculated using r_c from SPM measurements of the μgel particles. A grafting density of $\Gamma = 0.7\ chains * nm^{-2}$ was estimated.

Characterization of dispersions of μ-gel-g-PEMA particles in homopolymers

An investigation of the distribution and dispersion behavior of the μ-gel-g-PEMA particles in PEMA homopolymer matrices was conducted at two core volume fractions $\phi_c = 0.26$ and 0.49. Therefore, the correlation length of our samples was deducted form the position of the correlation peak in the GISAXS data (Figure 4). The correlation length determined by the position of the correlation peak from GISAXS measurements (Fig. 4.10) can be seen as a measure for the distribution of the μ-gel-g-PEMA particles in the matrix. A correlation length is in general defined as the distance from a certain point beyond which there is no further correlation of a physical property associated with that point. One can interpret the measured correlation length as the average center of mass distance between neighboring particles. A distance of $\Lambda = 41 \pm 9nm$ was calculated in the case of the μ-gel-g-PEMA without homopolymer matrix (referred to as 0k and marked with a star in Fig. 4.11). One can conclude that the brushes are contracted and possibly interpenetrated to some extend, as depicted in Fig. 4.1. The inter-particle distance should exhibit the smallest value of all samples under investigation.

Due to the absence of a homopolymer matrix one can calculate the distance between two neighboring μ-gel-g-PEMA particles, in other words the brush shell thickness ($l_{b(GISAXS)}$), from GISAXS data using

$$l_{b(GISAXS)} = \frac{\Lambda - 2r_c}{2} \tag{4.9}$$

where $r_c = 9 \pm 1\, nm$ is the core radius of the particles. A brush shell thickness of $l_{b(GISAXS)} = 11.5 \pm 10\, nm$ was obtained. The brushes were thus contracted to nearly a third of their length ($l_{b(DLS)} = 34 \pm 2\ nm$) in the wet case as measured by DLS in the good solvent toluene.

An increase in inter-particle distance was observed when mixing the μ-gel-g-PEMA particles with homopolymer matrices of increasing molecular weight independent of the core volume fraction ϕ_c. A maximum in inter-particle distance was reached once the matrix molecular weight resembled that of the polymer brushes ($N/P \sim 1$, dashed line in Fig. 4.11). The higher fill factor

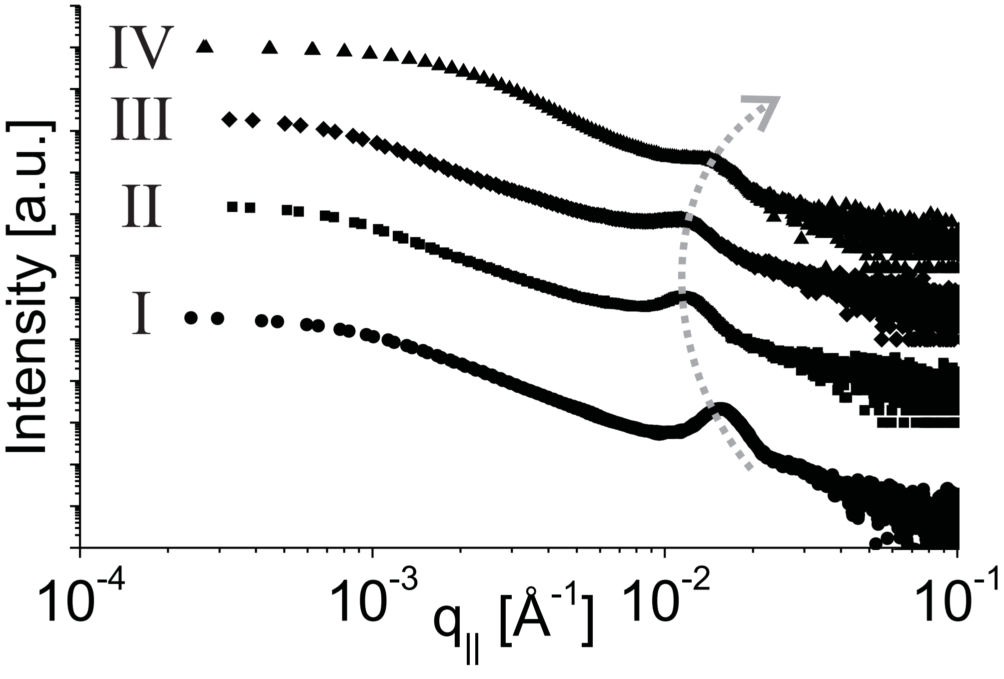

Fig. 4.10: GISAXS spectra of four μ-gel-g-PEMA - PEMA homopolymer dispersions at core volume fraction of $\phi_c = 0.49$. The molecular weight of the matrix polymer was varied from I to IV as follows: I = no homopolymer; II = 19k; III = 36k; IV = 178k. The dotted arrow indicates the change in correlation distance for the different matrices.

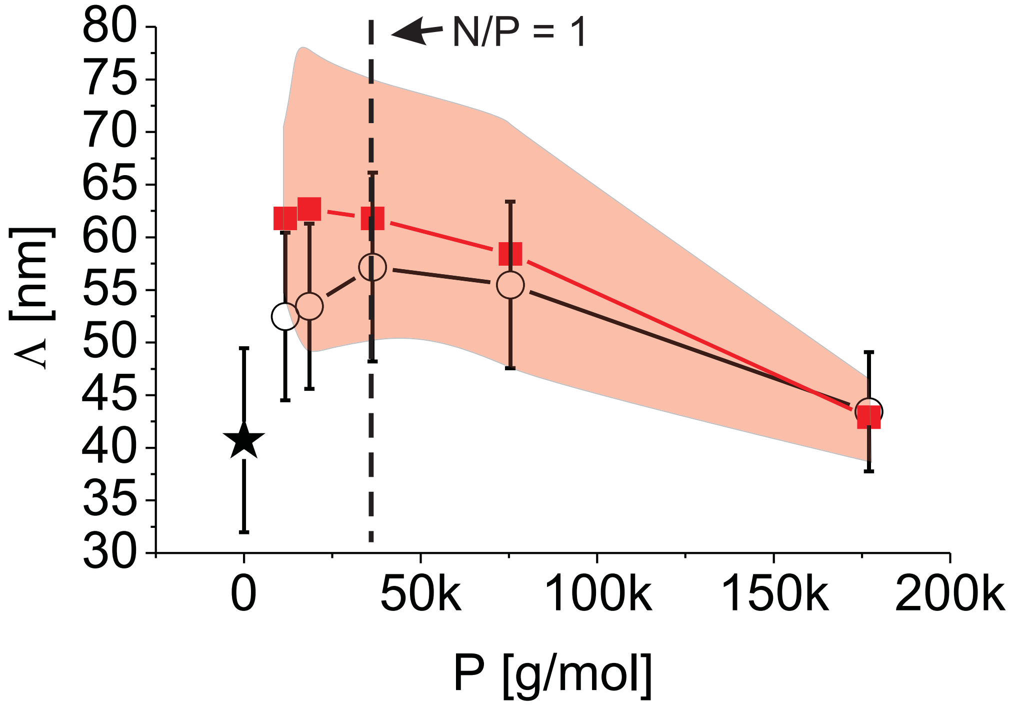

Fig. 4.11: Correlation length Λ as a function of homopolymer matrix molecular weight P. Red squares correspond to core volume fraction $\phi_c = 0.26$, open circles to $\phi_c = 0.49$, and star to $\phi_c = 1$ (without matrix). The shaded region is related to the FWHM error of $\phi_c = 0.26$ data points. The error bars indicate the FWHM error of $\phi_c = 0.49$ data points. The dashed line indicates the theoretically predicted matrix molecular weight where microphase separation should occur for brushes with molecular weight of 37k.

is the reason why the inter-particle distance became smaller for samples with core volume fraction of $\phi_c = 0.49$ compared to samples with core volume fraction of $\phi_c = 0.26$.

A decrease in inter-particle distance was observed for matrix molecular weights beyond $N/P \sim 1$ independent of the core volume fraction. The brushes started to expel the surrounding matrix and the dispersion became unstable. The intensity of the correlation peak was starting to decrease with increasing molecular weight of the matrix. Contributions of other correlation lengths were leading to a more shoulder-like shape of the peak (Fig. 4.10, IV). These contributions may have come from a broader inter-particle distance distribution which was cross-checked with SPM (Figure 6).

The inter-particle distance reached a value of $\Lambda = 43 \pm 4nm$ at the highest molecular weight of the matrix at $178kg * mol^{-1}$ measured with GISAXS. The particles formed aggregates and inside these aggregated the inter-particle distance was as low as for the above mentioned particles without a homopolymer matrix (Fig. 4.10, I).

In the phase-contrast images the μ-gel-g-PEMA particles appeared as bright dots and the homopolymer matrix as darker areas. A dense packing of μ-gel-g-PEMA particles was observed without a homopolymer matrix (Fig. 4.12, P = 0k). A distribution of particles was observed for the nanocomposite with the lowest matrix molecular weight (Fig. 4.12, P = 12k). The dispersion became unstable (Fig. 4.12, P = 101k) with increasing matrix molecular weight and finally aggregates (Fig. 4.12, P = 269k) were observed. The smallest NN_1-Distance of $38 \pm 4nm$ (referred to as 0k and marked with a star in Fig. 4.13) was measured for the sample without homopolymer (Fig. 4.12, P = 0k). Due to the absence of a homopolymer matrix one can calculate the distance between two neighboring μ-gel-g-PEMA particles, in other words the brush shell thickness ($l_{b(SPM,assembly)}$), in analogy to Eq. 4.9.

$$l_{b(SPM,assembly)} = \frac{NN_1 - 2r_c}{2} \tag{4.10}$$

$r_c = 9 \pm 1\ nm$ is the core radius of the particles. A brush shell thickness of $l_{b(SPM,assembly)} = 10 \pm 5\ nm$ was obtained. This is in agreement with the

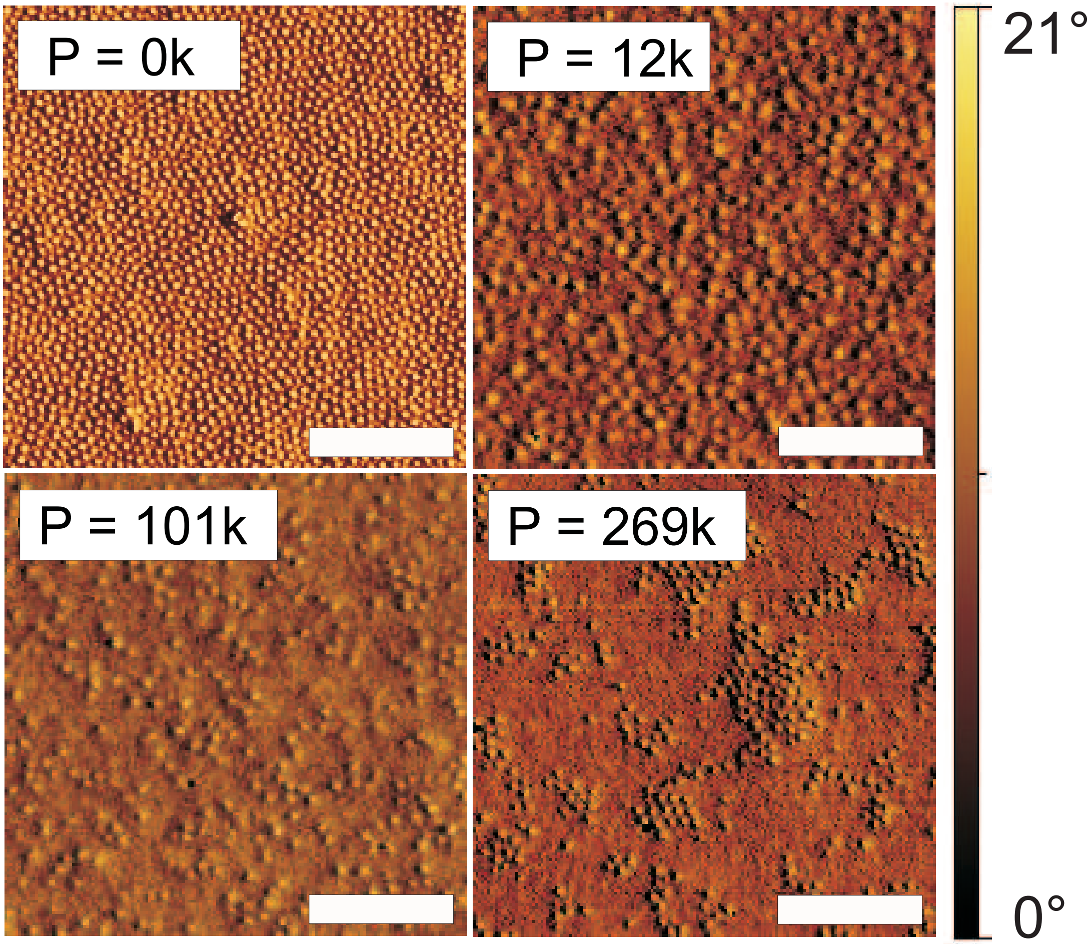

Fig. 4.12: Phase-contrast images of μ-gel-g-PEMA particles dispersed in PEMA matrices of different molecular weights. The core volume fraction was kept at $\phi_c = 0.26$ in every case. Particles appear as bright dots embedded in a matrix with darker contrast. Scalebar = 1 μm.

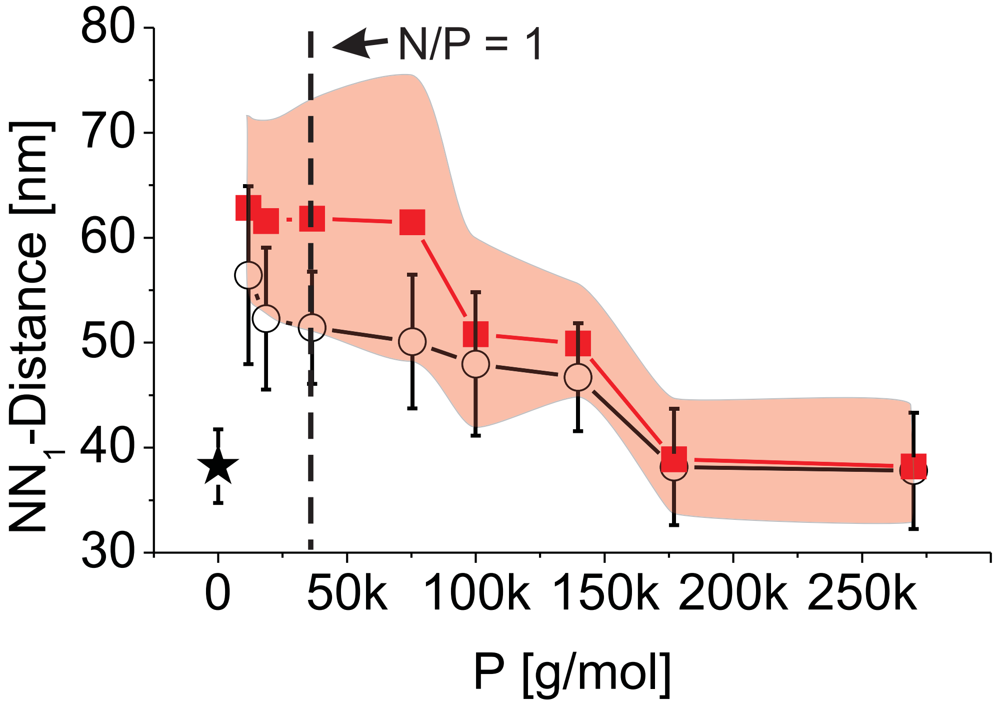

Fig. 4.13: First nearest neighbor distance NN_1 as a function of homopolymer matrix molecular weight P. Red squares correspond to core volume fraction $\phi_c = 0.26$, open circles to $\phi_c = 0.49$, and star to $\phi_c = 1$ (without matrix). The shaded region is related to the standard deviation of $\phi_c = 0.26$ data points. The error bars indicate the standard deviation of $\phi_c = 0.49$ data points. The dashed line indicates the theoretically predicted matrix molecular weight where microphase separation should occur for brushes with molecular weight of 37k.

data obtained by GISAXS ($l_{b(GISAXS)} = 11.5 \pm 10\ nm$). The brushes were contracted and possibly interpenetrated to some extend.

An increase in inter-particle distance was observed when mixing the μ-gel-g-PEMA particles with homopolymer matrices of increasing molecular weight independent of the core volume fraction ϕ_c. A maximum in inter-particle distance of $63 \pm 15\ nm$ for $\phi_c = 0.26$ and $56 \pm 12\ nm$ for $\phi_c = 0.49$ was reached. The particles were distributed throughout the matrix and no aggregates were detected.

A decrease in inter-particle distance was observed for matrix molecular weights beyond $N/P \sim 1$, as observed with GISAXS, up to a molecular weight of 178k independent of the core volume fraction. The brushes started to expel the surrounding matrix and particle aggregates with contracted brushes were observed. An increase in matrix molecular weight beyond 178k did not lead to further changes in NN_1-Distance. The NN_1-Distance remained at $38 \pm 6nm$ and $39 \pm 6nm$ respectively. Most particles were located inside aggregates with a close packing and contracted brushes, as the fixed NN_1-Distance demonstrated for matrix molecular weight beyond 178k. Therefore, the interparticle distance reached a value similar to that of the particles without a matrix (dry brushes, referred to as 0k and marked with a star in Fig. 4.13). One can thus conclude that GISAXS and SPM measurements provided evidence in support of the model depicted in Fig. 4.1.

The changes in brush conformation with matrix molecular weight could have a direct influence on the stability of the nanoparticles at the surface. Nanowear tests [249] were therefore carried out on composites with a core volume fraction of $\phi_c = 0.26$. Two different matrices were employed, one with a 12k and the other one had 98k. An area of 5 x 5 μm^2 was imaged with an atomic force microscope in contact mode with the lowest force possible, prior to the nanowear test (Fig. 4.14 (a) and (c)). The wear test was performed subsequently by scanning an area of 2.5 2.5 μm^2 with a defined force of 10 nN for 100 times with a scan velocity of 25 $\mu m/s$. An image of 5 x 5 μm^2 was finally acquired at low force (Fig. 4.14 (b) and (d)), including the previously rippled area.

The nanowear test of the sample with 12k matrix revealed that material was moved by the tip to the left and right border of the rippled area due to the scanning at elevated force (Fig. 4.14 (a) and (b)). The smooth shape of the line scan demonstrates that the tip did not pull out bigger material clusters, i.e. particles, from the surface. The root mean square (rms) roughness of the rippled area increased from 0.78 to 1.29 nm. The situation was totally different for the 98k sample. Small holes in the rippled area were observed (Fig. 4.14 (c) and (d)). The holes had a depth of 10 nm, which indicates that particles were detached from the matrix by the SPM tip during the wear test (graph related to Fig. 4.14 (d)). Furthermore the rms roughness had increased from 1.29 to 5.8 nm.

The results of the nanowear tests can be regarded as direct proof of the changes

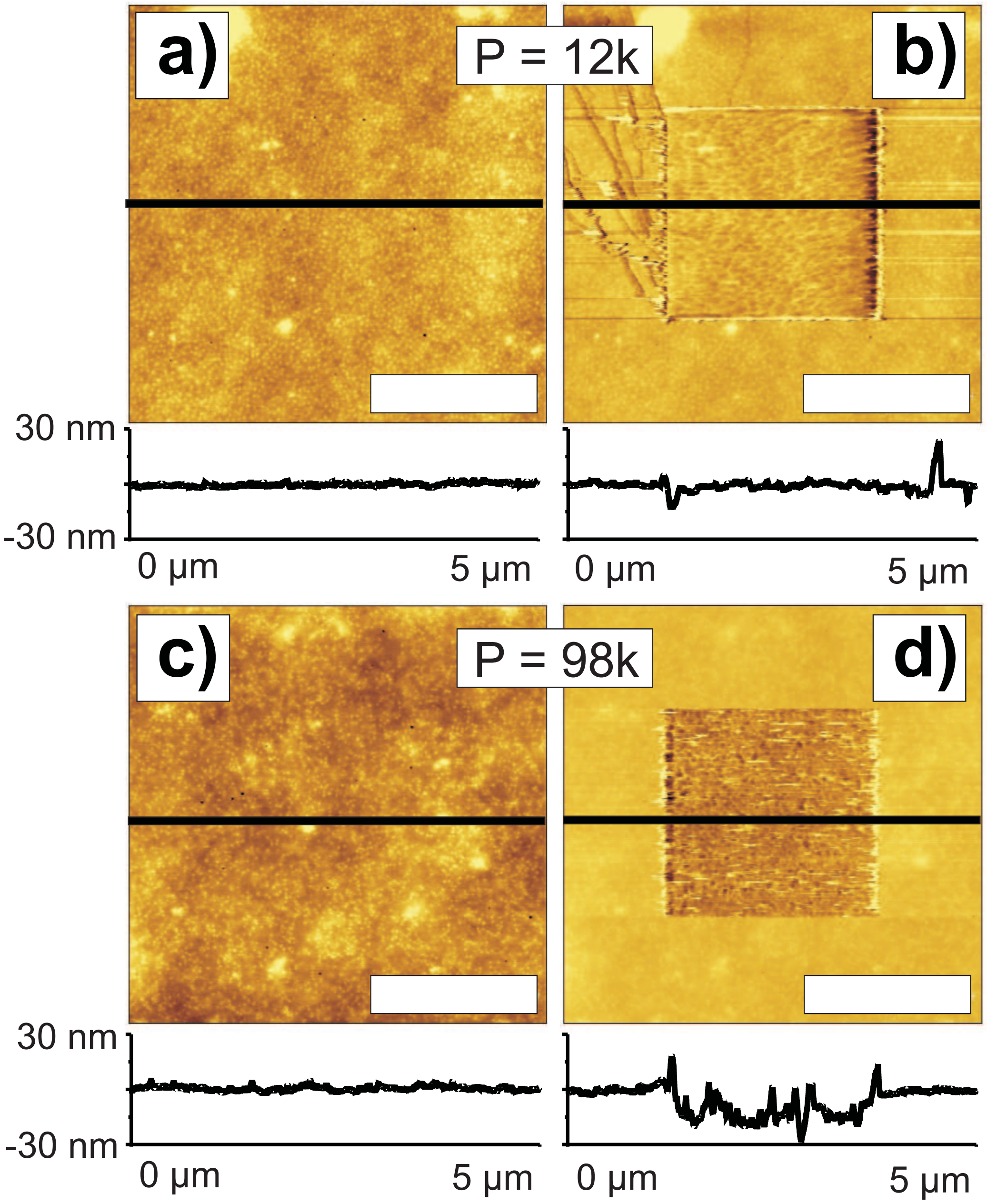

Fig. 4.14: SPM topography images taken before (a), (c) and after (b), (d) the wear test. Scale-bar = 2 μm. Images were taken in contact mode at lowest force possible. The inner square (2.5 2.5 µm^2) in (b) and (d) was scanned 100 times at a force of 10 nN and a scan velocity of 25$\mu m/s$. The rms roughness of the inner area was increased from 0.78 to 1.29 nm for P=12k and from 1.66 to 5.8 nm for P=98k. Solid lines in the images are horizontal scans and the cross-sections correspond to the graphs underneath the images.

in interaction between matrix and brushes. The interactions between matrix and brushes are dominated by the brush conformation. Changes in brush conformation are triggered by the molecular weight of the matrix. The μ-gel-g-PEMA particles with contracted brushes behaved like hard spheres rather than soft spheres. Thus it becomes possible to detach individual particles from the surface of such a composite film with a SPM tip.

4.1.5 Discussion

In the publication [240] of Lindenblatt and coworkers the authors developed a semiquantitative model to describe the compatibility of hairy spheres with linear homopolymer chains. This will be discussed here in context with the presented results. The presented results for entangled matrix chains are in agreement with the model developed by Lindenblatt et al. for unentangled matrix chains. Microphase separation was observed for the nanocomposites with a matrix molecular weight higher than the one of the brushes, as indicated by a continuous decay in inter-particle distance (Fig. 4.11 & Fig. 4.13). Lindenblatt et al. saw the reason for the microphase separation in the impenetrability of the unentangled matrix chains into the brush. Thus, an excluded volume zone is formed around the particles. Once two particles get into close contact an overlap in excluded volume zone is the result. The overlap leads to a reduction in total excluded volume of the system, increasing the free volume available to the matrix chains. However, Lindenblatt et al. [240] investigated unentangled matrix chains. The presented results indicate that brushes in contact with an entangled matrix behave in a similar way to the unentangled system investigated by Lindenblatt et al.

The origin of the impenetrability in the presented entangled system is a contraction of the brushes induced by the matrix leading to a decrease of inter-particle distance. The particles with contracted brushes behave more like hard spheres exhibiting an attractive interaction among the particles which induces the microphase separation. The nanowear tests showed additionally that particles with contracted brushes can be pulled out of a microphase separated composite with a SPM tip (Fig. 4.14). An analog behavior of the particles in the bulk can be expected and the mechanical properties would thus be similar to a system composed of hard spheres mixed in a polymer matrix.

4.1.6 Experimental

Preparation of PEMA matrix polymers

A Schlenk flask equipped with a magnetic stir bar was flushed with argon and CuBr added under argon counterflow. $CuBr_2$ had to be added additionally to ensure reaction control in the case of lower target molecular weight polymers. Deoxygenated anisole (10 mL), EMA (10 mL) and PMDETA were added via syringes under a stream of argon. The active copper complex formed during stirring for 10 min and the initiator 2-EiBBr was added via a syringe subsequently. The reaction vessel was sealed with a stopper and 3 freeze-pump-thaw cycles executed. The vessel was placed in an oil bath at 32 °C for a preset time, as specified in Table 4.2. The polymerization was stopped by introducing air to the vessel. Residual copper was removed by diluting the solution with 40 mL THF and stirring with Dowex Marathon Msc (Aldrich) for 10 min. The resin was removed by filtering (G2 glass filter crucible). Finally the polymer was recovered by precipitating into 240/60 mL MeOH/Millipore water. Excess solvent was decanted, the polymer filtered (G2 glass filter crucible) and washed with MeOH. The recovered polymer was redissolved in 30 mL of THF and precipitated, filtered again and dried in a vacuum. The amount of particular reagents can be found in Table 4.2. In the case of the anionically prepared PEMA, sec-buthyllithium/1,1-diphenylethylene in THF at -70 °C was used as the initiator system. MeOH was chosen for termination.

Microgel synthesis

A 250 mL round-bottom flask equipped with a magnetic stir bar was charged with 100 mL Millipore water and 13.6 mL of an aqueous solution containing 10 wt-% DBA (97%, Aldrich). 21 mL of freshly distilled monomer methyl-

Table 4.2: Synthesis conditions for PEMA matrix polymers.

Abbrev.	**anisole, EMA / ml**	**CuBr / mmol**	**$CuBr_2$ / mmol**	**PMDETA / mmol**	**2-EiBBr / mmol**	**time / h**
12k	10	0.183	1.12	1.30	1.30	22
19k	10	0.183	0.548	0.73	0.73	24
36k	10	0.183	0.183	0.365	0.365	24
75k	10	0.183	-	0.183	0.183	21
98k	10	0.0913	-	0.0913	0.0913	24
101k	10	0.0913	-	0.0913	0.0913	27
140k	10	0.0609	-	0.0609	0.0609	48
178k	10	0.0609	-	0.0609	0.0609	46
269k	anionic polymerization					

trimethoxysilane (99%, Aldrich) was introduced dropwise (1h 15 min) under stirring using a dropping funnel. After stirring for 6 h the unmodified nanoparticles had formed, yielding an opaque dispersion. The first surface modification step was carried out by adding 4 mL trimethylethoxysilane (98%, Wacker) dropwise within 35 min to the dispersion. After stirring overnight, 3 g ATRP-Et (40 min) were introduced dropwise and stirring was continued overnight. The dispersion was filtered and destabilized by pouring it into 1.3 L MeOH (HPLC-grade, Fisher). For the second modification step the precipitate had to be transferred to toluene. However, filtration of the precipitate leads to gelation. Therefore, the excess MeOH was decanted (500 mL)

and fresh MeOH (500 mL) was added. This procedure was repeated 6 times to remove unreacted reactants and surfactants. Decanting of the excess MeOH in the last cycle was followed by the addition of 300 mL toluene (Sigma-Aldrich, p.a.-grade). The dispersion was concentrated to 500 mL under reduced pressure and fresh toluene (400 mL) added. This procedure was repeated four times. The dispersion was reduced to 300 mL after the final addition of toluene and subsequently transferred to a 500 mL round-bottom flask equipped with a magnetic stir bar. A pressure-equalizing dropping funnel was connected to the flask and charged with ATRP-Cl (3 g). The setup was flushed with argon to prevent the hydrolysis of the chlorosilane. The ATRP-

Cl was added dropwise to the dispersion (1 h) while stirring. Subsequently the dropping funnel was exchanged for a condenser and the dispersion refluxed overnight (140 °C). Complete reaction of the chlorosilane with the silanol groups on the surface of the particles was achieved by stirring for 30 h at room temperature. Unreacted silanol endgroups were capped by 1,1,1,3,3,3-hexamethyldisilazane (Jansen, 97%), which was added dropwise (5.2 mL) within 1 h while stirring. Full conversion of all endgroups was ensured by refluxing the dispersion overnight at 140 °C . The stabilized particles were filtered and poured in 1.6 L of MeOH. Excess solvent was decanted, μgel particles recovered by filtration with a sintered glass crucible (porosity G 4) and washed repeatedly with MeOH. Remaining unbound ATRP-initiator was removed by redispersing the wet product in toluene (100 mL) and precipitation in MeOH (1 L). Finally the microgel macroinitiators were dried under reduced pressure.

SI-ATRP polymerization

Oxygen-free conditions were ensured by carrying out the reaction in an argon atmosphere and flushing the solvent toluene (14 mL) for 30 min with argon prior to use. The μgel particles (0.5 g), the CuBr (10 mg), and the $CuBr_2$ (140 mg) were degassed in a 100 mL Schlenk flask at $4 * 10^-1\ mbar$. Toluene was added under an argon flow and the solid components were dispersed (ultrasonication 10 min; stirring 5 min). EMA (10 ml) and PMDETA (0.15 ml) were added under an argon flow subsequently. The flask was immediately capped and a freeze-pump-thaw cycle was executed. The copper complex formed during 10 min of ultrasonication, indicated by the dark green color. Two more freeze-pump-thaw cycles were performed to remove remaining traces of oxygen and the reaction vessel was placed in an oil bath at 32 °C for 5 h. Exposing the solution to air interrupted the reaction. 50 mL of THF (Acros, p.a.-grade) were added and the copper was removed by stirring for 10 min with ion-exchange resin (Dowex Marathon Msc, Aldrich). The resin was removed by filtering with a sintered glass crucible (porosity G2) and the μ-gel-g-PEMA particles precipitated in 240/60 mL MeOH/Millipore water.

Excess solvent was decanted and particles recovered by filtering (G2 glass filter crucible). Repeated washing with MeOH, followed by redispersing the particles in THF and precipitation were done to obtain particles. Finally the μ-gel-g-PEMA particles were dried under reduced pressure for 24 h.

Cleaving of the grafted PEMA-chains

80 mg of the μ-gel-g-PEMA particles were mixed with 10 mL of toluene in a poly(ethylene) flask. Dispersion of the particles was achieved by means of 10 min ultrasonication and 90 min of vigorous stirring. 0.7 g of the phase transfer catalyst Aliquat 336 (Alfa-Aesar) and 3 mL of 5 wt-% HF were added. After two hours of stirring the cores were dissolved. Stirring was stopped and the aqueous layer was allowed to separate from the organic layer. The aqueous layer was removed from the bottom of the flask using a syringe and discarded after neutralization. The organic layer containing the PEMA was stirred with 20 mL of a saturated aqueous solution of $NaHCO_3$ to neutralize residual HF. A separatory funnel was used to obtain the organic phase, which was concentrated under reduced pressure subsequently. The polymer was precipitated in a mixture of 8/2 ml of MeOH/Millipore water, filtered (G2 glass filter crucible) and dried in a vacuum.

Instrumentation

Light scattering experiments were carried out with the set-up described in Section 7.8.

Analysis of the cleaved/matrix PEMA and the μgel/μ-gel-g-PEMA particles was carried out with the gel permeation chromatography (GPC) set-up described in Section 7.4.

Thermogravimetric analysis of the μgel/μ-gel-g-PEMA particles was carried out with the thermobalance set-up described in Section 7.6.

GISAXS experiments were carried out with set-up described in Section 7.9.

Materials

Ally alcohol (99%, Aldrich), 2-bromoisobutyryl bromide (97%, Alfa), chlorodimethylsilane (95%, Fluka), ethoxydimethylsilane (97%, ABCR), dihydrogen hexachloroplatinate(IV) hexahydrate (99,9% metals basis, Alfa), ethyl α-bromoisobutyrate (97%, Fluka), $CuBr_2$ (99.999%, Aldrich), diethyl ether (p.a. - grade, VWR), and hydrochloric acid (37%, Aldrich) were used as received. Copper bromide (98%, Aldrich) was purified by boiling it for a short time in a mixture of 50:50 v/v Millipore water/glacial acetic acid and thereafter filtered off. This was followed by rinsing the precipitate with water, ethanol, diethyl ether, and finally it was dried under reduced pressure for 24h [177]. EMA (99%, Acros) was purified by passing it through an alumina column, distilled under reduced pressure from CaH_2, and stored under argon at -20 °C .
N,N,N′,N′,N″-Pentamethyldiethylenetriamine (PMDETA) (99%, Aldrich) was purified by distillation under reduced pressure and triethylamine (Aldrich) by distillation from CaH_2 in an argon atmosphere.

4.2 Polymer brushes on nanoparticles for advanced solid-state NMR spectroscopy

[†]Advanced solid state NMR spectroscopy techniques provide unique information about the conformation, chain order and dynamics of polymers not only in the bulk, but also at the interphase in nanocomposites. Recently developed techniques such as ^1H-^1H-, ^1H-^{13}C- double quantum NMR [250], or ^{13}C chemical shift anisotropy [251] allow to investigate extended chain conformations and dynamics close to solid surfaces. Additionally, NMR spin diffusion is of ample interest because it allows to probe the spatial extension of polymer chains from a solid surface [252]. Recently it has become possible to probe segmental dynamics site-selectively [253].
The macroscopic behavior of polymers is influenced by a change of confor-

---

[†] NMR measurements of the produced particles are currently carried out by Cornelius Friedrichs and Robert Graf in the group of Prof. H.W. Spiess; MPIP.

mation and dynamics due to the interaction with surfaces. Prominent examples are filled elastomers which can be studied by various spectroscopic techniques [254]. Recent developments and applications of advanced NMR techniques in this area were reviewed by Saalwächter [255].

Little attention has thus far been attributed to the effect of particles on structure and dynamics of the chains in the interphase at slightly larger distances from the surface. Information about the phenomena occurring at slightly larger distances from surfaces can only be obtained on the basis of profound knowledge of structure and dynamics of the polymers themselves. Previously unknown chain order as well as structural heterogeneities have been found for homopolymers. The heterogeneities were detected during studies of chain order, conformation and dynamics of polymers in bulk and attached to surfaces by various NMR and EPR techniques. Example for polymers exhibiting conformational order in the melt are poly(n-alkylmethacrylates). NMR has provided the link between the nanostructures, that were also detected via mechanical/dielectric measurements [256], as well as X-ray scattering [257], and the conformational memory on a molecular level [258]. Even the factors controlling the occurrence of such nanostructures were identified using the well-known Nuclear Overhauser Effect (NOE) [259,260], e.g., tacticity, incompatibility of backbone and side groups, degree of polymerization, and confinement of the chains. The role that the different degrees of chain organization play in the interaction of polymers with surfaces has not been investigated to date. Thus, the aim of this study is to investigate how the presence of sub-micron particles influences the chain organization and formation of nanostructures.

The size of nanostructures in polymer melts is typically in the range of a few nanometers, which is short compared to the dimension of a polymer chain or the entanglement length. The thickness of surface layers and the size of nanoparticles is comparable however. A match in the size of nanostructures and the distance between nanoparticles can be achieved by varying the filler concentration.

The macroscopic behavior of a polymer is in part determined by the nanostructures that can be found throughout the whole system. Weakening or

strengthening the nanostructures by the presence of a surface can lead to changes in chain organization at an interphase, amenable to NMR techniques. Changes in the nanostructures can affect the dynamic behaviour of the polymer at the interphase. Advanced NMR allows one to measure slow molecular dynamics with unprecedented sensitivity. Slow molecular dynamics are directly affected by heterogeneities in polymers, such as nanostructures. The aim of this study to determine the factors that determine the interaction of the surface with the nanostructured polymer. Based on the aforementioned findings one can expect a dependence of the interaction on the chemistry of the repeat unit, the molar mass and other factors governing the tendency to form extended chain conformations and nanostructures. A dependence on curvature of the surface and the distance between the nanoparticles can also be expected.
The NMR results should provide information about crucial length scales involved in the interactions of polymers with surfaces. The relationship between chain organization on the nanoscale and the macroscopic behavior should thus become more clear. A link between the NMR results and the macroscopic behavior of nanocomposites in general, as discussed in Section 4.1, will potentially be established. The three main goals of this project can be summarized as follows:

- Understanding the formation of molecular structures at the interphase.
- Understanding the influence of the interphase on the macroscopic properties.
- Designing a model describing the structure-property relationship.

Poly(n-alkylmethacrylates) are suitable candidates for this project, because extended conformations and nanostructures in the bulk have been studied already. PEMA is more suitable compared to PMMA, since it exhibits a much higher tendency for chain organization [257,258]. A thorough understanding of the conformation of the PEMA chains on the μ-gel-g-PEMA particles is a prerequisite for understanding the influence of the μ-gel-g-PEMA particles on the chain organization in the bulk. ^{13}C chemical shift anisotropy provides

Table 4.3: Synthesis conditions for μ-gel-g-PEMA-b-^{13}C-PEMA (Fig. 4.15 (I)) nanoparticles with outer shell of ^{13}C-PEMA - CuBr/CuBr$_2$-system. (MM $\equiv$ monomer (in ml); Cu(I)Br in mg; Cu(II)Br$_2$ in mg; L $\equiv$ ligand/PMDETA (in ml); S $\equiv$ solvent/toluene; l_b $\equiv$ brush length of the "block" calculated from DLS-data using Eq. 4.5)

region	**MM-type**	**μgel / mg**	**MM; L CuBr; CuBr$_2$**	**S / ml**	**time / h; min**	**yield / g**	**l_b / nm**
inner	EMA	0.17	1.5; 0.05; 7; 46	7	3; 40	0.13	25
outer	^{13}C-EMA	0.13	1.5; 0.05; 5; 46	7	3; 30	0.05	3

an access to the extended conformations in PEMA chains immobilized on the μ-gel-g-PEMA particles.

Enriching selected regions with ^{13}C leads to an increase in signal from these regions and thus allow to probe the extended conformations in the PEMA brushes site-selectively. One might expect the conformation of chain parts close to the surface, where the confinement typically leads to strong stretching, to be different from the conformation of the chain parts near the fringe, where the distance between neighboring chains is bigger. The challenge from the synthesis point of view was to produce selected regions with higher ^{13}C content. As a first experiment an enrichment of the part of the chains near the fringe was targeted. The intention was to polymerize the μgel nanoparticles with "regular" EMA under ATRP-conditions and to reinitiate the chains in a second ATRP-polymerization with EMA of 20% carboxylic ^{13}C carbon content. This synthetic pathway is depicted in Fig. 4.15 (I) and resembles the synthetic procedure one would take in order to produce a block copolymer on the μgel nanoparticles.

A detailed description of the SI-ATRP procedure can be found in Section 4.1.6, whereas the reaction details for the polymerization of each "block" can be found in Table 4.3. A brush length $l_{b(DLS)}$ of 25 nm was obtained for the PEMA-block. The second block using ^{13}C-EMA was smaller and a brush length of $l_{b(DLS)}$ of 3 nm was obtained. The value of 3 nm for the second block is unusually low, although similar amounts of μgel macroinitiator and monomer were used. The experiment was repeated in order to discover the reason that lead to the small brush length of the second block.

The reaction details for the polymerization of each "block" in the repetition

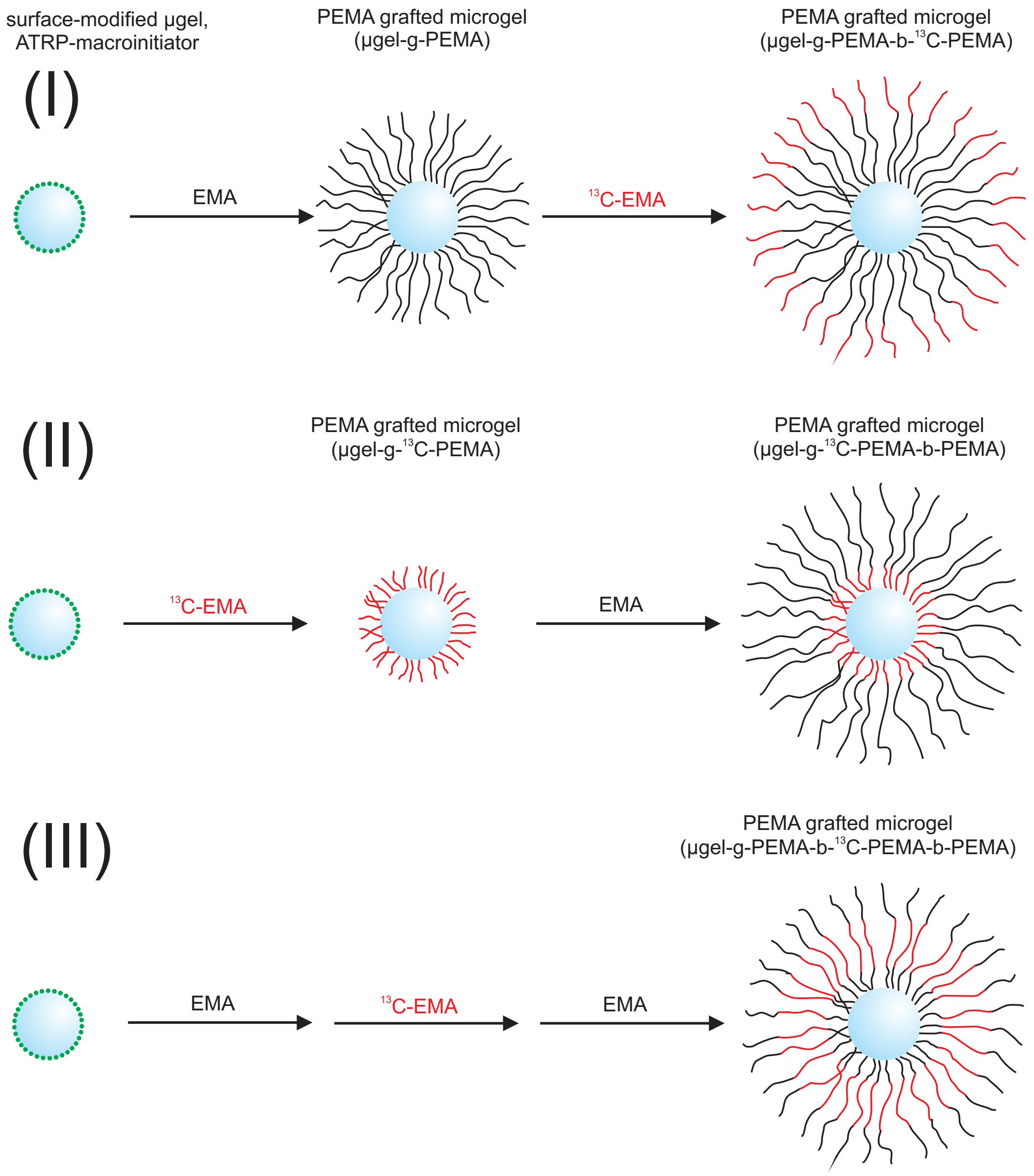

Fig. 4.15: Scheme illustrating the synthetic pathway using SI-ATRP to produce PEMA-grafted μgel nanoparticles with regions of higher ^{13}C content (red). (I) Nanoparticle with outer shell of ^{13}C-EMA; μ-gel-g-PEMA-b-^{13}C-PEMA. (II) Nanoparticle with ^{13}C-EMA shell at the surface; μ-gel-g-^{13}C-PEMA-b-PEMA. (III) Nanoparticle with central shell of ^{13}C-EMA; μ-gel-g-PEMA-b-^{13}C-PEMA-b-PEMA.

Table 4.4: Synthesis conditions for μ-gel-g-PEMA-b-^{13}C-PEMA (Fig. 4.15 (I)) nanoparticles with outer shell of ^{13}C-PEMA - CuBr/CuBr$_2$-system; repetition. (MM $\equiv$ monomer (in ml); Cu(I)Br in mg; Cu(II)Br$_2$ in mg; L $\equiv$ ligand/PMDETA (in ml); S $\equiv$ solvent/toluene; $l_b \equiv$ brush length of the "block" calculated from DLS-data using Eq. 4.5)

region	**MM-type**	**μgel / mg**	**MM; L CuBr; CuBr$_2$**	**S / ml**	**time / h; min**	**yield / g**	**l_b / nm**
inner	EMA	0.34	3; 0.1; 8; 92	14	4; 45	0.9	34
outer	^{13}C-EMA	0.17	1.5; 0.05; 7; 51	7	4	0.12	3

can be found in Table 4.4. A brush length $l_{b(DLS)}$ of 35 nm was obtained for the PEMA-block. The bigger PEMA-block was a result of the prolonged reaction time, compared to the first experiment. The ^{13}C-PEMA block was smaller again and a brush length of $l_{b(DLS)}$ of 3 nm was obtained.

A scattering in the DLS data (Fig. 4.16) was obvious, which could be an indication of irregular shape of the particles as a result of a decrease in grafting density. Judging from the bond dissociation energy ($iodo < bromo < chloro$) of the leaving group, one can come to the conclusion that elimination of a bromo group from the dormant chain end is more likely to occur than loss of a chloro group. Dormant chain without an endgroup cannot be reinitiated by the addition of monomer. Chains that cannot be reinitiated lead to a decrease in grafting density, which was most likely the reason for the small brush length of the second block.

CuCl-based systems seem to be much more suitable for the preparation of block copolymers. The slower activation of C-Cl leads to a lower rate of propagation with respect to the rate of initiation and thus an increased initiation efficiency from the macroinitiator, as discussed in Section 2.1.1. The reaction details for the polymerization of each "block" relying on the CuCl/CuCl$_2$-system can be found in Table 4.5.

A brush length $l_{b(DLS)}$ of 13 nm was obtained for the PEMA-block. The PEMA-block prepared with the CuCl/CuCl$_2$-system was thus smaller compared to the one prepared with the CuBr/CuBr$_2$-system (34 nm, Table 4.4), although less deactivator (CuCl$_2$) was added and similar reaction conditions were deployed. The reason for this decrease in PEMA-block length was the

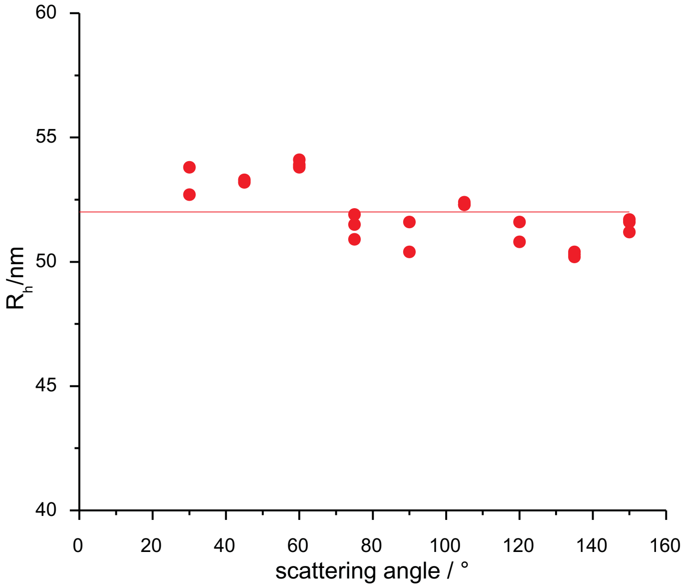

Fig. 4.16: Dynamic light scattering data of μ-gel-g-PEMA-b-^{13}C-PEMA particles prepared by SI-ATRP using the CuBr/CuBr$_2$-system. The solid line is indicating the average value.

Table 4.5: Synthesis conditions for μ-gel-g-PEMA-b-^{13}C-PEMA (Fig. 4.15 (I)) nanoparticles with outer shell of ^{13}C-PEMA - CuCl/CuCl$_2$-system. (MM ≡ monomer (in ml); Cu(I)Cl in mg; Cu(II)Cl$_2$ in mg; L ≡ ligand/PMDETA (in ml); S ≡ solvent/toluene; l_b ≡ brush length of the "block" calculated from DLS-data using Eq. 4.5)

region	**MM-type**	**μgel / mg**	**MM; L CuCl; CuCl$_2$**	**S / ml**	**time / h; min**	**yield / g**	**l_b / nm**
inner	EMA	0.34	3; 0.1; 6; 59	14	4; 30	0.5	13
outer	^{13}C-EMA	0.17	1.5; 0.05; 5; 28	7	4; 50	0.23	28

Table 4.6: Synthesis conditions for μ-gel-g-^{13}C-PEMA-b-PEMA (Fig. 4.15 (II)) nanoparticles with inner shell of ^{13}C-PEMA - CuCl/CuCl$_2$-system. (MM ≡ monomer (in ml); Cu(I)Cl in mg; Cu(II)Cl$_2$ in mg; L ≡ ligand/PMDETA (in ml); S ≡ solvent/toluene; l_b ≡ brush length of the "block" calculated from DLS-data using Eq. 4.5)

region	**MM-type**	**μgel / mg**	**MM; L CuCl; CuCl$_2$**	**S / ml**	**time / h; min**	**yield / g**	**l_b / nm**
inner	^{13}C-EMA	0.4	1.5; 0.1; 7; 59	20	0; 15	0.38	11
outer	EMA	0.17	1.5; 0.05; 5; 28	6	5; 10	0.31	33

slower rate of propagation associated with CuCl-based systems. The increase in initiation efficiency expected for CuCl-based macroinitiators led to a second block composed of ^{13}C-PEMA with a brush length of $l_{b(DLS)}$ of 28 nm. The μ-gel-g-PEMA-b-^{13}C-PEMA nanoparticles with an outer shell of 28 nm ^{13}C-PEMA prepared via the CuCl/CuCl$_2$-system are ideal for studying the extended conformations of the part of the chains near the fringe.

The next synthetic task was to polymerize the μgel nanoparticles with EMA of 20% carboxylic ^{13}C carbon content under ATRP-conditions and to reinitiate the chains in a second ATRP-polymerization with "regular" EMA. This synthetic pathway is depicted in Fig. 4.15 (II). The reaction details for the polymerization of each "block" relying on the CuCl/CuCl$_2$-system can be found in Table 4.6.

A brush length $l_{b(DLS)}$ of 11 nm was obtained for the ^{13}C-PEMA block. The ^{13}C-PEMA-block was thus smaller compared to the PEMA-block prepared for the μ-gel-g-PEMA-b-^{13}C-PEMA nanoparticles (13 nm, Table 4.5). The decrease in monomer content must have been the reason for the smaller ^{13}C-PEMA-block length, besides the shorter reaction time.

The second block composed of PEMA had a brush length of $l_{b(DLS)}$ of 33 nm. The μ-gel-g-^{13}C-PEMA-b-PEMA nanoparticles with an inner shell of 11 nm ^{13}C-PEMA prepared via the CuCl/CuCl$_2$-system are ideal for studying the extended conformations of the part of the chains near the surface that experience the strongest stretching.

PEMA-functionalized nanoparticles with a middle part composed of ^{13}C-PEMA would require a synthetic procedure as depicted in Fig. 4.15 (III). The synthetic procedure resembles a procedure one would take in order to produce a triblock copolymer on the μgel nanoparticles. The CuCl/CuCl$_2$-system should be suitable to produce a PEMA-b-^{13}C-PEMA-b-PEMA "triblock copolymer" on the μgel nanoparticles in the future.

Three synthetic procedures were developed in order to produce particles with PEMA brushes that were enriched with ^{13}C in selected regions. Two of these synthetic procedures were successfully carried out the produced particles are currently measured by Cornelius Friedrichs. The presented work was conducted as part of the SPP1369 Priority Program (Polymer-Solid Contacts: Interfaces and Interphases) funded by the DFG. Preliminary results of the NMR measurements provide evidence that the dynamics of the chains are slowed down with decreasing distance to the surface. More data needs to required though in order to be able to draw reliable conclusions.

4.3 Controlling the grafting density

Thus far μ-gel-g-PEMA particles with a grafting density of $\Gamma = 0.7\ chains * nm^{-2}$ and dispersions of these particles in homopolymers with varying molecular weight were investigated (Section 4.1). The grafting density has a strong influence on the dispersion behavior, as Smith et al. [261] found out using molecular dynamics simulations. These simulations revealed that relatively sparse grafting is enough to create repulsive interactions between nanoparticles in a polymer matrix. The repulsive interactions between the nanoparticles are dominating the brush matrix repulsion that sets in once the matrix chain length exceeds the length of the brushes, leading to a dispersion even in the case of long matrix chains.

Control over the grafting density can be achieved by immobilizing a lower amount of ATRP-initiator molecules on the surface of the μgel particles during the synthesis (see Section 4.1.6). This would require a new synthesis of μgel particles for each desired grafting density, which would be rather time consuming.

In Section 3.1 of this thesis it was demonstrated that the saponification of surface-immobilized ATRP initiators containing an ester bond is possible.

One would expect this approach to be applicable not only to ATRP initiators on silicon wafers, but also to ATRP initiators on the μgel nanoparticles, as long as the initiator molecules contain an ester bond. The advantage of saponification-approach could be seen in the fact that a batch of particles could be synthesized and modified in a second step. Thus one would receive particles with the exact same core size and different coverage with ATRP initiator molecules.

The challenge from a synthetic point of view was to bring the nanoparticles into contact with diluted sulfuric acid in order to let the saponification reaction proceed. The use of a phase transfer catalyst was the solution to this problem. Saponification was accomplished adapting the procedure described in Section 4.1.6 for the cleavage of the the grafted PEMA-chains from the μ-gel-g-PEMA particles. 150 mg of the μgel particles, that had also been used for the study of the dispersion behavior in Section 4.1, were mixed with 10 ml of toluene in a poly(ethylene) flask. Dispersion of the particles was achieved by 10 min of ultrasonication and 5 min of vigorously stirring. 50 mg of the phase transfer catalyst Aliquat 336 (Alfa-Aesar) was added and the stirring continued for another 5 min. 10 ml of 1 mol/L H_2SO_4 were added and the mixture was stirred for a preset time interval of 3, 6, 10, 25 or 60 min in order to let the saponification proceed. Stirring was stopped and the aqueous layer was allowed to separate from the organic layer. The aqueous layer was removed in a separatory funnel and the organic layer was concentrated under reduced pressure subsequently. The μgel particles were precipitated in 20 ml of MeOH and a centrifuge (4000 rpm; 10 min) was used to separate the particles. Excess MeOH was decanted, the remaining particles redispersed in 2 ml of toluene and the particles precipitated again. This procedure was repeated two more times to remove the phase transfer catalyst. 120 mg of modified particles were thus obtained on average, after drying for 12 h in vacuum.

SI-ATRP was conducted on all samples of modified μgel nanoparticles using MMA as described in Section 4.1.6. The reaction details were the same for all samples and can be found in Table 4.7.

350 mg μ-gel-g-PMMA particles were obtained on average after SI-ATRP. The increase in mass was seen as a first indication that the polymerization had

Table 4.7: Synthesis conditions for μ-gel-g-PEMA particles with varying grafting density. (MMA (in ml); Cu(I)Br in mg; Cu(II)Br_2 in mg; L ≡ ligand/PMDETA (in ml))

μgel / mg	MMA; L CuBr; $CuBr_2$	toluene / ml	reaction time / h; min
0.1	5; 0.1; 10; 50	10	4; 0

(I) 3 min

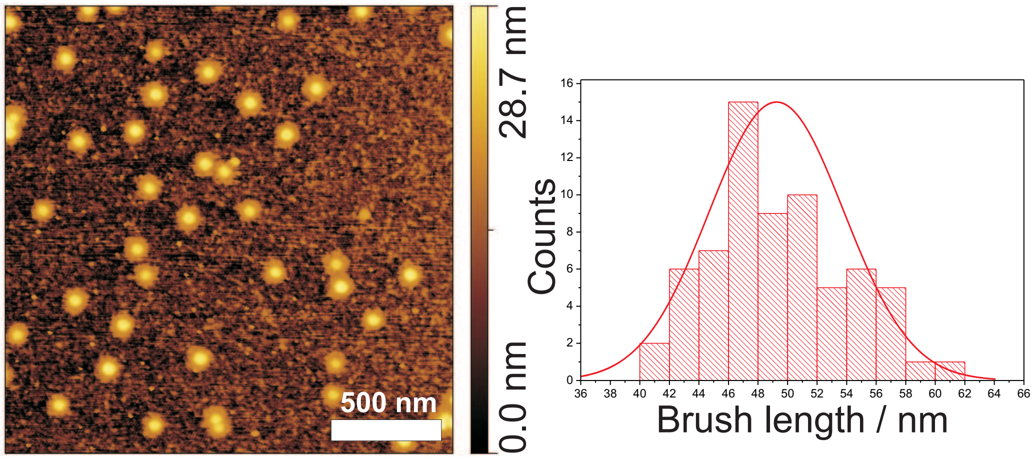

(II) 25 min

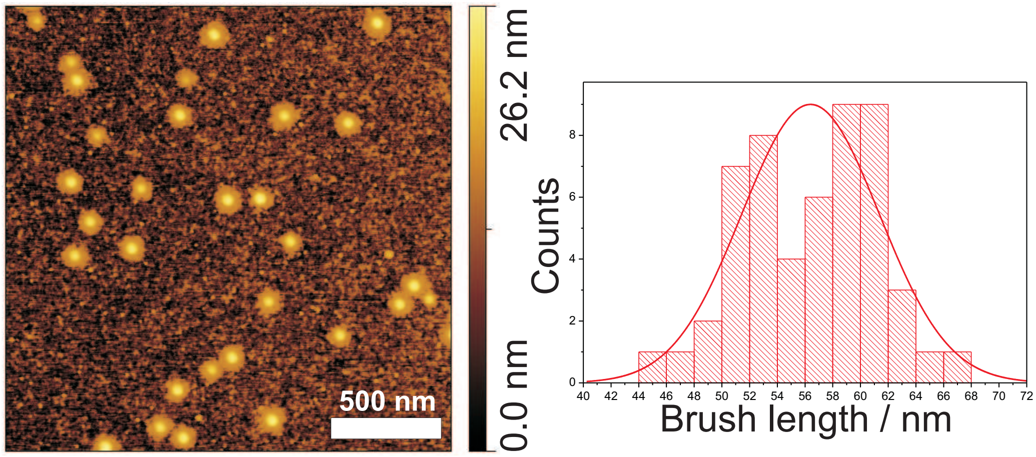

Fig. 4.17: (I) Topography image of μ-gel-g-PMMA particles and histogram indicating the PMMA brush length. Particles had been in contact with 1 mol/L H_2SO_4 for 3 min prior to polymerization. (II) Topography image of μ-gel-g-PMMA particles and histogram indicating the PMMA brush length. Particles had been in contact with 1 mol/L H_2SO_4 for 25 min prior to polymerization.

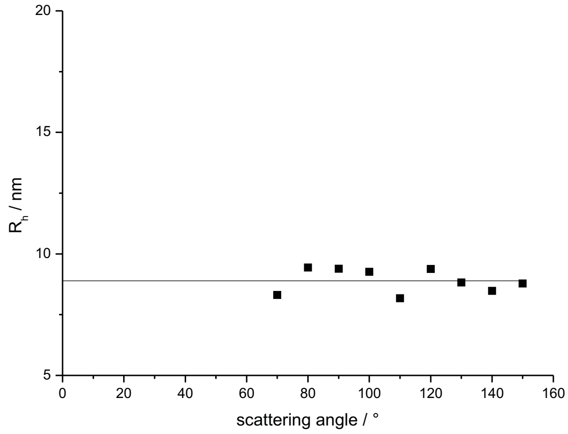

Fig. 4.18: Dynamic light scattering data of μgel particles functionalized with the tertiary initiator. The solid line is indicating the average value obtained from five different scattering angles.

been successful. Reliable DLS data could not be obtained however, due to the low scattering intensity of all samples.

SPM measurements were conducted and revealed that there was a shell of PMMA surrounding the μgel cores. In Fig. 4.17 (left) are two topography images shown of particles that had been in contact with acid for 3 min prior to polymerization (I) and 25 min (II), respectively.

More than 100 μgel particles were analyzed and a Gaussian distribution was fitted to the histogram of the brush length distribution, as shown on the right in Fig. 4.17. The maximum of the fit was at 49 *nm* for 3 min contact time and 56 *nm* for 25 min contact time. An increase in contact time seems to lead to an increase in brush length. All other samples were in support of this trend. An explanation could be that with increasing contact time more initiator molecules are destroyed. Less initiator molecules lead to higher molecular weight brushes, because there is more monomer available for the remaining initiators. The results can be seen as first evidence that stirring μgel macroinitiators with sulfuric acid leads to changes in grafting density. The challenge, however, is to detect these changes in grafting density.

If the changes in grafting density were bigger, analysis would become easier. One way to accomplish this could be the use of an ATRP-initiator with a more labile ester bond. The novel initiator, presented in Section 3.1 derived from a tertiary alcohol is such an initiator with a more labile ester bond. μgel particles decorated with the tertiary initiator were synthesized according to the procedure described in Section 4.1.6. The exact same amounts of reagents were used and ATRP-Et and ATRP-Cl derived from a tertiary alcohol were deployed. DLS measurements (Fig. 4.18) revealed that the hydrodynamic radius $R_{h(\mu gel)}$ was slightly smaller with 9 nm in the case of the tertiary initiator compared to the particles with primary initiator (14 nm). These μgel particles decorated with tertiary initiator have not been treated with sulfuric acid to date.

A synthetic protocol has been developed that allows to prepare with varying grafting density without dealing with a new synthesis for each desired grafting density. A batch of particles can be synthesized and modified in a second step. The characterization of the particles with varying grafting density is a challenge however and more work is required.

The particles with varying grafting density would allow an investigation of the influence of the grafting density on the dispersion behavior. Mixtures with matrix chains of varying molecular weight should be prepared and should be checked for the matrix molecular weight where phase separation occurs.

4.4 Comparison of brush length on curved and flat substrates

A series of polymerizations using EMA were conducted in the presence of ATRP-initiator functionalized silicon wafers, for a comparison of brush length on curved and flat substrates. The silicon wafers were cleaned and functionalized with the primary initiator according to the procedures described in Section 3.1.17. The reaction details, the molecular weights and film thickness can be found in Table 4.8. Free PEMA with molecular weight of up to M_n = 157000 g/mol and narrow molecular weight distribution was produced. The molecular weight was measured using GPC, as described in Section 7.4. Several samples were measured with light scattering additionally. A deviation in molecular weights obtained by the two methods was observed. The biggest deviation was found for the sample with M_n = 152.5k g/mol in GPC (M_w = 201.3k g/mol). Light scattering gave a molecular weight of M_w = 225.7k g/mol. More experiments would be necessary to draw a reliable conclusion from this observation.

The corresponding film thickness were measured with ellipsometry, as described in Section 7.2. Several samples were measured with X-ray reflectivity (see Section 7.3) additionally (72.2k - 25.7 nm; 83.1k - 32.8 nm; 152.5k - 62.4 nm) and the reflectivity data gave higher film thicknesses in each case. The biggest deviation was found for the samples with high molecular weight brushes. X-ray reflectivity is a more accurate method compared to ellipsometry. Data treatment in X-ray reflectivity does not require to make assumptions concerning the refractive index of the brushes (1.49), as in ellipsometry. The increase in the deviation between the two methods with increasing molecular weight can be a hint that the refractive index is changing with increasing film thickness. More experiments would be necessary to clarify this.

A plot of film thickness measured via ellipsometry versus molecular weight from GPC is shown in Fig. 4.19. The PEMA that was cleaved from the μ-gel-g-PEMA particles by dissolving the core with diluted HF had a number average molecular weight of M_n = 26100 g/mol. This molecular weight is indicated by the dashed black line. PEMA brushes on a silicon wafer with the exact same molecular weight as the one on the particles would have a thickness of 8.8 nm. This length of the brushes on the silicon wafer is within the error of the brush thickness measured by SPM and GISAXS of $l_{b(SPM,assembly)} = 10 \pm 5\ nm$ and ($l_{b(GISAXS)} = 11.5 \pm 10\ nm$) on the μ-gel-g-PEMA particles.

One might have expected a shorter brush length in the case of the μ-gel-g-PEMA particles. The volume accessible to the individual chains is growing as the distance from the grafting site increases (see Section 2.2.3) in the case of a curved substrate. Crowding, and thus stretching, of the chains becomes less severe, as a result. Chances are that this effect due to curvature is balanced by the difference in grafting density on the particles and the wafers. The PEMA chains on the μ-gel-g-PEMA particles are attached at a grafting

Table 4.8: Synthesis conditions and film thickness *d* for PEMA-brushes on silicon wafers. 10 ml anisole and EMA were used for each polymerization. I and L were employed 1:1. (L ≡ ligand/PMDETA; I ≡ initiator/2-EiBBr)

d / nm	**CuBr / mmol**	**$CuBr_2$ / mmol**	**L; I / mmol**	**time / h**	**M_n / $g * mol^{-1}$**	**PDI / $M_w * M_n^{-1}$**
3.5	0.183	1.12	1.30	22	9.8k	1.2
5.1	0.183	0.548	0.730	24	15.3k	1.1
6.2	0.122	-	0.122	24	21.9k	1.1
9.2	0.183	0.183	0.365	24	25.2k	1.2
13.2	0.0913	-	0.0913	24	43.5k	1.1
12.7	0.0609	-	0.0609	72	46.2k	1.1
19	0.183	-	0.183	24	56.2k	1.4
25.1	0.0913	-	0.0913	24	62.4k	1.2
22.7	0.122	-	0.122	24	72.2k	1.2
30.5	0.0913	-	0.0913	27	83.1k	1.2
38.3	0.0609	-	0.0609	48	110k	1.3
54.7	0.0475	-	0.0475	70	152.5k	1.3
47.2	0.0475	-	0.0475	48	157k	1.3

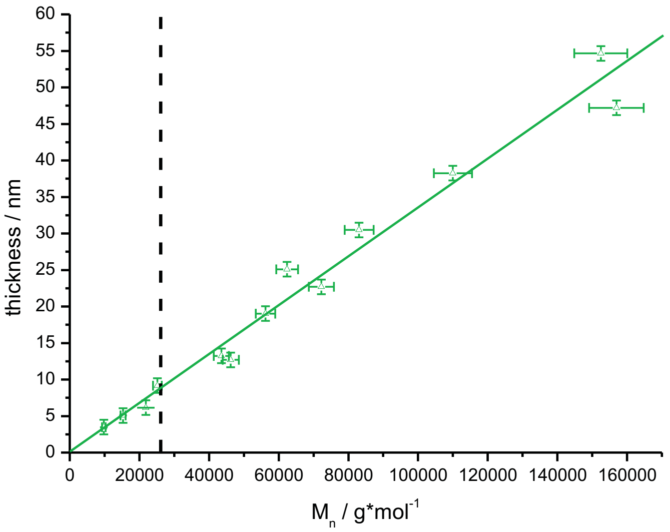

Fig. 4.19: Correlation of PEMA film thickness with the molecular weight M_n of free PMMA produced by the sacrificial initiator in solution. The solid green line shows the linear fit. The dashed black line indicates the molecular weight of the PEMA brushes on the *μ*-gel-g-PEMA used in Section 4.1.

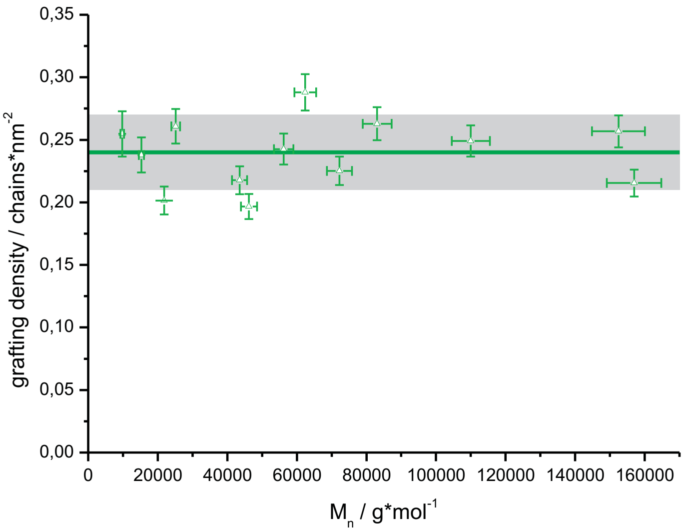

Fig. 4.20: Correlation of the calculated grafting density with the molecular weight M_n of free PEMA produced by the sacrifical initiator in solution. The solid line is indicating the average grafting density. The shaded region is related to the standard deviation from the average value.

density of $\Gamma = 0.7\ chains * nm^{-2}$, whereas the PEMA chains on the silicon wafers are attached at an average grafting density of 0.24 ± 0.03 chains/nm^2. The average value for the grafting density on the silicon wafers was obtained from Fig. 4.20 (green solid line). The shaded regions are related to the standard deviation from this average value.

A comparison of the results obtained for the grafting from of MMA on silicon wafers (Section 3.1.15) to the results obtained for MMA show that the SI-ATRP of EMA proceeds in a controlled fashion, both on the surface and in solution. A linear dependency of film thickness on M_n is found in the case of EMA. The slope in the plot of film thickness vs M_n is comparable for both monomers and thus also growth rate (slope^{-1}). The M_n has to increase by roughly 3000 g/mol for increase in film thickness of 1 nm in the case of EMA and for MMA a value of 2600 g/mol per 1 nm had been found. The average value of grafting density is comparable for both monomers, additionally. Whereas a value of 0.24 ± 0.03 chains/nm^2 was found for EMA, the value for MMA was slightly higher at 0.26 ± 0.04 chains/nm^2.

The polymerization of EMA and MMA proceeds in a similar fashion on flat silicon substrates using SI-ATRP. The grafting density for both monomers was comparable, as well as the growth rate.

The polymerization of EMA on flat and curved substrates yields brushes of similar length, which comes as a surprise. The effect of curvature seems not to play a dominant role. It seems that the effect of curvature is balanced by the difference in grafting density on the particles and the wafers.

5 ”Grafting to” - Fullerenes on flat substrates

5.1 Active ester chemistry in grafting to of fullerenes

5.1.1 Introduction

* The unique properties of the Buckminsterfullerene (C_{60}), which became available in macroscopic amounts of sufficient purity in 1990 [262], have attracted the interest of researchers worldwide. A variety of outstanding conducting [263], magnetic [264], electrochemical [265], and electrical properties [266] have been discovered. The described properties can be utilized directly, but the versatility of the fullerene system is limited by the poor processability.

One way to enhance the versatility is the covalent functionalization of C_{60}. A rich covalent fullerene chemistry has been developed to date, as these reviews demonstrate [267,268]. Materials with biological activity [269] or non-linear optical properties have thus become available [270].

The chemistry developed for the covalent functionalization of C_{60} has paved the way for the synthesis of polymeric fullerene materials. A combination of polymers and fullerenes offers the following advantages:

- The properties of C_{60} can be combined with those of polymers, which have outstanding physicomechanical properties.

---

[*] The active ester polymer used in this Section was supplied by Daniel Kessler from the group of PD Dr. Patrick Theato; University of Mainz.

- Polymeric fullerene materials should be characterized by their superior processability and should enable spin-coating, solvent-casting and melt extrusion.
- Surface-bound polymeric fullerene materials should have unique electronic, optical and catalytic properties.

The synthesis of such polymeric fullerene materials, however proved to be challenging. Three approaches have been developed to date. The predominant approach is based on the reaction of a side-chain of the preformed polymer with functionalized C_{60} molecules. Polymer molecules with pendant fullerene molecules ((1) *on-chain*) have thus been maintained [271–274]. A drawback of this approach can be the complexity of the synthesis required and the limited choice of polymers. The second approach is based on the polymerization of a monomer in the presence of C_{60} molecules. Fullerene units have thus been incorporated into the backbone ((2) *in-chain*) of polymers [275–277]. Multiaddition to the fullerene molecules cannot be avoided completely and microgel particles [278] or cross-linked, insoluble networks can be formed. The third approach (3) is a combination of both the above. Functionalized C_{60} molecules are tagged to vinyl monomers which are subsequently polymerized [279]. Reaction between the growing radicals and the fullerene nucleus can lead to crosslinking.

Whereas the fabrication of polymeric fullerene materials has excelled, as the discussion demonstrates, little is known about the synthesis and properties of surface-attached polymeric fullerene materials. Bergbreiter et al. [280] succeeded in grafting C_{60} to a polyethylene surface. The polyethylene surface with terminal diphenylmethyl groups was deprotonated with butyllithium and fullerenes reacted with the anions formed on the surface. Remaining anions were subsequently quenched with MeOH.

The focus of this part of the thesis is on the preparation of grafted polymeric fullerene materials. The synthetic pathway that was selected relies on active ester chemistry. Active ester chemistry is a basic principle in peptide synthesis [281]. A carbonyl group can be activated by transforming it into an active ester. Nucleophilic displacement at the carbonyl group is thus facilitated, as depicted in Fig. 5.1. The carbonyl group (red) in the amino acid

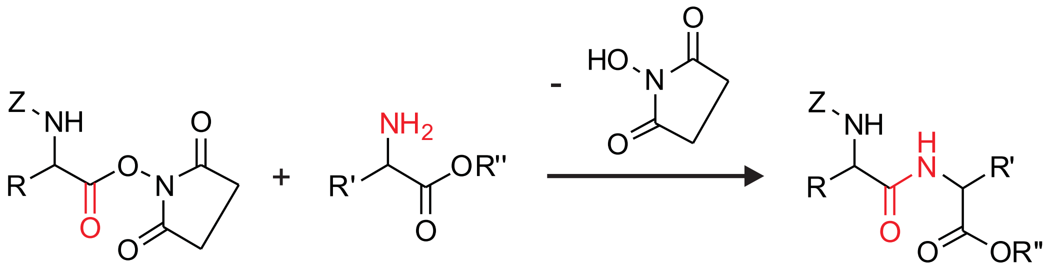

Fig. 5.1: Active ester chemistry facilitates the coupling of two amino acids by activation of the carbonyl group.

with the Z-protected amino-group and the R moiety was activated through coupling with N-hydroxysuccinimide. The nucleophilic attack of the amino-group (red) in the amino acid with the R″-protected carboxyl group and the R′ moiety is facilitated by this activation. N-hydroxysuccinimide is displaced and a new peptide bond is formed (red).

Batz et al. were the first to transfer the concept of active ester chemistry to polymers [282]. Active ester polymers were prepared and proved to be excellent precursors for functional polymers with pharmacological activity, for example. The reaction of active ester polymers with amines is usually quantitative and side reactions are seldom observed. Mild conditions, such as stirring at room temperature are sufficient to facilitate the reaction with amines. After these early observations of Batz et al. active ester chemistry has played a minor role owing to the popularity of the 1,3-dipolar cycloadditions (*click* reactions). Active ester chemistry has recently resurfaced, due to the efforts of Theato et al [283–289]. Theato et al. succeeded in preparing functional polymers that had not been accessible directly by polymerization of the respective acrylamide monomers via the reaction of active ester polymers with various amines (Fig. 5.2. The advantage of active ester chemistry over 1,3-dipolar cycloadditions is that no metal catalyst is required and thus no residue of this catalyst can contaminate the prepared materials.

The styrene derivate, poly(pentafluorophenyl 4-vinylbenzoate) was selected as the active ester polymer for this study, because the polymer exhibits a combination of the excellent properties of poly(styrene) with the functionaliza-

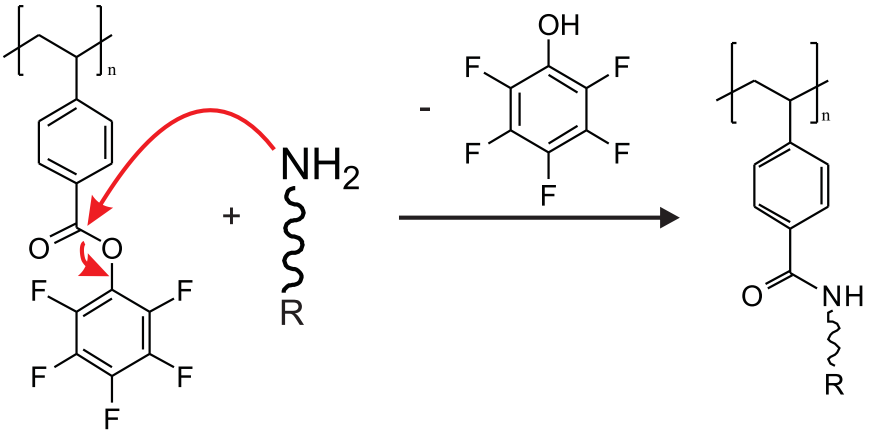

Fig. 5.2: Reaction between the active ester polymer poly(pentafluorophenyl 4-vinylbenzoate) and an amine yielding a functional polymer carrying R side chains.

tion flexibility of an active ester. The solubility in a variety of organic solvents compared to poly(N-hydroxysuccinimide acrylates) and the low tendency for hydrolysis are additional advantages of the selected active ester polymer [290].

The reaction between poly(pentafluorophenyl 4-vinylbenzoate) and amines proceeded quantitatively, as discussed above. The synthetic task was thus to prepare amino-functionalized surfaces, graft the polymer on these surfaces covalently through the formation of amide bonds. Unreacted active ester groups should remain on these polymer-grafted surfaces and reactions with amino-functionalized fullerenes should be feasible. Such surfaces should exhibit a combination of the unique properties of the fullerenes with the excellent physicomechanical properties of poly(styrene). These surfaces should additionally be stable under hostile conditions due to the covalent amide bonds formed between the constituents.

5.1.2 Results and Discussion

Preparation of amino-functionalized silicon surfaces

The functionalization of silicon wafers and glass slides with amino-groups was the first step towards grafted polymeric fullerene materials. Amino-

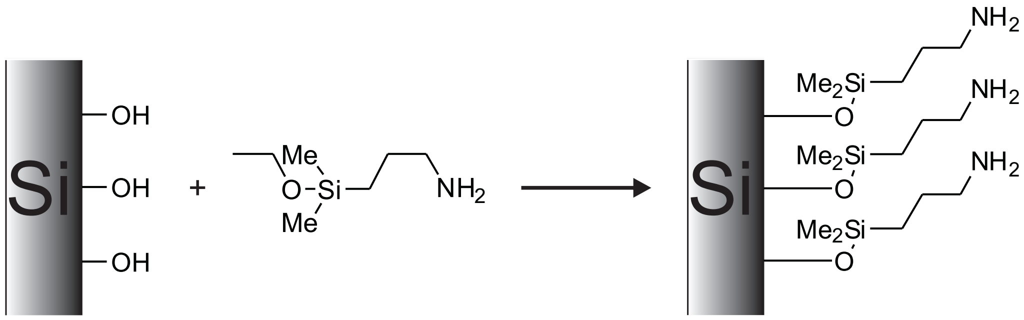

Fig. 5.3: Immobilization of 3-aminopropyldimethylethoxysilane on silicon substrates leads to surfaces functionalized with amino-groups.

propylethoxysilanes are suitable for the functionalization of silicon substrates with amino-groups. A stable Si-O-Si bond is formed between an ethoxy moiety and the surface hydroxyl groups covalently anchoring the aminosilane on the surface with the amino-group extending from the surface.

The functionalization of silicon substrates with the commonly employed 3-aminopropyltriethoxsilane (APTES) using organic solvents suffered from a lack of reproducibility, however. The quality of the prepared films depended strongly on the deposition conditions, such as silane concentration, water content of the solvent and postcuring. Significant differences in the thickness of the silane layer were observed using APTES in organic solvents, because the silane formed a 3D network on the surface. The origin of these differences was the competition between self-polymerization occurring with water and surface reactions.

Self-polymerization can be avoided however if water is excluded. Trace quantities of water contaminate all organic solvents. The use of organic solvents can be avoided and thus removal of water can be accomplished using gas-phase reactions. 3-Aminopropyldimethylethoxysilane has a sufficient vapor pressure and was thus chosen for the amino-functionalization of silicon substrates, as depicted in Fig. 5.3. The exact procedure and the reaction conditions can be found in Section 5.1.3. Static contact angle measurements using water on glass slides gave a contact angle of 6 ± 1 degrees before the gas-phase silanization and 70 ± 4 degrees afterwards. Kanan et al. reported a

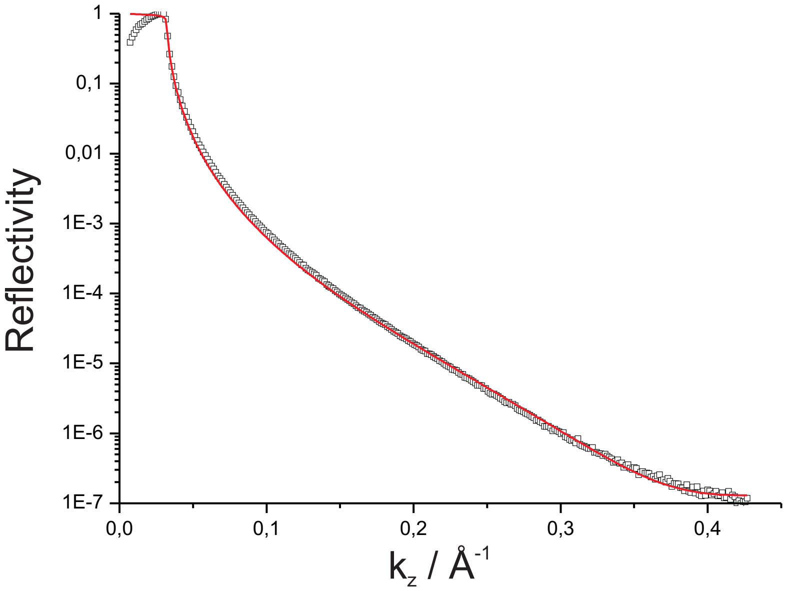

Fig. 5.4: Representative X-ray reflectivity profile and corresponding fit (red solid line) of silicon wafer after functionalization with 3-aminopropyldimethylethoxysilane.

contact angle of 68 ± 1.9 degrees [291] for glass slides treated with APDMES, which is within the error of our observation. The silane layer thickness on a silicon wafer was measured with X-ray reflectivity. A thickness of 8.6$\AA$ and roughness of 1.6$\AA$ were obtained. A maximum silane layer thickness of 9$\AA$ was estimated assuming an all-trans conformation of all bonds. The estimated maximum layer thickness is in agreement with the experimental data. A gas-phase reaction using APDMES is thus useable to functionalize silicon substrates with amino-groups.

Preparation and Characterization of Poly(pentafluorophenyl 4-vinylbenzoate)

The monomer pentafluorophenyl 4-vinylbenzoate was synthesized according to the procedure described in Section 5.1.3 and characterized using ^{1}H NMR, ^{1}3C NMR and ^{1}9F NMR. The active ester polymer poly(pentafluorophenyl 4-vinylbenzoate) was synthesized by Daniel Kessler (Group of PD Dr. Patrick Theato; University Mainz) as shown in Fig. 5.5 and characterized

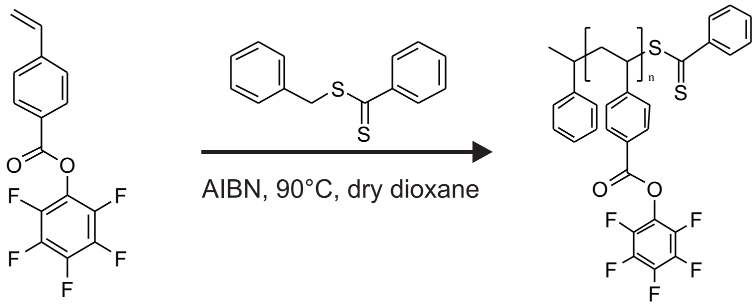

Fig. 5.5: RAFT polymerization of pentafluorophenyl 4-vinylbenzoate.

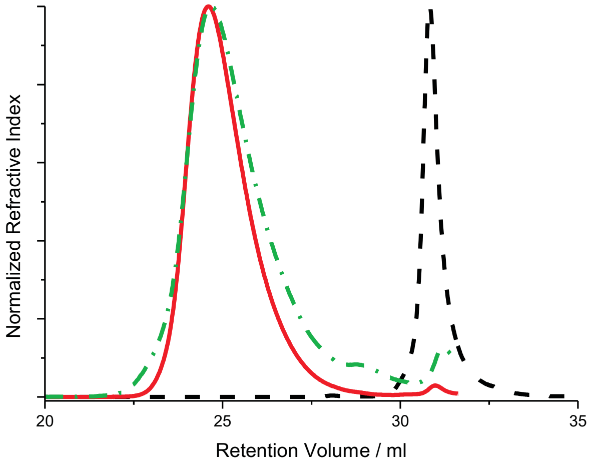

Fig. 5.6: GPC-results for the monomer PFPVB (black dashed line), the polymer PPFPVB (red solid line), and the fullerene-functionalized PPFPVB (green dash-dotted line).

using ^{1}H NMR and ^{1}9F NMR (see Section 5.1.3).

The active ester polymer had a M_n = 6500 g/mol and a polydispersity of 1.64. The corresponding elution diagrams of the monomer PFPVB (black dashed line) and the polymer poly(pentafluorophenyl 4-vinylbenzoate) (red solid line) are depicted in Fig. 5.6.

A decrease in retention volume from 31 ml to 25 ml was observed after polymerization. A minute amount of monomer remained in the polymer after workup, as the small peak in the red solid curve at higher retention volume demonstrates. The retention volume of this small peak is comparable to that of the monomer.

Synthesis of the amino-functionalized C_{60}-Fullerene

The 3′H-cyclopropa[1,9][5,6]fullerene-$_{60}$-Ih-3′,3′-dicarboxylic acid 3-[[(1,1-dimethylethoxy)carbonyl]amino]propyl ethyl ester (Fig. 5.7) was synthesized according to Zakharian et al. [270]. However, it was opted to do the Bingel-Hirsch addition [292] with 1,8-diazabicyclo[5.4.0]undec-7-ene (DBU) and CBr_4.

The deprotection of the t-butoxycarbonyl-protected amino-group was carried out in the last step and the amino-functionalized fullerene recovered as trifluoroacetate salt. A detailed description of the procedure, reaction details and ^{1}H NMR data can be found in Section 5.1.3.

Preparation of Fullerene-funtionalized surfaces

Two preparation routines for the grafting to of fullerene molecules can be envisioned. The straightforward routine involves the grafting to of the PPFPVB on the amino-functionalized surface in a first step. The second step involves the grafting to of the amino-functionalized fullerenes on the grafted polymer. The routine is depicted in Fig. 5.8. The advantage of this routine can be seen in the fact that no workup is required between the individual steps, except for extraction of the wafers in a Soxhlett apparatus.

Solutions with PPFPVB-content of 25, 50, 80, 100 and 200 mg were used for the grafting to of the PPFPVB. A detailed description of the procedure can be found in Section 5.1.3. An increase in contact angle from 70 ± 4 degrees for the silanized surface to 80 ± 3 degrees was observed independent of the polymer content of the solution. Kessler et al. [285] observed a contact angle of 93 degrees for a grafted poly(pentafluorophenyl acrylate) polymer. The reason for this deviation in contact angles can be seen in the grafting density of the polymer layers. Kessler et al. studied a densely grafted polymer layer, whereas one can expect the grafting density to be rather low in the case of the grafting to of the PPFPVB.

The film thickness was measured via ellipsometry, assuming a refractive index of 1.55 for the polymer layer. The thin silane layer was neglected for these measurements. A film thickness of 2 nm was measured independent of

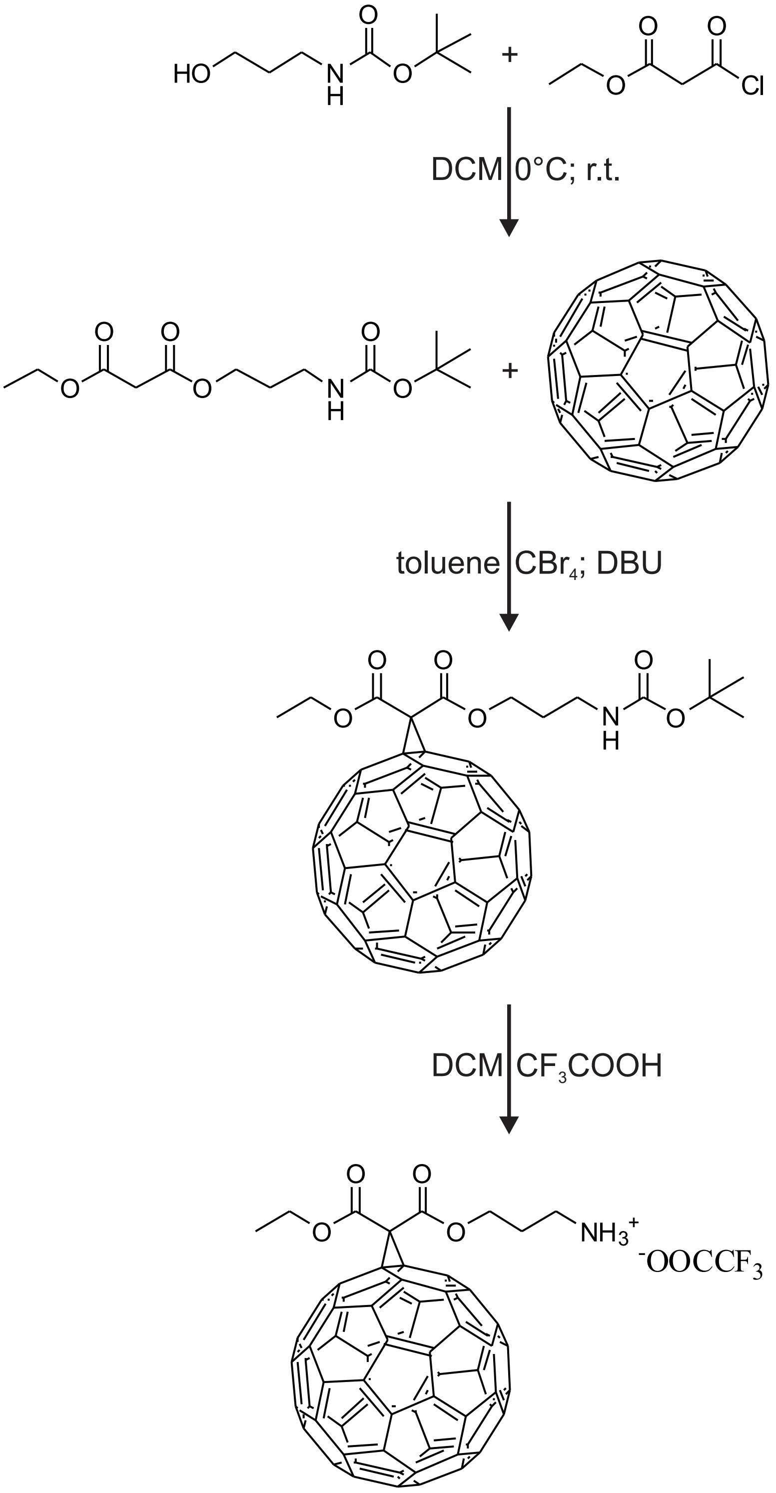

Fig. 5.7: Synthesis of functionalized C_{60} and deprotection of amino-group in the last step.

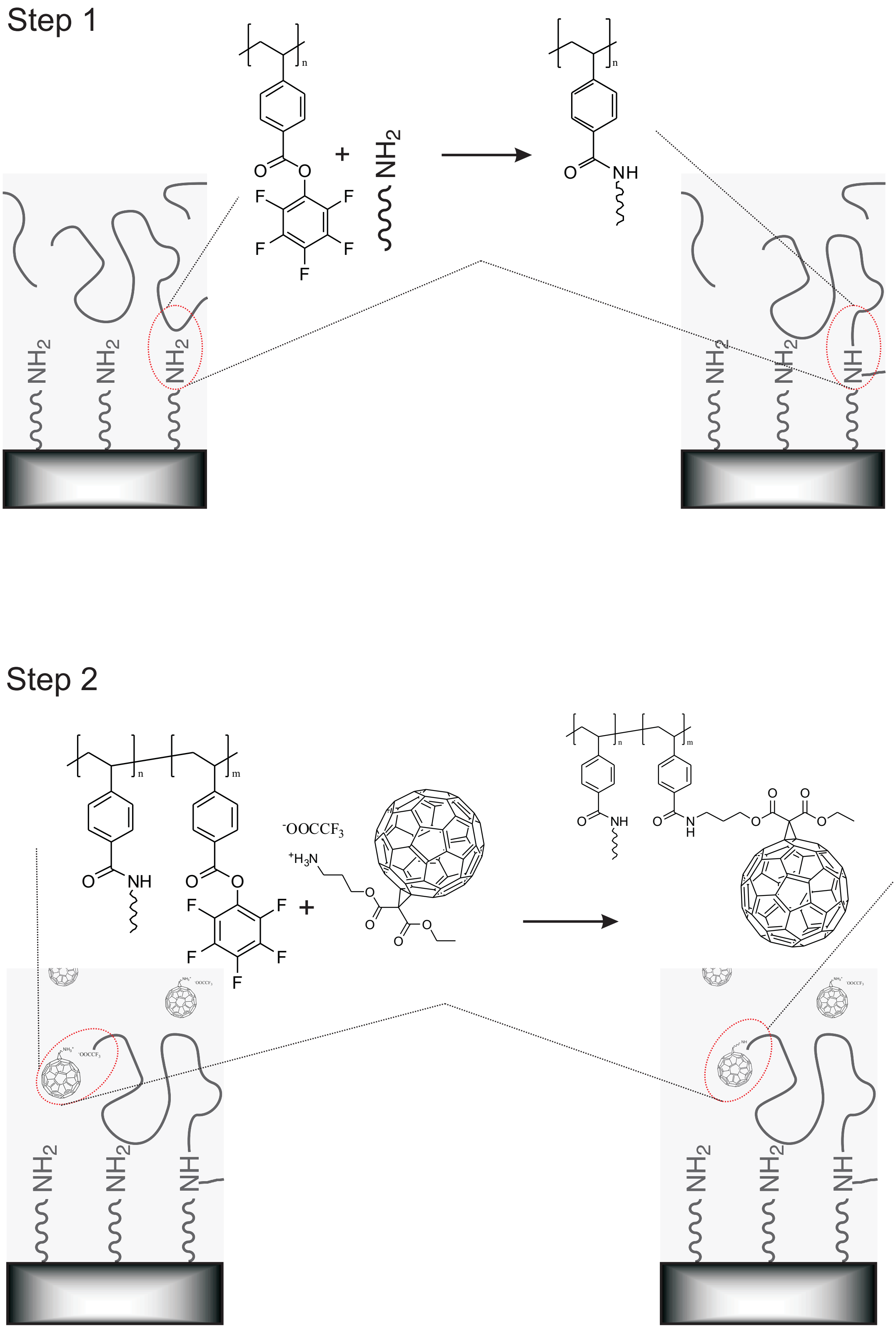

Fig. 5.8: Preparation routine 1 for fullerene-funtionalized surfaces.

the polymer content of the solution that had been used for the grafting to. Although this is just a rough estimate of the film thickness, 2 nm is an expectable value for a grafting to procedure (see discussion in Section 2.1.3). No change in film thickness was observed after treatment of the polymer functionalized wafers with ultrasound in DCM (5 min). The formation of an amide bond on the surface and on the polymer can be seen as the reason for this film stability.

Solutions with fullerene trifluoroacetate salt-content of 5, 10, 20, 25, 40, 50 and 95 mg were used for the grafting to of the fullerene on the polymer-functionalized surfaces. A detailed description of the procedure can be found in Section 5.1.3. No change in contact angle was observed for the fullerene-functionalized surfaces.

Gold electrodes were evaporated on these grafted polymeric fullerene films. The gold electrodes were 300 μm in size and were spaced 1 cm apart. A Yokogawa GS610 potentiostat was connected to these electrodes and the conductivity measured. None of the measured samples showed a detectable conductivity. The conductivity was also measured on a more microscopic level. Gold electrodes were evaporated on the grafted polymeric fullerene films through grids for transmission electrode microscopy. The electrodes were connected to a potentiostat using two needles. The shape of the IV-curves was independent of the polymer or fullerene content of the solution used for the preparation. A representative IV-curve is shown in Fig. 5.9. No significant conductivity was detected.

The second preparation routine is based on the reaction between the polymer and the fullerenes in solution. The second step involves the grafting to of the fullerene-functionalized polymer. The routine is depicted in Fig. 5.10. A workup of the fullerene-functionalized polymer is necessary before the grafting step, which can be seen as a drawback. The advantage of the routine is that the fullerene-functionalized polymer can be investigated before it is grafted.

The synthesis of the fullerene-functionalized polymer is depicted in Fig. 5.11. The reaction details can be found in Section 5.1.3. The fullerene trifluoroac-

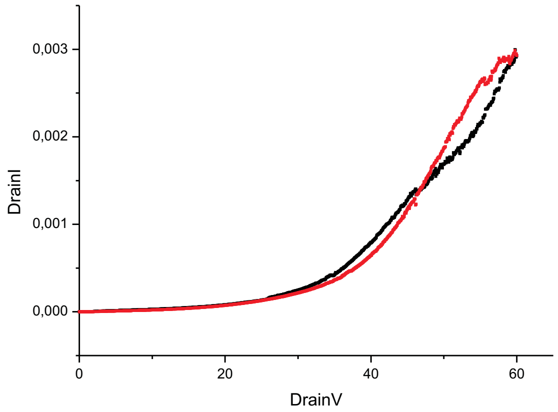

Fig. 5.9: Representative IV-curve of a grafted polymeric fullerene film. The voltage was ramped up (red) and down (black) 3 times.

etate salt is treated with TEA and a minute amount of fullerenes carrying free amino-group is generated. Rapid reaction between the amino-group and the active ester polymer occurs and an attack of the amino-group on fullerene double bonds is thus prevented. The fullerene-functionalized polymer was characterized using ^{1}H NMR (see Section 5.1.3), GPC and FT-IR. A broadening in polydispersity was observed after the functionalization, as the elugram in Fig. 5.6 (green dash-dotted line) demonstrates. No shift in retention volume was observed compared to the unfunctionalized PPFPVB (red curve).
The FT-IR spectra are shown in Fig. 5.12. The blue curve belongs to the active ester polymer poly(PPFPVB). The characteristic band of the active ester is the one of the carbonyl group at 1758 cm^{-1}. The characteristic band in the spectrum of the functionalized C_{60} belongs to the t-butoxycarbonyl-protected amino-group found at 1638 cm^{-1}. This amide band is present as a shoulder of the carbonyl band in the spectrum of the fullerene-functionalized PPFPVB. One can thus conclude that active ester groups were converted into amide groups after a nucleophilic attack of the amino-functionalized fullerene. The amide band in the spectrum of the fullerene-functionalized PPFPVB allows one to draw this conclusion. The carbonyl band is still present in the spectrum of the fullerene-functionalized PPFPVB, but has decreased in intensity to some extent. Thus one can draw the conclusion that only a fraction of ac-

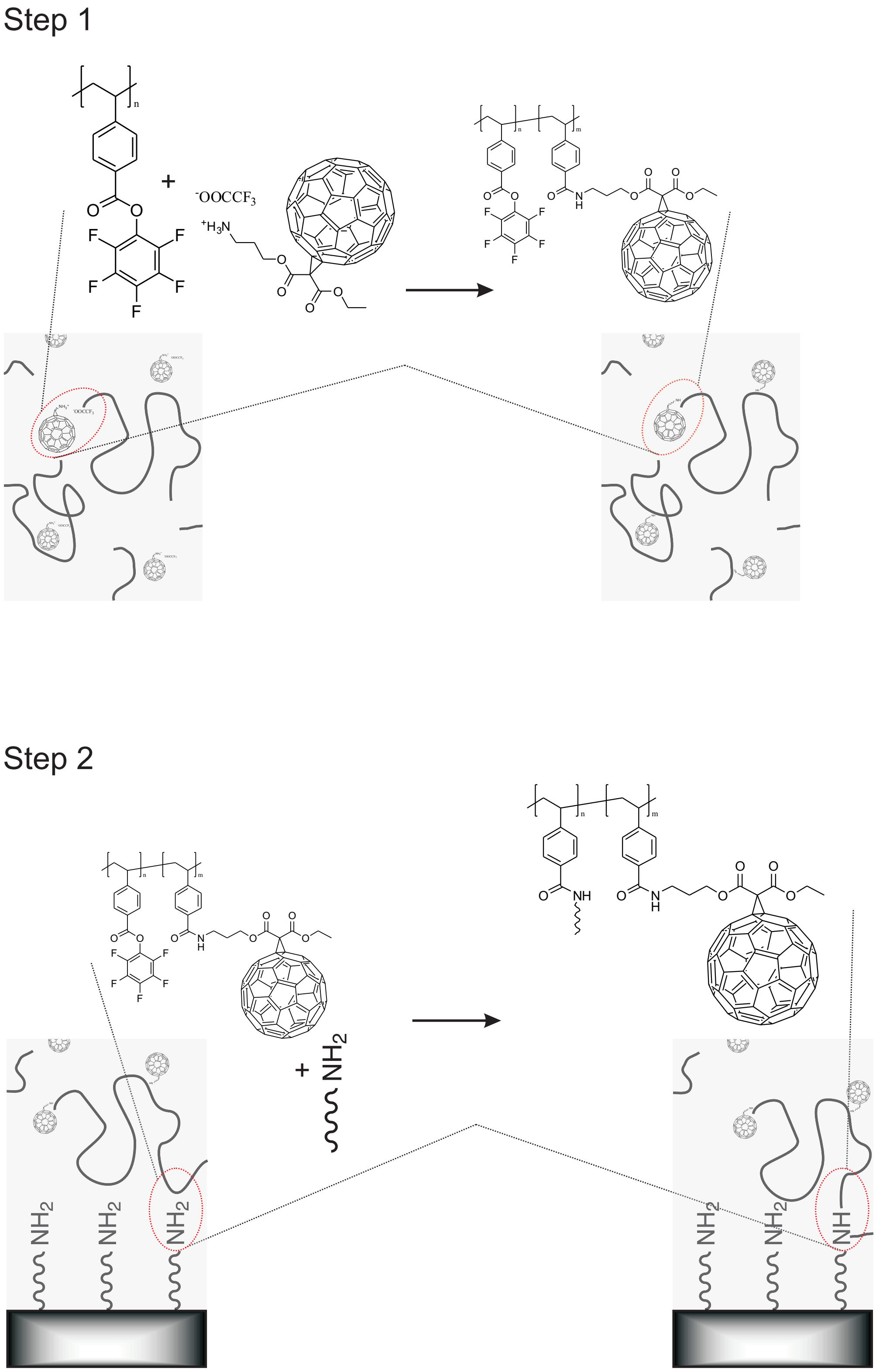

Fig. 5.10: Preparation routine 2 for fullerene-funtionalized surfaces.

tive ester groups was converted into amide groups.
The grafting of the fullerene-functionalized PPFPVB has not been attempted to date.

It has been demonstrated that active ester chemistry can be used to prepare polymeric fullerene materials and graft these materials covalently on amino-functionalized substrates. First attempts have been made to characterize these grafted polymer fullerene materials and to measure their properties. The presented data serve as a proof of concept. More reliable data need to acquired however in order to draw dependable conclusions.

5.1.3 Syntheses

All chemicals were commercially available and used as received, unless otherwise stated.

Immobilization of 3-Aminopropyldimethylethoxysilane

First step: Cleaning of silicon wafers/glass slides

The wafers/glass slides were cleaned and it was ensured that the silicon oxide was in a defined hydration state as described in Section 3.1.17.

Second step: Gas-phase silanization

The gas-phase reaction of (3-aminopropyl)dimethylethoxysilane (APDMES) on silicon wafers/glass slides was used to create surfaces functionalized with free aminopropyl groups. Moisture-free conditions are of importance in this step since APDMES is easily hydrolyzed. The wafers/glass slides were mounted in a modified Schlenk tube. The Schlenk tube was evacuated and purged with dry argon twice in order to remove any traces of water. 0.05 ml of APDMES was added to the tube in a dry argon counter flow. The tube was partially evacuated and placed in an oven for 12 h at 120 °C . The resulting

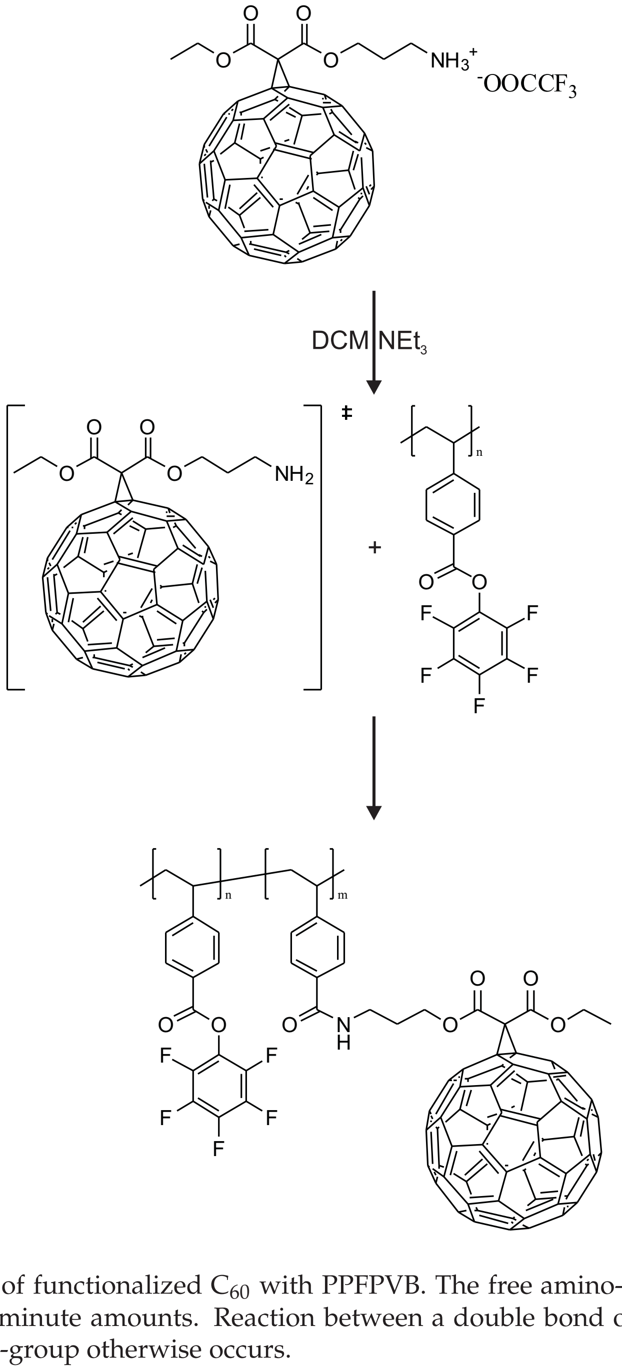

Fig. 5.11: Coupling of functionalized C_{60} with PPFPVB. The free amino-group is generated in-situ in minute amounts. Reaction between a double bond of the fullerene and the amino-group otherwise occurs.

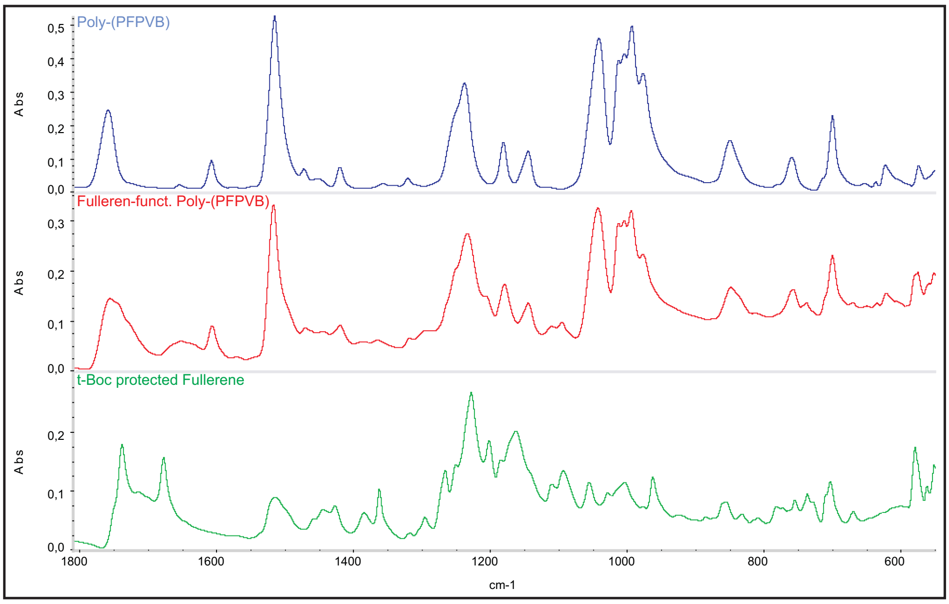

Fig. 5.12: FT-IR spectra of the amino-functionalized fullerene (bottom; green curve), the active ester polymer poly(pentafluorophenyl 4-vinylbenzoate) (top; blue curve) and the C_{60}-fullerene functionalized poly(pentafluorophenyl 4-vinylbenzoate) (middle, red curve).

silanated wafers/glass slides were placed in a Soxhlet apparatus with DCM overnight to remove any traces of physisorbed APDMES molecules.

Monomer synthesis

The active ester based monomer 4-vinylbenzoyl chloride (left structure in Fig. 5.5) was synthesized according to Nilles et al. [286].

First step: Synthesis of 4-Vinylbenzoyl chloride (4-VBC)

Moisture-free conditions were ensured by conducting the experiment in a dry argon atmosphere. The reaction was carried out in a 25 ml Schlenk tube with a condenser and a magnetic stir bar. The Schlenk tube was loaded with 4-vinylbenzoic acid (3 g; 20 mmol) and dry benzene (9 ml) added under argon counter flow. Subsequently, oxalyl chloride (3.4 ml; 40 mmol) was added and the reaction solution stirred until the evolution of gas had ceased. The 4-vinylbenzoic acid was completely dissolved after refluxing for 2 h (oil bath; 100 °C). The benzene and excess oxalyl chloride ($\sim$ 10 ml) were removed under reduced pressure and elevated temperature (oil bath; 55 °C). 4-VBC with sufficient purity was obtained in a quantitative yield ($\sim$ 20 mmol).

Second step: Synthesis of Pentafluorophenyl 4-vinylbenzoate (PFPVB)

Pentafluorophenol is hygroscopic and thus was directly weighed (3.8 g; 20 mmol) into a 100 ml three-neck round-bottom flask in a glove box. The flask was equipped with a condenser, a thermometer, a magnetic stir bar and connected to an argon line. 20 ml of dry THF and triethylamine (2.8 ml; 20 mmol) were added under an argon counter flow. The dropping funnel was charged with 20 ml of dry THF and the 4-VBC ($\sim$ 20 mmol) in a glove box. The dropping funnel was connected to the flask and the reaction solution cooled in an ice bath. The temperature was kept below 4 °C and the diluted 4-VBC slowly added to the pentafluorophenol. The solution was stirred for 12 h at room temperature and the precipitated ammonium salts were filtered off

afterwards. The brown, viscous filtrate was washed twice with 50 ml of Milli-Q water. The aqueous layers were combined and extracted once with 20 ml of THF and twice with 15 ml of DCM. The organic layers were combined and dried over anhydrous $MgSO_4$. A thin layer chromatogram (toluene: n-hexane; 1:1) revealed one product with a RF-value of 0.7. The solvent was evaporated under reduced pressure to yield the crude product (3.8 g; brown, viscous liquid). Clean PFPVB (3.3 g; 52.5 %) was obtained as white powder by column chromatography (silica gel 60; mesh size 63 - 200 μm) using toluene : n-hexane (1:1) as eluent.
Characterization:
^{1}H NMR ($CDCl_3$, 250 MHz) δ (ppm): 8.06 (d, 2H, **benzoate, para**); 7.45 (d, 2H, **benzoate, meta**); 6.73 (dd, 1H, **=CH-**); 5.85 (d, 1H, **=CH$_2$**); 5.38 (d, 1H, **=CH$_2$**).
^{1}3C NMR ($CDCl_3$, 500 MHz) δ (ppm) 162.35 (**COO**); 143.77 (**benzoate, para**); 142.43 140.42 138.95 138.51 136.95 (**pentafluorophenyl, ortho, meta and para**); 135.67 (**=CH-**); 131.08 (**benzoate, ortho**); 126.55 (**benzoate, meta and ipso**); 125.86 (**pentafluorophenyl, ipso**); 117.8 (=CH$_2$).
^{1}9F NMR ($CDCl_3$, 500 MHz) δ (ppm) -152.39 (d, 2F, **pentafluorophenyl, ortho**); -157.97 (t, 1F, **pentafluorophenyl, para**); -162.31 (dd, 2F, **pentafluorophenyl, meta**).

Polymer Synthesis

The active ester polymer poly(pentafluorophenyl 4-vinylbenzoate) was synthesized as shown in Fig. 5.5. *Characterization:*
^{1}H NMR ($CDCl_3$, 500 MHz) δ (ppm): 8.11-7.71 (br, 2H, **benzoate, ortho**); 6.85-6.46 (br, 2H, **benzoate, meta**); 1.94-1.36 (br, 3H, **backbone**).
^{1}9F NMR ($CDCl_3$, 500 MHz) δ (ppm) -152.61 to - 153.44 (br, 2F, **pentafluorophenyl, ortho**); -157.07 to - 157.91 (br, 1F, **pentafluorophenyl, para**); -161.84 to -162.89 (br, 2F, **pentafluorophenyl, meta**).

Synthesis of Functionalized C_{60}-Fullerene

First step: Synthesis of 3-((tert-Butoxycarbonyl)amino)propyl ethyl malonate

The reaction was carried out in a 500 ml two-neck round-bottom flask equipped with a pressure-equalizing dropping funnel, condenser, and a magnetic stir bar. The flask was charged with dry pyridine (2 ml) and 200 ml dry DCM, as well as tert-butyl (3-hydroxypropyl)carbamate (2.3 g; 13 mmol) added under an argon counter flow. Ethyl malonyl chloride (2 g; 13 mol) was added slowly (15 min), while cooling the flask in an ice bath. Agitation was continued overnight under ambient conditions. The solvent was removed under reduced pressure from the blue reaction solution. A thin layer chromatogram (ethyl acetate: petroleum ether; 1:1) showed a major product with a RF-value of 0.5 and a minor product of 0.2. Clean product (2.5 g; 65 %; lit. 60%) was obtained as a pale yellow oil by column chromatography (silica gel 60; mesh size 63 - 200 μm) using EtOAc : petroleum ether (1:1) as eluent.
Characterization:
^{1}H NMR ($CDCl_3$, 250 MHz) δ (ppm) 4.83 (b, 1H, **N-H**); 4.20 (m, 4H, **O-CH_2**); 3.33 (s, 2H, **CO-CH_2-CO**); 3.19 (m, 2H, **NH-CH_2**); 1.85 (m, 2H, **C-CH_2-C**); 1.39 (s, 9H, **C-$(CH_3)_3$**); 1.26 (t, 3H, **C-(CH_3)**.

Second step: Synthesis of 3'H-Cyclopropa[1,9][5,6]fullerene-$_{60}$-Ih-3',3'-dicarboxylic acid, 3-[[(1,1-dimethylethoxy)carbonyl]amino]propyl ethyl ester

The Bingel-Hirsch reaction was used for the addition of the 3-((tert-butoxycarbonyl)amino)propyl ethyl malonate to the Fullerene-$_{60}$-Ih. The reaction was carried out in a 750 ml round-bottom flask equipped with a condenser and a magnetic stir bar. The flask was charged with toluene (400 ml) and the C_{60} (0.5 g; 0.694 mmol) dissolved in it. CBr_4 (0.331 g; 0.998 mmol), 3-((tert-butoxycarbonyl)amino)propyl ethyl malonate (0.3 g; 0.998 mmol), DBU (0.3 ml; 2 mmol) were added and the reaction solution stirred for 30 min. The solvent was removed in vacuo and unreacted C_{60} removed by column chro-

matography (silica gel 60; mesh size 63 - 200 μm) using toluene as eluent. Clean product (340 mg; 48.6 %; lit. 54%) was obtained as obtained as brown solid by column chromatography (silica gel 60; mesh size 63 - 200 μm) using EtOAc : toluene (1:10) as eluent.
Characterization:
^{1}H NMR (CDCl$_3$, 250 MHz) δ (ppm) 4.83 (b, 1H, **N-H**); 4.69 (m, 4H, **O-CH$_2$**); 3.70 (m, 2H, **NH-CH$_2$**); 2.23 (m, 2H, **C-CH$_2$-C**); 1.51 (m, 12H, **C-(CH$_3$)$_3$** & **C-(CH$_3$)**).

Deprotection of amino-group in 3'H-Cyclopropa[1,9][5,6]fullerene-$_{60}$-Ih-3',3'-dicarboxylic acid, 3-[[(1,1-dimethylethoxy)carbonyl]amino]propyl ethyl ester

The deprotection of the t-butoxycarbonyl-protected amino-group of the functionalized C$_{60}$ was carried out in a 100 ml round-bottom flask equipped with a magnetic stir bar. The flask was charged with 25 ml of DCM and the functionalized C$_{60}$ (100 mg; 100 mmol). The functionalized C$_{60}$ was not completely dissolved. 25 ml of trifluoroacetic acid (0.36 mmol) were added and the C$_{60}$ was completely dissolved upon stirring for 70 min. The solvent was removed in vacuo and the pure product dried in vacuum at 70 °C (12 h). The 3'H-cyclopropa[1,9][5,6]fullerene-$_{60}$-Ih-3',3'-dicarboxylic acid, 3-aminopropyl ethyl ester, trifluoroacetate was obtained in quantitative yield.
Characterization:
^{1}H NMR (DMSO, 250 MHz) δ (ppm) 7.98 (s, 3H, **N-H**); 4.67 (m, 4H, **O-CH$_2$**); 3.08 (m, 2H, **N-CH$_2$**); 2.18 (m, 2H, **C-CH$_2$-C**); 1.52 (t, 3H, **C-(CH$_3$)**).

Grafting to of Poly(pentafluorophenyl 4-vinylbenzoate)

The amino-functionalized wafers and a predetermined amount of PPFPVB were placed in a Schlenk tube equipped with a magnetic stir bar. The tube was purged with argon and 20 ml dry THF added. The solution was stirred overnight and the silicon wafers were removed. The wafers were placed in a

Soxhlet apparatus with DCM for 8 h in order to remove physisorbed polymer.

Grafting to of C_{60}-Fullerene salt on PPFPVB functionalized substrate

The wafers with grafted PPFPVB and a predetermined amount of 3′H-cyclo - propa[1,9][5,6]fullerene-$_{60}$-Ih-3′,3′-dicarboxylic acid, 3-aminopropyl ethyl ester, trifluoroacetate were placed in a Schlenk tube with a magnetic stir bar. The tube was purged with argon, 15 ml of dry DCM were added and a dropping funnel was connected to the tube. The dropping funnel was charged with 10 ml of dry DCM and 0.1 ml of TEA. The suspension containing the C_{60}-fullerene salt was stirred and the mixture of DCM and TEA was added dropwise (1 h). The C_{60}-fullerene salt was completely dissolved after the complete addition of the DCM/TEA. The silicon wafers were removed from the reaction solution and placed in a Soxhlet apparatus with DCM for 8 h in order to remove physisorbed or polymerized fullerene.

Synthesis of C_{60}-Fullerene Functionalized Poly(pentafluorophenyl 4-vinylbenzoate)

The coupling of 3′H-cyclopropa[1,9][5,6]fullerene-$_{60}$-Ih-3′,3′-dicarboxylic acid, 3-aminopropyl ethyl ester, trifluoroacetate with PPFPVB was carried out in a 100 ml Schlenk flask equipped with a dropping funnel and a magnetic stir bar. The flask was charged with the C_{60}-Fullerene salt (95 mg; 0.093 mmol), PPFPVB (154 mg; 0.024 mmol), 25 ml of DCM and purged with argon. The suspension was treated with ultrasound for 5 min. The suspension turned into a brown solution upon the slow addition of TEA (0.2 ml; 1.4 mmol) in 10 ml of DCM over 30 min. The reaction solution was concentrated in vacuo and precipitated in 40 ml of MeOH. The precipitate was recovered using filter paper and dried in vacuum (12 h). 107 mg of a brown powder was obtained.
Characterization:
^{1}H NMR ($CDCl_3$, 500 MHz) δ (ppm): 8.13-7.60 (br, **benzoate, ortho**); 6.99-6.38 (br, **benzoate, meta**); 4.58 (m, **O-CH$_2$**); 3.06 (m, **N-CH$_2$**); 2.20-0.93 (br, **backbone** & **C-CH$_2$-C** & **C-(CH$_3$)**).

6 Functionalization of Poly(butadiene)

6.1 Conversion of Poly(butadiene) into a Polyelectrolyte

6.1.1 Introduction

Macromolecules bearing ionic repeating units are in general referred to as polyelectrolytes. Decher et al. used such polyelectrolytes and developed a layer-by-layer (LbL) self assembly technique whereby polyelectrolyte multilayers can be deposited [293, 294]. A polyelectrolyte multilayer is typically formed starting from a charged substrate surface and alternate absorption of polyanions/polycations from solution onto this substrate. The advantage of such coatings can be seen in the fact that the thickness can be controlled precisely, the deposition of each layer does not require elaborate procedures, and the absence of limitations concerning shape and size of substrate [295–297]. Coatings prepared by the LbL technique might be suitable for various technical applications, viz. in optoelectronic devices [298, 299] or as superhydrophobic surfaces [300]. The properties of polyelectrolyte multilayers and their preparation are described in reviews and books [43,301,302].

A current issue of great interest concerning polyelectrolyte multilayers is the internal structure of the deposited layers. Little attention has thus far been attributed to the conformation and dynamics of chains near the solid surface, where the properties of individual molecules have not quite reached the bulk values. The DFG SPP1369 (Polymer-Solid Contacts: Interfaces and Interphases) Priority Program is focusing on the properties of polyelectrolytes

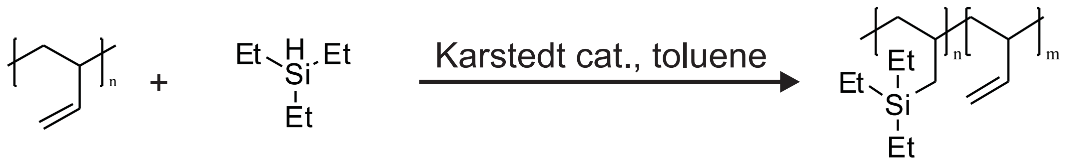

Fig. 6.13: Hydrosilylation of Poly(butadiene) with triethylsilane using Karstedt catalyst.

near the surface, the so-called interphase. Experimentalists and theoreticians are collaborating within this Priority Program in order to investigate the properties of this interphase. The group of Prof. Dr. R. von Klitzing at the Technical University of Berlin is focusing on the preparation of polyelectrolyte multilayers and their characterization using X-ray/neutron scattering techniques and optical spectroscopy. A close cooperation with the theoreticians Prof. Dr. W. Paul at the University Halle-Wittenberg, Prof. Dr. K. Binder and Dr. P. Virnau at the Johannes Gutenberg-University of Mainz has been established within the Priority Program. The obstacle however is, that the atomistic computer simulations performed by the theory groups were focusing on poly(butadiene), a highly suitable polymer for such simulations. The experimental and theoretical results are thus not comparable, because poly(butadiene) cannot be used for the preparation of polyelectrolyte multilayers, unless it is functionalized with ionic units.

The focus of this part of the thesis is on the conversion of poly(butadiene) into a polyelectrolyte.

Chemical modification of poly(butadiene) is possible because of the reactivity of the double bonds. Catalytic hydrosilylation of the vinyl groups in poly(butadiene) has been chosen for chemical modification by several researchers [303–305], since it is a high conversion transformation. A silicon-hydrogen moiety is added across a carbon-carbon double bond of the poly(butadiene) using a platinum catalyst, as shown in Fig. 6.13.

Guo et al. were able to show that the hydrosilylation reaction takes exclusively place at pendant vinyl groups, viz. double bonds resulting from 1,2-addition of butadiene during polymerization [303]. This is consistent with the results obtained for small molecules. The vinyl bond in cyclohexene, for

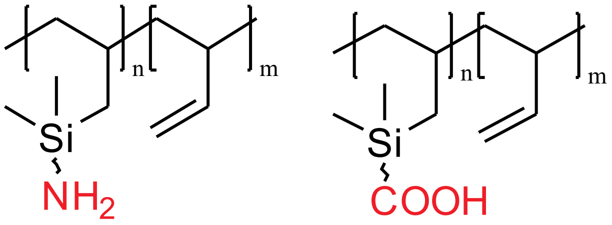

Fig. 6.14: Poly(butadiene) functionalized with ionic groups, such as the carboxyl- and amino-group, suitable for the preparation of polyelectrolyte multilayers.

example, cannot be accessed in a hydrosilylation reaction [306]. Based on this knowledge from hydrosilylation reactions using small molecules it can be concluded that steric effects are the reason why only the 1,2-microstructures in poly(butadiene) can take part in hydrosilylation reactions.

Guo et al. were able to show additionally that the hydrosilylation of poly(butadiene) follows a anti-Markovnikov addition mechanism (as depicted in Fig. 6.13). The bulky polymer chains are the reason for this regioselectivity. The results of an experiment where 1-hexene and triethylsilane were used in an hydrosilylation reaction are in support of this conclusion [306]. 60 % of n-hexyltriethylsilane were obtained. The hexyl-chain is not bulky enough to direct the hydrosilylation completely towards the anti-Markovnikov product.

The first task was thus to produce poly(butadiene) comprised of 100 % 1,2-microstructures, because it is possible to add silanes across the double bonds in the 1,2-microstructures in a hydrosilylation reaction. The second task was to synthesize silanes carrying ionic groups, such as the carboxyl- and amino-group. A hydrosilylation reaction using these silanes would yield poly(butadiene) with ionic groups, as depicted in Fig. 6.14. Poly(butadiene) with ionic groups would be suitable for the preparation of polyelectrolyte multilayers, which are investigated by experimentalists and theoreticians alike as part of the SPP1369 Priority Program.

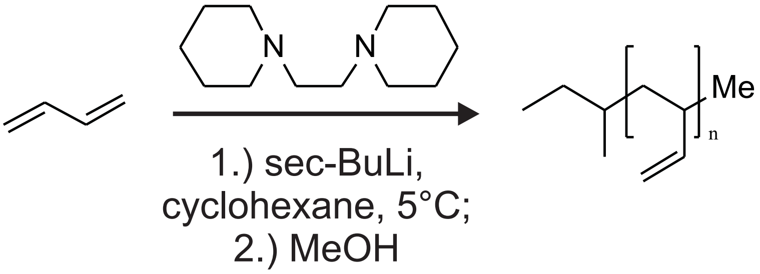

Fig. 6.15: Anionic polymerization of 1,3-butadiene. The diamine ligand 1,2-dipiperidinoethane is responsible for the 1,2-arrangement in the poly(butadiene).

6.1.2 Results and Discussion

Preparation of Poly(butadiene)

Poly(butadiene) with 100 % 1,2-content was prepared anionically using the chelating diamine ligand 1,2-dipiperidinoethane (DPE), as depicted in Fig. 6.15. Reaction details can be found in Scetion 6.1.3.

The poly(butadiene) had a M_n = 16200 g/mol and a polydispersity of 1.08.

The 1,2-content of the poly(butadiene) was estimated using the ^{1}H NMR spectrum shown in Fig. 6.16. The peaks in the olefinic region above 4.6 ppm were integrated. The major peak in the olefinic region at 4.89 ppm (marked with the red rectangle; *a)*, contains exclusively the 1.2-vinylic methylene protons (marked with *a* in the inset). The smaller peak at 5.44 ppm (marked with the blue rectangle, *b)*) corresponds to the methine protons of the 1,2- and 1,4-microstructure (marked with *b* in the inset). The smallest peak at 5.75 ppm (marked with the blue rectangle, *c)*) corresponds solely to the terminal vinyl monomer unit (marked with *c* in the inset).

The degree of polymerization of the 1,2-microstructure is assigned to y, whereas the degree of polymerization of the 1,4-microstructure is assigned to y'. Thus the area under the peak *a)* (red box) is given by $2y$. The area under the peaks marked with *b)* and *c)* (blue box) is equal to $y + 2y'$. One obtains the following equations taking the relative values of the integrated areas from the spectrum.

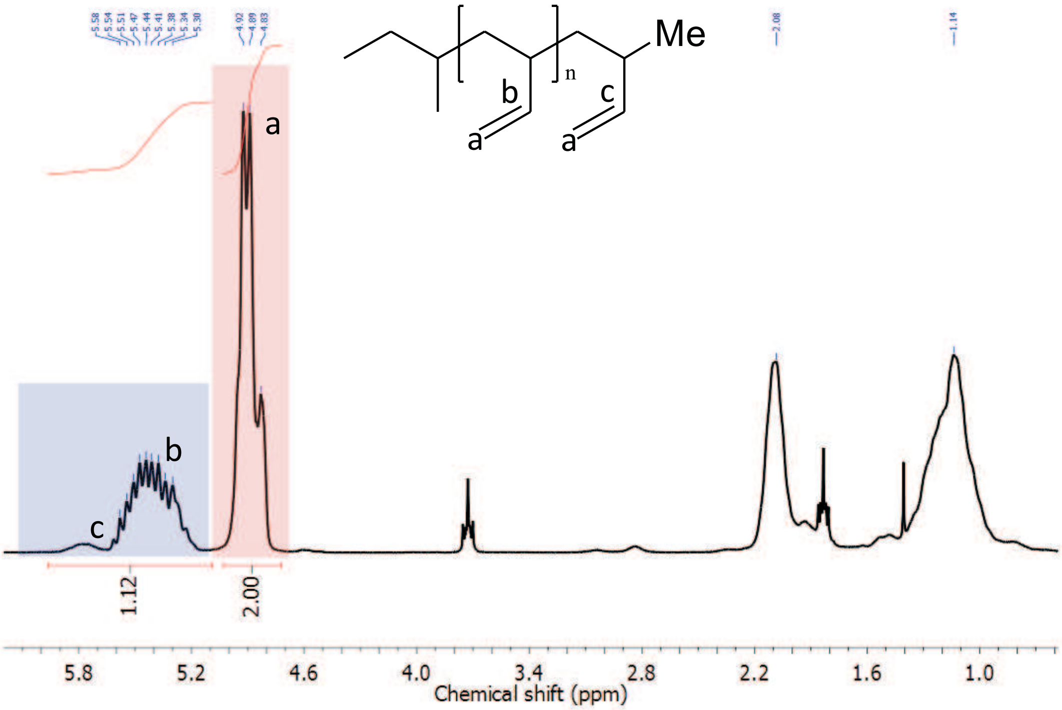

Fig. 6.16: ^{1}H NMR spectrum after anionic polymerization of 1,3-butadiene. The peaks in the olefinic region were used for an estimation of 1,2-microstructure content.

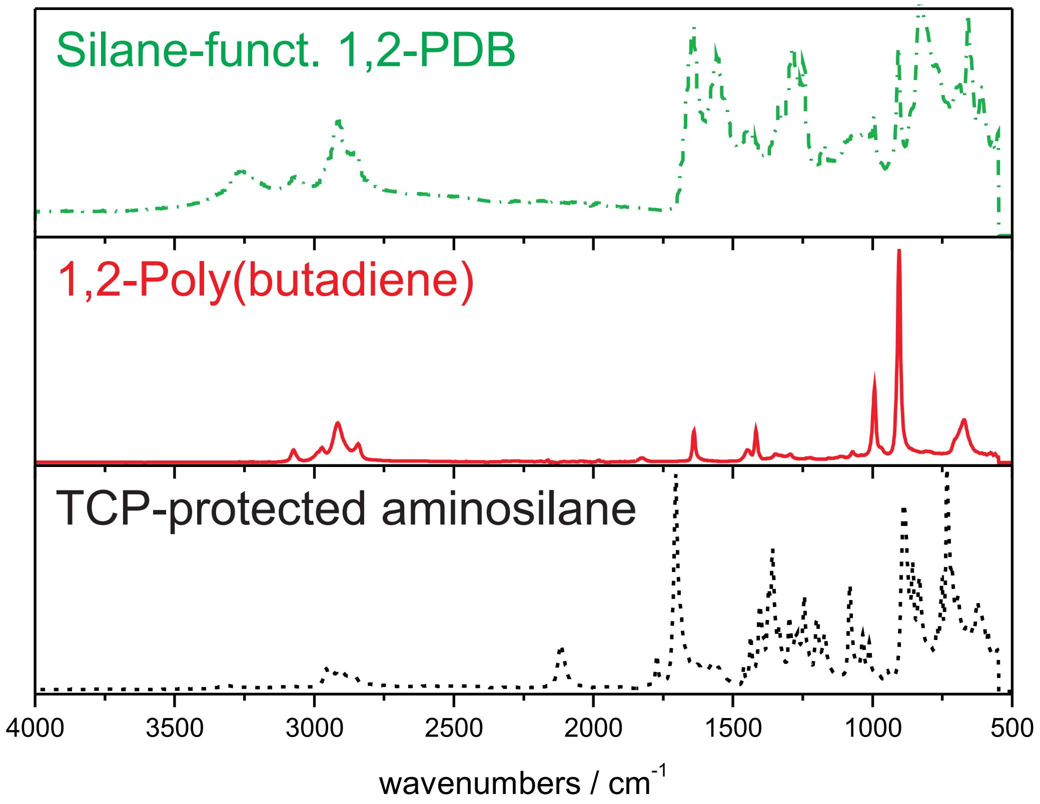

Fig. 6.17: FT-IR spectra of the TCP-protected aminosilane (bottom; black dotted curve), the 1,2-poly(butadiene) (middle; red solid curve) and the aminosilane-functionalized 1,2-poly(butadiene) (top, red dash-dotted curve).

$$a = 2.0 = 2y \Rightarrow y = 1 \tag{6.1}$$

$$b + c = 1.12 = y + 2y' \Rightarrow 1.12 - y = 2y' \tag{6.2}$$

Using Eq. 6.1 to replace y in Eq. 6.2 yields

$$0.12 = 2y' \Rightarrow 0.12/2 = 0.06 = y' \tag{6.3}$$

and thus the one gets a ratio of 94 to 6 percent of 1,2- to 1,4-content. The synthesized poly(butadiene) was comprised of 1,2-microstructures therefore. The IR-spectrum of the synthesized poly(butadiene), as shown in Fig. 6.17

(middle; red solid curve), exhibits exclusively spectral characteristics of 1,2-microstructures. A peak at 906 and one at 991 cm^{-1} was identified. These peaks are characteristic for the vinyl 1,2-deformation. Peaks associated with the cis- and trans-1,4-deformation, typically found at 968 and 729 cm^{-1} [307, 308], were not identified. The characteristic peak for the stretching of the pendant vinyl groups was identified at 3074 cm^{-1} however [303, 309].
^{1}H NMR and IR both provide evidence that the synthesized PBD was composed exclusively of 1,2-microstructures. Pendant vinyl groups can be functionalized in hydrosilylation reactions with silanes. The catalyst can access these groups, but not the vinyl groups in 1,4-microstructures. Vinyl groups in 1,4-microstructures are shielded by the backbone, as discussed earlier.

Preparation of the Carboxyl-funtionalized silane

Two synthetic procedures were implemented for the preparation of the carboxyl-funtionalized silane 4-(dimethylsilyl)benzoic acid, as depicted in Fig. 6.18. On the left is a one-step procedure depicted, that did not require workup and purification of the 4-(bromophenyl)dimethylsilane. A two-step procedure is depicted on the right and promised to produce the carboxyl-functionalized silane in higher yield, which was not reached however. Both procedures allowed to produce pure 4-(dimethylsilyl)benzoic acid suitable for hydrosilylation reactions, as the ^{1}H NMR data showed.
A detailed description of the procedures, reaction details and ^{1}H NMR data can be found in Section 6.1.3.

Preparation of the Amino-functionalized silane

The amino-functionalized silane aminobutyldimethylsilane was synthesized as depicted in Fig. 6.19. The procedure allowed to produce pure aminobutyldimethylsilane suitable for hydrosilylation reactions, as the ^{1}H NMR data showed.
A detailed description of the procedure, reaction details and ^{1}H NMR data can be found in Section 6.1.3.

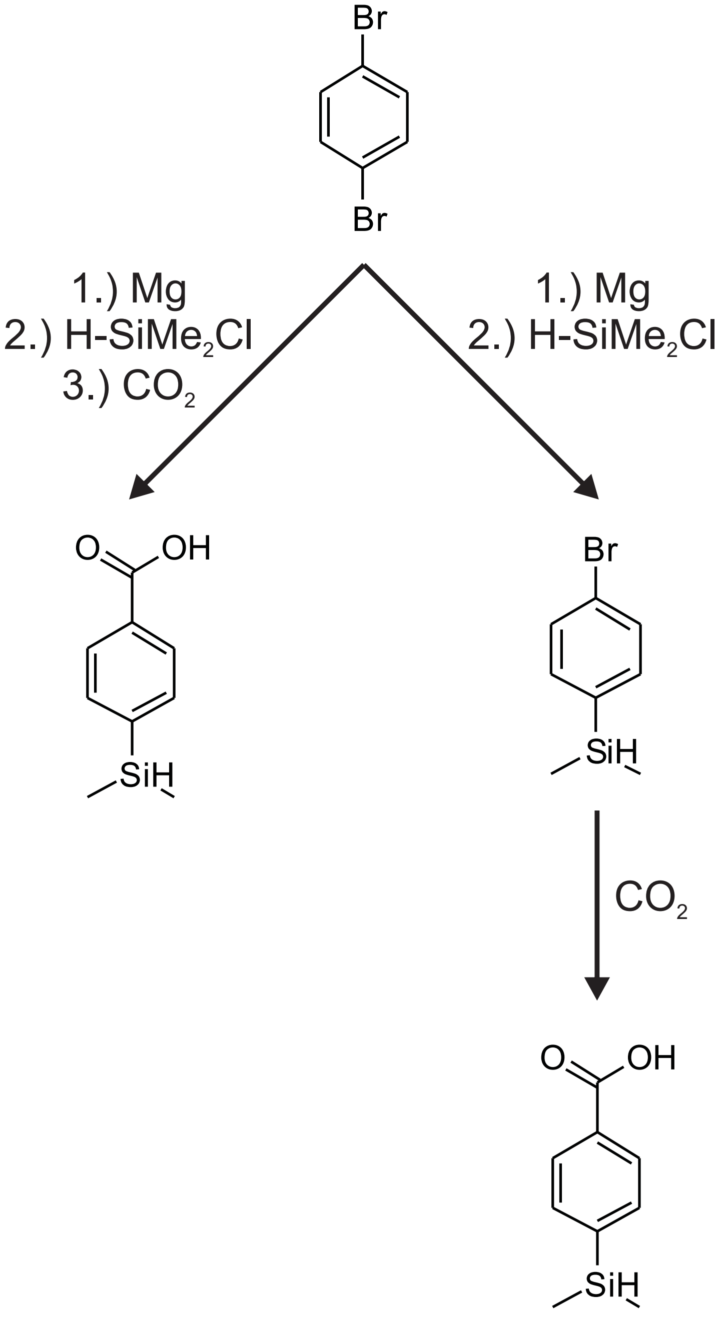

Fig. 6.18: The two implemented synthetic procedures for the preparation of the carboxyl-funtionalized silane 4-(dimethylsilyl)benzoic acid.

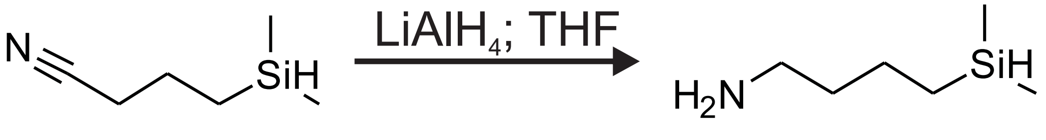

Fig. 6.19: Synthesis of the amino-functionalized silane aminobutyldimethylsilane.

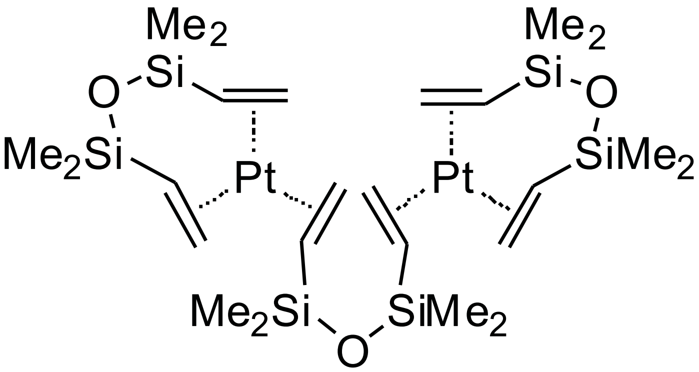

Fig. 6.20: Structure of Karstedt catalyst used for the hydrosilylation reactions.

Hydrosilylation reaction using unprotected silanes

Both functionalized silanes, the 4-(dimethylsilyl)benzoic acid and the aminobutyldimethylsilane, were utilized as prepared in a hydrosilylation reaction. The problem was however, that no reaction between the poly(butadiene) and the silanes occurred, as ^{1}H NMR data revealed. One can only speculated which species was acting as inhibitor, rendering the catalyst ineffective. Platinum bis(divinyltetramethyldisiloxane), commonly referred to as Karstedt catalyst (depicted in Fig. 6.20), is a highly reactive platinum(0)-tetraolefine complex. It degrades rapidly if not stored in a glove box. It seems to be reasonable therefore that the amino- and carboxyl-functionality might have formed a complex with the Pt(0) in the Karstedt catalyst. Granados-Focil et al. came to a similar conclusion [310]. They were not able to carry out a hydrosilylation reaction of vinyl-substituted triazoles using Karstedt catalyst, unless they capped the remaining hydrogen on the triazole ring with a protective group.

In order to be able to use the functionalized silanes in hydrosilylation reac-

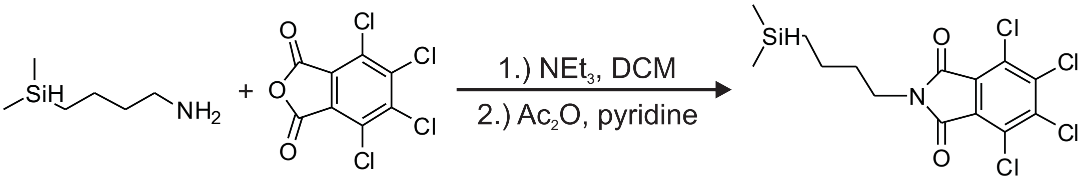

Fig. 6.21: Synthesis of N-tetrachlorophthaloyl-aminobutyldimethylsilane. The amino-functionality was thus protected as TCP-imide.

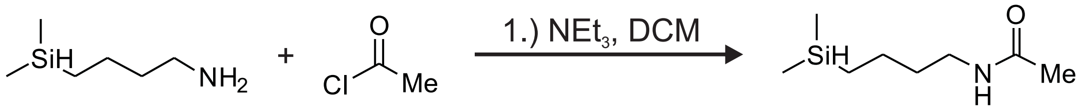

Fig. 6.22: Synthesis of Acetoxy-aminobutyldimethylsilane. The amino-functionality was thus protected as acetoxy-amide.

tions it became necessary to protect the functional groups.

Protective groups for Aminobutyldimethylsilane

It was not possible to use the aminobutyldimethylsilane in hydrosilylation reactions without protection of the amino-functionality.
The tetrachlorophthaloyl (TCP) group was chosen as imidic protection of the amino-functionality. The installation of the TCP-group was carried out as depicted in Fig. 6.21. A detailed description of the procedure, reaction details and ^{1}H NMR data can be found in Section 6.1.3.
The procedure allowed to produce pure N-tetrachlorophthaloyl-aminobutyldimethylsilane suitable for hydrosilylation reactions, as the ^{1}H NMR data showed. The IR-spectrum of the TCP-protected aminosilane (Fig. 6.17 bottom; black dotted curve) is dominated by the strong band of the carbonyl group at 1758 cm^{-1}. Peaks associated with the $N-H$-stretching, typically found at 3300-3500 cm^{-1} cannot be identified. ^{1}H NMR and IR both provide evidence that the protection of the amino-functionality was successful.

The acetoxy (Ac) group was chosen as alternative protection for the amino-functionality, because the successful installation can be identified using ^{1}H

NMR. The installation of the acetoxy-group was carried as depicted in Fig. 6.22. A detailed description of the procedure, reaction details and ^{1}H NMR data can be found in Section 6.1.3.

The procedure allowed to produce pure acetoxy-aminobutyldimethylsilane suitable for hydrosilylation reactions, as the ^{1}H NMR data showed.

Protective groups for 4-(Dimethylsilyl)benzoic acid

It was not possible to use 4-(dimethylsilyl)benzoic acid in hydrosilylation reactions without protection of the carboxyl-functionality.

Several protective groups were tested, but the installation failed in the majority of cases, as Fig. 6.23 demonstrates. The major problem was the low reactivity of the 4-(dimethylsilyl)benzoyl chloride. Thus the two attempts to install a t-butoxy protection group [311] failed (first and second reaction in Fig. 6.23) and 4-(dimethylsilyl)benzoic acid was obtained after the installation.

The installation of a tetrahydrofuranyl-(THF)-ether protection group failed as well [312]. The reaction conditions were too harsh and the Si-H bond in the silane was destroyed.

An amide protection of the carboxyl-functionality was successfully performed using N,N-diisopropylamine. The nucleophility of the amine must have been high enough for an efficient attack on the carbonyl group in the 4-(dimethylsilyl)benzoyl chloride.The reaction with N,N-diisopropylamine was carried out as depicted in Fig. 6.23 (third reaction). A detailed description of the procedure, reaction details and ^{1}H NMR data can be found in Section 6.1.3.

The procedure allowed to produce pure 4-(dimethylsilyl)-N,N-diisopropylbenzamide suitable for hydrosilylation reactions, as the ^{1}H NMR data showed.

Hydrosilylation reaction using protected silanes

Three protected silanes, the N-tetrachlorophthaloyl-aminobutyldimethylsilane, the acetoxy-aminobutyldimethylsilane and the 4-(dimethylsilyl)-N,N-diisopropylbenzamide, were utilized in a hydrosilylation reaction, as depicted schematically in Fig. 6.24.

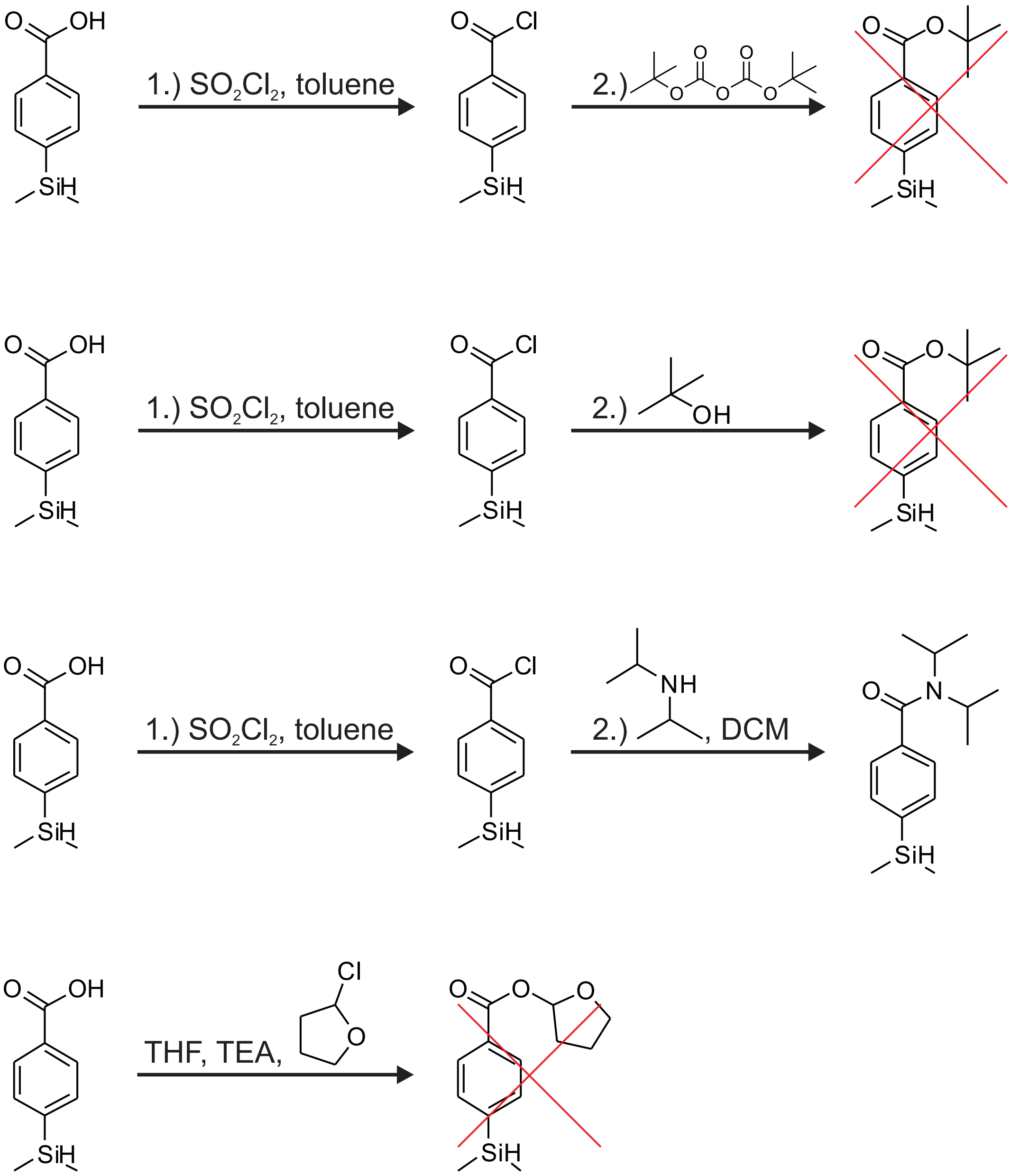

Fig. 6.23: Synthesis of 4-(Dimethylsilyl)-N,N-diisopropylbenzamide (third) reaction. The carboxy-functionality was thus protected as N,N-diisopropyl-amide. All other attempts to protect the carboxyl-functionality failed.

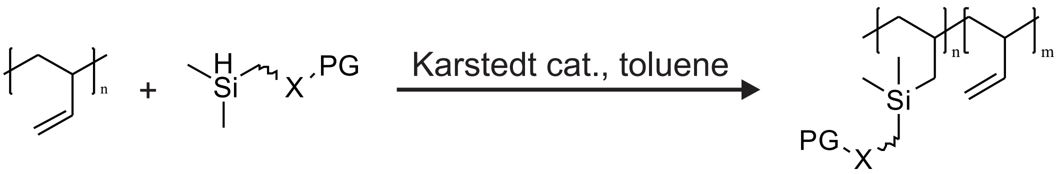

Fig. 6.24: Hydrosilylation of Poly(butadiene) using Karstedt catalyst. X represents the functional group of the silane that had been protected previously with a protective group, represented by PG.

A detailed description of the procedures, reaction details and ^{1}H NMR data can be found in Section 6.1.3.

The ^{1}H NMR data revealed that the $Si - H$ signal disappeared after the reaction, which can be seen as first evidence of a successful hydrosilylation.

More evidence for a successful hydrosilylation reaction in the case of the TCP-protected aminobutyldimethylsilane was gathered using GPC. A representative elution diagram is shown in the upper part of Fig. 6.25. The black dashed line represents the data of the untreated PBD and the red solid line the data of the N-tetrachlorophthaloyl-aminobutyldimethylsilane-functionalized poly(butadiene) (structure in the upper left corner of Fig. 6.25). A second peak at lower retention volume appeared after the hydrosilylation reaction. It seems reasonable that this peak is representing PBD with several side groups of N-tetrachlorophthaloyl-aminobutyldimethylsilane. The bulky side groups increase the hydrodynamic radius of the polymer and thus a decrease in retention volume was observed. Unreacted PBD was still present after the hydrosilylation as the second peak in the red solid curve demonstrates. This second peak appeared at the exact same retention volume as the starting material.

The green dash-dotted line is representing the aminobutyldimethylsilane-functionalized poly(butadiene) after the removal of the TCP-protection group. No change in retention volume was observed upon removal of the protection group. The peak got broader though, but the starting material was completely removed after the deprotection step.

The GPC-data yields strong evidence that the hydrosilylation of PBD using N-tetrachlorophthaloyl-aminobutyldimethylsilane and removal of the TCP-

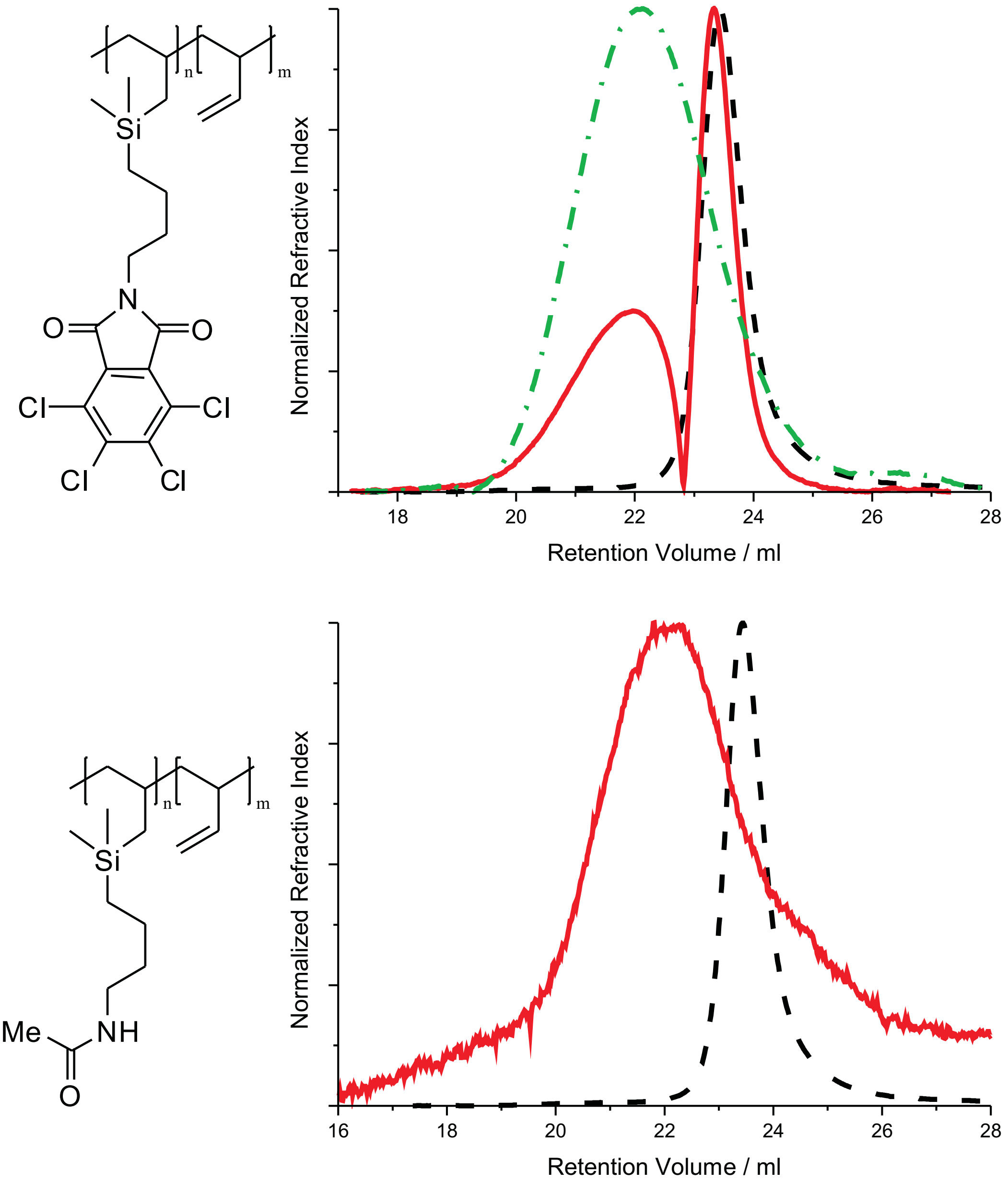

Fig. 6.25: Upper diagram: Representative GPC-results for poly(butadiene) (black dashed line), N-tetrachlorophthaloyl-aminobutyldimethylsilane-functionalized poly(butadiene) (red solid line; structure on the left side), and aminobutyldimethylsilane-functionalized poly(butadiene) (green dash-dotted line).
Lower diagram: Representative GPC-results for poly(butadiene) (black dashed line), acetoxy-aminobutyldimethylsilane-functionalized poly(butadiene) (red solid line; structure on the left side).

protection group was successful and that this synthetic procedure can be used to prepare PBD carrying amino-groups.
More evidence for a successful hydrosilylation reaction in the case of the Ac-protected aminobutyldimethylsilane was gathered using GPC. A representative elution diagram is shown in the lower part of Fig. 6.25. The black dashed line represents the data of the untreated PBD and the red solid line the data of the acetoxy-aminobutyldimethylsilane-functionalized poly(butadiene) (structure in the lower left corner of Fig. 6.25). A second peak at lower retention volume appeared after the hydrosilylation reaction. It seems reasonable that this peak is representing PBD with several side groups of acetoxy-aminobutyldimethylsilane. The bulky side groups increase the hydrodynamic radius of the polymer and thus a decrease in retention volume was the result. Unreacted PBD was not found after the hydrosilylation reaction, as the absence of a second peak at the exact same retention volume as the starting material demonstrates. A broadening of the peak after the hydrosilylation was observed however.
The GPC-data yields strong evidence that the hydrosilylation of PBD using acetoxy-aminobutyldimethylsilane was successful.

Deprotection of Amino-groups in TCP-aminobutyldimethylsilane functionalized PBD

The deprotection of the amino-groups in N-tetrachlorophthaloyl-aminobutyldimethylsilane functionalized poly(butadiene) was carried out as depicted in Fig. 6.26. Ethylenediamine reacted with the imide-functionality yielding a poly(butadiene) with free amino-functionalities. A detailed description of the procedure, reaction details and ^{1}H NMR data can be found in Section 6.1.3.
^{1}H NMR is not conclusive in the case of the deprotection step, because the N-tetrachlorophthaloyl group has no protons. GPC data (Fig. 6.25; green dash-dotted line in the upper diagram) is not conclusive either, because no change in retention volume was observed. IR-data provides evidence that the deprotection was successful however (Fig. 6.17; red dash-dotted curve). The strong band of the carbonyl group at 1758 cm^{-1} has disappeared. Two

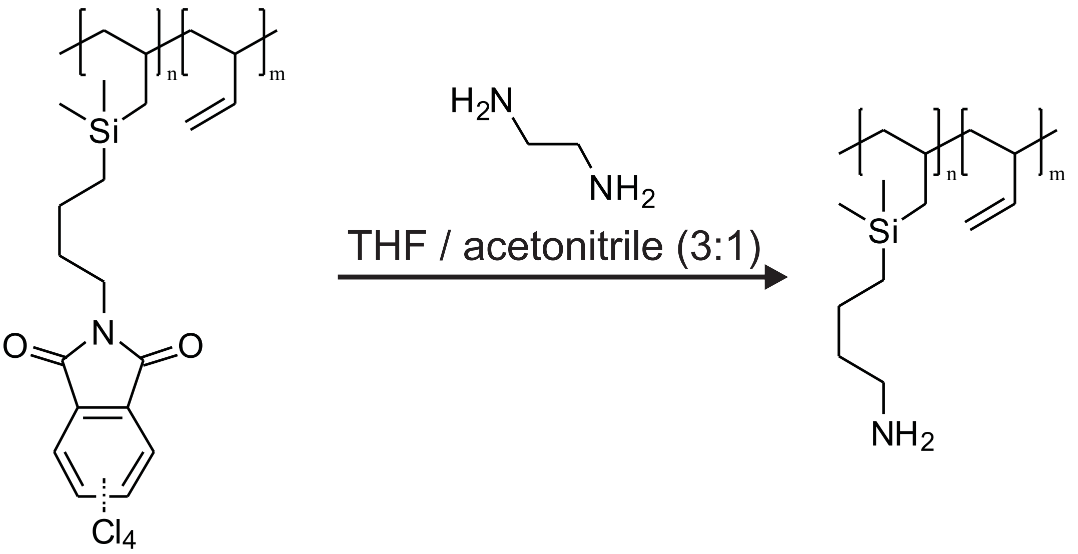

Fig. 6.26: Deprotection of Amino-groups in N-Tetrachlorophthaloyl-aminobutyldimethylsilane functionalized PBD using ethylenediamine.

peaks associated with the $N-H$-stretching can be identified at 3100-3500 cm^{-1} however.

Evidence can be found that the hydrosilylation of PBD using N-tetrachlorophthaloyl-aminobutyldimethylsilane and removal of the TCP-protection group was successful and that this synthetic procedure can be used to prepare PBD carrying amino-groups.

It has been demonstrated that hydrosilylation of poly(butadiene) with silanes carrying functional groups such as amino- and carboxyl groups is possible. Protection groups for these functionalities have to be introduced, otherwise it is not possible to carry out the hydrosilylation due to side reactions between the functionalized silanes and the Karstedt catalyst. Several protection groups were tested and it was demonstrated that they can be removed from the polymer after the hydrosilylation reaction.

The developed synthetic protocol allows preparation of poly(butadiene) with ionic groups, suitable for preparation of polyelectrolyte multilayers, which are investigated by experimentalists and theoreticians alike as part of the

SPP1369 Priority Program.
The presented data serve as a proof of concept. More reliable data need to acquired however in order to draw dependable conclusions.

6.1.3 Syntheses

All chemicals were commercially available and used as received, unless otherwise stated.

Preparation of Poly(butadiene)

Poly(butadiene) with 100 % 1,2-content was prepared anionically using the chelating diamine ligand 1,2-dipiperidinoethane in cyclohexane at 5 °C [313]. Sec-buthyllithium was used as initiator and MeOH was chosen for termination.
Characterization:
^{1}H NMR ($CDCl_3$, 250 MHz) δ (ppm): 5.44 (m, $-C\mathbf{H}{=}CH_2$); 4.89 (m, $-CH{=}C\mathbf{H}_2$); 2.08-1.14 (**backbone**).

Preparation of 4-(Dimethylsilyl)benzoic acid

The first procedure chosen is a one-pot reaction designed by Wang et al. [314]. The reaction was carried out in a 500 mL two-neck round-bottom flask equipped with a pressure-equalizing dropping funnel, a condenser and a magnetic stir bar. Magnesium turnings (6.18 g; 0.254 mol), which had been activated with HCl previously, were placed in the flask in a protective argon atmosphere. A solution of 1,4-dibromobenzene (30 g; 0.127 mol) in dry THF (100 mL) was added under stirring at such a rate, that the THF was boiling. After the addition was completed, the solution was refluxed overnight under stirring. A solution of chlorodimethylsilane (12.04 g; 0.127 mol) in dry THF (100 mL) was added dropwise under stirring and refluxed overnight. While cooling (0 °C), CO_2 was bubbled through the reaction solution using a gas dispersion tube for 2 h and refluxed overnight under stirring. 100 mL of Milli-Q

was added to the reaction solution and 30 mL of conc. HCl introduced slowly under stirring. The solid residue was filtered off and the solution was transferred to a separatory funnel for further work-up. The aqueous layers was extracted three times with 50 mL of diethylether. The organic layers were combined, washed three times with 20 mL of Milli-Q water and dried over anhydrous $MgSO_4$. The crude product was obtained as a viscous oil after evaporating the solvent in vacuo. Pure product (6.5 g; 28.3 %; lit. 34 %) was obtained as white powder by column chromatography (silica gel 60; mesh size 63 - 200 μm) using DCM : acetone (10:1) as eluent.
Characterization:
^{1}H NMR ($CDCl_3$, 250 MHz) δ (ppm): 8.08 (d, 2H, **ArH**); 7.66 (d, 2H, **ArH**); 4.48 (septet, 1H, **-Si(Me)$_2$-H**); 0.37 (d, 6H, **-Si(CH$_3$)$_2$-**).

The second procedure chosen is a two-step synthesis designed by Kreuzer et al. [315].

First step: Synthesis of 4-(Bromophenyl)dimethylsilane

The reaction was carried out in a 500 mL two-neck round-bottom flask equipped with a pressure-equalizing dropping funnel, a condenser and a magnetic stir bar. A solution of 1,4-dibromobenzene (23.6 g; 0.1 mol) in dry THF (150 mL) was placed in the flask and purged with dry argon. Magnesium turnings (2.4 g; 0.1 mol), which had been activated with HCl previously, were added to the flask under argon counterflow. The reaction solution was heated slightly until the Grignard reaction had started and as identified by boiling. After the boiling had ceased, the reaction solution was refluxed for 2 h. The chlorodimethylsilane (9.46 g; 0.1 mol) was added under stirring at such a rate, that the THF was boiling. After the addition was completed, the solution stirred for 2 h under ambient conditions. The reaction solution was poured onto 300 mL of ice and 30 mL of half-concentrated HCl was added dropwise. Further work-up was carried out in a separatory funnel. The aqueous layers was extracted three times with 50 mL of diethylether. The organic layers

were combined, washed twice with 20 mL of Milli-Q water and dried over anhydrous $MgSO_4$. The crude product was obtained as a viscous oil after evaporating the solvent in vacuo. The final product (14.45 g; 67.2 %; lit. 70 %) was attained by fractional destillation and had a boiling point of 87 °C at 15 mbar (lit. 77-80 °C ; 15 hPa).
Characterization:
^{1}H NMR ($CDCl_3$, 250 MHz) δ (ppm): 7.55 (d, 2H, **ArH**); 7.41 (d, 2H, **ArH**); 4.45 (septet, 1H, **-Si(Me)$_2$-H**); 0.36 (d, 6H, **-Si(CH$_3$)$_2$-**).

Second step: Synthesis of 4-(Dimethylsilyl)benzoic acid

The reaction was carried out in a 250 mL two-neck round-bottom flask equipped with a pressure-equalizing dropping funnel, a condenser and a magnetic stir bar. A solution of 4-(bromophenyl)dimethylsilane (14.4 g; 0.067 mol) in dry THF (100 mL) was placed in the flask and purged with dry argon. Magnesium turnings (2.63 g; 0.067 mol), which had been activated with HCl previously, were added to the flask under argon counterflow. The reaction solution was heated slightly until the Grignard reaction had started as identified by boiling. After the boiling had ceased, the reaction solution was refluxed for 1 h. While cooling (0 °C), CO_2 was bubbled through the reaction solution using a gas dispersion tube for 3 h. The reaction solution was poured onto 220 mL of ice and 30 mL of half-concentrated HCl was added dropwise. Further work-up was carried out in a separatory funnel. The aqueous layers was extracted three times with 50 mL of diethylether. The organic layers were combined, washed twice with 20 mL of Milli-Q water and dried over anhydrous $MgSO_4$. The crude product was obtained as a viscous oil after evaporating the solvent in vacuo. Pure product (3.5 g; 30 %; lit. 67.8 %) was obtained as white powder by column chromatography (silica gel 60; mesh size 63 - 200 μm) using THF : hexane (1:1) as eluent.
Characterization:
^{1}H NMR ($CDCl_3$, 250 MHz) δ (ppm): 8.08 (d, 2H, **ArH**); 7.66 (d, 2H, **ArH**); 4.48 (septet, 1H, **-Si(Me)$_2$-H**); 0.37 (d, 6H, **-Si(CH$_3$)$_2$-**).

Preparation of Aminobutyldimethylsilane

The amino-functionalized silane aminobutyldimethylsilane was synthesized according to Blackledge et al. [316].

The reaction was carried out in a 500 mL two-neck round-bottom flask equipped with a pressure-equalizing dropping funnel, a condenser and a magnetic stir bar. Lithium aluminium hydride (10 g; 0.257 mol) and dry diethylether (100 mL) were placed in the flask in a protective argon atmosphere. A solution of (3-cyanopropyl)dimethylchlorosilane (10 g; 0.122 mol) in 80 mL of dry diethylether was added dropwise under stirring. After the addition was completed, the solution was refluxed overnight under stirring. Aqueous Na_2CO_3 was added while cooling (0 °C) and stirring until aluminium hydroxide started to precipitate. The precipitate was filtered off and washed with diethylether. The organic layer was separated from the aqueous layer and the latter extracted twice with 50 mL of diethylether. The ether extracts were combined and dried over anhydrous Na_2SO_4. The crude product was obtained as a brown oil after evaporating the solvent in vacuo. The final product (13.2 g; 82 %) was attained by fractional destillation and had a boiling point of 40 °C at 20 mbar (lit. 40 °C ; 10 Torr).

Characterization:

^{1}H NMR ($CDCl_3$, 250 MHz) δ (ppm): 3.82 (m, 1H, **ArH**); 2.67 (t, 2H, **ArH**); 1.50 (m, 4H, **-Si(Me)$_2$-H**); 0.58 (m, 2H, **-Si(CH$_3$)$_2$-**); 0.02 (d, 6H, **-Si(CH$_3$)$_2$-**).

Preparation of N-Tetrachlorophthaloyl-aminobutyldimethylsilane

The installation of the TCP-group was carried out according to Debenham et al. [317].

The reaction was carried out in a 500 mL Schlenk flask equipped with a magnetic stir bar. The flask was charged with aminobutyldimethylsilane (2 g; 15.2 mmol), 250 mL dry DCM, tetrachlorophthaloyl-anhydride (4.6 g; 16.1 mmol) and purged with dry argon. The mixture was stirred for 5 min, but the TCP-

anhydride was not completely dissolved. The TCP-anhydride became completely dissolved upon addition of dry TEA (2.2 mL; 15.8 mmol) under an argon counterflow. Stirring was continued for 1 h and the solvent removed in vacuo subsequently. A yellow oil was obtained, which was transferred to a 500 mL round-bottom flask equipped with a magnetic stir bar. Pyridine (210 mL), acetic anhyride (8.4 mL) were added and the reaction solution stirred for 20 h. Excess pyridine was removed in vacuo yielding a brown oil. The oil was transferred to a separatory funnel and 150 mL DCM were added. The organic layer was washed four times with 100 mL aqueous $NaHCO_3$ and the combined aqueous layers extracted with 100 mL DCM (2 x). The organic layer was concentrated leaving a brown solid residue. A thin layer chromatogram (ethyl acetate: petroleum ether; 1:4) showed a major product with a RF-value of 0.6 and unreacted TCP-anhydride with a RF-value of 0.1. Clean product (2.8 g; 46 %; lit. 56 %) was obtained as white needles by column chromatography (silica gel 60; mesh size 63 - 200 μm) using EtOAc : petroleum ether (1:4) as eluent.
Characterization:
^{1}H NMR ($CDCl_3$, 250 MHz) δ (ppm): 3.86 (m, 1H, **Si-H**); 3.73 (t, 2H, **N-CH_2**); 1.77 (m, 2H, **-CH_2-**); 1.45 (m, 2H, **-CH_2-**); 0.65 (m, 2H, **-Si-CH_2-**); 0.05 (d, 6H, **-Si$(CH_3)_2$-**).

Preparation of Acetoxy-aminobutyldimethylsilane

The reaction was carried out in a 50 mL two-neck round-bottom flask equipped with a septum, a condenser and a magnetic stir bar. The flask was purged with dry argon and 25 mL of dry DCM, 3 mL of aminobutyldimethylsilane (3 g; 22.9 mmol), 4.8 mL of TEA (3.5 g; 34.4 mmol) were added using a syringe. 2 mL of acetyl chloride (2.2 g; 27.4 mmol) were added slowly using a syringe while cooling (4 °C). An orange solid residue formed during 1 h 30 min of stirring. The reaction solution was transferred to a separatory funnel for work-up. The organic layer was washed with 15 mL of Milli-Q water (3 x) and the solid residue disappeared. The combined aqueous layers were

washed twice with 15 mL DCM. The organic layers were combined, dried over anhydrous $MgSO_4$ and the solvent removed in vacuo. 3.5 g (20 mmol; 89 %) acetoxy-aminobutyldimethylsilane of sufficient purity was obtained.
Characterization:
^{1}H NMR ($CDCl_3$, 250 MHz) δ (ppm): 5.84 (broad, 1H, **N-H**); 3.81 (t, 1H, **Si-H**); 3.21 (m, 2H, **N-CH_2**); 1.92 (s, 3H, **CO-CH_3**); 1.52-1.28 (m, 4H, **-$(CH_2)_2$-**); 0.58 (t, 2H, **-Si-CH_2-**); 0.02 (d, 6H, **-Si$(CH_3)_2$-**).

Preparation of 4-(Dimethylsilyl)-N,N-diisopropylbenzamide

First step: Synthesis of 4-(Dimethylsilyl)benzoyl chloride

The synthesis of 4-(dimethylsilyl)benzoyl chloride was carried out as described by Kreuzer et al. [315]. The reaction was carried out in a 25 mL Schlenk flask equipped with a magnetic stir bar and a condenser. The flask was purged with dry argon prior to the reaction. 4-(Dimethylsilyl)benzoic acid (5.6 g; 31 mmol), 8 mL of dry toluene and freshly distilled thionyl chloride (2.4 mL; 31 mmol) were added under an argon counter flow. The reaction solution was stirred overnight at 50 °C , followed by removal of the solvent in vacuo. The product was attained in quantitative yield by fractional destillation and had a boiling point of 93 °C at 0.03 mbar (lit. 64 °C ; 0.03 hPa).

Second step: 4-(Dimethylsilyl)-N,N-diisopropylbenzamide

The reaction was carried out in a 50 mL two-neck round-bottom flask equipped with a dropping funnel, a condenser and a magnetic stir bar. The flask was purged with dry argon prior to the reaction. 4-(dimethylsilyl)benzoyl chloride (1.1 g; 5.54 mmol) and 9 mL of dry DCM were added under an argon counter flow. The dropping funnel was charged with N,N-diisopropylamine (1.6 mL; 11.8 mmol) and added dropwise to the solution under stirring. The reaction solution started to boil immediately, if the amine was added too fast.

Table 6.1: Synthesis conditions for hydrosilylation of poly(butadiene). TCP-aminosilane represents N-tetrachlorophthaloyl-aminobutyldimethylsilane, Ac-aminosilane represents acetoxy-aminobutyldimethylsilane and Isoprop.-carboxysilane represents 4-(dimethylsilyl)-N,N-diisopropylbenzamide.

type of silane	**amount silane / mmol**	**amount PBD / g**
TCP-aminosilane	3	0.16
TCP-aminosilane	0.4	0.16
TCP-aminosilane	1.8	1.14
Ac-aminosilane	4	1.09
Isoprop.-carboxysilane	0.6	0.16

The reaction solution was stirred for 3 h under ambient conditions and transferred to a separatory funnel for further work-up. 20 mL of DCM and 20 mL of Milli-Q water were added in order to facilitate separation of the organic and aqueous layer. The aqueous layer was removed and the organic layer washed with 20 mL of Milli-Q water three times. The combined aqueous layers were washed with 30 mL of DCM. The organic layers were combined, dried over anhydrous $MgSO_4$ and the solvent removed in vacuo. Clean product (0.9 g; 62 %) was obtained by column chromatography (silica gel 60; mesh size 63 - 200 μm) using EtOAc : petroleum ether (1:1) as eluent.

Characterization:

^{1}H NMR ($CDCl_3$, 250 MHz) δ (ppm): 7.45 (d, 2H, **ortho-ArH**); 7.20 (d, 2H, **meta-ArH**); 4.36 (m, 2H, **-N-CH-**); 3.52 (broad, 1H, **Si-H**); 1.38 (broad, 12H, **CH-(CH_3)$_2$**); 0.26 (d, 6H, **-Si(CH_3)$_2$-**).

Hydrosilylation of Poly(butadiene) using Karstedt catalyst

The hydrosilylation reactions were carried out in a 50 mL Schlenk flask equipped with a magnetic stir bar. The flask was charged with a predetermined amount of poly(butadiene) and a predetermined amount of the respective protected silane (see Tab. 6.1). The flask was evacuated, purged with argon and 5 mL of dry toluene added. The flask was capped with a stopper, and three freeze-pump-thaw cycles were executed. 3 drops of Karstedt catalyst

(~20 μL) were added to the flask after transfer to a glove box. The flask was removed from the glove box and the reaction solution refluxed overnight. The catalyst was removed by pressing the reaction solution through a short column filled with silica gel (silica gel 60; mesh size 63 - 200 μm) and the solvent removed in vacuo subsequently, yielding a brown viscous liquid. The liquid was precipitated into MeOH to remove unreacted silane. Excess MeOH was decanted and the functionalized polymer dried in vacuum.

Characterization of N-tetrachlorophthaloyl-aminobutyldimethylsilane functionalized PBD:

^{1}H NMR ($CDCl_3$, 250 MHz) δ (ppm): 5.62 (m, -C**H**=CH_2); 4.92 (m, -CH=C**H$_2$**); 3.73 (t, **N-CH$_2$**); 2.08-1.14 (**backbone** & **-CH$_2$-**); 0.56 (m, **-Si-CH$_2$-**); 0.05 (d, **-Si(CH$_3$)$_2$-**).

Characterization of acetoxy-aminobutyldimethylsilane functionalized PBD:

^{1}H NMR ($CDCl_3$, 250 MHz) δ (ppm): 5.83 (m, -C**H**=CH_2); 5.00 (m, -CH=C**H$_2$**); 3.33 (m, **N-CH$_2$**); 2.41-1.36 (**backbone** & **-(CH$_2$)$_2$-** & **CO-CH$_3$**); 0.58 (t, **-Si-CH$_2$-**); 0.00 (d, **-Si(CH$_3$)$_2$-**).

Characterization of 4-(dimethylsilyl)-N,N-diisopropylbenzamide functionalized PBD:

^{1}H NMR ($CDCl_3$, 250 MHz) δ (ppm): 7.45 (d, **ortho-ArH**); 7.20 (d, **meta-ArH**); 5.44 (m, -C**H**=CH_2); 4.89 (m, -CH=C**H$_2$**); 4.42 (m, **-N-CH-**); 2.08-1.14 (**backbone & CH-(CH$_3$)$_2$**); 0.26 (d, **-Si(CH$_3$)$_2$-**).

Deprotection of Amino-groups in N-Tetrachlorophthaloyl-aminobutyldimethylsilane functionalized PBD

The reaction was carried out in a 25 mL round-bottom flask equipped with a magnetic stir bar. The flask was charged with the functionalized PBD (0.1 g), 9 mL of THF, 3 mL acetonitrile and 55 μL ethylenediamine (0.8 mmol) and the reaction solution stirred overnight at 60 °C . The reaction solution was transferred to a separatory funnel for work-up. 5 mL of Milli-Q water and 5 mL of DCM were added in order to facilitate separation of the organic and aqueous layer. The aqueous layer was extracted with 10 mL of DCM. The combined organic layers were washed with 10 mL of Milli-Q water (2 x), dried over anhydrous $MgSO_4$ and the solvent removed in vacuo. The residue was dissolved in 3 mL THF and precipitated into 8 mL MeOH. Excess solvent was decanted and the amino-functionalized PBD dried in vacuum.

Characterization:

^{1}H NMR ($CDCl_3$, 250 MHz) δ (ppm): 5.62 (m, -C**H**=CH_2); 4.92 (m, -CH=C**H**$_2$); 3.70 (t, **N-CH$_2$**); 2.08-1.14 (**backbone** & **-CH$_2$-**); 0.56 (m, **-Si-CH$_2$-**); 0.05 (d, **-Si(CH$_3$)$_2$-**).

7 Methods

7.1 Drop-on-Demand Inkjet Printing

Inkjet printing setup

Manufacturer: Gesellschaft fuer Silizium-Mikrosysteme mbH (GeSIM),
Grosserkmannsdorf, Germany

Device: Nano-Plotter$^{©}$ NP 2.0

Dispensing area: 302 x 410 mm / width x depth

Mechanical repeatability: $\pm 10\ \mu m$

xy-speed: 0-50 cm/s

Micropipette: Piezoelectric tip / Pico-Tip
droplet volume $\sim 100 pl$

Software: NPC16 V. 2.14

The Nano-Plotter$^{©}$ NP 2.0 is a highly advanced drop-on-demand inkjet system [318, 319]. The most important part of the system is the mobile pipet dispenser, which is moved using step motors. The dispenser is equipped with a piezo-driven microdosage head that works in a noncontact regime. The drop-volume can be precisely controlled with the piezo-driven microdosage head. A high reproducibility in drop-volume is thus achieved and only 2% of 1000 drops deviate from the desired volume. The software provided by the manufacturer allows for fully automated control and operation of the system. Manual control of the drop position is possible, in addition. The respective drop position can be defined in the live image provided by the video microscope. The video assisted drop positioning is suitable for more complex substrate, like microcantilever arrays.

7.2 Ellipsometry

Ellipsometry setup

Manufacturer: Nanofilm Technologies GmbH, Goettingen, Germany

Device: Imaging Spectroscopic Ellipsometer EP^3

Light Source: Laser ($\lambda = 532\ nm$)
Xenon lamp ($\lambda = 403\ -\ 1000\ nm$)

Detector: CCD-camera (768 x 572 $pixel$)

Objective: 10x (field of view 390 x 300 $\mu m\ /\ horizontal\ x\ verticalsize$)

Lateral resolution: $\sim 2\ \mu m$

Angle of incidence: 60 $degrees$

Theoretical background [176,320]

Ellipsometry provides information on the optical properties and thickness of thin layers. Reliable data regarding film thickness can be obtained from films as thin as a monolayer of atoms up to tens of micrometers. Ellipsometry is relying on the fact that polarized light is reflected at a surface, at least to a large part, as shown in Fig. 7.1. Interactions between the surface and the incident polarized light upon reflection leads to a change in polarization state, which can be measured. A polarization state of light is be characterized by two orthogonal polarization components. One component is oriented parallel to the plane of incidence, and the other one perpendicular. Differences in phase and amplitude between the electric waves in the two polarization directions can be measured precisely, but have no direct meaning. Ellipsometry is considered an indirect technique therefore. Data evaluation has to

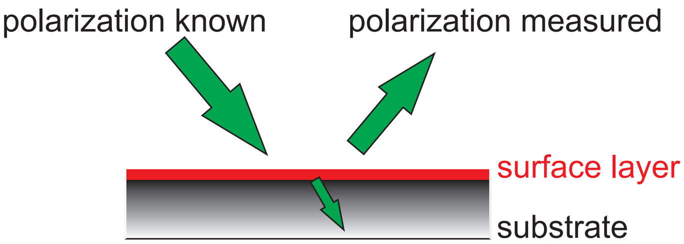

Fig. 7.1: Schematic illustration of the measurement principle in ellipsometry.

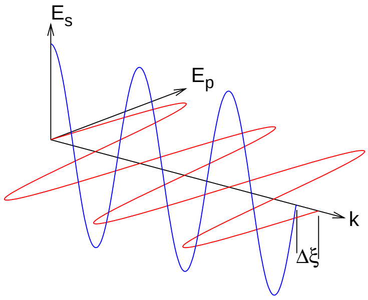

Fig. 7.2: Schematic illustration of an electromagnetic wave with the wave vector k split up into its two orthogonal components.

be implemented in order to extract the optical properties and the film thickness. The evaluation has to take into account that the measured quantities are functions of wavelength, angle of incidence and polarization state of incident light. Data evaluation typically requires the construction of a model, which in turn allows to predict the parameters of interest. The unknown parameters defining the model, e.g. film thickness or optical constants, are varied in such a way, that the model data resembles the experimental data. Once an acceptable fit is achieved, one assumes that the model represents the true structure of the studied sample.

The theory of light, as described by Maxwells equation, is the basis of ellipsometry. Maxwells equations allow one to describe a monochromatic, polarized beam of light as an electromagnetic wave with the wave vector $\overrightarrow{E}$. A polarization state is characterized by two orthogonal electric waves.

One wave is oriented parallel to the plane of incidence E_P and the other one perpendicular E_S, as shown in Fig. 7.2. The time-dependent terms of the

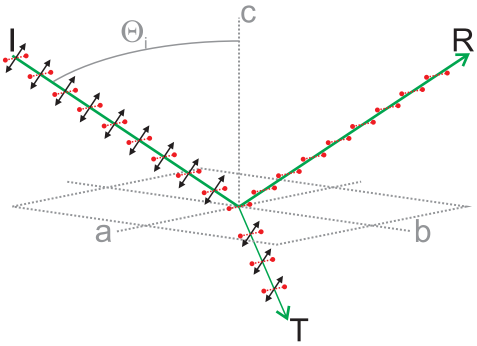

Fig. 7.3: Scheme illustration the polarization state of (I)ncident beam, (R)eflected beam, and (T)ransmitted beam.

wave equation are described by

$$E_S = E_{S0} * sin(\varpi t); \; E_P = E_{P0} * sin(\varpi t + \zeta) \tag{7.1}$$

with E_{S0} and E_{P0} as the amplitude of the particular component, the angular frequency ϖ, and the phase shift ζ. The phase shift is the most important parameter in ellipsometry and its measurement is rather simple. A beam is regarded as elliptically polarized, if the phase shift between the two components is unequal to zero ($\zeta \neq 0$). The resulting wave vector $\overrightarrow{E}$ is thus rotating on an elliptical orbit. The general equation describing such an ellipse is derived by eliminating the time in Eq. 7.1.

$$\left(\frac{E_S}{E_{S0}}\right)^2 + \left(\frac{E_P}{E_{P0}}\right)^2 - 2 * \frac{E_S * E_P}{E_{S0} * E_{P0}} * cos\, \zeta = sin^2\, \zeta \tag{7.2}$$

Eq. 7.2 describes the orbit of the resulting wave vector using the polarization components. After measuring the elliptical polarization state of a beam one can calculate the phase shift between the two components by using Eq. 7.2. The elliptical polarization state is typically measured by rotating a so-called analyzer, which is placed in front of a detector, while mapping the intensity of the transmitted beam as a function of polarizer position.

Light impinging on an interface between two media (e.g. air and glass) at an angle of incidence between $0^\circ < \Theta_i < 90^\circ$ experiences a change in polarization. The transmitted beam and the reflected beam become partially polarized, as shown in Fig. 7.3. The plane of incidence is defined by the incident beam (I) and the reflected beam (R). The beam can be divided into two orthogonal electric waves, as introduced above. The electric wave perpendicular to the plan of incidence is represented by the red dotted lines with spherical end caps, whereas the wave with parallel orientation is represented by the black lines with arrows as end caps. A beam impinging on an interface is typically passing from an optically less dense medium, such as air, into a denser medium. Thus one finds that the reflected beam is composed preferentially of the component oriented perpendicular to the plane of incidence. The transmitted beam (T), on the other hand, is composed preferentially of the component oriented parallel to the plane of incidence. The angle of incidence in Fig. 7.3 is chosen in such a way, that it matches the Brewster angle ($tan(\Theta_B) = n_i/n_t$ with n_i and n_t as the refractive indices of the two media). The component oriented parallel to the plane of incidence is thus not reflected at all. It is possible to produce linear polarized S-light in this configuration. The Fresnel equations can be used in order to calculate the reflection coefficients of the S- and P-component of the electric field.

$$r_S = \frac{E_{RS}}{E_{IS}} = \frac{n_I cos(\Theta_I) - n_T cos(\Theta_T)}{n_I cos(\Theta_I) + n_T cos(\Theta_T)};\ r_P = \frac{E_{RP}}{E_{IP}} = \frac{n_T cos(\Theta_I) - n_I cos(\Theta_T)}{n_T cos(\Theta_I) + n_I cos(\Theta_T)} \tag{7.3}$$

The reflection coefficients r_S and r_P are also referred to as the amplitudes of two components of the reflected wave. It is more convenient to use the ratio of the amplitude reflectivities r_P/r_S instead of the individual amplitudes in order to eliminate the influence of the intensity and its fluctuations. The fundamental ellipsometric equation is obtained using this ratio of amplitude reflectivities.

$$tan\Psi\ exp(i\Delta) = \frac{r_P}{r_S} \tag{7.4}$$

Ψ and Δ are referred to as the ellipsometric angles. This definition has historical reasons. The polarizer and analyzer in "nulling ellipsometers" are set at such angles, that no intensity is hitting the detector. These angles are the ellipsometric angles Ψ and Δ. The ellipsometric parameter Δ holds the information of the phase shift between the orthogonal polarized components of the beam. Thus it is related to the phase shift ζ, as introduced above. The ellipsometric parameter Ψ is related to the change in amplitude of the P- and S-components.

A typical setup for measuring the ellipsometric angles is shown in Fig. 7.4. Polarizers and retarders are the main components of any ellipsometer. A polarizer produces light in a special polarization state, as the name suggests. Linear polarizers are typically used in ellipsometers. They produce linearly polarized light by allowing one component of the incident light to pass, whereas the other component is fully suppressed. The direction of polarization of the beam can be adjusted by rotating a linear polarizer. If a polarized beam is passing through a polarizer one observe a direct dependence of the transmitted intensity on the amplitude of the component along the axis of the polarizer. A polarizer used in such a way is referred to as analyzer, because it enables one to measure the ratio of the p- and s-component of the polarized beam.

Retarders, on the other hand, allow one change the phase of the two components with respect to each other. ″Quarter-wave plates″ are commonly used as retarders. One component of a beam is passing such a plate along the ″fast″ axis, whereas the other component is passing it along the ″slow″ axis. A phase shift of 90 degrees between the two components can thus be achieved. Linearly polarized light can be transformed into circularly polarized light, if the quarter-waver plate is oriented at an angle of 45 degrees with respect to the linear polarization axis. The term compensator has be coined for a retarder that is used to transform linearly polarized light into circularly polarized light.

A combination of a linear polarizer (p) with a quarter-wave compensator (c) in rotatable mounts is a variable polarization filter. The pc-combination can be used for the generation of any desired elliptical polarization state, provided that the incident beam had S- and P-components with equal amplitudes.

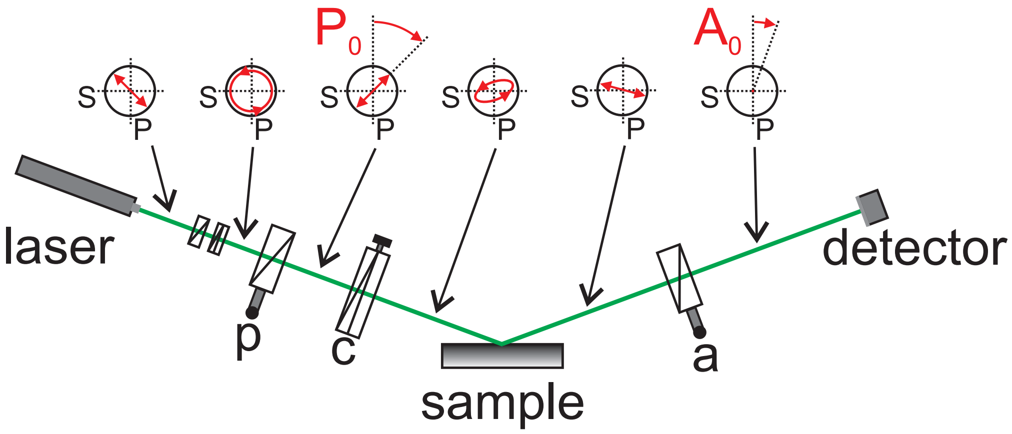

Fig. 7.4: Schematic illustration of a nulling ellipsometer in (p)olarizer - (c)ompensator-(s)ample - (a)nalyzer configuration. The polarization state after every optical component is shown in the upper part of the scheme.

Nulling ellipsometers rely on pc-combinations in order to generate light with such an elliptical polarization that perfect linearly polarized light is produced after reflection on the surface of the sample (s). The linearly polarization of the reflected beam is detected by an analyzer. The analyzer is set to a 90 degrees position compared to the axis of the linear polarization. The linearly polarized beam is extinguished, as a result, which is indicated by a minimum in detector signal.
Any nulling ellipsometer in a PCSA-configuration is operating according to the following recipe:

- Light is passed through a pc-combination and the angular setting of p and c recorded.
- p and c are adjusted in order to maintain linearly polarized light after reflection.
- Detection of the minimum in detector signal by changing the a settings.

A proper iterative routine allows one to identify the correct angle settings of p, c and a that fulfill the null conditions. The most common method is referred to as "fixed compensator nulling scheme". After fixing the compensator at a certain angle p and a are rotated subsequently. First p is rotated until the minimum in detector signal is reached and then a is rotated until no signal is recorded on the detector. Repeating the procedure iteratively leads to reliable results.

The EP^3 ellipsometer is programmed in such a way, that the described procedure is executed at two fixed values for c at ±45 *degrees*. The following equation is used by the software in order to calculate the ellipsometric angles.

$$tan\Psi\ exp(i\Delta) = \frac{r_P}{r_S} = \pm tan(A_0)\ exp\left[i\left(2P_0 + \frac{\pi}{2}\right)\right];\ \text{if}\ \ c = \pm 45^\circ \tag{7.5}$$

$$\Rightarrow (\hat{P}_0, \hat{A}_0) = (P_0 + 90^\circ,\ 180^\circ - A_0);\ \text{if}\ I(P_0, A_0) = 0 \tag{7.6}$$

The ellipsometric nulling requirement $I(P_0, A_0) = 0$ is fulfilled at four distinct positions of p, c and a. These four distinct positions are referred to as 4 zones. The ellipsometric angles are thus given by:

$$\underline{\text{Zone } 1+3:}\ \Psi = A_0;\ \Delta = 2P_0 \pm 90^\circ;\ \text{if}\ c = -45^\circ \tag{7.7}$$

$$\underline{\text{Zone } 2+4:}\ \Psi = A_0;\ \Delta = -2P_0 \pm 90^\circ;\ \text{if}\ c = 45^\circ \tag{7.8}$$

4-zone measurements have the advantage that they are free of systematic errors and have a much higher accuracy.

Model

Data evaluation was carried out using a multilayer model (Air, PMMA, initiator monolayer/SiO_2, amorphous Si), as shown in Fig. 7.5 [176]. The SiO_2 ($n_{SiO_2} = 1.46$) and initiator layer ($n_{Initiator} = 1.4603$) were treated as one layer due to the small difference in refractive indices and set to $n = 1.46$. Furthermore, for the refractive index of the dry PMMA brush film $n_{PMMA} = 1.49$ was used.

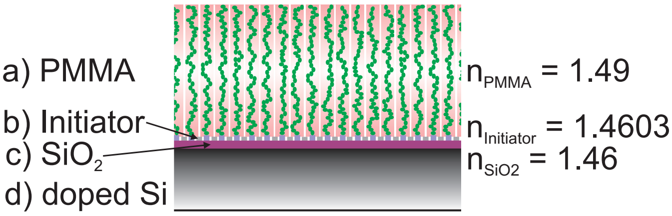

Fig. 7.5: Schematic illustration of the multilayer model used for evaluation of the data obtained by ellipsometry.

7.3 X-ray reflectivity

X-ray setup

Manufacturer: Seifert, Rudolstadt, Germany

Device: XTD 3003 TT

X-ray source: Cu-Anode ($\lambda_{Cu-K\alpha} = 1.5486 \AA$)

Monochromator: Multilayer mirror

Beam size: 1000 *x* 100 μm^2 / *horizontal x vertical size*

Resolution: $q_z \sim 6 * 10^{-3} \pm 2 * 10^{-3} \AA$

Data Evaluation Software: Parratt32 Scattering Length Density Calculator (http://www.ncnr.nist.gov/resources/sldcalc.html)

Theoretical background [321,322]

Radiation impinging on an interface will be both refracted and reflected, given that the refractive indices of the two media at the the interface are different. In general, the refractive index of a materials is less than 1 and described by

$$n = 1 - \delta + i\beta \tag{7.9}$$

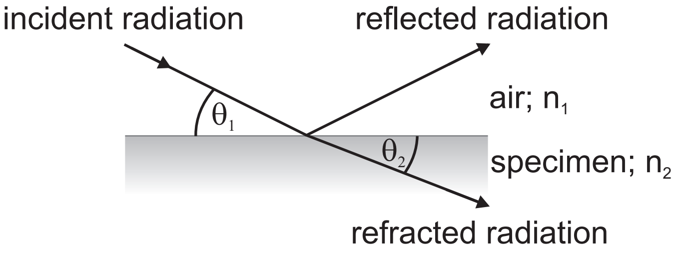

Fig. 7.6: Schematic illustration of the relationship between a beam impinging on material at an angle θ_1. A fraction of the beam is reflected at an angle θ_1, whereas the other fraction of the beam is refracted into the specimen at an angle θ_2 with respect to the interface.

The imaginary component of n is taking account of absorption by the material, whereas the real component is taking account of the scattering. Scattering of X-rays depend on the electron density ρ_{el} of the material and the wavelength λ of the incident radiation. Thus δ_X for X-rays is given by

$$\delta_X = \frac{\lambda^2 * \rho_{el} * r_0}{2\pi} \tag{7.10}$$

with the classical electron radius $r_0 = 2.82 * 10^{-13} cm$. The mass absorption coefficient μ can be used to express β_X.

$$\beta_X = \frac{\mu\lambda}{4\pi} \tag{7.11}$$

Typical values for δ_X at a wavelength of $\lambda = 1.5486 \mathring{A}$ are on the order of 10^{-6} and positive. Since air or vacuum has a refractive index of 1, most materials have an refractive index, which is less than 1. The absorption term β_X is typically smaller than δ_X by two or even three orders of magnitude. No significant error is introduced if β_X is ignored when measuring materials with low or medium atomic number.

A beam impinging on an interface between two media with refractive indices n_1 and n_2 will be refracted and reflected, as shown in Fig. 7.6. The ratio of the refractive indices determines the angle of refraction θ_2 with respect to the grazing angle of incidence θ_1, as given by Snell‘s law.

$$n_1\, cos\, \theta_1 = n_2\, cos\, \theta_2 \tag{7.12}$$

In the special case that the interface is one between air/vacuum ($n_1 = 1$) and another material (n_2), Eq. 7.12 can be rewritten as follows

$$cos\, \theta_2 = \left(\frac{1}{n_2}\right)\, cos\, \theta_1 \tag{7.13}$$

Most materials have a refractive index which is less than 1 ($n_2 < 1$), i.e. $\delta_X > 1$ following Eq. 7.9 and thus $\theta_2 < \theta_1$. This implies that the angle of refraction θ_2 is $\neq 0$ for all angles of incidence θ_1 larger than the so-called critical angle θ_c. For all angles of incidence smaller than the critical angle ($\theta_1 < \theta_c$) total external reflection is observed and the refracted beam is extinguished. The angle of refraction θ_2 becomes 0 at

$$cos\, \theta_c = cos\, \theta_1 = n_2 \tag{7.14}$$

The critical angle depends on δ_X as follows

$$\theta_c = (2 * \delta_X)^{1/2} \tag{7.15}$$

with the consequence that the critical angle is not only a material property through the electron density, but is also dependent on the wavelength of the incident radiation. Snells law (Eq. 7.12) can be rewritten using the critical angle.

$$n_2^2\, sin^2\, \theta_2 = n_1^2\, sin\, \theta_1 - n_1^2\, sin^2\, \theta_c \tag{7.16}$$

The fraction of a beam that is reflected at an interface is directly depending on the difference in wavevectors, also referred to as momentum transfer, on both sides of the interface. The geometry in reflectivity experiments is chosen in such a way, that the angle of incidence is equal to the detection angle. Solely the component of the wavevector k_z normal to the surface is thus interest in reflectivity measurements. $k_{z,0}$ (subscript 0 indicates vacuum) is defined using the wavelength of incident radiation λ and the angle of incidence θ.

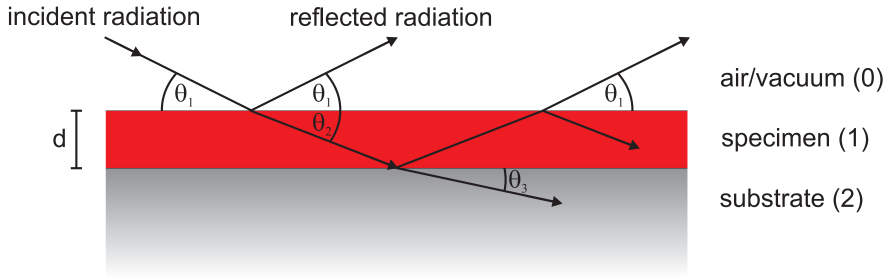

Fig. 7.7: Illustration of the beam path in a specimen on a substrate. At the interface between vacuum/specimen reflection occurs at an angle θ_1, whereas refraction occurs at an angle θ_2. Reflection and refraction events also take place at the specimen/substrate interface.

$$k_{z,0} = (2\pi/\lambda) sin\ \theta \tag{7.17}$$

Eq. 7.16 can be rewritten using the wavevector.

$$k_{z,i} = \left(k_{z,i}^2 - k_{c,i}^2\right)^{1/2} \tag{7.18}$$

The subscript indicates the specimen in this case and $k_{c,i}$ denotes the critical value of $k_{z,i}$ below which total reflection is observed. The condition of total reflection is typically identified by varying the angle of incidence while keeping λ constant. The reflection coefficient at an infinitely sharp interface separating air/vacuum and a polymer is given by

$$r_{0,1} = \frac{k_{z,0} - k_{z,1}}{k_{z,0} + k_{z,1}} \tag{7.19}$$

where the z-component of the wavevector in air is $k_{z,0}$ and in the polymer $k_{z,1}$ respectively. The reflection coefficient can be used to express the reflectivity R.

$$R = \left|\frac{k_{z,0} - k_{z,1}}{k_{z,0} + k_{z,1}}\right|^2 \tag{7.20}$$

The reflectivity is the simply the Fresnel reflectivity, in other words the fraction of an incident beam that is reflected at an interface.

Reflectivity is typically used to determine the thickness d of a specimen on a substrate. Such a system is depicted in Fig. 7.7. Two interfaces, one between vacuum/specimen and the other one between specimen/substrate, can be identified where reflection/refraction events can occur. Index 0 correspond to air/vacuum in the following, whereas index 1 corresponds to specimen and index 2 to substrate, respectively. Two reflectivity coefficients, which are described by Eq. 7.19, can be identified: between air/vacuum - specimen ($r_{0,1}$) and the other one between specimen - substrate ($r_{1,2}$). The reflectance depends on $r_{0,1}$, $r_{1,2}$ and thickness d as follows

$$r = \frac{r_{0,1} + r_{1,2}\, exp(2ik_{z,1}\, d)}{1 + r_{0,1}\, r_{1,2}\, exp(2ik_{z,1}\, d)} \tag{7.21}$$

where $k_{z,1}$ represents the scattering vector within the specimen. The reflectivity can be expressed according to Eq. 7.20 as follows

$$R(k_{z,0}) = \left| \frac{r_{0,1} + r_{1,2}\, exp(2ik_{z,1}\, d)}{1 + r_{0,1}\, r_{1,2}\, exp(2ik_{z,1}\, d)} \right|^2 \tag{7.22}$$

and can be reduce to

$$R(k_{z,0}) = \frac{r_{0,1}^2 + r_{1,2}^2 + 2\, r_{0,1}\, r_{1,2}\, cos(2k_{z,1}\, d)}{1 + r_{0,1}^2\, r_{1,2}^2 + 2\, r_{0,1}\, r_{1,2}\, cos(2k_{z,1}\, d)} \tag{7.23}$$

in the case where the reflectivity coefficients are real.

A calculated X-ray reflectivity profile [323] for a $200\AA$ thick poly(styrene) film on a glass substrate is shown in Fig. 7.8. It was assumed that both interfaces are infinitely sharp. The thickness of the film is characterized by the minima, the so-called Kiessig fringes. Differentiation of Eq. 7.23 allows one to demonstrate that minima in reflectivity are occurring once the argument of the sine function, in other words $2k_{z,1}\, d$, is a even multiple of π. The relationship between π and the argument of the sine function can be used to calculate the film thickness directly from the position of two neighboring minima.

$$d = \frac{2\pi}{\Delta k_{z,0}} \tag{7.24}$$

Determination of the film thickness using the Kiessig fringes is a first step

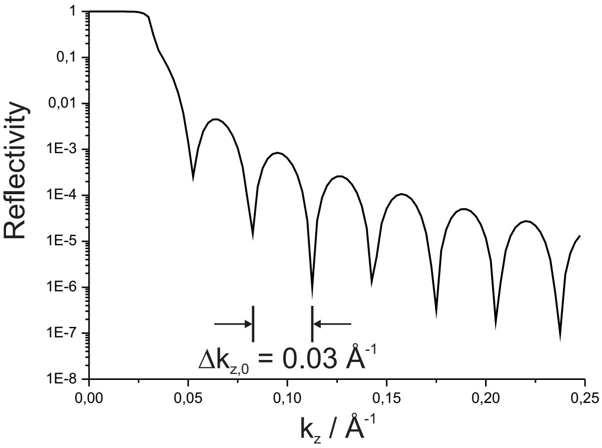

Fig. 7.8: Calculated X-ray reflectivity profile for a 200$\mathring{A}$ thick, perfectly smooth poly(styrene) film on a perfectly smooth glass substrate. The film thickness can directly be obtained from the separation distance of the minima $\Delta k_{z,0}$.

in analyzing the reflectivity profile of a sample. The film thickness can then directly be used in order to construct a model for calculating a reflectivity profile. The model parameters are varied until the calculated data resembles the experimental one. Computer programs like Parrat32 allow to calculate reflectivity profiles and fit these profiles to the experimental data.

Dampening of the Kiessig fringes is observed in the majority of reflectivity measurements. Dampening can either be a result of low contrast at the interfaces or increased interface roughness. The latter one can be taken into account by using Gaussian statistics in order to describe the deviations of the rough interface from an average value of the interface. From a mathematically point of view, one needs to convolute the infinitely sharp profile with a Gaussian smoothing function. A smearing function with a depth dependence $G(z)$ is the result of this mathematical operation.

$$G(z) = \frac{1}{(2\pi)^{1/2}\sigma} exp\left(\frac{-z^2}{2\sigma^2}\right) \tag{7.25}$$

σ represents the standard deviation of the rough interface from the average value. The smearing function leads to an expression for the Fresnel reflectivity R including the effect of roughness, as introduced by the parameter σ.

$$R(k_{z,0}) = R_F(k_{z,0})\, exp(-4k_z^2\, \sigma^2) \tag{7.26}$$

The parameter σ has a strong influence on the reflectivity profile. The absolute value of reflectivity is affected by roughness and thus the decay of the oscillations. The features of the profile are not changed by roughness however.

7.4 Gel Permeation Chromatography

GPC setup

Pump: Waters 515 HPLC Pump

Autosampler: Waters WISP 717

Columns: 3 Polymer standard service columns (SDV) in series
dimension 8 × 300 nm
porosity 500, 10^5, 10^6 Å
filled with poly(styrene/divinyl benzene)

Detector: RI ERMA Inc. ERC 7512 ERC

Eluent: Toluene at a flow rate of 1 ml/min
Tetrahydrofuran at a flow rate of 1 ml/min

Standards: low-polydispersity poly(methyl methacrylate)

Operating temperature: 20 °C

All measurements were performed by Sandra Seywald.

Theoretical background [324, 325]

Any given property of a polymer, be it of rheological nature or any other, is influenced by its molar mass M_w and to an even greater extend by its molar mass distribution. The choice of polymerization mechanism predetermines

Table 7.1: Polydispersity of selected polymerization mechanisms [78,324]

Polymer	M_w/M_n	**distribution**
Monodisperse Polymer (hypothetical)	1.000	
Living Polymer	1.01-1.05	Poisson
Controlled radical polymer	< 1.5	
Radical polymer (combination)	1.5	
Radical polymer (disproportionation) or condensation polymer	2.0	Schulz-Flory

the molar mass distribution of a polymer. This implies that knowledge of the molar mass distribution of a polymer enables to identify the polymerization mechanism, which was for the preparation of the polymer.

A selection of polymerization mechanisms is itemized in table 7.1 along with the respective polydispersity indices PDI = M_w/M_n. The PDI is a measure for the breadth of the molar mass distribution. Synthesis of polymers with predictable properties has become a major research goal. Knowledge of the molar mass distribution can give a first indication of the properties that a polymer might exhibit. Gel permeation chromatography, also referred to as size exclusion chromatography (SEC), is nowadays regarded as the standard method for determination of the molecular weight and the molar mass distribution of polymers.

GPC resembles High Performance Liquid Chromatography (HPLC) inasmuch as the sample solution is pressed through columns filled with a porous material, applying pressures ranging from 30 to 100 bar. The separation originates not from interactions between the sample and column material as in HPLC, but ideally from a size exclusion mechanism. Interactions between the column material and sample molecules have to be eliminated under all circumstances.

The gel that is filling the columns is typically swollen and all pores are occupied by solvent molecules. A concentration gradient is thus generated among the solvent filled pores and the interstitial volume, causing polymer molecules to penetrate the pores. Molecules with sizes smaller than the pores can enter them. Molecules that are bigger than the pores cannot enter them and are leaving the column at once. Molecules bigger than the pores are not separated at all, since their size is above the upper exclusion limit. Smaller molecules with the ability to enter all pores also leave the column without separation, not until the end however. This is called the separation threshold. All molecules with sizes in between those limits will be separated based on their hydrodynamic volume. The hydrodynamic radius is thus the key property that stipulates the elution time of a polymer molecule. Molecules with the same molecular weight can have different hydrodynamic volumes arising from diversity in chemical structure or topology. GPC cannot detect these differences in chemical structure or topology. Thus they will leave the column at different elution times. In contrast to that can two polymers of different molecular weight and different structure leave the column at the exact same elution time because they have equal hydrodynamic volumes, by coincidence.

Detection of sample molecules is typically done using refractive index detectors or UV-detectors. The quantity to be measured is proportional to the mass-concentration of sample molecules in the eluent, regardless of the kind of detector used.

GPC is a relative method for determining the molar mass of a polymer. Calibration with polymer standards of well-known molar mass is inevitable. The standards should have a similar structure and topology as the polymer molecules that one wants to analyze, in order to obtain reliable data.

7.5 Nuclear Magnetic Resonance Spectroscopy

^{1}H NMR setup

Manufacturer: Bruker

Device: Avance DPX 250

Frequency: 250 MHz

All samples were measured in deuterated chloroform as solvent and spectra were calibrated on that solvent. Analysis of the spectra was performed with the software MestReC.

7.6 Thermogravimetric analysis (TGA)

TGA setup

Manufacturer: Mettler-Toledo GmbH, Giessen, Germany

Device: TGA 851

Temperature range: 25 to 1000 °C

Temperature ramp: 10 °C per 60 seconds

Sample environment: nitrogen

Software: STAR^e SW 9.20

All measurements were performed by Jürgen Thiel.

Thermogravimetry is a widely used method to investigate the thermal decomposition of polymers and nanoparticles. Hence, the sample is placed on an arm of a recording microbalance, situated in a furnace. Mass changes of the material under investigation are recorded continuously while heating the sample up at a constant rate.

7.7 Differential scanning calorimetry (DSC)

DSC setup

Manufacturer: Mettler-Toledo GmbH, Giessen, Germany

Device: DSC 822

Temperature range: -140 to 220 °C
2 heating and 1 cooling run

Temperature ramp: 10 °C per 60 seconds

Sample environment: nitrogen at 30 ml per minute

Software: STAR^e SW 9.20

All measurements were performed by Jürgen Thiel.

Theoretical background [326, 327]

Differential scanning calorimetry is a thermoanalytic technique. DSC can be employed to gain information on the thermal behavior of solid and liquid materials. Glass transition, crystallization and melting can thus be observed directly. The material under investigation and a reference material of well-known heat capacity are supplied with heat in order to increase the average temperature of both with a pre-set constant rate. The sample is supplied with additional heat, once the sample temperature diverges from that of the reference. The additional heat is registered and plotted on the y-axis, whereas the average temperature of the reference is plotted on the x-axis. Physical transformations, such as phase transitions, are the reason for the divergence in sample and reference temperature. Endothermic transitions, like glass transition or melting, require an additional heat flow to maintain the compliance between sample and reference temperature and are thus registered as negative peaks. Vice versa, exothermic transitions, e.g. crystallization, produce heat in the sample and are thus registered as positive peaks.

7.8 Light Scattering

LS setup

Manufacturer: ALV, Langen, Germany

Correlator: ALV-5000

Goniometer: ALV-SP81

Light Source: Krypton-Ion-Laser ($\lambda = 647.1\ nm$)
Spectra Physics model Kr 2025

Detector: Avalanche Photodiode Module

Temperature: 25 °C

Software: ALV 5000/E

All measurements were performed by Christine Rosenauer.

7.9 Grazing Incidence Small Angle X-ray Scattering

GISAXS setup

Beamline: BW4, HASYLAB @ DESY, Hamburg, Germany

Beam size: $32\ x\ 17\ \mu m^2\ /\ horizontal\ x\ vertical\ size$ [203, 328]

Wavelength: $\lambda = 0.138\ nm$

Sample-Detector distance: 2 m

Detector: marCCD165, Rayonix, Norderstedt, Germany
2048 x 2048 pixels
79.1 μm pixel size

Angle of incidence: α_i = 0.7 degree

Data Evaluation Software: FIT-2D

7.10 Reversed Particle Interaction Apparatus

Droplet evaporation was investigated using a home-made modified AFM-related Reversed Particle Interaction Apparatus [174, 329]. Calibration of the cantilever spring constant was carried out with this apparatus, additionally. The setup is comprised of three units. The first unit is the Reversed Particle Interaction Apparatus itself. The second unit is a piezoelectric drop generator. A standard video microscope for visualizing drop deposition and evaporation is the third unit.

Setup

Laser: 5 mW
$\lambda = 670\ nm$

Photo-sensitive diode: $20\ x\ 20\ mm^2$ active area
-10 to 10 V dynamic range

Cantilever: Octosensis arrays (Micromotive GmbH, Mainz, Germany)
$500\ \mu m$ length
$2\ \mu m$ thickness

Piezoelectric drop generator: Piezodropper (Universität Bremen)
operated in drop-on-demand mode
2 m/s droplet velocity

Camera system: 5x objective (Mitutoyo Crop., Kawasaki, Japan)
6.5x ultra zoom tube (Navitar Inc., Rochester, NY)
uEye UI-2210-C CCD camera; 640 x 480 pixels (IDS GmbH, Obersulm, Germany)
KL 1500 white light source (Schott, Mainz, Germany)

Software: LabView (National Instruments Corp., Austin, TX)

Calibration of cantilever spring constant needs to be carried out prior to any investigation of drop evaporation. The added-mass method, proposed by Cleveland [330], was chosen. A small known mass was deposited on the very end of a cantilever and the shift in resonance frequency due to the additional mass was measured. The small know mass was in this case a water microdroplet placed on the cantilever with the piezodropper.

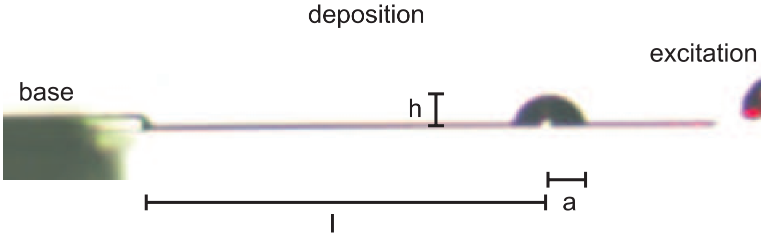

Fig. 7.9: Image of water drop on microcantilever acquired with the camera system. The dimension of the drop (h, a) and its exact position(l) were extracted from this image.

The exact mass of the water microdroplet needs to be determined. The dimensions of the drop can be obtained from images, such as the one shown in Fig. 7.9, which can be acquired with the camera system. The drop volume was calculated using the height of the drop h and its radius a relying on Eq. 3.4. Determining the mass was then a matter of multiplying the volume with the density of water. Eq. 7.27 was obtained by rearranging Eq. 3.3 and allows to calculate the spring constant k using the mass of the water droplet m_i.

$$k = \frac{4\pi^2 f_0^2 f_i^2 m_i}{\left(f_0^2 - f_i^2\right)} \tag{7.27}$$

The added-mass method is only applicable if the droplet is placed on the very end of a cantilever, as stated above. The image in Fig. 7.9 shows that the drops cannot be placed at the very end of a cantilever due to its spatial extension. It is necessary to take the drop position into account when calculating the spring constant. The dependence of the spring constant on the drop position is given by

$$k_d = \frac{k}{l_0^3} * l_d^3 \tag{7.28}$$

where k_d is the spring constant of the cantilever with the drop placed at a distance from the base l_d and not on the very end. k is the spring constant as calculated from Eq. 7.27, assuming that the drop would be position at the very end of the cantilever with length l_0. k_d can be used for the drop evaporation experiments as is.

Bibliography

[1] Feynman, R. P., *Science and Engineering* **1960**, *23*(5), 22–36.

[2] Ball, P., *Chemistry World* **2009**, *6*(1), 58–62.

[3] Matheson, R. R., *Polymer Reviews* **2006**, *46*(4), 341–346.

[4] Grest, G. S.; Advances in polymer science; polymers in confined environments; In Granick, S., Eds., *Advances in Polymer Science; Polymers in confined environments*, Vol. 138 of *Advances in Polymer Science : 138*, pages 149–183. Springer-Verlag New York, Inc., 1999.

[5] Ratner, B. D., Hoffmann, A. S., Schoen, F., und Lemons, J., *Biomaterials Science. An Introduction to Materials in Medicine;* Academic Press, San Diego, 1996.

[6] Rühe, J., Novotny, V., Clarke, T., und Street, G., *Journal of Tribology Transactions ASME* **1996**, *118*, 663.

[7] Webster, O. W., *Science* **1991**, *251*(4996), 887–893.

[8] Szwarc, M., *Nature* **1956**, *178*(4543), 1168–1169.

[9] Shipp, D. A., *Journal of Macromolecular Science-Polymer Reviews* **2005**, *C45*(2), 171–194.

[10] Solomon, E. H., Rizzardo, E., und Cacioli, P.; Patent: New polymerization process and polymers produced thereby, **1985**.

[11] Georges, M. K., Veregin, R. P. N., Kazmaier, P. M., und Hamer, G. K., *Macromolecules* **1993**, *26*(11), 2987–2988.

[12] Hawker, C. J., Bosman, A. W., und Harth, E., *Chemical Reviews* **2001**, *101*(12), 3661–3688.

[13] Chiefari, J., Chong, Y. K., Ercole, F., Krstina, J., Jeffery, J., Le, T. P. T., Mayadunne, R. T. A., Meijs, G. F., Moad, C. L., Moad, G., Rizzardo, E., und Thang, S. H., *Macromolecules* **1998**, *31*(16), 5559–5562.

[14] Le, T. P., Moad, G., Rizzardo, E., und Thang, S. H.; Patent: Polymerization with living characteristics with controlled dispersity, polymers prepared thereby, and chain-transfer agents used in the same., **1998**.

[15] Moad, G., Chiefari, J., Chong, Y. K., Krstina, J., Mayadunne, R. T. A., Postma, A., Rizzardo, E., und Thang, S. H., *Polymer International* **2000**, *49*(9), 993–1001.

[16] Wang, J. S. und Matyjaszewski, K., *Journal of the American Chemical Society* **1995**, *117*(20), 5614–5615.

[17] Kato, M., Kamigaito, M., Sawamoto, M., und Higashimura, T., *Macromolecules* **1995**, *28*(5), 1721–1723.

[18] Matyjaszewski, K. und Xia, J., *Chemical Reviews* **2001**, *101*, 2921–2990.

[19] Barner-Kowollik, C., *Handbook of RAFT;* Wiley-VCH, Weinheim, Germany, 2008.

[20] Fischer, H., *Chemical Reviews* **2001**, *101*(12), 3581–3610.

[21] Yoshikawa, C., Goto, A., und Fukuda, T., *Macromolecules* **2002**, *35*(15), 5801–5807.

[22] Kamigaito, M., Ando, T., und Sawamoto, M., *Chemical Reviews* **2001**, *101*(12), 3689–3745.

[23] Litvinenko, G. und Müller, A. H. E., *Macromolecules* **1997**, *30*(5), 1253–1266.

[24] Matyjaszewski, K., *Macromolecules* **1999**, *32*(26), 9051–9053.

[25] Qiu, J. und Matyjaszewski, K., *Macromolecules* **1997**, *30*(19), 5643–5648.

[26] Matyjaszewski, K., Wang, J. L., Grimaud, T., und Shipp, D. A., *Macromolecules* **1998**, *31*(5), 1527–1534.

[27] Matyjaszewski, K., Shipp, D. A., McMurtry, G. P., Gaynor, S. G., und Pakula, T., *Journal of Polymer Science Part a-Polymer Chemistry* **2000**, *38*(11), 2023–2031.

[28] Matyjaszewski, K., Shipp, D. A., Wang, J. L., Grimaud, T., und Patten, T. E., *Macromolecules* **1998**, *31*(20), 6836–6840.

[29] Gillies, M. B., Matyjaszewski, K., Norrby, P. O., Pintauer, T., Poli, R., und Richard, P., *Macromolecules* **2003**, *36*(22), 8551–8559.

[30] Le Grognec, E., Claverie, R., und Poli, R., *Journal of the American Chemical Society* **2001**, *123*(39), 9513–9524.

[31] Kotani, Y., Kamigaito, M., und Sawamoto, M., *Macromolecules* **1999**, *32*(8), 2420–2424.

[32] Matyjaszewski, K., Wei, M. L., Xia, J. H., und McDermott, N. E., *Macromolecules* **1997**, *30*(26), 8161–8164.

[33] Granel, C., Dubois, P., Jerome, R., und Teyssie, P., *Macromolecules* **1996**, *29*(27), 8576–8582.

[34] Lecomte, P., Drapier, I., Dubois, P., Teyssie, P., und Jerome, R., *Macromolecules* **1997**, *30*(24), 7631–7633.

[35] Pintauer, T. und Matyjaszewski, K., *Coordination Chemistry Reviews* **2005**, *249*(11-12), 1155–1184.

[36] Tang, W. und Matyjaszewski, K., *Macromolecules* **2006**, *39*(15), 4953–4959.

[37] Xia, J. H. und Matyjaszewski, K., *Macromolecules* **1997**, *30*(25), 7697–7700.

[38] Patten, T. E., Xia, J. H., Abernathy, T., und Matyjaszewski, K., *Science* **1996**, *272*(5263), 866–868.

[39] Advincula, R. C., Brittain, W. J., Baster, K. C., und Rühe, J., *Polymer Brushes: Synthesis, Characterization, Applications;* Wiley-VCH, Weinheim, 2004.

[40] Halperin, A., Tirrell, M., und Lodge, T. P., *Advances in Polymer Science* **1992**, *100*, 31–71.

[41] Jones, R. A. L. und Richards, R. W., *Polymers at Surfaces and Interfaces;* Cambridge University Press, Cambridge, 1999.

[42] Fleer, G. J., Cohen Stuart, M. A., Scheutjens, J. M. H. M., Cosgrove, T., und Vincent, B., *Polymers at Interfaces;* Chapman & Hall, London, 1993.

[43] Decher, G., *Multilayer Thin Films: Sequential Assembly of Nanocomposite Materials;* Wiley-VCH, Weinheim, Germany, 2002.

[44] Mathauer, K., Embs, F., und Wegner, G.; Comprehensive polymer science; Vol. 1, Suppl., page 449. Pergamon Press, Oxford, 1992.

[45] Ulman, A., *An Introduction to Ultrathin Organic Films. From Langmuir-Blodgett to Self-assembly;* Academic Press Inc., New York, 1991.

[46] Pellerite, M. J., Wood, E. J., und Jones, V. W., *Journal of Physical Chemistry B* **2002**, *106*(18), 4746–4754.

[47] Hoffmann, P. W., Stelzle, M., und Rabolt, J. F., *Langmuir* **1997**, *13*(7), 1877–1880.

[48] Xia, Y. N. und Whitesides, G. M., *Angewandte Chemie-International Edition* **1998**, *37*(5), 551–575.

[49] Krenkler, K. P., Laible, R., und Hamann, K., *Angewandte Makromolekulare Chemie* **1976**, *53*(JUL), 101–123.

[50] Tsubokawa, N., Hosoya, M., Yanadori, K., und Sone, Y., *Journal of Macromolecular Science-Chemistry* **1990**, *A27*(4), 445–457.

[51] Kopf, A., Baschnagel, J., Wittmer, J., und Binder, K., *Macromolecules* **1996**, *29*(5), 1433–1441.

[52] Mansky, P., Liu, Y., Huang, E., Russell, T. P., und Hawker, C. J., *Science* **1997**, *275*(5305), 1458–1460.

[53] Prucker, O. und Rühe, J., *Macromolecules* **1998**, *31*(3), 592–601.

[54] Kawaguchi, M. und Takahashi, A., *Advances in Colloid and Interface Science* **1992**, *37*(3-4), 219–317.

[55] Wu, T., Efimenko, K., und Genzer, J., *Journal of the American Chemical Society* **2002**, *124*(32), 9394–9395.

[56] Husemann, M., Malmstrom, E. E., McNamara, M., Mate, M., Mecerreyes, D., Benoit, D. G., Hedrick, J. L., Mansky, P., Huang, E., Russell, T. P., und Hawker, C. J., *Macromolecules* **1999**, *32*(5), 1424–1431.

[57] Emmerling, S. G. J., Langer, L. B. N., Pihan, S. A., Lellig, P., und Gutmann, J. S., *Macromolecules* **2010**, *43*(11), 5033–5042.

[58] Prucker, O. und Rühe, J., *Macromolecules* **1998**, *31*(3), 602–613.

[59] Prucker, O. und Rühe, J., *Langmuir* **1998**, *14*(24), 6893–6898.

[60] Edmondson, S., Osborne, V. L., und Huck, W. T. S., *Chemical Society Reviews* **2004**, *33*(1), 14–22.

[61] Boyes, S. G., Granville, A. M., Baum, M., Akgun, B., Mirous, B. K., und Brittain, W. J., *Surface Science* **2004**, *570*(1-2), 1–12.

[62] Tsujii, Y., Ejaz, M., Sato, K., Goto, A., und Fukuda, T., *Macromolecules* **2001**, *34*(26), 8872–8878.

[63] Ejaz, M., Yamamoto, S., Ohno, K., Tsujii, Y., und Fukuda, T., *Macromolecules* **1998**, *31*(17), 5934–5936.

[64] Pyun, J., Kowalewski, T., und Matyjaszewski, K., *Macromolecular Rapid Communications* **2003**, *24*(18), 1043–1059.

[65] Matyjaszewski, K., Miller, P. J., Shukla, N., Immaraporn, B., Gelman, A., Luokala, B. B., Siclovan, T. M., Kickelbick, G., Vallant, T., Hoffmann, H., und Pakula, T., *Macromolecules* **1999**, *32*(26), 8716–8724.

[66] Xiao, D. Q. und Wirth, M. J., *Macromolecules* **2002**, *35*(8), 2919–2925.

[67] von Werne, T. und Patten, T. E., *Journal of the American Chemical Society* **1999**, *121*(32), 7409–7410.

[68] Pyun, J., Jia, S. J., Kowalewski, T., Patterson, G. D., und Matyjaszewski, K., *Macromolecules* **2003**, *36*(14), 5094–5104.

[69] Blomberg, S., Ostberg, S., Harth, E., Bosman, A. W., Van Horn, B., und Hawker, C. J., *Journal of Polymer Science Part a-Polymer Chemistry* **2002**, *40*(9), 1309–1320.

[70] Koylu, D. und Carter, K. R., *Macromolecules* **2009**, *42*(22), 8655–8660.

[71] Devaux, C., Chapel, J. P., Beyou, E., und Chaumont, P., *European Physical Journal E* **2002**, *7*(4), 345–352.

[72] Goto, A. und Fukuda, T., *Progress in Polymer Science* **2004**, *29*(4), 329–385.

[73] Fukuda, T., *Journal of Polymer Science Part a-Polymer Chemistry* **2004**, *42*(19), 4743–4755.

[74] Ramakrishnan, A., Dhamodharan, R., und Rühe., *Macromol. Rapid Commun.* **2002**, *23*, 612616.

[75] Jones, D. M. und Huck, W. T. S., *Advanced Materials* **2001**, *13*(16), 1256–1259.

[76] Shah, R. R., Merreceyes, D., Husemann, M., Rees, I., Abbott, N. L., Hawker, C. J., und Hedrick, J. L., *Macromolecules* **2000**, *33*(2), 597–605.

[77] Tsujii, Y., Ohno, K., Yamamoto, S., Goto, A., und Fukuda, T., *Advances in Polymer Science* **2006**, *197*, 1–45.

[78] Elias, H.-G., *Macromolecules;* Vol. 3 of *Physical Structures and Properties;* Wiley-VCH, Weinheim, 2008.

[79] Kim, J. B., Bruening, M. L., und Baker, G. L., *Journal of the American Chemical Society* **2000**, *122*(31), 7616–7617.

[80] Jordan, R., Ulman, A., Kang, J. F., Rafailovich, M. H., und Sokolov, J., *Journal of the American Chemical Society* **1999**, *121*(5), 1016–1022.

[81] Yamamoto, S., Ejaz, M., Tsujii, Y., und Fukuda, T., *Macromolecules* **2000**, *33*(15), 5608–5612.

[82] Ejaz, M., Yamamoto, S., Tsujii, Y., und Fukuda, T., *Macromolecules* **2002**, *35*(4), 1412–1418.

[83] Jones, D. M., Brown, A. A., und Huck, W. T. S., *Langmuir* **2002**, *18*(4), 1265–1269.

[84] Yamamoto, S., Ejaz, M., Tsujii, Y., Matsumoto, M., und Fukuda, T., *Macromolecules* **2000**, *33*(15), 5602–5607.

[85] Milner, S. T., *Science* **1991**, *251*(4996), 905–914.

[86] deGennes, P. G., *Macromolecules* **1980**, *13*(5), 1069–1075.

[87] Flory, P. J., *Principles of Polymer Chemistry;* Cornell University Press, London, 1971.

[88] Alexander, S., *Journal De Physique* **1977**, *38*(8), 983–987.

[89] Ferry, J. D., *Macromolecules* **1980**, *13*(6), 1719–1720.

[90] Noda, I., Kato, N., Kitano, T., und Nagasawa, M., *Macromolecules* **1981**, *14*(3), 668–676.

[91] Daoud, M., Cotton, J. P., Farnoux, B., Jannink, G., Sarma, G., Benoit, H., Duplessix, R., Picot, C., und Gennes, P. G. D., *Macromolecules* **1975**, *8*(6), 804–818.

[92] Auroy, P., Auvray, L., und Leger, L., *Physical Review Letters* **1991**, *66*(6), 719–722.

[93] deGennes, P. G.; Scaling concepts in polymer physics, **1979**.

[94] des Cloizeaux, J. und Jannink, G., *Polymers in solution;* Clarendon Press, Oxford, 1990.

[95] Cosgrove, T., Heath, T., Vanlent, B., Leermakers, F., und Scheutjens, J., *Macromolecules* **1987**, *20*(7), 1692–1696.

[96] Wijmans, C. M., Scheutjens, J. M. H. M., und Zhulina, E. B., *Macromolecules* **1992**, *25*(10), 2657–2665.

[97] Milner, S. T., Witten, T. A., und Cates, M. E., *Macromolecules* **1988**, *21*(8), 2610–2619.

[98] Milner, S. T., Witten, T. A., und Cates, M. E., *Europhysics Letters* **1988**, *5*(5), 413–418.

[99] Zhulina, E. B., Borisov, O. V., Pryamitsyn, V. A., und Birshtein, T. M., *Macromolecules* **1991**, *24*(1), 140–149.

[100] Auroy, P., Mir, Y., und Auvray, L., *Physical Review Letters* **1992**, *69*(1), 93–95.

[101] Murat, M. und Grest, G. S., *Macromolecules* **1989**, *22*(10), 4054–4059.

[102] Daoud, M. und Cotton, J. P., *Journal De Physique* **1982**, *43*(3), 531–538.

[103] Milewski, J. V., *History of Polymer Science and Technology;* Marcel Dekker Inc., New York, 1982.

[104] Bianconi, P. A., Lin, J., und Strzelecki, A. R., *Nature* **1991**, *349*(6307), 315–317.

[105] Berg, J. M., Tymoczko, J. L., und Stryer, L., *Biochemistry;* W. H. Freeman and Company, New York, 5 ed., 2003.

[106] Delmonte, J., *Metal Polymer Composites;* Kluwer Academic Publishers, Norwell, MA, 1989.

[107] Newnham, R. E., *Reports on Progress in Physics* **1989**, *52*(2), 123–156.

[108] Lyons, A. M., Nakahara, S., Marcus, M. A., Pearce, E. M., und Waszczak, J. V., *Journal of Physical Chemistry* **1991**, *95*(3), 1098–1105.

[109] Alexandre, M. und Dubois, P., *Materials Science & Engineering R-Reports* **2000**, *28*(1-2), 1–63.

[110] Balazs, A. C., Emrick, T., und Russell, T. P., *Science* **2006**, *314*(5802), 1107–1110.

[111] Odian, G., *Principles of Polymerization;* John Wiley & Sons, Inc., Hoboken, NJ, 2004.

[112] Mayes, A. M., *Nature Materials* **2005**, *4*(9), 651–652.

[113] Ahmad, Z. und Mark, J. E., *Materials Science & Engineering C-Biomimetic and Supramolecular Systems* **1998**, *6*(2-3), 183–196.

[114] Theng, B. K. G., *The Chemistry of Clay-Organic Reactions;* Wiley, New York, 1974.

[115] Calvert, P., *Potential applications of nanotubes;* Carbon Nanotubes. CRC Press, Boca Raton, FL, 1997.

[116] Breuer, O. und Sundararaj, U., *Polymer Composites* **2004**, *25*(6), 630–645.

[117] Favier, V., Canova, G. R., Shrivastava, S. C., und Cavaille, J. Y., *Polymer Engineering and Science* **1997**, *37*(10), 1732–1739.

[118] Gauthier, R., Joly, C., Coupas, A. C., Gauthier, H., und Escoubes, M., *Polymer Composites* **1998**, *19*(3), 287–300.

[119] Mayer, A. B. R., *Materials Science & Engineering C-Biomimetic and Supramolecular Systems* **1998**, *6*(2-3), 155–166.

[120] Lechmann, M. C., Kessler, D., und Gutmann, J. S., *Langmuir* **2009**, *25*(17), 10202–10208.

[121] Mark, J. E., *Polymer Engineering and Science* **1996**, *36*(24), 2905–2920.

[122] Herron, N. und Thorn, D. L., *Advanced Materials* **1998**, *10*(15), 1173–+.

[123] Jones, R. A. L., *Soft Condensed Matter;* Oxford University Press, New York, 2002.

[124] Herron, N., *The Handbook of Nanophase Materials;* Marcel Dekker, New York, 1997.

[125] Calvert, P., Lin, T. L., und Martin, H., *High Performance Polymers* **1997**, *9*(4), 449–456.

[126] Breuer, O., Sundararaj, U., und Toogood, R. W., *Polymer Engineering and Science* **2004**, *44*(5), 868–879.

[127] Edwards, D. C., *Journal of Materials Science* **1990**, *25*(10), 4175–4185.

[128] Bartholome, C., Beyou, E., Bourgeat-Lami, E., Chaumont, P., und Zydowicz, N., *Macromolecules* **2003**, *36*(21), 7946–7952.

[129] von Werne, T. und Patten, T. E., *Journal of the American Chemical Society* **2001**, *123*(31), 7497–7505.

[130] Zhou, Q. Y., Wang, S. X., Fan, X. W., Advincula, R., und Mays, J., *Langmuir* **2002**, *18*(8), 3324–3331.

[131] Flesch, C., Bourgeat-Lami, E., Mornet, S., Duguet, E., Delaite, C., und Dumas, P., *Journal of Polymer Science Part a-Polymer Chemistry* **2005**, *43*(15), 3221–3231.

[132] Caseri, W., *Macromolecular Rapid Communications* **2000**, *21*(11), 705–722.

[133] Corbierre, M. K., Cameron, N. S., Sutton, M., Laaziri, K., und Lennox, R. B., *Langmuir* **2005**, *21*(13), 6063–6072.

[134] Calvert, P. und Crockett, R., *Chemistry of Materials* **1997**, *9*(3), 650–663.

[135] Nguyen, Q. T. und Baird, D. G., *Advances in Polymer Technology* **2006**, *25*(4), 270–285.

[136] Yuan, Q. W. und Mark, J. E., *Macromolecular Chemistry and Physics* **1999**, *200*(1), 206–220.

[137] Schmelmer, U., Jordan, R., Geyer, W., Eck, W., Golzhauser, A., Grunze, M., und Ulman, A., *Angewandte Chemie-International Edition* **2003**, *42*(5), 559–563.

[138] Farhan, T. und Huck, W. T. S., *European Polymer Journal* **2004**, *40*(8), 1599–1604.

[139] Li, H. W., Muir, B. V. O., Fichet, G., und Huck, W. T. S., *Langmuir* **2003**, *19*(6), 1963–1965.

[140] Tovar, G., Paul, S., Knoll, W., Prucker, O., und Rühe, J., *Supramolecular Science* **1995**, *2*(2), 89–98.

[141] Rühe, J.; Polymers grafted from solid surfaces; In Jacobasch, H. J., Eds., *6th Dresden Polymer Discussion on Surface Modification*, Vol. 126, pages 215–222, Meissen, Germany, 1997. Huthig & Wepf Verlag.

[142] Tsai, I. Y., Crosby, A. J., und Russell, T. P.; Surface patterning; In *Cell Mechanics*, Vol. 83 of *Methods in Cell Biology*, pages 67–87. Elsevier Academic Press Inc, San Diego, 2007.

[143] Husemann, M., Morrison, M., Benoit, D., Frommer, K. J., Mate, C. M., Hinsberg, W. D., Hedrick, J. L., und Hawker, C. J., *Journal of the American Chemical Society* **2000**, *122*(8), 1844–1845.

[144] Ducker, R., Garcia, A., Zhang, J. M., Chen, T., und Zauscher, S., *Soft Matter* **2008**, *4*(9), 1774–1786.

[145] Kaholek, M., Lee, W. K., LaMattina, B., Caster, K. C., und Zauscher, S., *Nano Letters* **2004**, *4*(2), 373–376.

[146] Zapotoczny, S., Benetti, E. M., und Vancso, G. J., *Journal of Materials Chemistry* **2007**, *17*(31), 3293–3296.

[147] Kumar, A. und Whitesides, G. M., *Applied Physics Letters* **1993**, *63*(14), 2002–2004.

[148] Husemann, M., Mecerreyes, D., Hawker, C. J., Hedrick, J. L., Shah, R., und Abbott, N. L., *Angewandte Chemie-International Edition* **1999**, *38*(5), 647–649.

[149] Jones, D. M., Smith, J. R., Huck, W. T. S., und Alexander, C., *Advanced Materials* **2002**, *14*(16), 1130–1134.

[150] Zhou, F. und Huck, W. T. S., *Chemical Communications* **2005**, (48), 5999–6001.

[151] Zhou, F., Zheng, Z. J., Yu, B., Liu, W. M., und Huck, W. T. S., *Journal of the American Chemical Society* **2006**, *128*(50), 16253–16258.

[152] Love, J. C., Wolfe, D. B., Chabinyc, M. L., Paul, K. E., und Whitesides, G. M., *Journal of the American Chemical Society* **2002**, *124*(8), 1576–1577.

[153] Dyer, D. J., *Advanced Functional Materials* **2003**, *13*(9), 667–670.

[154] Jeon, N. L., Choi, I. S., Whitesides, G. M., Kim, N. Y., Laibinis, P. E., Harada, Y., Finnie, K. R., Girolami, G. S., und Nuzzo, R. G., *Applied Physics Letters* **1999**, *75*(26), 4201–4203.

[155] Kim, N. Y., Jeon, N. L., Choi, I. S., Takami, S., Harada, Y., Finnie, K. R., Girolami, G. S., Nuzzo, R. G., Whitesides, G. M., und Laibinis, P. E., *Macromolecules* **2000**, *33*(8), 2793–2795.

[156] Tu, H., Heitzman, C. E., und Braun, P. V., *Langmuir* **2004**, *20*(19), 8313–8320.

[157] Calvert, P., *Chemistry of Materials* **2001**, *13*(10), 3299–3305.

[158] Tekin, E., Smith, P. J., und Schubert, U. S., *Soft Matter* **2008**, *4*(4), 703–713.

[159] Derby, B. und Reis, N., *Mrs Bulletin* **2003**, *28*(11), 815–818.

[160] Shimoda, T., Morii, K., Seki, S., und Kiguchi, H., *Mrs Bulletin* **2003**, *28*(11), 821–827.

[161] Burns, S. E., Cain, P., Mills, J., Wang, J. Z., und Sirringhaus, H., *Mrs Bulletin* **2003**, *28*(11), 829–834.

[162] Zaugg, F. G. und Wagner, P., *Mrs Bulletin* **2003**, *28*(11), 837–842.

[163] Sankhe, A. Y., Booth, B. D., Wiker, N. J., und Kilbey, S. M., *Langmuir* **2005**, *21*(12), 5332–5336.

[164] Ramakrishnan, A., Dhamodharan, R., und Rühe, J., *Journal of Polymer Science Part a - Polymer Chemistry* **2006**, *44*(5), 1758–1769.

[165] Sormunen, G. J. und Lewis, D. E., *Synthetic Communications* **2004**, *34*(19), 3473–3480.

[166] Saytzeff, M. und Saytzeff, A., *Liebigs Annalen der Chemie* **1877**, *185*, 151–169.

[167] Einhorn, A. und Hollandt, F., *Justus Liebigs Annalen der Chemie* **1898**, *301*(1), 95–115.

[168] Marciniec, B., Gulinski, J., Urbaniak, W., und Kornetka, Z., *Comprehensive Handbook on Hydrosilylation;* Pergamon Press, 1993.

[169] Kawase, T., Shimoda, T., Newsome, C., Sirringhaus, H., und Friend, R. H.; Inkjet printing of polymer thin film transistors; In *5th International Conference on Nano-Molecular Electronics (ICNME2002)*, pages 279–287, Kobe, Japan, 2002. Elsevier Science Sa.

[170] Nett, S. K., Kircher, G., und Gutmann, J. S., *Macromolecular Chemistry and Physics* **2009**, *210*(11), 971–976.

[171] Miyake, T., Tanii, T., Kato, K., Hosaka, T., Kanari, Y., Sonobe, H., und Ohdomari, I., *Chemical Physics Letters* **2006**, *426*(4-6), 361–364.

[172] http://www.solvaychlorinatedinorganics.com/; Hydrochloric acid - boiling point, **2010**.

[173] http://www.inorganics.basf.com/; Sulfuric acid - boiling point, **2010**.

[174] Liu, C. J. und Bonaccurso, E., *Review of Scientific Instruments* **2010**, *81*(1).

[175] http://www.seilnacht.com/; Sulfuric acid - density, **2010**.

[176] Azzam, N. M. und Bashara, R. M. A., *Ellipsometry and Polarized Light;* Elsevier Science Publishing Co Inc., North-Holland, Amsterdam, 1977.

[177] Bumbu, G. G., Kircher, G., Wolkenhauer, M., Berger, R., und Gutmann, J. S., *Macromolecular Chemistry and Physics* **2004**, *205*(13), 1713–1720.

[178] Thundat, T., *ORNL Reviews* **2004**, *37*(1), 16.

[179] Bhushan, B., *Handbook of Nanotechnologies;* Nanomechanical Cantilever Array Sensors. Springer, Berlin, Heidelberg, New York, 2 ed., 2007.

[180] Barnes, J. R., Stephenson, R. J., Welland, M. E., Gerber, C., und Gimzewski, J. K., *Nature* **1994**, *372*(6501), 79–81.

[181] Berger, R., Delamarche, E., Lang, H. P., Gerber, C., Gimzewski, J. K., Meyer, E., und Güntherodt, H. J., *Science* **1997**, *276*(5321), 2021–2024.

[182] Battiston, F. M., Ramseyer, J. P., Lang, H. P., Baller, M. K., Gerber, C., Gimzewski, J. K., Meyer, E., und Güntherodt, H. J., *Sensors and Actuators B-Chemical* **2001**, *77*(1-2), 122–131.

[183] Brunt, T. A., Rayment, T., Oshea, S. J., und Welland, M. E., *Langmuir* **1996**, *12*(24), 5942–5946.

[184] Gimzewski, J. K., Gerber, C., Meyer, E., und Schlittler, R. R., *Chemical Physics Letters* **1994**, *217*(5-6), 589–594.

[185] Moulin, A. M., O'Shea, S. J., und Welland, M. E., *Ultramicroscopy* **2000**, *82*(1-4), 23–31.

[186] Fritz, J., Baller, M. K., Lang, H. P., Rothuizen, H., Vettiger, P., Meyer, E., Güntherodt, H. J., Gerber, C., und Gimzewski, J. K., *Science* **2000**, *288*(5464), 316–318.

[187] McKendry, R., Zhang, J. Y., Arntz, Y., Strunz, T., Hegner, M., Lang, H. P., Baller, M. K., Certa, U., Meyer, E., Güntherodt, H. J., und Gerber, C., *Proceedings of the National Academy of Sciences of the United States of America* **2002**, *99*(15), 9783–9788.

[188] Lang, H. P., Berger, R., Andreoli, C., Brugger, J., Despont, M., Vettiger, P., Gerber, C., Gimzewski, J. K., Ramseyer, J. P., Meyer, E., und Guntherodt, H. J., *Applied Physics Letters* **1998**, *72*(3), 383–385.

[189] Meyer, G. und Amer, N. M., *Applied Physics Letters* **1988**, *53*(12), 1045–1047.

[190] Butt, H. J., *Journal of Colloid and Interface Science* **1996**, *180*(1), 251–260.

[191] Bumbu, G. G., Wolkenhauer, M., Kircher, G., Gutmann, J. S., und Berger, R., *Langmuir* **2007**, *23*(4), 2203–2207.

[192] Helm, M., Servant, J. J., Saurenbach, F., und Berger, R., *Applied Physics Letters* **2005**, *87*(6), 3.

[193] Zhao, J., Berger, R., und Gutmann, J. S., *Applied Physics Letters* **2006**, *89*(3).

[194] Berger, R., Lang, H. P., Gerber, C., Gimzewski, J. K., Fabian, J. H., Scandella, L., Meyer, E., und Güntherodt, H. J., *Chemical Physics Letters* **1998**, *294*(4-5), 363–369.

[195] Lang, H. P., Hegner, M., und Gerber, C., *Materials Today* **2005**, *8*(4), 30–36.

[196] Lang, H. P. und Gerber, C.; Microcantilever sensors; In *Stm and Afm Studies On*, Vol. 285 of *Topics in Current Chemistry*, pages 1–27. Springer-Verlag Berlin, Berlin, 2008.

[197] Baller, M. K., Lang, H. P., Fritz, J., Gerber, C., Gimzewski, J. K., Drechsler, U., Rothuizen, H., Despont, M., Vettiger, P., Battiston, F. M., Ramseyer, J. P., Fornaro, P., Meyer, E., und Güntherodt, H. J., *Ultramicroscopy* **2000**, *82*(1-4), 1–9.

[198] Jensenius, H., Thaysen, J., Rasmussen, A. A., Veje, L. H., Hansen, O., und Boisen, A., *Applied Physics Letters* **2000**, *76*(18), 2615–2617.

[199] Thundat, T., Warmack, R. J., Chen, G. Y., und Allison, D. P., *Applied Physics Letters* **1994**, *64*(21), 2894–2896.

[200] Bietsch, A., Zhang, J. Y., Hegner, M., Lang, H. P., und Gerber, C., *Nanotechnology* **2004**, *15*(8), 873–880.

[201] Bietsch, A., Hegner, M., Lang, H. P., und Gerber, C., *Langmuir* **2004**, *20*(12), 5119–5122.

[202] Lenz, S., Nett, S. K., Memesa, M., Roskamp, R. F., Timmann, A., Roth, S. V., Berger, R., und Gutmann, J. S., *Macromolecules* **2010**, *43*(2), 1108–1116.

[203] Wolkenhauer, M., Bumbu, G. G., Cheng, Y., Roth, S. V., und Gutmann, J. S., *Applied Physics Letters* **2006**, *89*(5).

[204] Nicholas, T., *Shock and Vibration Bulletin* **1968**, *38*, 13.

[205] Whiting, R., Angadi, M. A., und Tripathi, S., *Materials Science and Engineering B-Solid State Materials for Advanced Technology* **1995**, *30*(1), 35–38.

[206] Deegan, R. D., Bakajin, O., Dupont, T. F., Huber, G., Nagel, S. R., und Witten, T. A., *Nature* **1997**, *389*(6653), 827–829.

[207] Deegan, R. D., Bakajin, O., Dupont, T. F., Huber, G., Nagel, S. R., und Witten, T. A., *Physical Review E* **2000**, *62*(1), 756–765.

[208] Ko, H. Y., Park, J., Shin, H., und Moon, J., *Chemistry of Materials* **2004**, *16*(22), 4212–4215.

[209] van der Wel, G. K. und Adan, O. C. G., *Progr. Org. Coat.* **1999**, *37*(1-2), 1–14.

[210] Fan, X. J., Lee, S. W. R., und Han, Q., *Microelectronics Reliability* **2009**, pages 861–71.

[211] Han, H., Seo, J., Ree, M., Pyo, S. M., und Gryte, C. C., *Polymer* **1998**, *39*(13), 2963–2972.

[212] Barrer, R. M., *Trans. Faraday Soc.* **1939**, *35*(1), 0628–0643.

[213] Prager, S. und Long, F. A., *J. Am. Chem. Soc.* **1951**, *73*(9), 4072–4075.

[214] Berger, C. M. und Henderson, C. L., *Polymer* **2003**, *44*(7), 2101–2108.

[215] Hossenlopp, J., Jiang, L. H., Cernosek, R., und Josse, F., *J. Polymer Sci. B - Polymer Phys.* **2004**, *42*(12), 2373–2384.

[216] Xu, J. R. und Balik, C. M., *Appl. Spectroscopy* **1988**, *42*(8), 1543–1548.

[217] Linossier, I., Gaillard, F., Romand, M., und Feller, J. F., *J. Appl. Polymer Sci.* **1997**, *66*(13), 2465–2473.

[218] Yang, H. X., Sun, M., und Zhou, P., *Polymer* **2009**, *50*(6), 1533–1540.

[219] Kuhn, W., *Angewandte Chemie - Int. Ed.* **1990**, *29*(1), 1–19.

[220] Ghi, P. Y., Hill, D. J. T., und Whittaker, A. K., *Biomacromolecules* **2002**, *3*(5), 991–997.

[221] Bradley, C., Jalili, N., Nett, S. K., Chu, L. Q., Förch, R., Gutmann, J. S., und Berger, R., *Macromolecular Chemistry and Physics* **2009**, *210*(16), 1339–1345.

[222] Lang, H. P., Hegner, M., Meyer, E., und Gerber, C., *Nanotechnology* **2002**, *13*(5), R29–R36.

[223] Singamaneni, S., LeMieux, M. C., Lang, H. P., Gerber, C., Lam, Y., Zauscher, S., Datskos, P. G., Lavrik, N. V., Jiang, H., Naik, R. R., Bunning, T. J., und Tsukruk, V. V., *Adv. Mater.* **2008**, *20*(4), 653–680.

[224] Igarashi, S., Itakura, A. N., Toda, M., Kitajima, M., Chu, L., Chifene, A. N., Förch, R., und Berger, R., *Sensors and Actuators B-Chemical* **2006**, *117*(1), 43–49.

[225] Wang, W., Kaune, G., Perlich, J., Paradakis, C. M., Koumba, A. M. B., Laschewsky, A., Schlage, K., Rohlsberger, R., Roth, S. V., Cubitt, R., und Müller-Buschbaum, P., *Macromolecules* **2010**, *43*(5), 2444–2452.

[226] Winey, K. I. und Vaia, R. A., *Mrs Bulletin* **2007**, *32*(4), 314–322.

[227] Ajayan, P. M., Schadler, L. S., und Braun, P. V., *Nanocomposite Science and Technology;* Wiley-VCH, Weinheim, 2003.

[228] Poon, W. C. K. und Pusey, P. N., *Observation, Prediction and Simulation of Phase Transitions in Complex Fluids;* Vol. 460 of *NATO ASI series : Series C, Mathematical and physical sciences; 460;* Kluwer Academic Publishers, Dordrecht, 1995.

[229] Vrij, A., *Pure and Applied Chemistry* **1976**, *48*(4), 471–483.

[230] Asakura, S. und Oosawa, F., *Journal of Chemical Physics* **1954**, *22*(7), 1255–1256.

[231] Bechinger, C., Rudhardt, D., Leiderer, P., Roth, R., und Dietrich, S., *Physical Review Letters* **1999**, *83*(19), 3960–3963.

[232] Liu, Q., Ding, J., Chambers, D. E., Debnath, S., Wunder, S. L., und Baran, G. R., *Journal of Biomedical Materials Research* **2001**, *57*(3), 384–393.

[233] Bauer, F., Glasel, H. J., Decker, U., Ernst, H., Freyer, A., Hartmann, E., Sauerland, V., und Mehnert, R., *Progress in Organic Coatings* **2003**, *47*(2), 147–153.

[234] Zhang, H., Cui, Z. C., Wang, Y., Zhang, K., Ji, X. L., Lu, C. L., Yang, B., und Gao, M. Y., *Advanced Materials* **2003**, *15*(10), 777–+.

[235] Schärtl, W., Lindenblatt, G., Strack, A., Dziezok, P., und Schmidt, M., *Progress in Colloid and Polymer Science* **1998**, *110*, 285–290.

[236] Lan, Q., Francis, L. F., und Bates, F. S., *Journal of Polymer Science Part B-Polymer Physics* **2007**, *45*(16), 2284–2299.

[237] Xu, C., Ohno, K., Ladmiral, V., und Composto, R. J., *Polymer* **2008**, *49*(16), 3568–3577.

[238] Lindenblatt, G., Schärtl, W., Pakula, T., und Schmidt, M., *Macromolecules* **2001**, *34*(6), 1730–1736.

[239] Wang, X. R., Foltz, V. J., Rackaitis, M., und Böhm, G. G. A., *Polymer* **2008**, *49*(26), 5683–5691.

[240] Lindenblatt, G., Schärtl, W., Pakula, T., und Schmidt, M., *Macromolecules* **2000**, *33*(25), 9340–9347.

[241] Shull, K. R., *Macromolecules* **1996**, *29*(26), 8487–8491.

[242] Maas, J. H., Fleer, G. J., Leermakers, F. A. M., und Stuart, M. A. C., *Langmuir* **2002**, *18*(23), 8871–8880.

[243] Green, D. L. und Mewis, J., *Langmuir* **2006**, *22*(23), 9546–9553.

[244] Ramakrishnan, A. und Dhamodharan, R., *Macromolecules* **2003**, *36*(4), 1039–1046.

[245] Baumann, F., Schmidt, M., Deubzer, B., Geck, M., und Dauth, J., *Macromolecules* **1994**, *27*(21), 6102–6105.

[246] Jakuczek, L., Gutmann, J. S., Müller, B., Rosenauer, C., und Zuchowska, D., *Polymer* **2008**, *49*(4), 843–856.

[247] Marutani, E., Yamamoto, S., Ninjbadgar, T., Tsujii, Y., Fukuda, T., und Takano, M., *Polymer* **2004**, *45*(7), 2231–2235.

[248] Yoneda, Y., *Physical Review* **1963**, *131*(5), 2010–2012.

[249] Berger, R., Cheng, Y., Förch, R., Gotsmann, B., Gutmann, J. S., Pakula, T., Rietzler, U., Schartl, W., Schmidt, M., Strack, A., Windeln, J., und Butt, H. J., *Langmuir* **2007**, *23*(6), 3150–3156.

[250] Wang, M. F., Bertmer, M., Demco, D. E., Blümich, B., Litvinov, V. M., und Barthel, H., *Macromolecules* **2003**, *36*(12), 4411–4413.

[251] Tonelli, A. E., *NMR Spectroscopy and Polymer Microstructure;* The Conformational Connection. Wiley-VCH, Weinheim, Germany, 1989.

[252] Schnell, I. und Spiess, H. W., *Journal of Magnetic Resonance* **2001**, *151*(2), 153–227.

[253] Cutajar, M., Ashbrook, S. E., und Wimperis, S., *Chemical Physics Letters* **2006**, *423*(4-6), 276–281.

[254] Litvinov, V. M. und De, P. P., *Spectroscopy of Rubbers and Rubbery Materials;* Rapra Technology, Shawberry, UK, 1989.

[255] Saalwächter, K., *Progress in Nuclear Magnetic Resonance Spectroscopy* **2007**, *51*(1), 1–35.

[256] Beiner, M. und Huth, H., *Nature Materials* **2003**, *2*(9), 595–599.

[257] Wind, M., Graf, R., Renker, S., Spiess, H. W., und Steffen, W., *Journal of Chemical Physics* **2005**, *122*(1).

[258] Wind, M., Graf, R., Heuer, A., und Spiess, H. W., *Physical Review Letters* **2003**, *91*(15).

[259] Wind, M., Graf, R., Renker, S., und Spiess, H. W., *Macromolecular Chemistry and Physics* **2005**, *206*(1), 142–156.

[260] Gaborieau, M., Graf, R., Kahle, S., Pakula, T., und Spiess, H. W., *Macromolecules* **2007**, *40*(17), 6249–6256.

[261] Smith, G. D. und Bedrov, D., *Langmuir* **2009**, *25*(19), 11239–11243.

[262] Krätschmer, W., Lamb, L. D., Fostiropoulos, K., und Huffman, D. R., *Nature* **1990**, *347*(6291), 354–358.

[263] Hebard, A. F., Rosseinsky, M. J., Haddon, R. C., Murphy, D. W., Glarum, S. H., Palstra, T. T. M., Ramirez, A. P., und Kortan, A. R., *Nature* **1991**, *350*(6319), 600–601.

[264] Stephens, P. W., Cox, D., Lauher, J. W., Mihaly, L., Wiley, J. B., Allemand, P. M., Hirsch, A., Holczer, K., Li, Q., Thompson, J. D., und Wudl, F., *Nature* **1992**, *355*(6358), 331–332.

[265] Jehoulet, C., Bard, A. J., und Wudl, F., *Journal of the American Chemical Society* **1991**, *113*(14), 5456–5457.

[266] Dubois, D., Moninot, G., Kutner, W., Jones, M. T., und Kadish, K. M., *Journal of Physical Chemistry* **1992**, *96*(17), 7137–7145.

[267] Hirsch, A., Brettreich, M., und Wudl, F., *Fullerenes: Chemistry and Reactions;* Georg Thieme Verlag Stuttgart, New York, 1994.

[268] Diederich, F. und Thilgen, C., *Science* **1996**, *271*(5247), 317–323.

[269] Sun, Y. P., Liu, B., und Moton, D. K., *Chemical Communications* **1996**, (24), 2699–2700.

[270] Zakharian, T. Y., Seryshev, A., Sitharaman, B., Gilbert, B. E., Knight, V., und Wilson, L. J., *Journal of the American Chemical Society* **2005**, *127*(36), 12508–12509.

[271] Geckeler, K. E. und Hirsch, A., *Journal of the American Chemical Society* **1993**, *115*(9), 3850–3851.

[272] Guhr, K. I., Greaves, M. D., und Rotello, V. M., *Journal of the American Chemical Society* **1994**, *116*(13), 5997–5998.

[273] Hawker, C. J., *Macromolecules* **1994**, *27*(17), 4836–4837.

[274] Wooley, K. L., Hawker, C. J., Frechet, J. M. J., Wudl, F., Srdanov, G., Shi, S., Li, C., und Kao, M., *Journal of the American Chemical Society* **1993**, *115*(21), 9836–9837.

[275] Cao, T. und Webber, S. E., *Macromolecules* **1995**, *28*(10), 3741–3743.

[276] Camp, A. G., Lary, A., und Ford, W. T., *Macromolecules* **1995**, *28*(23), 7959–7961.

[277] Sun, Y. P., Lawson, G. E., Bunker, C. E., Johnson, R. A., Ma, B., Farmer, C., Riggs, J. E., und Kitaygorodskiy, A., *Macromolecules* **1996**, *29*(26), 8441–8448.

[278] Nayak, P. L., Yang, K., Dhal, P. K., Alva, S., Kumar, J., und Tripathy, S. K., *Chemistry of Materials* **1998**, *10*(8), 2058–2066.

[279] Zhang, N. J., Schricker, S. R., Wudl, F., Prato, M., Maggini, M., und Scorrano, G., *Chemistry of Materials* **1995**, *7*(3), 441–442.

[280] Bergbreiter, D. E. und Gray, H. N., *Journal of the Chemical Society-Chemical Communications* **1993**, (7), 645–646.

[281] Walter, W. und Francke, W., *Beyer - Walter, Lehrbuch der Organischen Chemie;* S. Hirzel Verlag, Stuttgart, Germany, Leipzig, Germany, 2004.

[282] Batz, H. G., Franzmann, G., und Ringsdorf, H., *Angewandte Chemie-International Edition in English* **1972**, *11*(12), 1103–1104.

[283] Kessler, D., Teutsch, C., und Theato, P., *Macromolecular Chemistry and Physics* **2008**, *209*(14), 1437–1446.

[284] Kessler, D. und Theato, P., *Macromolecules* **2008**, *41*(14), 5237–5244.

[285] Kessler, D. und Theato, P., *Langmuir* **2009**, *25*(24), 14200–14206.

[286] Nilles, K. und Theato, P., *European Polymer Journal* **2007**, *43*(7), 2901–2912.

[287] Nilles, K. und Theato, P., *Journal of Polymer Science Part a-Polymer Chemistry* **2009**, *47*(6), 1696–1705.

[288] Theato, P., *Journal of Polymer Science Part a-Polymer Chemistry* **2008**, *46*(20), 6677–6687.

[289] Theato, P., Kim, J. U., und Lee, J. C., *Macromolecules* **2004**, *37*(15), 5475–5478.

[290] Eberhardt, M., Mruk, R., Zentel, R., und Theato, P., *European Polymer Journal* **2005**, *41*(7), 1569–1575.

[291] Kanan, S. A., Tze, W. T. Y., und Tripp, C. P., *Langmuir* **2002**, *18*(17), 6623–6627.

[292] Bingel, C., *Chemische Berichte-Recueil* **1993**, *126*(8), 1957–1959.

[293] Decher, G., Hong, J. D., und Schmitt, J., *Thin Solid Films* **1992**, *210*(1-2), 831–835.

[294] Decher, G., *Science* **1997**, *277*(5330), 1232–1237.

[295] Wong, J. E. und Richtering, W.; Surface modification of thermoresponsive microgels via layer-by-layer assembly of polyelectrolyte multilayers; In Richtering, W., Eds., *Smart Colloidal Materials*, Vol. 133 of *Progress in Colloid and Polymer Science*, pages 45–51. Springer-Verlag Berlin, Berlin, 2006.

[296] Wong, J. E. und Richtering, W., *Current Opinion in Colloid & Interface Science* **2008**, *13*(6), 403–412.

[297] Wong, J. E., Diez-Pascual, A. M., und Richtering, W., *Macromolecules* **2009**, *42*(4), 1229–1238.

[298] Zotti, G., Vercelli, B., und Berlin, A., *Accounts of Chemical Research* **2008**, *41*(9), 1098–1109.

[299] Hoven, C. V., Garcia, A., Bazan, G. C., und Nguyen, T. Q., *Advanced Materials* **2008**, *20*(20), 3793–3810.

[300] Han, J. T., Zheng, Y., Cho, J. H., Xu, X., und Cho, K., *Journal of Physical Chemistry B* **2005**, *109*(44), 20773–20778.

[301] Glinel, K., Dejugnat, C., Prevot, M., Schöller, B., Schönhoff, M., und von Klitzing, R., *Colloids and Surfaces A* **2007**, *303*, 3–13.

[302] Tripathy, S. K. und Kumar, J., *Handbook of Polyelectrolytes and Their Applications;* Vol. 1-3; American Scientific Publishers, Stevenson Ranch, CA, USA, 2002.

[303] Guo, X. Y., Farwaha, R., und Rempel, G. L., *Macromolecules* **1990**, *23*(24), 5047–5054.

[304] Fernyhough, C. M., Young, R. N., Poche, D., Degroot, A. W., und Bosscher, F., *Macromolecules* **2001**, *34*(20), 7034–7041.

[305] Marcos, A. G., Pusel, T. M., Thomann, R., Pakula, T., Okrasa, L., Geppert, S., Gronski, W., und Frey, H., *Macromolecules* **2006**, *39*(3), 971–977.

[306] Haszeldi, R. N., Parish, R. V., und Parry, D. J., *Journal of the Chemical Society A - Inorganic Physical Theoretical* **1969**, (4), 683.

[307] Jeyaprakash, J. D., Samuel, S., Dhamodharan, R., und Ober, C. K., *Journal of Polymer Science Part a-Polymer Chemistry* **2000**, *38*(7), 1179–1183.

[308] Lacoste, J., Delor, F., Pilichowski, J. F., Singh, R. P., Prasad, A. V., und Sivaram, S., *Journal of Applied Polymer Science* **1996**, *59*(6), 953–959.

[309] Guo, X. Y. und Rempel, G. L., *Macromolecules* **1992**, *25*(2), 883–886.

[310] Granados-Focil, S., Woudenberg, R. C., Yavuzcetin, O., Tuominen, M. T., und Coughlin, E. B., *Macromolecules* **2007**, *40*(24), 8708–8713.

[311] Takeda, K., Akiyama, A., Nakamura, H., Takizawa, S., Mizuno, Y., Takayanagi, H., und Harigaya, Y., *Synthesis-Stuttgart* **1994**, (10), 1063–1066.

[312] Kruse, C. G., Broekhof, N., und Vandergen, A., *Tetrahedron Letters* **1976**, (20), 1725–1728.

[313] Halasa, A. F., Lohr, D. F., und Hall, J. E., *Journal of Polymer Science Part a-Polymer Chemistry* **1981**, *19*(6), 1357–1360.

[314] Wang, M., Gan, D., und Wooley, K. L., *Macromolecules* **2001**, *34*(10), 3215–3223.

[315] Kreuzer, F.-H. und Winkler, P.-P.; Dimethylsilyl-substituierte benzoylchloride und verfahren zu ihrer herstellung, **1989**.

[316] Blackledge, C., Engebretson, D. A., und McDonald, J. D., *Langmuir* **2000**, *16*(22), 8317–8323.

[317] Debenham, J. S., Debenham, S. D., und FraserReid, B., *Bioorganic & Medicinal Chemistry* **1996**, *4*(11), 1909–1918.

[318] http://www.gesim.de/, **2010**.

[319] *Benutzerhanduch Nano-Plotter 2.0 / Software NPC16;* GeSIM mbh, Grosserkmannsdorf, Germany, 2004.

[320] Tompkins, H. G., Irene, E. A., und Haber, E. A., *Handbook of Ellipsometry;* Springer, Heidelberg, Germany, 2005.

[321] Russell, T. P., *Materials Science Reports* **1990**, *5*(4), 171–271.

[322] Tolan, M., *X-Ray Scattering from Soft-Matter Thin Films. Materials Science and Basic Research;* Vol. 148 of *Springer Tracts in Modern Physics;* Springer-Verlag, Berlin, Heidelberg, 1999.

[323] Parratt, L. G., *Physical Review* **1954**, *95*(2), 359–369.

[324] Mori, S. und Barth, H. G., *Size exclusion chromatography;* Springer, Berlin, 1999.

[325] Hunt, B. J. und Holding, S. R., *Size exclusion chromatography;* Blackie, Glasgow; London, 1989.

[326] Richardson, M. J., *Comprehensive Polymer Science;* Vol. Vol. I; Pergamon Press, Oxford 1989, 1989.

[327] Wunderlich, B., *Thermal Analysis;* Academic Press, Boston, 1990.

[328] Roth, S. V., Dohrmann, R., Dommach, M., Kuhlmann, M., Kroger, I., Gehrke, R., Walter, H., Schroer, C., Lengeler, B., und Müller-Buschbaum, P., *Review of Scientific Instruments* **2006**, *77*(8).

[329] Bonaccurso, E. und Butt, H. J., *Journal of Physical Chemistry B* **2005**, *109*(1), 253–263.

[330] Cleveland, J. P., Manne, S., Bocek, D., und Hansma, P. K., *Review of Scientific Instruments* **1993**, *64*(2), 403–405.

A

8 List of Abbreviations

λ	Wavelength
μm	Micrometer
μ-CP	μ-Contact Printing
μL	Microliter
^{1}H NMR	Proton Nuclear Magnetic Resonance
2-D	2-Dimensional
2-EiBBr	Ethyl 2-bromoisobutyrate
3-D	3-Dimensional
4-VBC	4-Vinylbenzoyl chloride
AFM	Atomic Force Microscopy
ATR-FT-IR	Attenuated Total Reflectance FT-IR
ATRP	Atom Transfer Radical Polymerization
b.p.	Boiling point
DCM	Dichloromethane
DSC	Differential Scanning Calorimetry
e-beam	electron beam
EBL	Electron Beam Lithography
EMA	Ethyl Methacrylate
Et$_2$O	Diethyl ether
EtOAc	Ethyl acetate
FRP	Free Radical Polymerization
FT-IR	Fourier Transform Infrared Spectroscopy
GPC	Gel Permeation Chromatography
h	Hour
HCl	Hydrochloric acid
HPLC	High Pressure Liquid Chromatography
I	Initiator

kcal	kilo calory
L	Ligand
l	Liter
LRP	Living Radical Polymerization
M_n	Number Average Molecular Weight
M_w	Weight Average Molecular Weight
mbar	Millibar
MC	Microcantilever
MeOH	Methanol
min	Minute
mL	Milliliter
mm	Millimeter
MM	Monomer
MMA	Methyl methacrylate
nL	Nanoliter
NMP	Nitroxide Mediated Polymerization
PDI	Polydispersity Index
PMDETA	N,N,N′,N″,N″-Pentamethyldiethylenetriamine
PMMA	Poly(methyl methacrylat)
QCM	Quarz Crystal Microbalance
RAFT	Reversible Addition Fragmentation Chain Transfer
React. time	Reaction time
ROP	Ring-Opening Polymerization
SAM	Self-Assembled Monolayer
SCF	Self Consistent Field
SEC	Size Exclusion Chromatography
SI-ATRP	Surface-Initiated Atom Transfer Radical Polymerization
SI-FRP	Surface-Initiated Free Radical Polymerization
SIP	Surface-Initiated Polymerization
SPL	Scanning Probe Lithography
T_g	Glass transition temperature
TEA	Triethyl amine
TGA	Thermogravimetric Analysis
THF	Tetrahydrofurane
UV	Ultraviolet

List of Figures

List of Tables